Synthesis, Characterization, and Reactivity of Early-Late Multimetallic Complexes Supported by Phosphinopyrrolides

A DISSERTATION
SUBMITTED TO THE FACULTY OF THE
UNIVERSITY OF MINNESOTA
BY

Peter L. Dunn

IN PARTIAL FULFILLMENT OF THE REQUIREMENTS
FOR THE DEGREE OF
DOCTOR OF PHILOSOPHY

Ian A. Tonks, Advisor

July 2018

Acknowledgements

First and foremost, I would like to thank my parents, Barbara and Bryan, for teaching, inspiring and providing me with a wealth of opportunities to grow as a scientist and person. I can confidently say I would not be the person I am today if it weren't for their continuous and unwavering support.

I would like Ian for welcoming me to the University of Minnesota and his group. I've learned a tremendous amount over the past five years. Thank you for always being patient and willing to talk chemistry! I'll never forget the memories of starting up the lab with Ryan, Mike, Alex, and Marie. I would like to thank all my fellow lab mates: Abby, Jimmy, Zach, Tong, Adam, Xin Yi, Ryan, Addison, Gereon and Evan. I had the privilege of working with a number of very talented undergraduate students: Alex R., T. Alex, Jacob and Qi. I couldn't have asked for a better group of people to spend time and learn with.

I grateful to many groups in the department I have worked closely with, the Lu, Ellis, Tolman, Hoye, and Douglas for helpful discussion, resources and chemicals throughout my career. In particular I would like to thank members of the Lu group, past and present, for making me feel like a member of their group. I would also like to thank Dr. Laura Clouston for synthetic and crystallographic advice over the years.

I am grateful to all my collaborators. Particularly Dr. Rebecca Carlson and Prof. Laura Gagliardi for computational aid. The ICDC subgroup crew: Camille, Wen Yang, Tom, Sai, and Zhao. I would also like to thank Dr. Sudipta Chatterjee, Dr. Samantha MacMillan and Prof. Kyle Lancaster for XAS and computational expertise.

Thanks to Dr. Victor Young Jr. and Dr. Letita Yao for help with XRD and NMR, respectively. Additionally, J.T. Moore and Dr. Ben Neisen for XRD help and discussion. I would also like to thank the Inorganometallic Catalyst Design Center and a UMN Doctoral Dissertation Fellowship for funding.

Last but not least, I would like to thank my lovely wife Diana for always being there for me. I couldn't have done it without you, and I look forward to our next adventure together.

Table of Contents

List of Figures

List of Tables

List of Schemes

Chapter 1

Bonding and Reactivity of Early-Late Multimetallic Complexes Featuring Metal-Metal Bonds

1.1 Motivation

An ongoing goal in chemistry is the further development of sustainable practices, including the use of benign and renewable reagents. A particular challenge to inorganic chemistry and industrial catalysis is the use of expensive and rare transition metals that are required for many common and necessary chemical transformations. To address this issue there has been significant focus on the development of catalysts that incorporate earth-abundant transition metals, like nickel and iron [1-2]. However, the performance of these metals compared to traditional noble metal catalysts is poor. To illustrate this, simple cross-coupling mechanisms can be compared (Figure 1.1). Palladium catalyzed cross-coupling typically proceeds from a Pd^0 starting material which then undergoes oxidative addition to form a $Pd^{II}ArX$ species. Transmetallation, with a variety of nucleophilic reagents such as organozinc (Negishi), organomagnesium (Kumada), alkenes (Heck), boronic acids (Suzuki), organotin (Stille), or organosilicon (Hiyama), then results in the formation of $Pd^{II}(R)(Nu)$ species, where both coupling partners are placed on the metal center. Reductive elimination then occurs to generate the desired cross-coupled product concomitant with regeneration of the precatalyst, Pd^0 [3-5].

In contrast to this, Ni catalyzed cross coupling is typically more complicated. Seminal work by Kochi outlined the mechanism of the homocoupling of aryl halides (Figure 1.1)[6,7]. The reaction proceeds through oxidative addition of ArX to a $LnNi^{I}X$ complex to form $LnNi^{III}X_2(Ar)$. Transmetallation with *in situ* generated $LnNi^{II}(Ar)(X)$ forms equivalents of $LnNi^{II}X_2$ and $LnNi^{III}X(Ar)_2$. The diaryl species then undergoes product forming reductive elimination to generate an Ar-Ar species while regenerating the active catalyst, $LnNi^{I}X$. The $LnNi^{II}X_2$ species is then reduced to form $LnNi^0$ and reoxidized by an equivalent of aryl halide to reform the transmetallation reagent, $LnNi^{II}(Ar)(X)$. In the case of Ni, four different metal oxidation states participate in catalysis: Ni^0, Ni^{I}, Ni^{II}, and Ni^{III}. Pd operates cleanly through a Pd^0/Pd^{II} redox couple. This makes identifying catalytically relevant intermediates difficult, as many of these oxidation states contain odd electron counts making them paramagnetic and difficult to characterize. Without knowledge of these intermediates, mechanism-based improvements are extremely challenging.

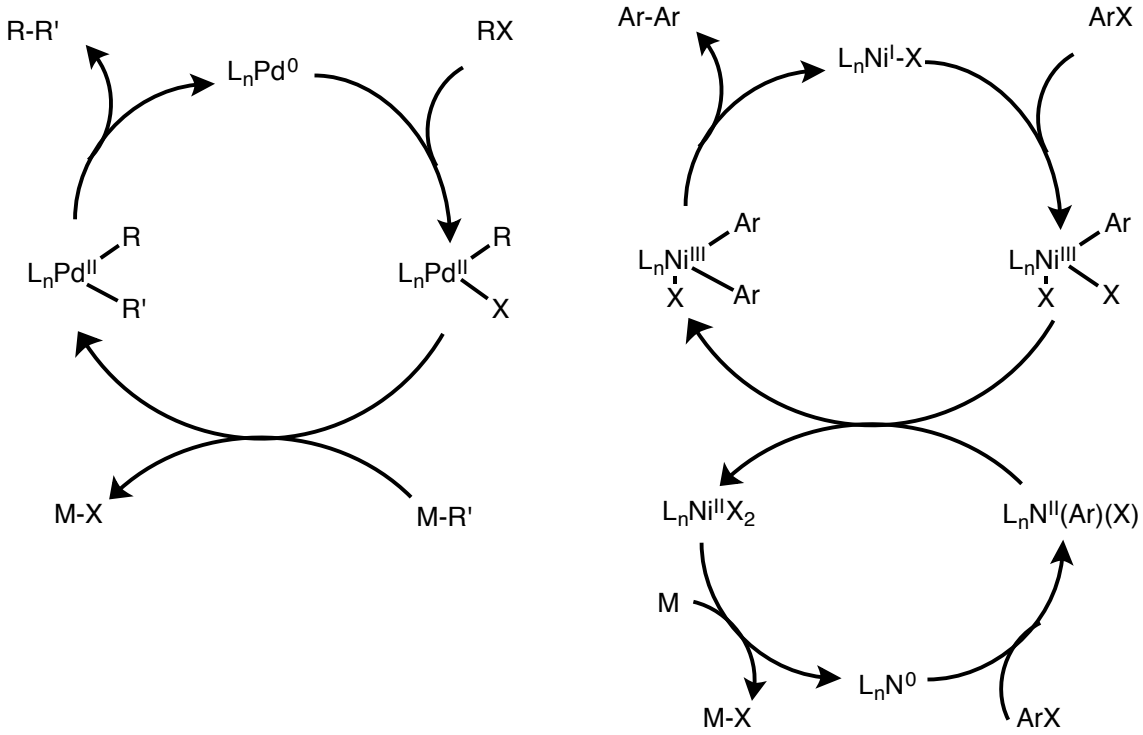

Figure 1.1: A typical cross-coupling mechanisms for Pd (left) and the mechanism of aryl-aryl coupling for Ni (right), displaying multiple possible pathways.

Since these seminal reports, nickel catalyzed cross coupling has received significant attention resulting in the development of methods for Suzuki, Negishi, Stille, Hiyama, Sonogashira, and Kumada coupling reactions [8-12]. Many of these methods exhibit wide substrate scopes and good functional group tolerance making them synthetically useful. However, mechanistic knowledge of these systems still lags behind and is often highly system dependent. For example, use of similar tridentate NNN ligands, bis(amino)amide or tripyridine (terpy), results in different mechanisms (Figure 1.2) [13-19]. While both systems proceed through the same *general* mechanism − single electron transfer (SET), radical recombination and then product forming reductive elimination − the intermediates have different oxidation states, geometries and degrees of ligand oxidation. Even the precatalysts have different electronic structures: (terpy)Ni^{II}(R) is best described as a Ni^{II} complex containing a ligand based radical while the ligand in bis(amino)amideNi^{II}(R) is monoanionic. Oxidation state assignment of the catalytic intermediates is even more difficult, ranging from Ni^{II} to Ni^{IV} depending on the degree of

ligand oxidation. In order to fine-tune these cycles towards productive product formation, intimate knowledge of the molecular and electronic structure of these intermediates is important. This is because relative reaction rates, such as reductive elimination or β hydrogen elimination, are oxidation state dependent.

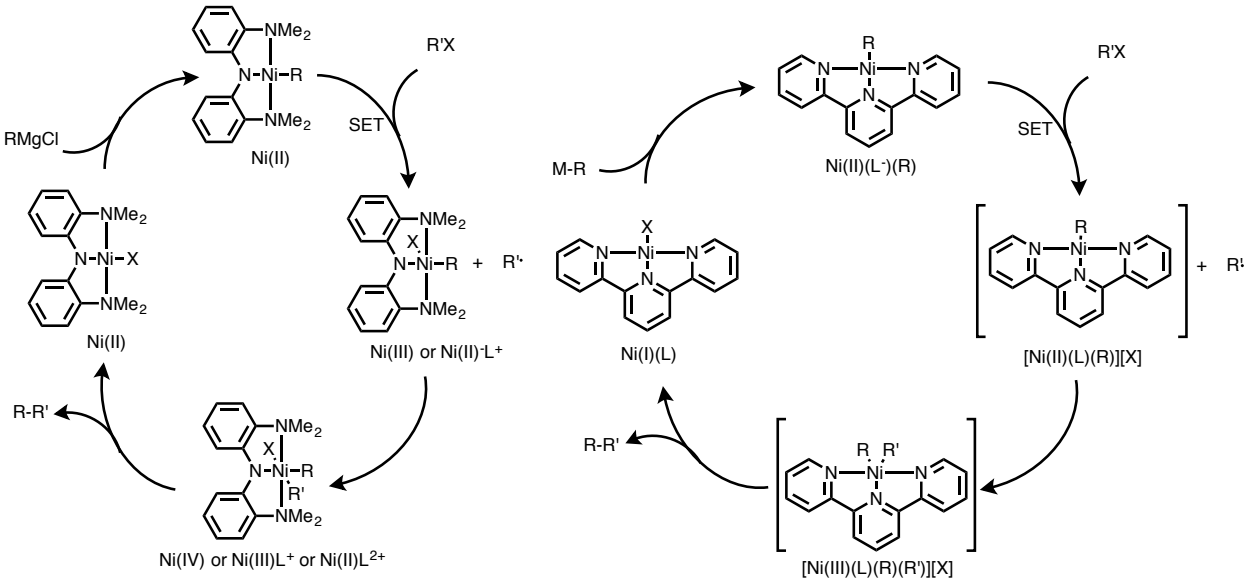

Figure 1.2: Proposed mechanisms for Ni catalyzed cross coupling for bisaminoamide (left) and terpy (right) ligand systems.

Cross-coupling reactions with first row metals typically take place at low temperatures and have short reaction times relative to Pd due to the highly reactive nature of the metal centers. Controllably harnessing the reactivity of these first-row metals represents an exciting yet difficult obstacle. Many successful and novel strategies have been developed to address this challenge including the use of redox non-innocent ligand scaffolds[20-33] and metal/ligand or metal/metal cooperative reactivity.

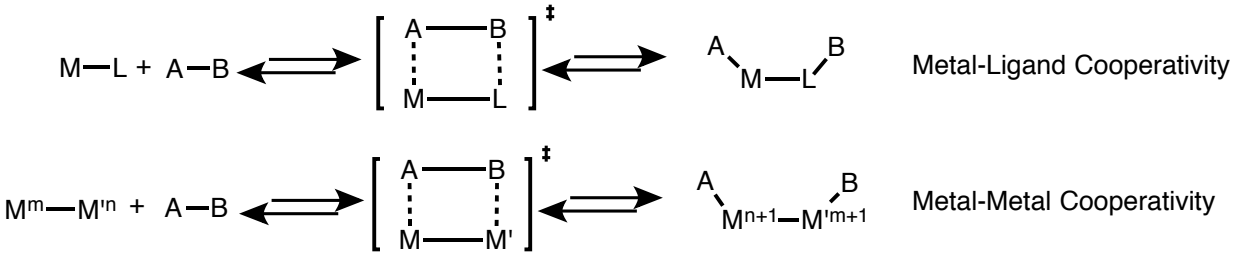

Figure 1.3: Generalized schemes for metal-ligand and metal-metal cooperativity.

Within the field of metal/ligand or metal/metal cooperativity, two main strategies have been employed. First, various research groups have designed systems in which reactivity occurs on both the metal and the ligand (Figure 1.3). For example, Milstein has taken advantage of PPN or PNP pincer ligands that couple ligand aromatization/dearomatization with H_2 oxidative addition (Figure 1.4) [34-36]. The resulting species are extremely active for hydrogenation, dehydrogenation and related reactions. Building on initial results, these systems were used to activate a variety of strong bonds including C-H, O-H, N-H, and B-H bonds [34-36]. Noyori performed enantioselective catalytic transfer hydrogenation with Ruthenium diamine complexes where heterolytic H_2 cleavage occurs across the Ru-N bond [37-40]. Use of chiral diamine and auxiliary phosphine ligands resulted in enantioselective hydrogenation. Shvo designed ruthenium complexes containing a tetraphenyl cyclopentanone ligand that works cooperatively with the Ru center to add H_2 generating a metal-hydride and cyclopentenol. This species is remarkably active for transfer hydrogenation type reactivity [41-42]. Casey expanded this strategy to iron and the resulting catalyst can hydrogenate ketones [43]. In each of these examples the ligand aids the metal center by participating in the central redox event, helping the metal center towards productive catalysis. It is important to note that these strategies also improve the performance of traditional noble metal catalysts.

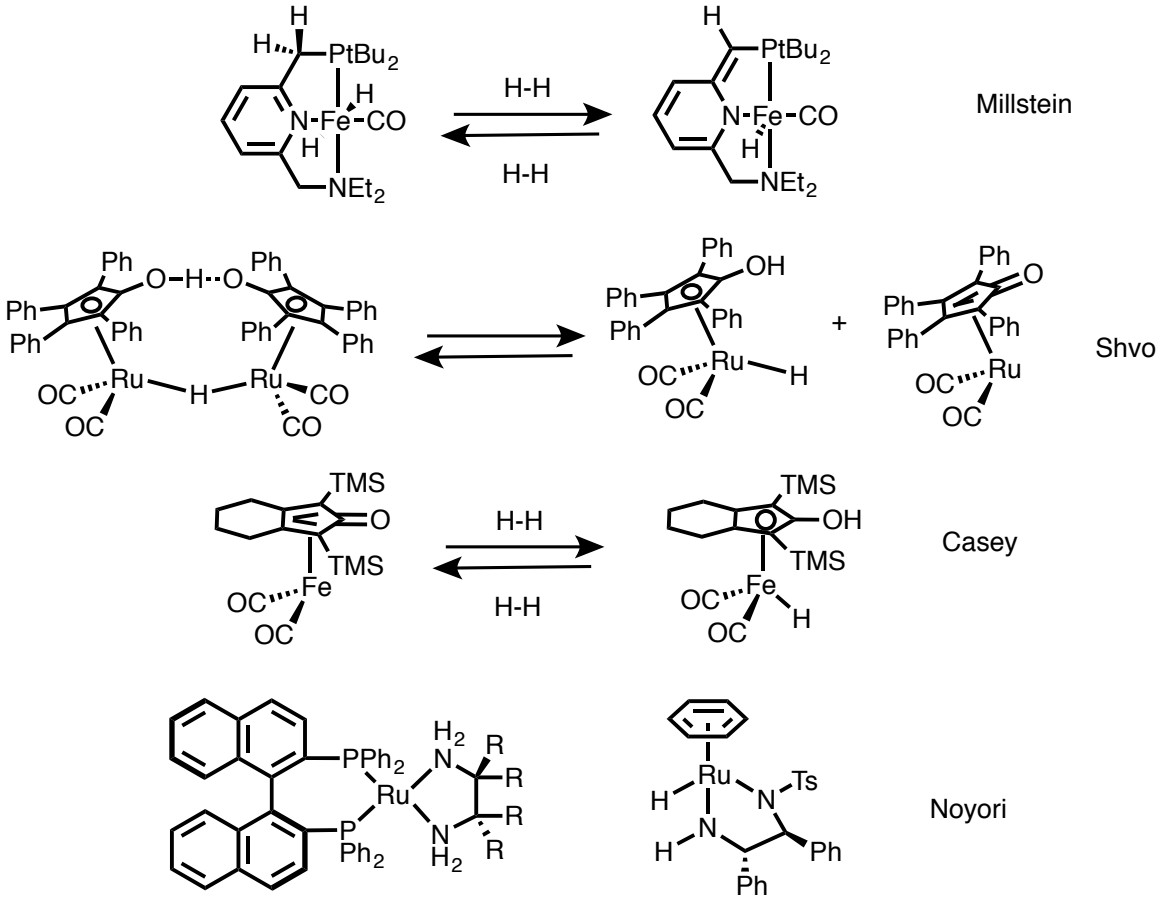

Figure 1.4: Select examples of metal-ligand cooperativity and catalysts.

If a second metal is used as a ligand, cooperative chemistry is still possible and can be broken down into two categories: first, where chemistry occurs across the two metal centers; and second, where the second metal alters the electronics of the first metal (Figure 1.3). Parkin has synthesized trigonally symmetric Ni-B complexes supported by 2-mercapto-1-t-butylimidazolyl ligands that contain dative Ni→B bonds. Reactions with various oxidants resulted in oxidative addition across the Ni-B bond [44]. Building upon this, Peters has reported several Ni borane complexes supported by bisphosphine ligands that cooperatively add H-H across the Ni-B bond en route to catalytic olefin hydrogenation (Figure 1.5) [45-46]. Mankad has recently utilized metal-metal cooperativity en route to borylation of arenes, selective hydrogenations, and Suzuki-Miyaura coupling of unactivated electrophiles [47-49]. These transformations were previously possible only with noble metals, but by using two base metals as cocatalysts, Mankad achieved high yields and selectivities.

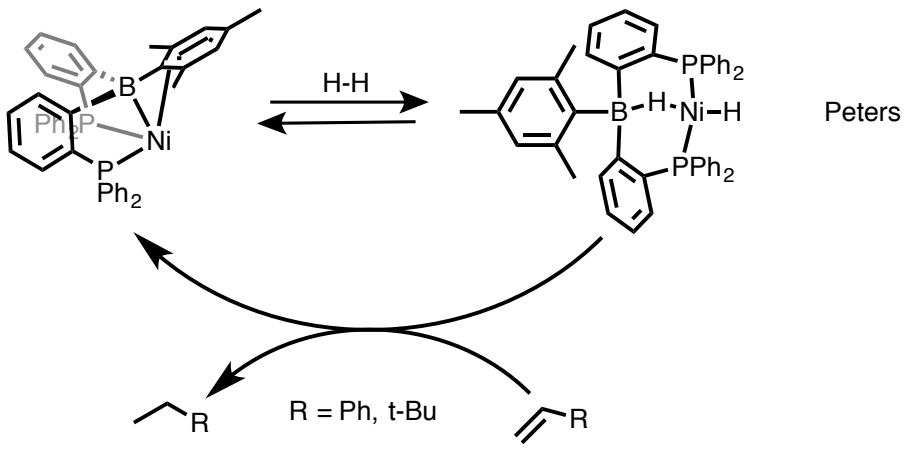

Figure 1.5: Cooperative H-H addition across a Ni-B bond.

Even more diverse reactivity is possible between two metal centers if a transition metal is substituted for the main group metal due to the enhanced redox ability of the molecule. Thomas has synthesized a variety of early-late bimetallics supported by phosphinoamides that have shown remarkable reactivity. In particular, the trigonally symmetric ZrCo complex can perform a plethora of multielectron transformations. ZrCo contains a strong metal-metal triple bond and can undergo elementary oxidative additions with both MeI and I_2, yielding a terminal iodide bound to cobalt and a bridging methyl or I- ligand (Figure 1.6) [50]. Building on these elementary oxidative addition reactions, these ZrCo complexes were also tested for various cross coupling reactions and found to be active for Kumada coupling. Reactions with nOctMgBr and various alkyl halides, including chlorides and bromides, showed good to moderate conversion to the desired C-C bond formed product. The monometallic counterpart, $CoI(PPh_2PNH^iPr)_3$, was less active for catalysis and less competent at coupling more sterically hindered substrates as well as chloride containing partners [51].

These ZrCo complexes are also capable of undergoing four electron transformations. Oxidation of $(THF)Zr(iPrNP(^iPr)_2)_3Co(N_2)$ with two equivalents of tolyl azide resulted in the formation of a new zwitterionic product, $(RN=)Zr(^iPrNP(^iPr)_2)_3Co(=NR)$ (R = Tolyl) [52] (Figure 1.6). The second oxidation event that occurs at a formally Zr(III) center must be facilitated by the presence of the

second metal center, as Zr(III) does not have the requisite electrons to undergo a two-electron oxidation.

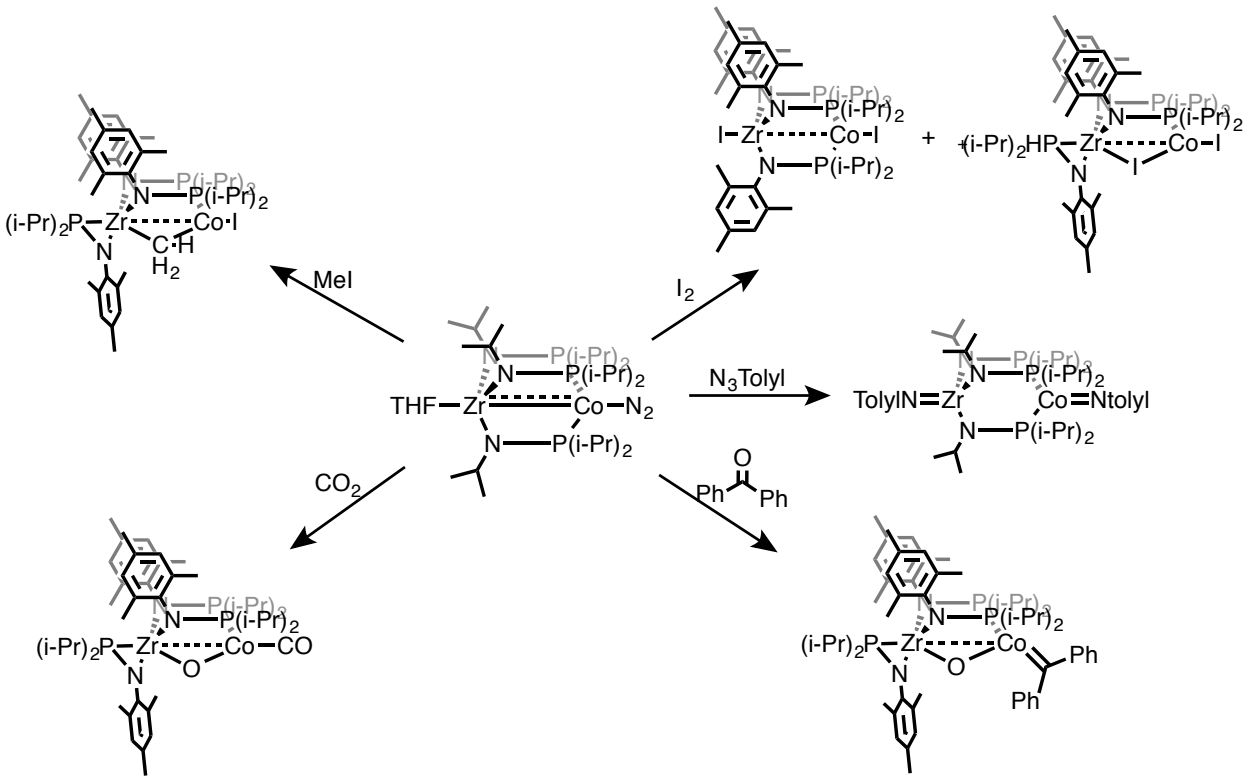

Figure 1.6: Reactivity of a ZrCo complex supported by phosphinoamides.

ZrCo can also activate strong double bonds. Reactions of (THF)Zr(MesNP(^{i}Pr)$_2$)$_3$Co with CO_2 or benzophenone resulted in full C=O cleavage and formation of (MesNP(^{i}Pr)$_2$)Zr(MesNP(^{i}Pr)$_2$)$_2$(μ-O)Co(CO) or the carbene complex (MesNP(^{i}Pr)$_2$)Zr(MesNP(^{i}Pr)$_2$)$_2$(μ-O)Co(=CPh$_2$) [53-54]. These remarkable transformations highlight the power of coupling two transition metal centers, and take advantage of the early metal's oxophilicity. Building on these results the related TiCo complex, ClTi(XylNP(^{i}Pr$_2$))$_2$CoPMe$_3$, promotes the stoichiometric McMurray coupling of aryl ketones to alkenes *via* a similar oxygen atom abstraction mechanism [55].

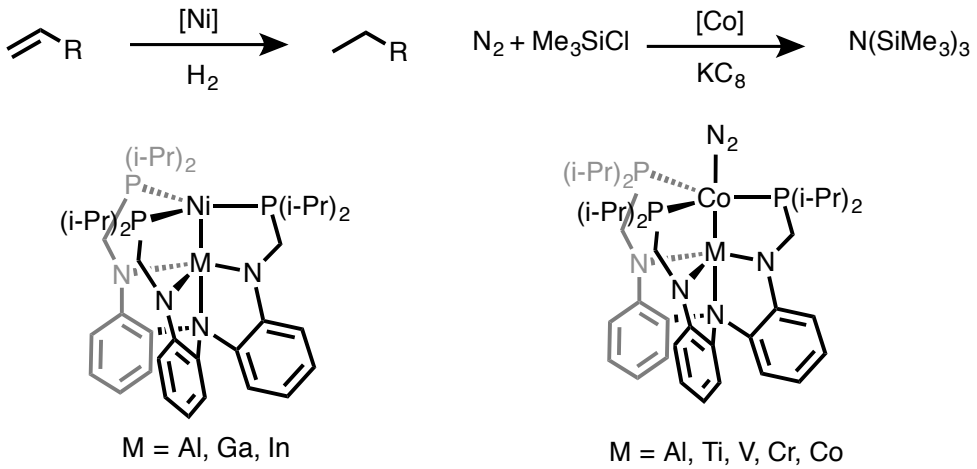

Figure 1.7: Bimetallic NiM (M = Al, Ga, In) and CoM (M = Al, Ti, V, Cr, Co) complexes supported by a heptadentate, trisphosphino(triamido)amine ligand and their catalytic N_2 silylation.

In contrast to the above examples where chemistry occurs across both metals, secondary metal centers have also been utilized to alter the electronics of a reactive metal site. Lu has synthesized several Ni-M (M = Al, Ga, In) complexes that contain short metal-metal bonds due to a dative interaction from Ni to the group 13 metal (Figure 1.7) [56]. LMNi (M = In, Ga) (L = trisphosphino(triamido)amine) both react with H_2 to form stable adducts and are active for olefin hydrogenation while the monometallic and Al adduct are inactive for catalysis. Further investigation showed that the catalyst activity tracks well with the size of the supporting metal, meaning the degree of activity can be tuned by changing the supporting metal. More recently, LGaNi has been utilized for CO_2 functionalization. Deprotonation of the LGaNi-H_2 adduct resulted in characterization of a rare anionic Ni-H species. Subsequent treatment with CO_2 resulted in the formation of a metal formate species. NiGa showed remarkable catalytic activity (3150 turnovers, TOF = 9700 h^{-1}) compared to the monometallic species, which is inactive [57].

Using the same ligand framework, CoM (M = Al, Ti, V, Cr, and Co) complexes were synthesized and utilized as N_2 reduction catalysts [58]. The dicobalt complex, LCo_2 can be synthesized from $CoCl_2$ in the presence of reductant. The reduced N_2 bound complex, K(crypt-222)$LCo_2(N_2)$ can be isolated by further reduction. Exposure of either

species to trimethylsilylchoride and reductant results in catalytic formation of tris(trimethylsilyl)amine (TON ~ 200) (Figure 1.7). Further work was performed to examine the role of the base metal in catalysis. Synthesis of a series of $LMCo(N_2)$ (M = Ti, V, Cr, Al) complexes and examination of bond N_2 lengths and stretching frequencies showed only a minor trend [59]. Subsequent examination of catalytic N_2 silylation showed all complexes were competent, though performed similarly. A slight trend was observed where more similar metal centers performed better via TON (CoCo > CoCr > CoV > CoTi > CoAl). Examination of the mechanism *via* DFT shows all complexes follow a similar mechanism, where AlCo has the largest barrier to catalysis. The remaining four bimetallic complexes are indistinguishable. However, examination of phosphine lability provides insight into catalysis: phosphine decoordination immediately follows the rate-determining step. Examination of the supporting metals' effect on phosphine labilization shows a clear trend where the more Lewis acidic metals disfavor phosphine decoordination (Al < Ti < V < Cr < Co), which coincides with catalyst rates (Co > Cr > V > Ti > Al). This indirect effect can still be used to tune the rate of catalysis.

Nagashima synthesized the heterobimetallic complexes, [(η^3-methallyl)M($Ph_2PN^tBu)2TiCl_2$](OTf) (M = Ni, Pd, Pt) from $(Ph_2PN^tBu)_2TiCl_2$ and [M(η^3-methallyl)$(acetone)_2$](OTf) (M = Ni, Pd, Pt) [60]. These complexes adopt a boat shape conformation allowing for overlap between the d_{z2} and d_{yz} orbitals resulting in strong dative bonds. This strong dative interaction increases the electrophilicity of the allyl moiety significantly enough to allow allylic amination with HNRR' substrates at room temperature (Figure 1.8). Importantly, the monometallic analogues, [(η^3-methallyl)M(dppp)](OTf) (M = Ni, Pd, Pt) do not react.

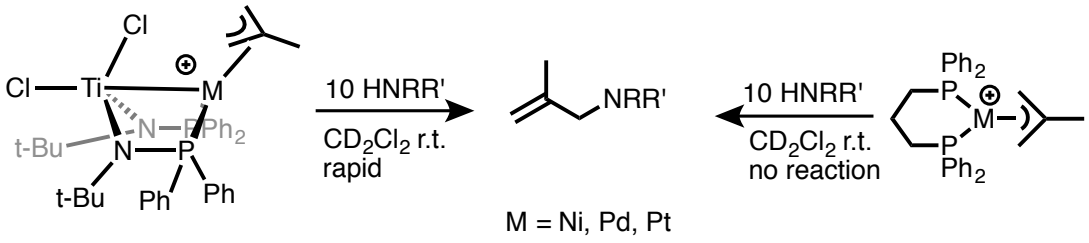

Figure 1.8. Bimetallic TiM (M = Ni , Pd, and Pt) and monometallic bisphosphine complexes and their divergent reactivity towards allylic amination.

Further examination of this reaction by the Michaelis group solidifies the role of the dative bond in this transformation [61]. Examining phosphines containing different bite angles and performing DFT calculations containing restricted geometries showed that the dative interaction lowers the activation barrier by ~ 5 kcal/mol, enabling fast catalysis. This shows that the presence of a second metal center can significantly modify reaction barriers. The Michaelis group capitalized on this phenomenon to achieve room temperature cyclizations with a variety of tethered enynes. Comparison to monometallic catalysts shows that the dative Pt->Ti interaction significantly lowers the reaction barrier towards cyclization, enabling catalysis to occur at room temperature.

In addition to acting as Lewic acids, the presence of a second metal center can also fundamentally alter bonding motifs. Berry has prepared dirhodium or diruthenium tetracarboxylate nitrene or carbene complexes that contain metal-ligand bonds that are both unusually long and measurably weaker. Spectroscopic and computational analysis of these systems shows that three (1σ and 2π) three-center/four-electron (3c/4e) bonds are present (Figure 1.9). This bonding motif results in 'superelectrophilic' character on the axial nitrene or carbene atom. The resulting species can react selectivity with C-H bonds *via* a electrophilic aromatic substitution mechanism [62-64].

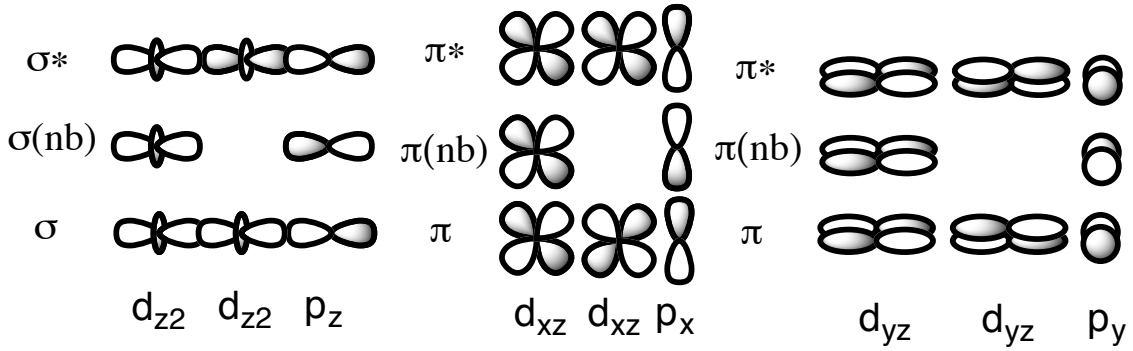

Figure 1.9: The three center Ru-Ru-N σ and π orbitals.

Given the multitude of transition metals available and the enhanced reactivity (relative to their monometallic counterparts) demonstrated by these complexes, this area is ripe for further exploration. Of particular interest are bimetallic complexes containing both an early (group 4 or 5) and late (groups 8, 9, or 10) transition metal. This is because pairing highly differentiated metal centers may result in the greatest extent of

modification compared to that of a monometallic species. The development of this field is reliant on the use of bifunctional ligands containing both hard and soft donors (often bearing hard oxygen/nitrogen and soft phosphorous donors). These ligands are amenable to stepwise metallations that allow the synthesis of heterobimetallic complexes with high site purity. The resulting complexes have significantly contributed to the fundamental study of metal-metal bonding, and have shown a diverse array of multi-electron reactivity facilitated by metal-metal cooperativity.

Accordingly, we are interested in using and studying metal-metal cooperativity to better harness the reactivity of first row metals. To achieve this, we have targeted early-late heterobimetallic complexes of bifunctional hard/soft phosphinopyrrolide ligands to further the systematic study of metal-metal bonding and reactivity in P,N-bridged complexes. While these ligands should impart σ-electronic properties somewhat similar to existing phosphinoamide or alkoxyphosphine ligand frameworks, they are much poorer N π-donors. Synthesis of early-late bimetallics based on this class of ligand should allow for systematic comparative studies of the effect of ligand π-donor ability, chelate ring size and rigidity on metal-metal bonding and reactivity.

Scope of Thesis:

The objective of this dissertation is to synthesize and characterize new molecules containing multiple metal atoms with different early/late combinations, and to explore their reactivity with small molecules. More specifically, a new NP (2-diphenylphosphinopyrrolide) ligand will be used to synthesize early-late multimetallic complexes. In chapter two, the synthesis of group 4 metalloligands supported by NP ligands will be detailed. Their structural and solution dynamics will be investigated to ascertain their ability to act as metalloligands. In the third chapter, the synthesis and characterization of a series of MNi (M = Ti, Zr, Hf) complexes will be presented. An in-depth examination of the bonding reveals all complexes contain strong dative bonds, dominated by a sigma interaction between the d_{z2} orbitals. TiPd complexes are also synthesized and the metal-metal bonding present is investigated. The fourth chapter contains the synthesis and characterization of two TiFe bimetallic complexes featuring strong metal-metal bonds. Computational and single crystal analysis suggests the presence of metal-metal triple bonds. The fifth chapter details the synthesis and reactivity of a trimetallic $TiNi_2$ species. Reactions with various L type ligands are performed to probe the ability of the metals to react cooperatively. Additionally, the 4-electron cleavage of the N=N double bond in benzo[c]cinnoline by $TiNi_2$ is reported. The mechanism of this transformation, which results in a phosphinimide and μ^3 imido, will be examined and compared to similar systems in the literature. In chapter six, the synthesis and characterization of group 5 – group 9/10 bimetallics is reported and the bonding trends present will be discussed. Finally, chapter seven contains the synthesis of a number of group 6 complexes and their application as metalloligands towards late metal carbonyl species.

Chapter 2

Synthesis, Characterization and Solution Dynamics of Group 4 Metalloligands

Reproduced in part with permission from:

Dunn, P. L.; Reath, A. H.; Clouston, L. J.; Young Jr., V. G.; Tonks, I. A. Homo- and Heteroleptic Group 4 2-(diphenylphosphino)pyrrolide Complexes: Synthesis, Coordination Chemistry and Solution State Dynamics. *Polyhedron*, **2014**, 84, 111.

2.1 Overview

The synthesis and solid state structures of homo- and heteroleptic Zr and Ti complexes of 2-(diphenylphosphino)pyrrolide (NP) are reported. The homoleptic $Zr(NP)_4$ (**2.1**) and $Ti(NP)_4$ (**2.2**) are 8-coordinate in the solid state, and both show extremely long M-P bonds of approximately 2.9 Å. In solution, the phosphine ligands in all complexes are labile: in the titanium complexes phosphine dissociation is rapid at room temperature and equilibrates all phosphines into a single ^{31}P resonance, whereas in the Zr complex **2**.**1** dissociation is slower and full equilibration does not occur until 90 °C. The potential to utilize these novel complexes as metalloligands toward other transition metals is discussed.

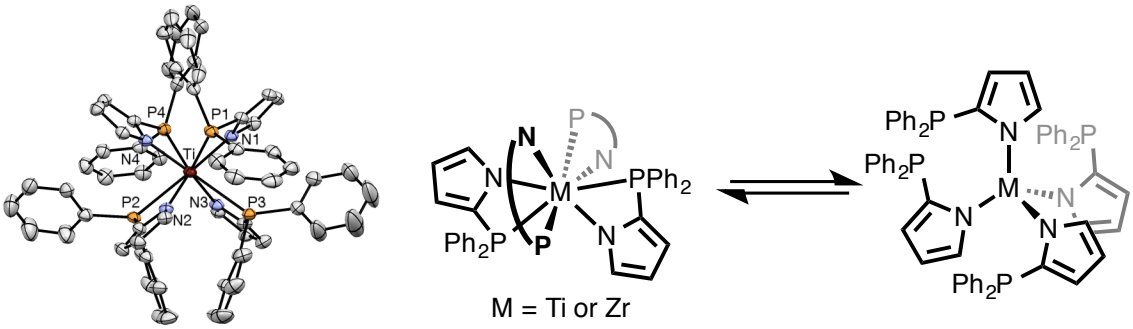

Figure 2.1. Solution dynamics of $M(NP)_4$ (M = Ti and Zr) complexes.

2.2 Introduction

Metal-metal interactions have the potential to significantly alter the electronic environment and reactivity of multimetallic complexes in comparison to their monometallic analogs [66-68]. While discrete synthetic examples containing metal-metal interactions have existed for decades, recent applications of multimetallic complexes in organometallic catalysis [47, 64, 68-73] and small molecule activation [74-77] have renewed significant interest in the fundamental structure, bonding and reactivity of this class of molecules, as well as the design and implementation of new bridging bifunctional supporting ligands.

Early/late heterobimetallic complexes have been the focus of extensive study, under the presumption that pairing highly differentiated metal centers may effect the

greatest modification of reactivity compared to that of a monometallic species [78-86]. In this regard, bulky, bridging phosphinoamide ligands have been extensively used to coordinate Lewis-acidic early transition metals to electron-rich late transition metals [87-90], resulting in a dative *Z*-type[29] $M_{Late} \rightarrow M_{Early}$ interaction that reduces electron density on the late transition metal center. This bonding motif is analogous to the *Z*-type bonding found in boratrane [91-95] and alumatrane[96-97] complexes. This electronic attenuation can be observed spectroscopically and can also have significant effects on the reactivity. For example, the CO stretching frequencies in $(CO)_3Mo(Ph_2PN^iPr)_3ZrCl$, which contains a dative Mo→Zr interaction, are shifted more than 50 cm^{-1} higher than monometallic (triphos)$Mo(CO)_3$[89]. Additionally, Nagashima has utilized this increased electrophilicity to carry out allylic amination reactions with [(η^3-methallyl)$Pd(Ph_2PN^tBu)_2TiCl_2$](OTf), which contains a dative Pd→Ti interaction that is necessary for electrophilic reactivity to occur at the Pd allyl fragment[87].

Thomas has reported on diverse chemistry stemming from trigonally-symmetric Zr/Co heterobimetallics supported by phosphinoamide ligand frameworks [50-55]. In addition to the abovementioned "*Z*-type" bonding and reactivity, Thomas has observed Zr-Co multiple bonding that yields a diverse range of 1- and 2- electron processes that can result from direct or indirect reactivity of the metal-metal multiple bond: for example, CO_2 activation, hydrosilylation, E-H and E-E (E = N, O, S) bond activation [98-108]. Based on the plethora of chemistry available from a single class of early/late metal-metal multiple bonds, it is apparent that further investigation of these types of structures is warranted.

Recent seminal work from Lu and Thomas have elucidated a number of factors that dictate the electronic structure and reactivity of trigonal homo- and heterobimetallic complexes of the first row transition metals[108]. Unlike traditional tetragonal bimetallics, trigonal systems with weaker ligand fields should promote more favorable metal-metal bonding interactions. Systematic analysis of different metal pairs and ligand donor sets has allowed Lu and Thomas to readily evaluate periodic trends on bonding. For example, metal-metal bonding with the first row transition metals is typically best when metals and coordination environments are similar, and becomes weaker (ultimately

leading to the inability to form δ- and π-bonds) as the metals and/or their coordination environments become more disparate[109-118]. In the case of first row late transition metals paired with heavier second and third row early metals, multiple bonding is possible, although highly polarized [83]. Thus, the extent of metal-metal bonding with first row transition metals is strongly dependent on the nature of the metal ions *and* metal coordination environment, rendering the bonding highly variable/tunable.

Accordingly, Nagashima and Thomas have found that subtle variation of the electronic and steric properties of phosphinoamide ligand frameworks can drastically affect the structure and reactivity of mono- and bimetallic complexes [87-90, 98-107]. Thus, we are interested in synthesizing trigonally symmetric heterobimetallic complexes of rigid, bifunctional hard/soft phosphinopyrrolide ligands to further the systematic study of metal-metal bonding and reactivity in P,N-bridged complexes. While these ligands should impart σ-electronic properties somewhat similar to existing phosphinoamide ligand frameworks, they are much poorer N π-donors. Synthesis of bimetallics based on this class of ligand should allow for systematic comparative studies of the effect of ligand π-donor ability on metal-metal bonding and reactivity, as well as the effect of chelate ring size and chelate rigidity. During our attempts to synthesize various heterobimetallics based on this ligand set, we have discovered monometallic species with unique solid state geometries and solution state dynamics that highlight significant electronic and steric differences between phosphinopyrrolide and phosphinoamide ligands. Herein we report the synthesis, structure and dynamics of several Zr and Ti complexes of 2-(diphenylphosphino)pyrrole that contain labile M-P bonds which make them ideal targets as metalloligands for a variety of other transition metals.

2.3 Results and Discussion

The homoleptic complexes, $Zr(NP)_4$ (**2.1**) and $Ti(NP)_4$ (**2.2**) (NP = 2-diphenylphosphinopyrrolide), were synthesized in moderate yield *via* salt metathesis of MCl_4 (M = Ti, Zr) with 4 equivalents of Li(NP) (Scheme 2.1).

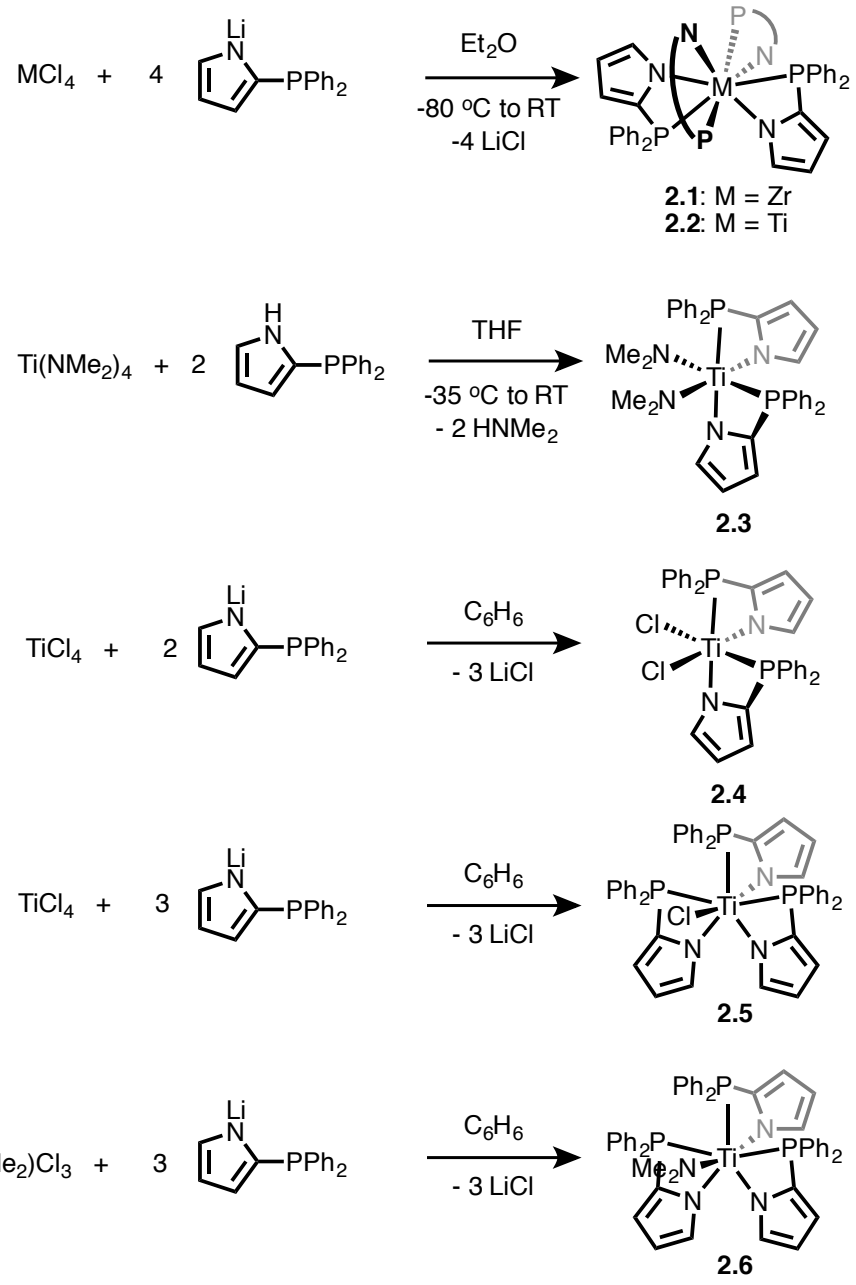

Scheme 2.1. Synthesis of group 4 complexes supported by phosphinopyrrolides.

Attempts to synthesize heteroleptic Zr phosphinopyrrolide $X_nZr(NP)_{4-n}$ complexes *via* salt metathesis were unsuccessful, giving only the homoleptic **2.1** in lower yield. Similar salt metathesis attempts by Eisen[127] and Nagashima[89] with phosphinoamide ligands have revealed that the number of successful metathesis events is sensitive to the steric environment around nitrogen, and it may be that bulkier substituents on the pyrrolide will be necessary to generate heteroleptic Zr complexes *via* direct salt metathesis. However, by prudent selection of ancillary ligands, heteroleptic Ti phosphinopyrrolides can be synthesized with 2 or 3 phosphinopyrrolide ligands (Scheme 2.1). Thomas successfully generated Zr *bis*(phosphinoamide) complexes *via* aminolysis of $Zr(NMe_2)_4$[100], and similar aminolysis of $Ti(NMe_2)_4$ with two equivalents of H(NP) yields the *bis*(pyrrolide), $(NMe_2)_2Ti(NP)_2$ (**2.3**). Interestingly, **2.3** does not yield further aminolysis products in the presence of additional equivalents of H(NP) ligand; presumably, the small Ti metal center is too sterically encumbered for additional pyrroles to coordinate and undergo deprotonation by the Ti-NMe_2 ligands. Although aminolysis attempts to *tris*(pyrrolide) Ti complexes were unsuccessful, salt metathesis of 2 or 3 equivalents of Li(NP) with $TiCl_4$ generated the *bis*(pyrrolide) $Cl_2Ti(NP)_2$ (**2.4**) *tris*(pyrrolide) $ClTi(NP)_3$ (**2.5**) and in good yield. Additionally, salt metathesis of $(NMe_2)TiCl_3$ with three equivalents of Li(NP) results in the formation of $(NMe_2)Ti(NP)_3$ (**2.6**). Complexes **2.1**-**2.5** have been characterized by X-ray crystallography, and their unique coordination geometries are discussed below.

The solid-state molecular structures of homoleptic **2.1** and **2.2** are presented in Figures 2.1 and 2.2, respectively. In the solid state, **2.1** contains an 8-coordinate Zr center with 4 κ^2-bound phosphinopyrrolide ligands. The structure is C_1-symmetric, and none of the phosphinopyrrolide ligands are related by crystallographic symmetry. The Zr-N bond lengths in **2.1** are all approximately 2.20 Å, consistent with other X-type pyrrolide bonds: a search of the CSD [121] gives a mean Zr-pyrrolide distance of 2.241 Å (range: 2.069-2.481 Å, standard deviation: 0.069 Å). Conversely, the Zr-P bonds are very long: approximately 2.90 Å compared to the mean L-type Zr-phosphine length of 2.768 Å (range: 2.606-3.033 Å, standard deviation: 0.064 Å). The overall structure of **2.2** is similar to **2.1**: somewhat surprisingly, **2.2** also adopts an 8-coordinate configuration with

4 κ^2-bound phosphinopyrrolide ligands despite the much smaller Ti metal center. The Ti-N bond lengths in **2.2** are all approximately 2.05 Å (CSD average: 2.082 Å, range: 1.955-2.293 Å, standard deviation 0.061 Å), and the Ti-P bond lengths are all approximately 2.85-2.90 Å, the longest reported in the CSD (CSD average: 2.597 Å, range: 2.485-2.876 Å, standard deviation 0.048 Å).

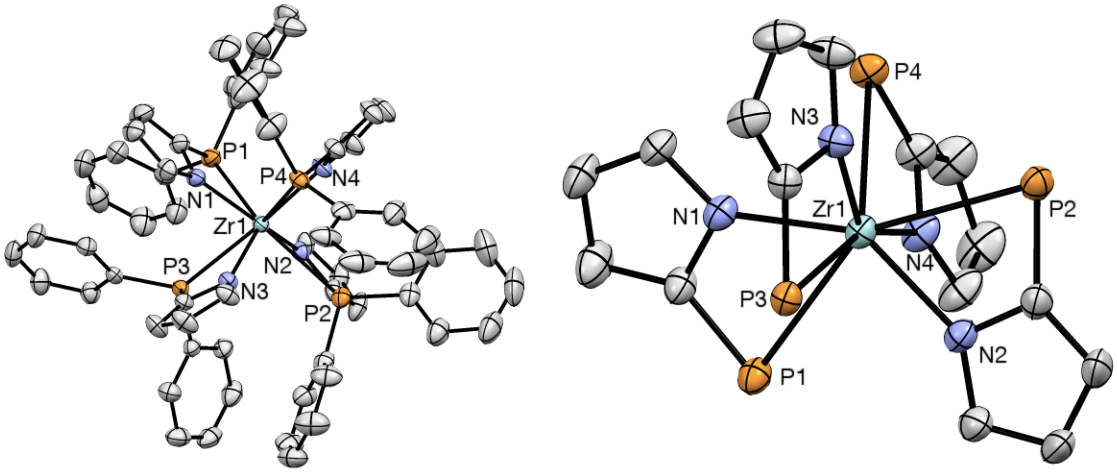

Figure 2.2. 50% thermal ellipsoid drawing of **2.1**. Top-down (left) and side-on view with phenyl groups removed (right) showing asymmetry in N,P chelate binding. Hydrogen atoms omitted for clarity. Selected bond lengths are presented in Table 2.1.

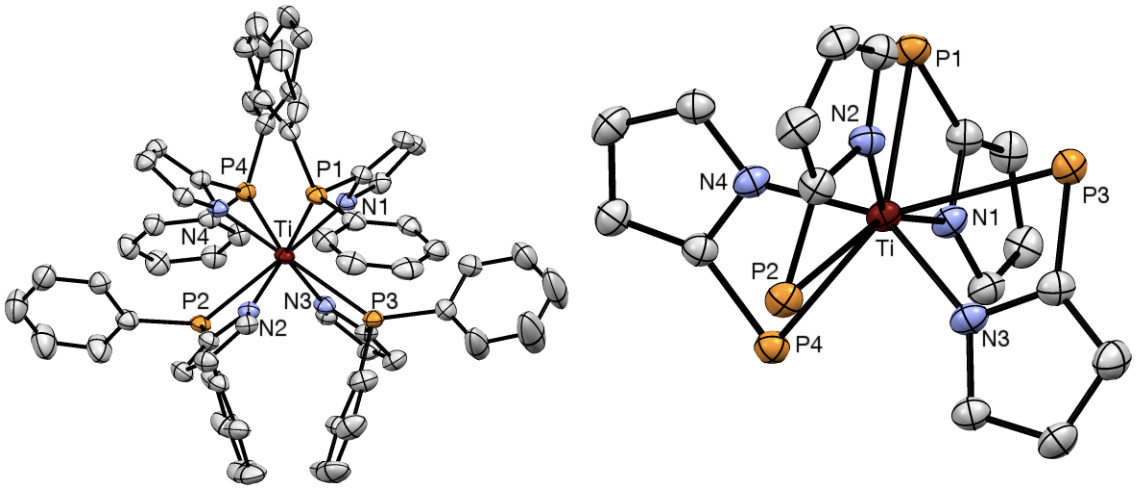

Figure 2.3. 50% thermal ellipsoid drawing of **2.2**. Top-down (left) and side-on view with phenyl groups removed (right) showing asymmetry in N,P chelate binding. Hydrogen atoms omitted for clarity. Selected bond lengths are presented in Table 2.1.

Table 2.1. Selected bond lengths (Å) for complexes **2.1**-**2.5**.

Bond	**$Zr(NP)_4$ (2.1)**	**$Ti(NP)_4$ (2.2)**	**$(NMe_2)_2Ti(NP)_2$ (2.3)[a]**	**Cl_2TiNP_2 (2.4)**	**$ClTi(NP)_3$ (2.5)**
M1-N1	2.193(2)	2.062(2)	2.047(4)	2.026(1)	2.054(1)
M1-N2	2.204(1)	2.055(2)	2.100(4)	2.032(1)	2.052(2)
M1-N3	2.194(2)	2.049(2)	1.903(4)[c]	-	2.048(1)
M1-N4	2.206(2)	2.055(2)	1.888(4)[c]	-	-
M1-P1	2.8809(7)	2.8848(8)	2.826(2)	2.6564(4)	2.6634(5)
M1-P2	2.9061(7)	2.9141(8)	2.762(2)	2.6488(4)	2.7426(5)
M1-P3	2.8877(8)	2.8988(9)	-	-	2.7608(6)
M1-P4	2.9178(6)	2.8519(9)	-	-	-
M1-Cl1	-	-	-	2.2565(5)	2.3314(6)
M1-Cl2	-	-	-	2.2529(4)	-
Avg M-N[b]	2.241	2.082	2.082	2.082	2.082
Avg M-P[b]	2.768	2.597	2.597	2.597	2.597

[a]Bond length measurements for one of two molecules ("A") in the asymmetric unit.
[b]Based on a search of the CSD for M-pyrrolide and M-phosphine bond lengths [61].
[c]Dimethylamide bonds.

Symmetric 8-coordinate complexes typically adopt one of two configurations: a dodecahedron (snub disphenoid) or a square antiprism [124]. Hoard and Silverton [125-126] described a method for distinguishing between the two: in the idealized configurations, two interlocking equivalent trapezoids, BAAB, lie on planes that pass through the metal center (Figure 2.3). In the case of a dodecahedron, these two planes are orthogonal, whereas in a square antiprism they intersect at an angle of 74.4°. By comparing the average plane measurements in **2.1** and **2.2**, intersecting trapezoid angles of 87.2° and 86.7° are obtained, respectively, indicating that both are best described as distorted dodecahedrons. This dodecahedral arrangement is expected on the basis of the 5-membered chelate ring size of the phosphinopyrrolide ligand: dodecahedral configurations are typically observed in complexes with bidentate ligands that give small

chelate ring sizes, while square antiprism configurations are common for bidentate ligands that give larger chelate ring sizes [124].

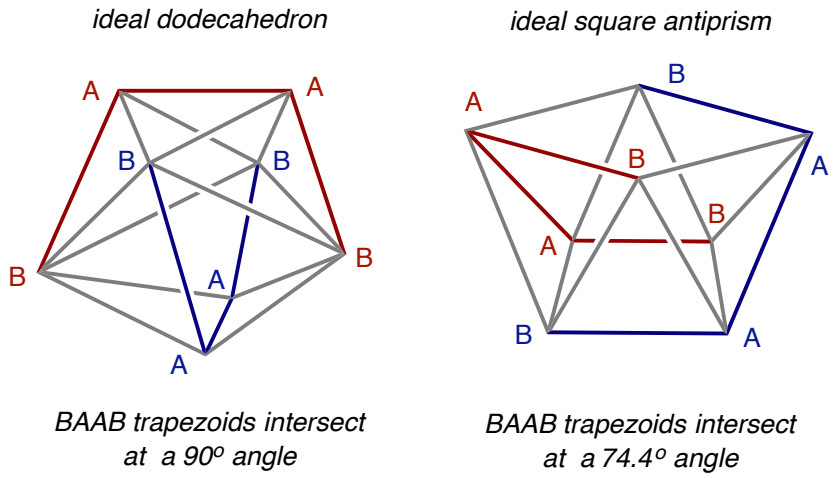

Figure 2.4. Left: ideal dodecahedron with BAAB trapezoid notation; Right: ideal square antiprism with BAAB trapezoid notation. The two similar configurations can be distinguished by examining the angle at which the trapezoidal planes intersect.

Complex **2.1** is only the second crystallographically characterized ZrN_4P_4 motif, and **2.2** is the only TiN_4P_4 motif. The other MN_4P_4 structure, $Zr(PhNPPh_2)_4$, contains 4 phosphinoamide ligands that exhibit η^2-binding to Zr[127]. $Zr(PhNPPh_2)_4$ also exhibits a distorted dodecahedral configuration in the solid state, but with one significant difference: in $Zr(PhNPPh_2)_4$, the four amides all occupy the same "B" coordination sites of the two interpenetrating trapezoids on the dodecahedron; however, in **2.1** and **2.2**, two pyrrolides occupy "A" sites and two occupy "B" sites (one per trapezoid) (Figure 4, center and right). The result is that $Zr(PhNPPh_2)_4$ is approximately D_2-symmetric and contains four bidentate ligands that are symmetry equivalent, whereas **2.1** and **2.2** are C_1-symmetric with four inequivalent bidentate ligands divided into two "classes" ("A" bound pyrrolides and "B" bound pyrrolides). The dodecahedral configuration (and "B" site π-donor occupation) of complexes such as $Zr(PhNPPh_2)_4$ results from maximum amide π overlap in the "B" sites relative to the "A" sites [128]. Since **2.1** and **2.2** do not possess strong π-donors, there is likely little electronic preference for the pyrrolide binding in one site over the other, yielding the mixed A/B pyrrolide species observed in

the solid state [129]. This asymmetry does not significantly affect bonding: all M-N and M-P distances are within 0.05 Å of each other in each structure. This change in coordination geometry between homoleptic phosphinopyrrolide complexes and phosphinoamide complexes demonstrates an important difference in ligand donor ability: although the σ-donor framework is the same in both ligand sets, the inability of phosphinopyrrolides to π-bond significantly impacts the structure of the complexes.

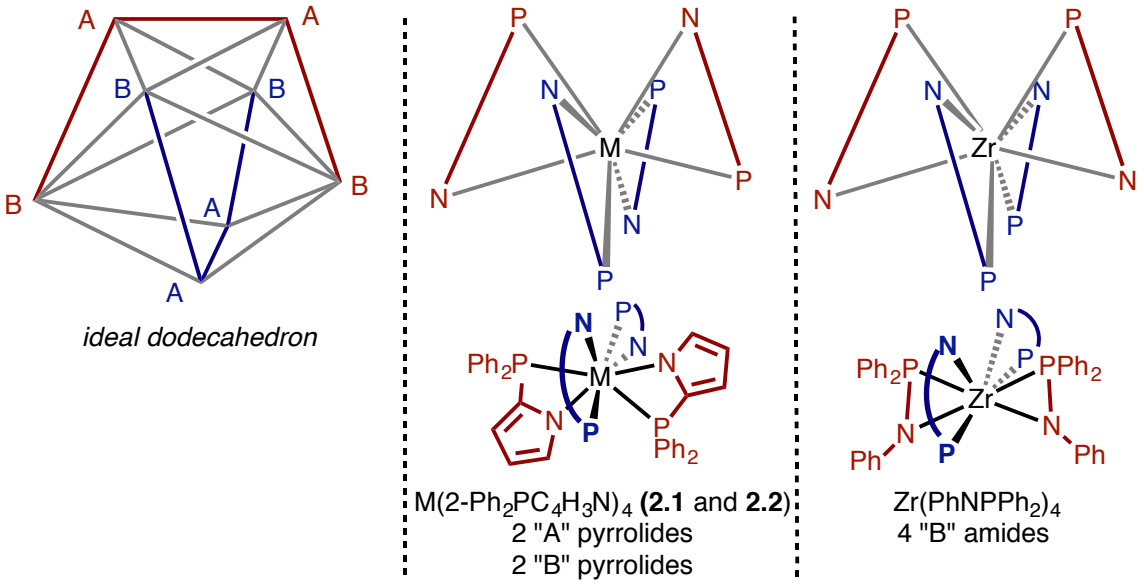

Figure 2.5. Left: ideal dodecahedron demonstrating the BAAB trapezoid orientation; Center: dodecahedral configuration of **2.1** and **2.2**; Right: dodecahedral configuration of $Zr(PhNPPh_2)_4$ from ref. 127.

The crystal structure of **2.3** is reported in Figure 2.5. Complex **2.3** crystallizes in the Pc space group with two nearly similar molecules of **2.3** in the asymmetric unit. The Ti metal center in **2.3** is pseudooctahedral, with both phosphinopyrrolide ligands bound in a κ^2-fashion. The phosphinopyrrolides in **2.3** are inequivalent: one of the phosphine ligands lies *trans* to an NMe_2 ligand, while the other lies *trans* to a pyrrolide ligand. This inequivalence is borne out in the M-P bond lengths: Ti-P1, which is *trans* to the stronger *trans*-influencing NMe_2 ligand, is almost 0.1 Å longer than Ti-P2, which is *trans* to the weaker *trans*-influencing pyrrolide ligand. Much like in **2.1** and **2.2**, the Ti-P bonds in **2.3** are significantly longer than average (2.762(2) Å and 2.826(2) Å *vs*. 2.597 Å), indicating weak binding.

Interestingly, the pyrrolide and amide donors in **2.3** bind in a distorted *cis* divacant octahedral arrangement, while in the related *bis*(phosphinoamide) complexes $(Ph_2PNPh)_2Zr(NMe_2)_2$ [100] and $(Ph_2PNR)_2TiCl_2$ [87] the nitrogen donors are more tetrahedrally arranged. This stark difference in geometry highlights the significant difference in steric properties of phosphinopyrrolide ligands as compared to phosphinoamide ligands: phosphinopyrrolide ligands impart increased steric pressure on the metal center through the larger 4-membered chelate ring, thus pushing the N donors closer together. Unfortunately, because *bis*(amide) *bis*(phosphinoamide) complexes of the type $(R_2PNR)_2Ti(NMe_2)_2$ have not been synthesized, a direct comparison of the electronic environment of these complexes by bond length analysis cannot be made. Similarly, **2.4** contains two κ^2-phosphinopyrrolides in a distorted octahedron (Figure 2.7). The two phosphine ligands lie trans to chlorines and have similar bond lengths, 2.6564(4) Å and 2.6488(4) Å. These Ti-P bond lengths are ~0.1 Å shorter than those found in complex **2.3**, most likely due to a more electron deficient electron center (Cl vs. NMe_2). The two pyrrole rings are pseudo trans (N-Ti-N) 143.11°. The distortion from an ideal octahedron is most likely due to the 4-membered chelate.

Complex **2.5** contains three κ^2-phosphinopyrrolides and is a 7-coordinate distorted pentagonal bipyramid (Figure 2.8). The three phosphine ligands and the pyrrolide nitrogen atoms N2 and N3 constitute the pentagonal equatorial plane, although N2 is canted roughly 34.3° out of plane, breaking the C_s-symmetry of the molecule. The Cl1-Ti1-N1 angle (149.6°) for the capping ligands also indicates significant distortion from ideal pentagonal bipyramidal geometry that results from the bidentate phosphinopyrrolide ligands' small chelate ring size. Similar to **2.3**, complex **2.5** contains two differing yet very long Ti-P bond lengths (Table 2.1): Ti-P1, which lies *trans* to the empty space that bisects the N2-Ti1-N3 angle, is significantly shorter (2.6634(5) Å) than Ti-P2 and Ti-P3 (2.7426(5) and 2.7608(6) Å), which lie roughly *trans* to each other. As with **2.3**, the geometry of complex **2.5** is different than the related *tris*(phosphinoamide) complex $(Ph_2PN^iPr)_3ZrCl$ [89], which is contains a pseudotetrahedral arrangement of amide and chloride ligands.

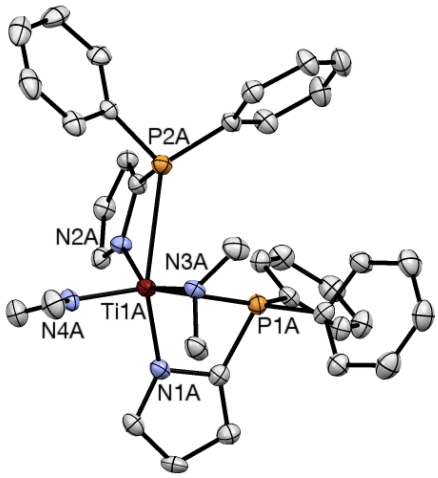

Figure 2.6. 50% thermal ellipsoid drawing of **2.3**. Hydrogen atoms and second molecule of the asymmetric unit omitted for clarity. Selected bond lengths are presented in Table 2.1.

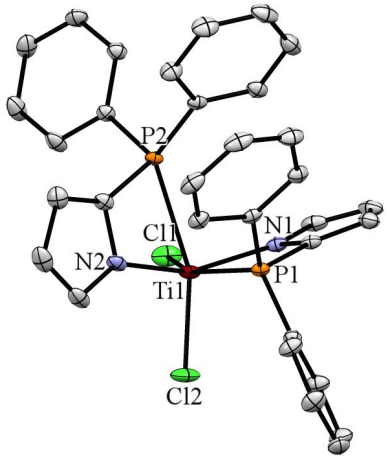

Figure 2.7. 50% thermal ellipsoid drawing of **2.4**. Hydrogen atoms and two molecules of benzene (solvent) omitted for clarity. Selected bond lengths are presented in Table 2.1.

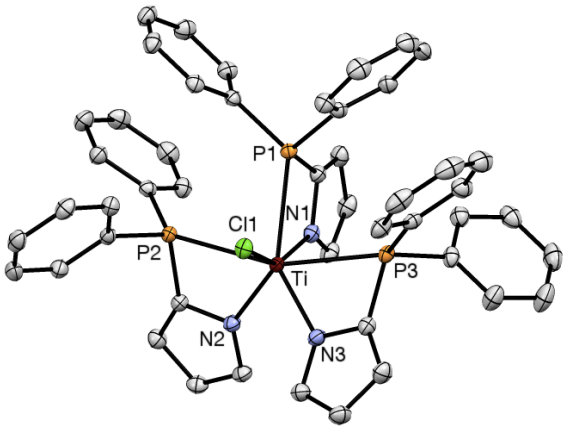

Figure 2.8. 50% thermal ellipsoid drawing of **2.5**. Hydrogen atoms and two molecules of benzene (solvent) omitted for clarity. Selected bond lengths are presented in Table 2.1.

Given that the M-P bond lengths in **2.1** and **2.2** are exceptionally long in comparison to **2.3**, **2.4,** and **2. 5** (2.9 Å versus 2.75 Å), it is reasonable to question whether there is actually an M-P bond in **2.1** or **2.2**, or if the M-P distances are just a result of crystal packing or ligand geometric constraints. Since the pyrrolide coordination geometries around Zr and Ti are extremely distorted from tetrahedral (for example, N1-Ti1-N3 is 88.16° and N1-Ti1-N3 is 145.01°), we favor an 8-coordinate structure with M-P bonds over the 4-coordinate alternative for both **2.1** and **2.2**. Nonetheless, the extremely long M-P bond distances in all of these complexes indicate that the L-type M-P bonds are relatively weak and may be susceptible to thermal dissociation under mild conditions. Computational experiments are currently underway to further determine the nature and extent of M-P bonding in these complexes.

Given the long M-P bonds and high coordination numbers observed in the solid state structures, we were interested in analyzing the solution state dynamics of **2.1**, **2.2**, **2.3**, and **2.5** in order to determine their propensity for phosphine dissociation and their potential to act as metalloligands for other metals.

The variable temperature ^{31}P NMR spectra of **2.1** in d_8-toluene are presented in Figure 2.9. At -65 °C, 7 signals corresponding to two species are observed. The first species (**2.1a**) contains 4 signals in a 1:1:1:1 ratio: one set of overlapping doublets at -32.5 ppm and a second set of overlapping doublets at -42 ppm, all with J_{PP} = 10-11 Hz.

The second species (**2.1b**) contains 3 signals in a 1:1:2 ratio: a doublet of doublets at -33.5 ppm, a second doublet of doublets at -35.5 ppm, and an apparent triplet at -36.5 ppm, all with J_{PP} = 6 Hz. Upon warming, the seven signals shift and broaden into three signals at room temperature before fully coalescing into a single broad signal at 90 °C.

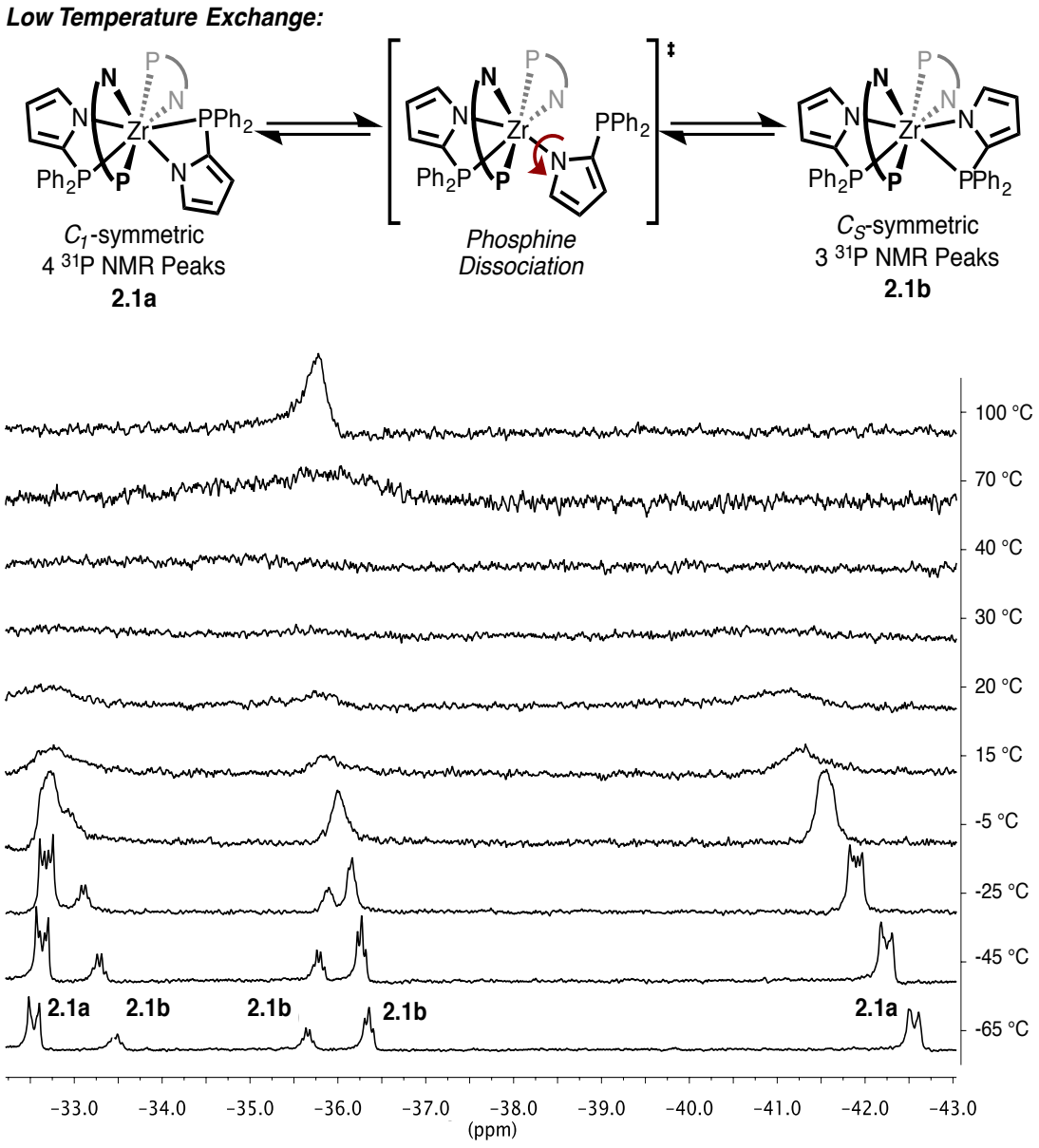

Figure 2.9. Variable temperature ^{31}P NMR spectra of **2.1** in d_8-toluene and the potential identity of low temperature species **2.1a** and **2.1b**.

The nature of low temperature species **2.1a** and **2.1b** remains ambiguous. We propose two possibilities: **2.1a** and **2.1b** could be different 8-coordinate conformations, one of C_1 symmetry as in the solid state (**2.1a**) and another of C_S symmetry (**2.1b**); or, **2.1a** and **2.1b** could be lower coordinate species where multiple phosphine arms have dissociated (2 free arms and 1 or 3 free arms, respectively). Two 8-coordinate structures best fit the available data: first, given the C_1-symmetric solid state structure, one would expect to observe four chemically inequivalent ^{31}P signals in two chemically similar classes ("A" type and "B" type in the dodecahedral trapezoid) as seen in **2.1a**; second, all of the low temperature phosphine signals have P-P coupling, which would not be expected for a "free" phosphine arm. The $^2J_{PP}$ values are low (6-12 Hz), but this could be a function of the relatively weak/long Zr-P bonds or non ideal P-Zr-P bond angles. Despite the fact that both low temperature species are likely 8-coordinate, fluxional processes that interconvert the two 8-coordinate conformations could certainly involve reversible phosphine arm binding (Figure 2.9). In the high temperature limit where only a single broad ^{31}P resonance is observed, phosphine exchange is rapid, and all phosphine ligands may be fully dissociated.

In contrast, the room temperature ^{31}P NMR spectrum of **2.2** in d_8-toluene displays only one sharp singlet. Since **2.1** and **2.2** share similar solid-state structures, a nonfluxional **2.2** would also be expected to yield 4 ^{31}P NMR signals. Thus, as in **2.1**, it is likely that **2.2** undergoes rapid phosphine dissociation to yield a single ^{31}P resonance at room temperature. Unfortunately, the rate of exchange in **2.2** was too fast to fully characterize individual phosphine-coordinated species even at low temperature. Upon cooling **2.2** from room temperature to -90 °C, the singlet observed at room temperature broadens into the baseline and then splits into two sets of broad resonances in a 1:2 ratio at -90 °C: three broad resonances centered at -23.5 ppm and two broad resonances centered at – 30.0 ppm (Figure 2.10). Although the low temperature resonances cannot be fully resolved, $\Delta G^{\ddagger}$ for phosphine dissociation can be estimated at the coalescence temperature (-60 °C) to be less than 9 kcal/mol, significantly lower than that for Zr (13.4 kcal/mol). Due to weaker Ti-P *vs.* Zr-P bonds, dissociation is more facile on Ti than on Zr, yielding full dissociation for **2.2** at room temperature instead of 90 °C as in **2.1**.

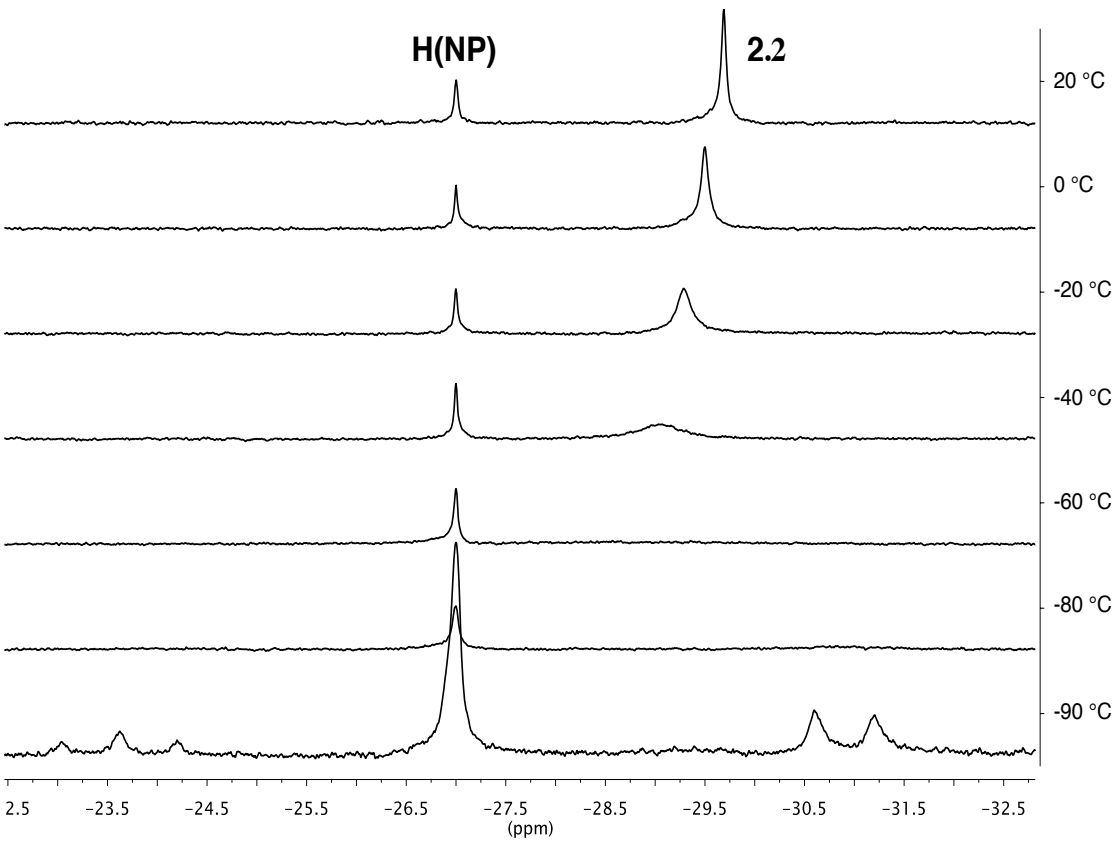

Figure 2.10. Variable temperature ^{31}P NMR spectra of **2.2** in d_8-toluene. The spectra taken at -80 °C and -90 °C have been vertically scaled to show the broadened decoalescing resonances. The singlet at -27 ppm is due to a free ligand impurity.

Much like compound **2.2**, compounds **2.3**, **2.4, 2.5** and **2.6** also display single resonances in the room temperature ^{31}P NMR spectra that are inconsistent with the chemical inequivalence observed in the solid state. Thus, these complexes must also be undergoing rapid phosphine dissociation at room temperature (Figure 2.11). Unlike **2.1**, where low temperature species could be identified, or **2.2**, where slow exchange between multiple species could at least be observed at low temperature, **2.3** and **2.5** exchange too rapidly: upon cooling both to -90 °C, their singlets only broaden out into the baseline.

The fluxionality of complex **2.3** provides support that phosphine coalescence in **2.1**, **2.2**, **2.4, 2.5** and **2.6** occurs *via* phosphine dissociation. Since **2.1**, **2.2**, **2.5,** and **2.6** are 8-, 8-, 7-, and 7-coordinate, respectively, they are inherently fluxional and their phosphine ligands could exchange *via* dissociation (as proposed above) or *via* turnstyle-

like mechanisms [130]. However, since **2.3** is 6-coordinate it should be conformationally rigid and incapable of easily undergoing turnstyle-like phosphine exchange. Thus, in **2.3**, phosphine dissociation is the only plausible mechanism for rapid phosphine exchange. Since the rate dissociation in **2.3** is very fast, it is reasonable to assume that the fast dissociation mechanism is operable in **2.1**, **2.2**, **2.4, 2.5,** and **2.6** as well (Figure 2.11). Eisen [127] and Nagashima [87] have also investigated the NMR fluxionality of $(Ph_2PNPh)_4Zr$, $(Ph_2PNPPh_2)TiCl_2$ and $(Ph_2PN^iPr)_2TiCl_2$ and found that these complexes also facilely dissociate phosphines at room temperature. Although no quantitative studies have been carried out on the barriers for phosphinoamide ligand dissociation, it appears that phosphinopyrrolide ligands dissociate at qualitatively similar rates to these previously reported complexes.

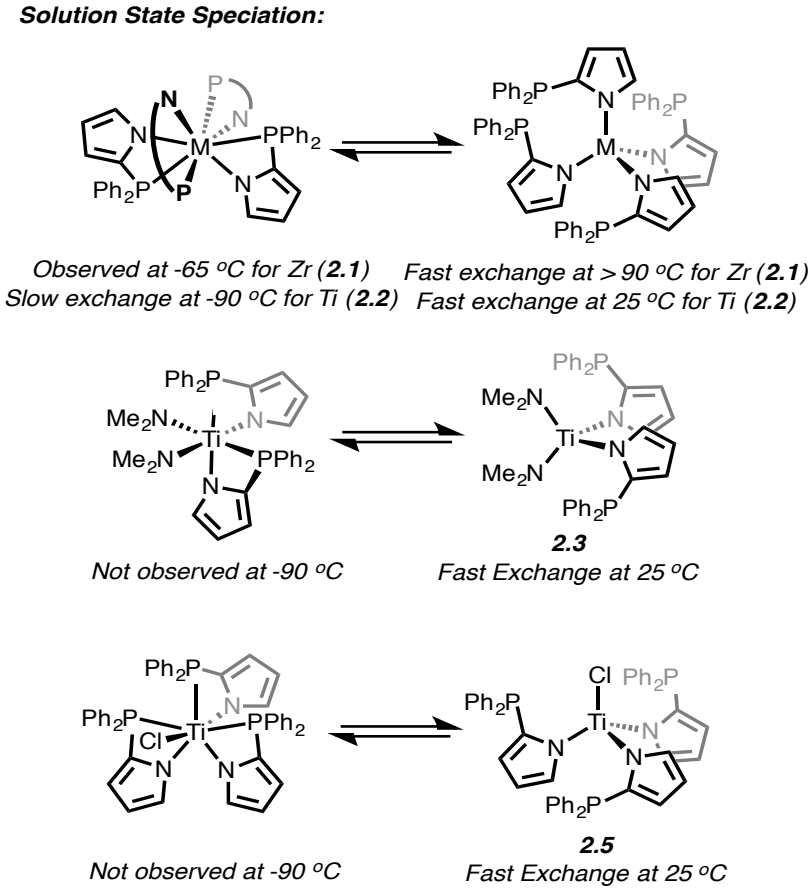

Figure 2.11. Temperature-dependent fluxionality as a result of rapid dissociation of phosphines in solution.

2.4 CONCLUSIONS

A new series of homo- and heteroleptic Zr and Ti phosphinopyrrolide complexes has been synthesized. Both of the homoleptic Ti and Zr complexes **2.1** and **2.2** are remarkably 8-coordinate in the solid state, although the M-P bonds are quite long and likely weak. Variable temperature NMR experiments have demonstrated that all of the reported complexes are fluxional in the solution state, with the fluxionality most likely resulting from phosphine decoordination events. Ultimately, we envision using these complexes as metalloligands for a variety of other transition metals, and understanding the fundamental coordination chemistry of the early metal pyrrolide framework is crucial for developing strategies for bimetallic syntheses. Critically, all of the reported complexes have labile phosphine ligands that could potentially decoordinate from the early transition metal center and bind to a second metal center. Furthermore, although these complexes have solution-state behavior qualitatively similar to related phosphinoamide ligands, the starkly different solid-state geometries reveal underlying differences in the steric and electronic properties of phosphinopyrrolide ligands as compared to phosphinoamide ligands. Currently, we are investigating the propensity of these species to act as metalloligands toward Mo, Fe and Co to generate trigonally symmetric $M_{Early}N_3$-P_3M_{Late} fragments with bridging phosphinopyrrolide ligands and varying metal-metal interactions.

2.5 EXPERIMENTAL CONSIDERATIONS

General Considerations and Instrumentation. All air- and moisture-sensitive compounds were manipulated in a glovebox under a nitrogen atmosphere. Solvents for air- and moisture-sensitive reactions were vacuum transferred from sodium benzophenone ketyl (THF, Et_2O, pentane, d_6-benzene and d_8-toluene) or predried on a Vacuum Atmospheres Solvent Purification System and filtered through activated basic alumina (hexanes, toluene and benzene). $Ti(NMe_2)_4$ and $TiCl_2(NMe_2)_2$ were prepared according to literature procedure [57-58]. ^{1}H, ^{13}C and ^{31}P NMR spectra were recorded on Varian INOVA 300 MHz or 500 MHz or Bruker Avance III 500 MHz spectrometers. Chemical shifts are reported with respect to residual protio-solvent impurity for ^{1}H (s,

7.16 ppm for C_6D_5H), solvent carbons for ^{13}C (t, 128.39 ppm for C_6D_6), and PPh_3 for ^{31}P (s, -6 ppm in C_6D_6).

X-ray Crystal Data: General Procedure. Crystals were removed quickly from a scintillation vial to a microscope slide coated with oil. Samples were selected and mounted on the tip of a 0.1 mm diameter glass capillary. Data collection was carried out on a Bruker APEX II CCD diffractometer with a 0.71073 Å Mo Kα source or on a Bruker-AXS D8 Venture diffractometer with a 1.54178 Å Cu Kα source. The structures were solved by direct methods. All non-hydrogen atoms were refined anisotropically. Details regarding refined data and cell parameters are available in Table 2.2.

Synthesis of 2-(diphenylphosphino)pyrrole, 2-(Ph_2P)C_4H_3NH, H(NP). (2-Ph_2P)C_4H_3NH was prepared *via* a modification of literature procedure [59-60]. Pyrrole (3.0 mL, 2.9 g, 43.2 mmol, 3 equiv) was dissolved in 50 mL Et_2O and cooled in the glovebox cold well. The reaction was removed from the cold well, and 14.4 mL of 3.0 M EtMgBr in Et_2O (43.2 mmol, 3 equiv) was added dropwise over the course of 30 minutes while the reaction was thawing. The reaction was left to stir at room temperature for an additional hour to ensure complete deprotonation of pyrrole. Afterward, 2.6 mL $ClPPh_2$ (3.18 g, 14.4 mmol, 1 equiv) was added dropwise to the reaction mixture over 10 minutes, and then stirred overnight at room temperature. The reaction was then quenched with 1:1 2M HCl/2M NH_4Cl, separated and washed with aqueous saturated sodium bicarbonate until neutral. The organic layer was separated, dried over $MgSO_4$ and solvent and pyrrole removed *in vacuo* to yield a yellow oil. The residue was purified by column chromatography (chloroform:hexanes 1:4), yielding 1.2 g (33%) of H(NP) as an off-yellow oil that solidifies to a white solid upon standing.

Synthesis of ((2-Ph_2P)C_4H_3N)Li, Li(NP). H(NP) (373 mg, 1.48 mmol, 1 equiv) was dissolved in 10 mL of hexanes in the glovebox. 1 mL of 2.5 M nBuLi in hexanes (1.67 equiv) was added dropwise over the course of 10 minutes, during which the clear hexanes solution turned cloudy. The reaction was stirred for 12 hours, yielding significant amounts of white precipitated Li(NP). The reaction slurry was filtered off and the white

precipitate was washed with 10 mL of hexanes to yield Li(NP), which was used without further purification or characterization.

Synthesis of Zr((2-Ph_2P)$C_4H_3N)_4$, Zr(NP)$_4$ (2.1). Slurries of Li(NP) (390.1 mg, 1.52 mmol, 4 equiv) in 10 mL Et_2O and $ZrCl_4$ (88.5 mg, 0.38 mmol, 1 equiv) in 5 mL Et_2O were cooled in the glovebox cold well. Under vigorous stirring, the $ZrCl_4$ slurry was added to the Li(NP) slurry. The reaction was allowed to warm to room temperature and stirred for 12 hours, resulting in a pale yellow/orange solution with significant white precipitate. The reaction mixture was filtered, and the precipitate was extracted into 20 mL of benzene. The benzene fraction was dried *in vacuo*, and the resulting yellow oil was dissolved in minimal (approx. 2 mL) toluene and cooled to -35 °C. Over the course of days, **2.1** precipitated out of toluene as a white solid (162 mg, 39%). X-ray quality crystals were obtained by layering a concentrated solution of **2.1** in CH_2Cl_2 with pentane and cooling the mixture to -35 °C. ^{1}H NMR (300 MHz, C_6D_6) δ, ppm: 6.48-6.60 (*br m*, 12H, pyrrole); 6.62-6.86 (*br m*, 24H, aryl); 6.93-7.01 (*br m*, 16H, aryl). ^{13}C NMR (125 MHz, C_6D_6) δ, ppm: 113.2 (*br*), 117.0 (*br*), 129.3 (*br*), 133.3 (*br*), 133.6, 135.4. ^{31}P NMR (121 MHz, C_6D_6) δ, ppm: -33 (*br*), -35.9 (*br*), -41.4 (*br*).

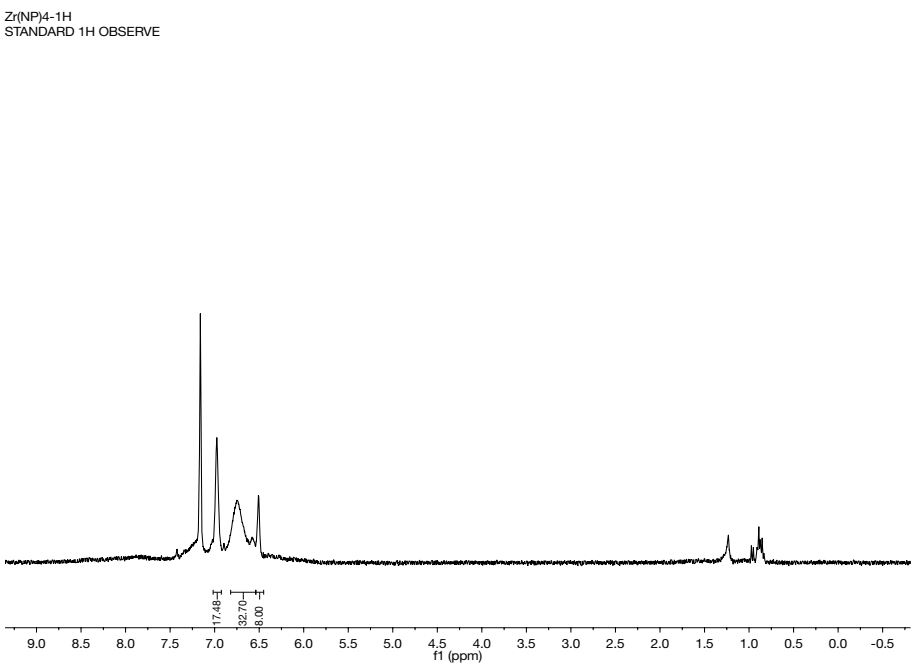

Figure 2.12. ^{1}H NMR of **2.1** in C_6D_6. Taken from PLD03014.

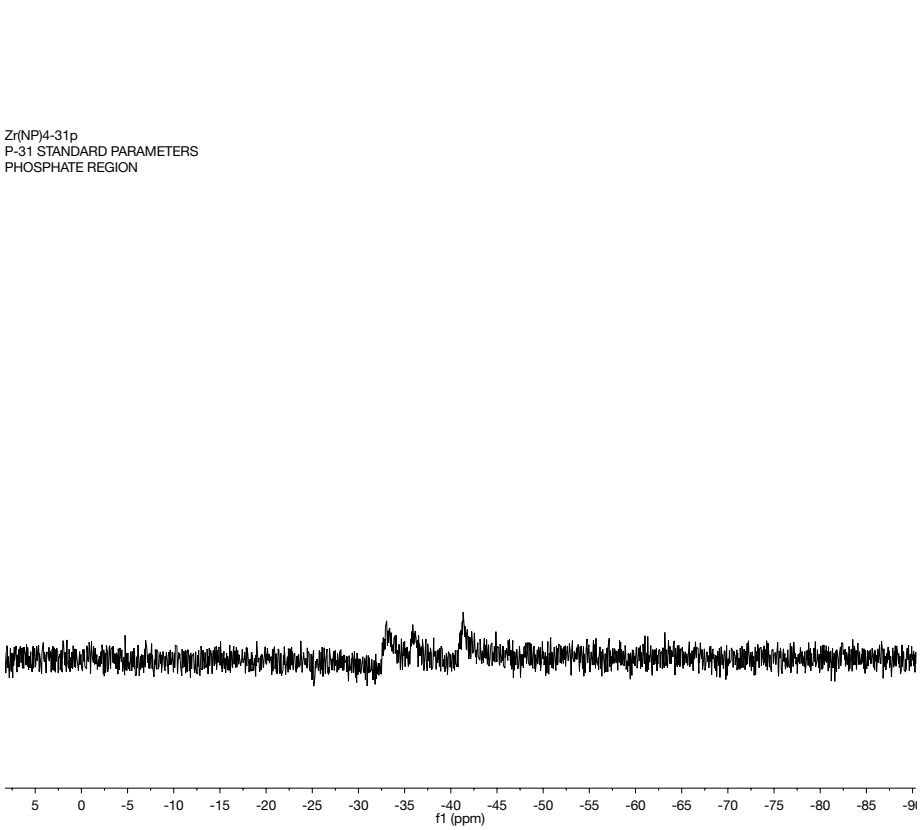

Figure 2.13. ^{31}P NMR of **2.1** in C_6D_6. Taken from PLD03014.

Synthesis of Ti((2-Ph$_2$P)C$_4$H$_3$N)$_4$, Ti(NP)$_4$ (2.2). A solution of $TiCl_4$ (24.9 mg, 0.131 mmol, 1 equiv) in 2 mL benzene was added dropwise over the course of 5 minutes to a slurry of Li(NP) (135 mg, 0.525 mmol, 4 equiv) in 10 mL benzene. The reaction solution quickly turned from pale yellow to dark red/brown, and was left to stir for 12 hours. The reaction mixture was then filtered through celite, and benzene was removed *in vacuo*, yielding crude **2.2** as a red/brown powder. **2.2** was recrystallized by cooling a concentrated toluene solution (approx. 2 mL) to -35 °C overnight, yielding pure **2.2** as dark brown crystals upon filtration and washing with pentane (137 mg, 43%). X-ray quality crystals were grown by slow diffusion of pentane into a saturated toluene solution of **2** at -35 °C. ^{1}H NMR (300 MHz, C_6D_6) δ, ppm: 6.01 (*t*, 4H, pyrrole); 6.24 (*d*, 4H, pyrrole); 6.8-7.0 (*m*, 24H, aryl); 7.15-7.25 (*m*, 16H, aryl); 7.58 (*br s*, 4H, pyrrole). ^{13}C NMR (125 MHz, C_6D_6) δ, ppm: 110.4, 116.9, 129.1, 129.7, 133.6, 134.0, 136.1 (*br*), 136.9 (*br*). ^{31}P NMR (121 MHz, C_6D_6) δ, ppm: -30.3.

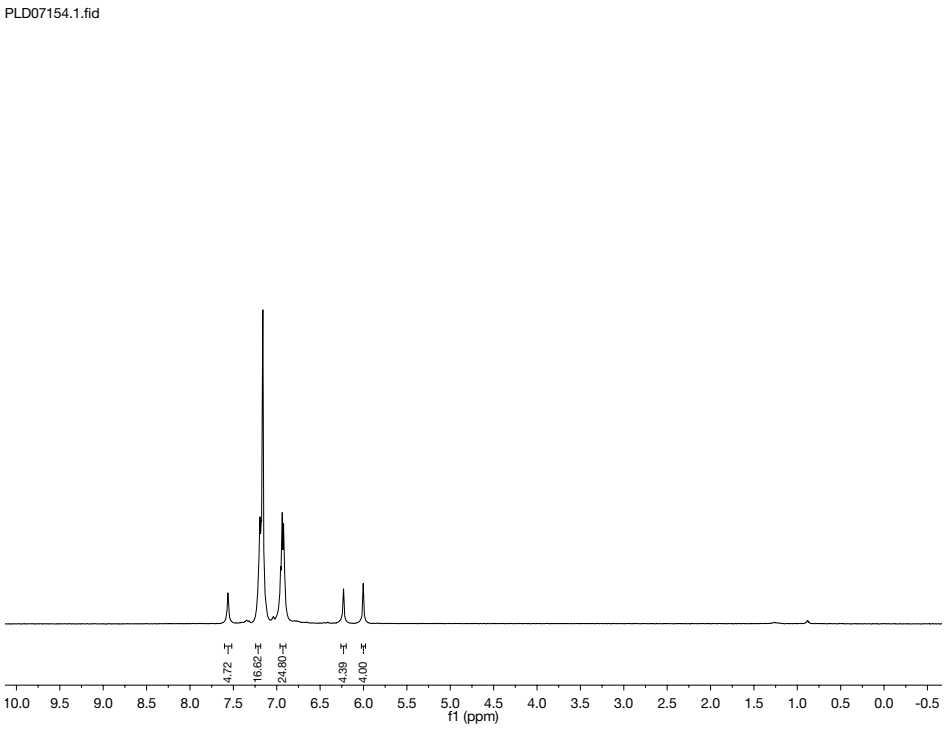

Figure 2.14. ^{1}H NMR of **2.2** in C_6D_6. Taken from PLD07154.

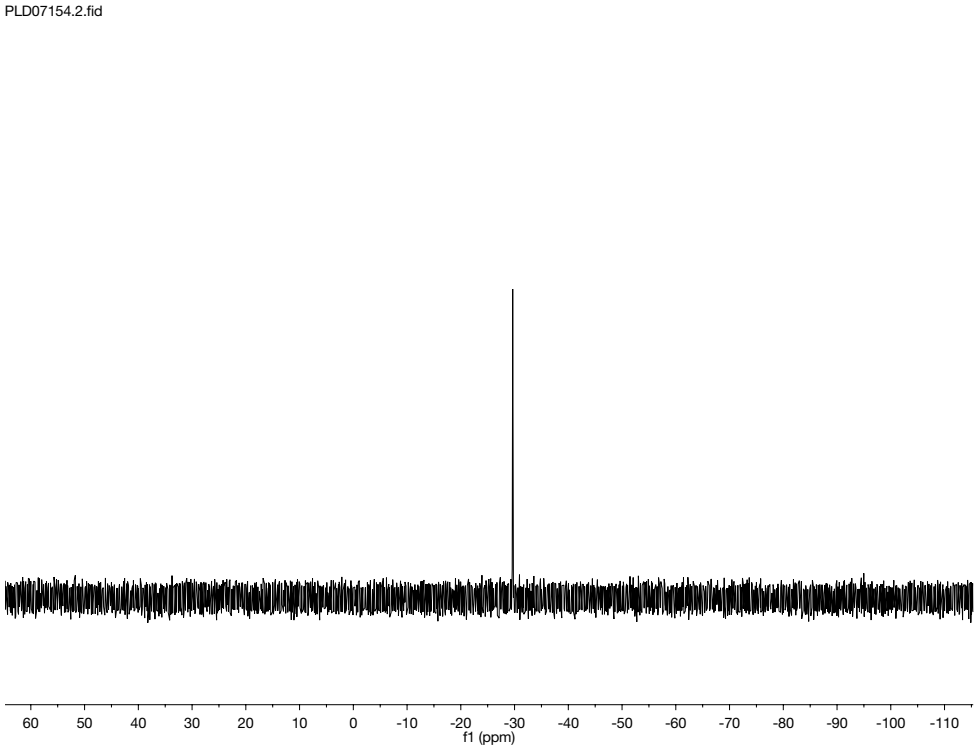

Figure 2.15. ^{31}P NMR of **2.2** in C_6D_6. Taken from PLD07154.

Synthesis of $(NMe_2)_2Ti((2\text{-}Ph_2P)C_4H_3N)_2$, $(NMe_2)_2Ti(NP)_2$ (2.3). Solutions of $Ti(NMe_2)_4$ (97 mg, 0.433 mmol, 1 equiv) in 1 mL THF and H(NP) (218 mg, 0.865 mmol, 2 equiv) in 1 mL THF were cooled to -35 °C. The cold $Ti(NMe_2)_4$ solution was then added dropwise to the ligand solution, and the reaction was thawed and stirred for 12 hours at room temperature, yielding a red solution. Solvent was removed *in vacuo*, yielding crude **2.3** as a red oil (124 mg, 45%). X-ray quality crystals were grown from a concentrated Et_2O solution of **2.3** cooled to -35 °C. ^{1}H NMR (300 MHz, C_6D_6) δ, ppm: 3.06 (*s*, 12H, N(C*H*$_3$)$_2$); 6.70 (*dd*, 2H, pyrrole); 6.77 (*m*, 2H, pyrrole); 7.0-7.1 (*m*, 12H, aryl); 7.21 (*m*, 2H, pyrrole); 7.48-7.55 (*m*, 8H, aryl). ^{13}C NMR (125 MHz, C_6D_6) δ, ppm: 47.7, 112.5, 116.5, 128.9, 129.2, 132.1, 133.6, 133.7, 137.3. ^{31}P NMR (121 MHz, C_6D_6) δ, ppm: -30.8.

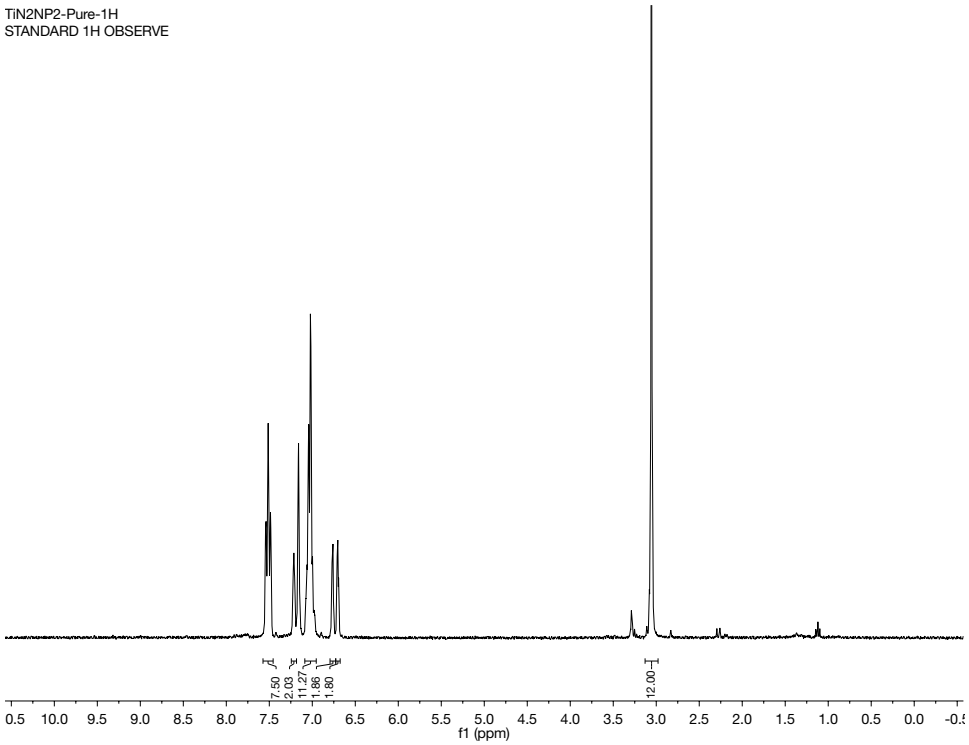

Figure 2.16. ^{1}H NMR of **2.3** in C_6D_6. Taken from PLD01068.

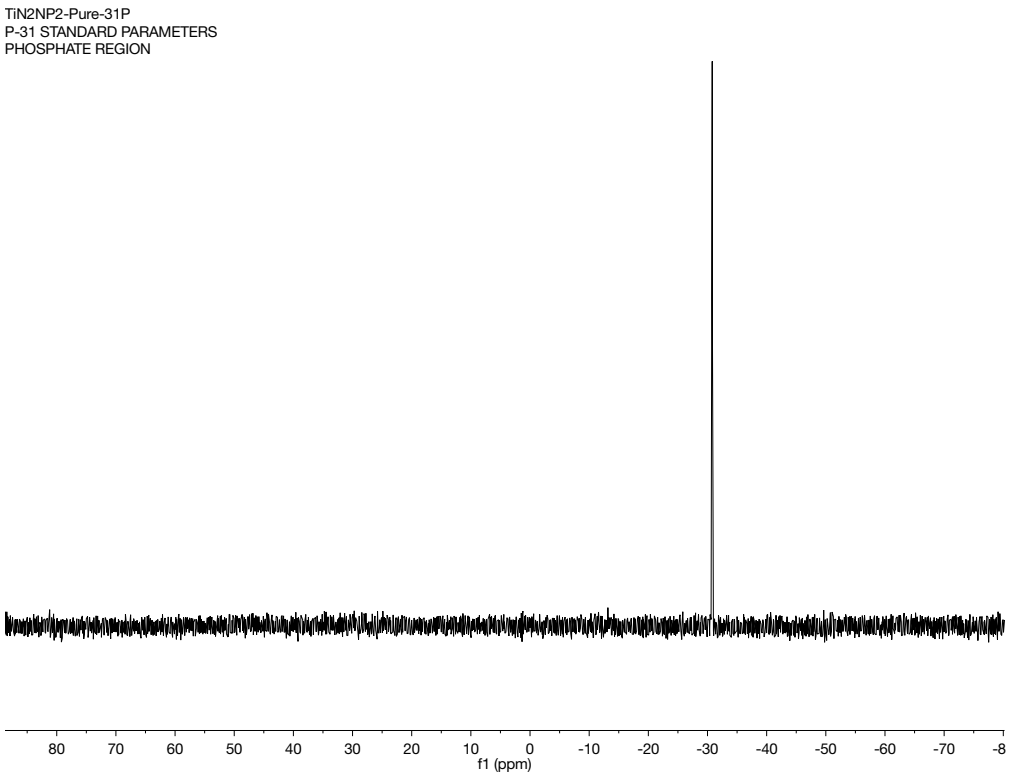

Figure 2.17. ^{31}P NMR of **2.3** in C_6D_6. Taken from PLD01068.

Synthesis of $Cl_2Ti((2\text{-}Ph_2P)C_4H_3N)_2$, $Cl_2Ti(NP)_2$ (2.4). A solution of $TiCl_4$ (28.7 mg, 0.151 mmol, 1 equiv) in 1 mL benzene was added dropwise over the course of 5 minutes to a slurry of Li(NP) (116.5 mg, 0.453 mmol, 2 equiv) in 5 mL benzene. The reaction solution quickly turned from pale yellow to dark red/brown, and was left to stir for 12 hours. The reaction mixture was then filtered through celite and benzene was removed *in vacuo*, yielding crude **2.4** as a red/brown powder. H NMR (300 MHz, C_6D_6) δ, ppm: 6.27 (*m*, 2H, pyrrole**);** 6.48 (*m*, 2H, pyrrole); 7.87 (*m*, 2H, pyrrole) 6.7-7.0 (*m*, 10H, aryl); 7.1-7.2 (*m*, 12H, aryl); 7.71 (*m*, 2H, pyrrole). ^{31}P NMR (121 MHz, C_6D_6) δ, ppm: -28.

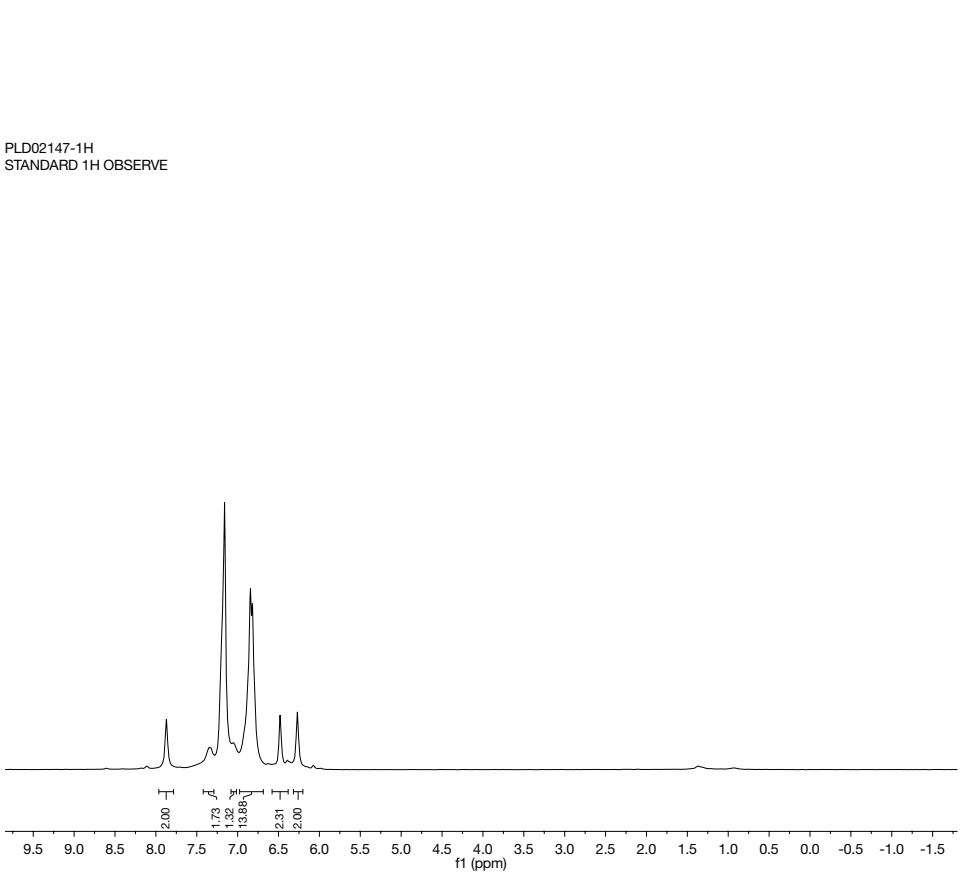

Figure 2.18. ^{1}H NMR of **2.4** in C_6D_6. Taken from PLD02147.

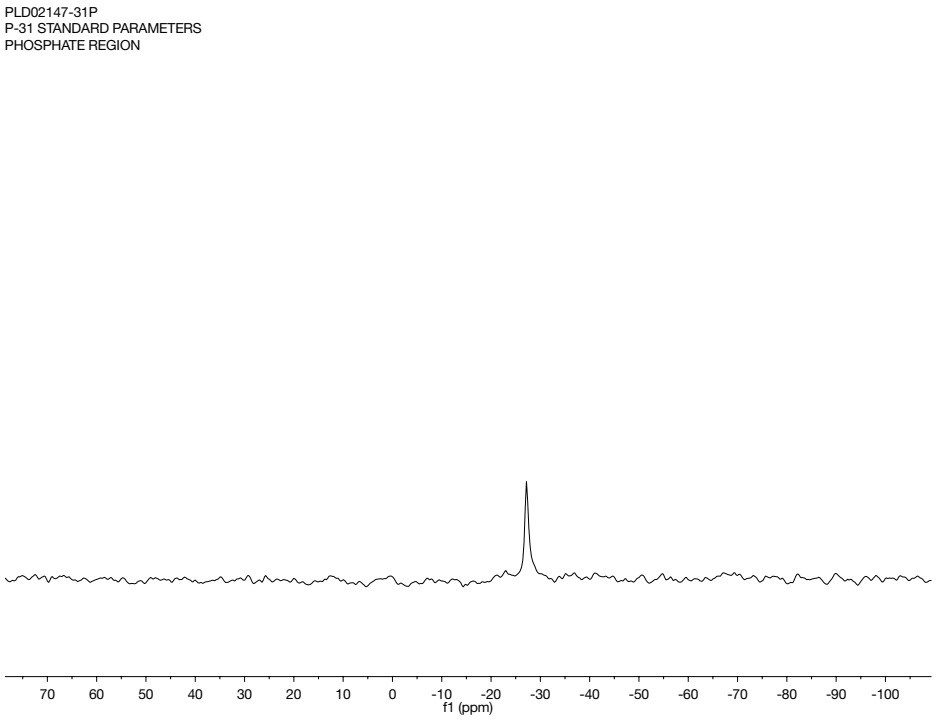

Figure 2.19. ^{31}P NMR of **2.4** in C_6D_6. Taken from PLD02147.

Synthesis of ClTi((2-Ph$_2$P)C$_4$H$_3$N)$_3$, ClTi(NP)$_3$ (2.5). A solution of $TiCl_4$ (28.7 mg, 0.151 mmol, 1 equiv) in 1 mL benzene was added dropwise over the course of 5 minutes to a slurry of Li(NP) (116.5 mg, 0.453 mmol, 3 equiv) in 5 mL benzene. The reaction solution quickly turned from pale yellow to dark red/brown, and was left to stir for 12 hours. The reaction mixture was then filtered through celite and benzene was removed *in vacuo*, yielding crude **2.5** as a red/brown powder. **5** was crystallized by layering pentane on a concentrated toluene solution of **2.5** and cooling to -35 °C overnight, yielding dark red/brown needles (41 mg, 33%). X-ray quality crystals were obtained from slow evaporation of a concentrated benzene solution of **2.5**. ^{1}H NMR (300 MHz, C_6D_6) δ, ppm: 6.40 (*m*, 3H, pyrrole); 6.57 (*m*, 3H, pyrrole); 6.7-7.0 (*m*, 18H, aryl); 7.1-7.2 (*m*, 12H, aryl); 7.71 (*m*, 3H, pyrrole). ^{13}C NMR (125 MHz, C_6D_6) δ, ppm: 110.4, 115.6, 128.9, 129.6, 130.6, 133.4, 134.8, 135.7. ^{31}P NMR (121 MHz, C_6D_6) δ, ppm: -29.9.

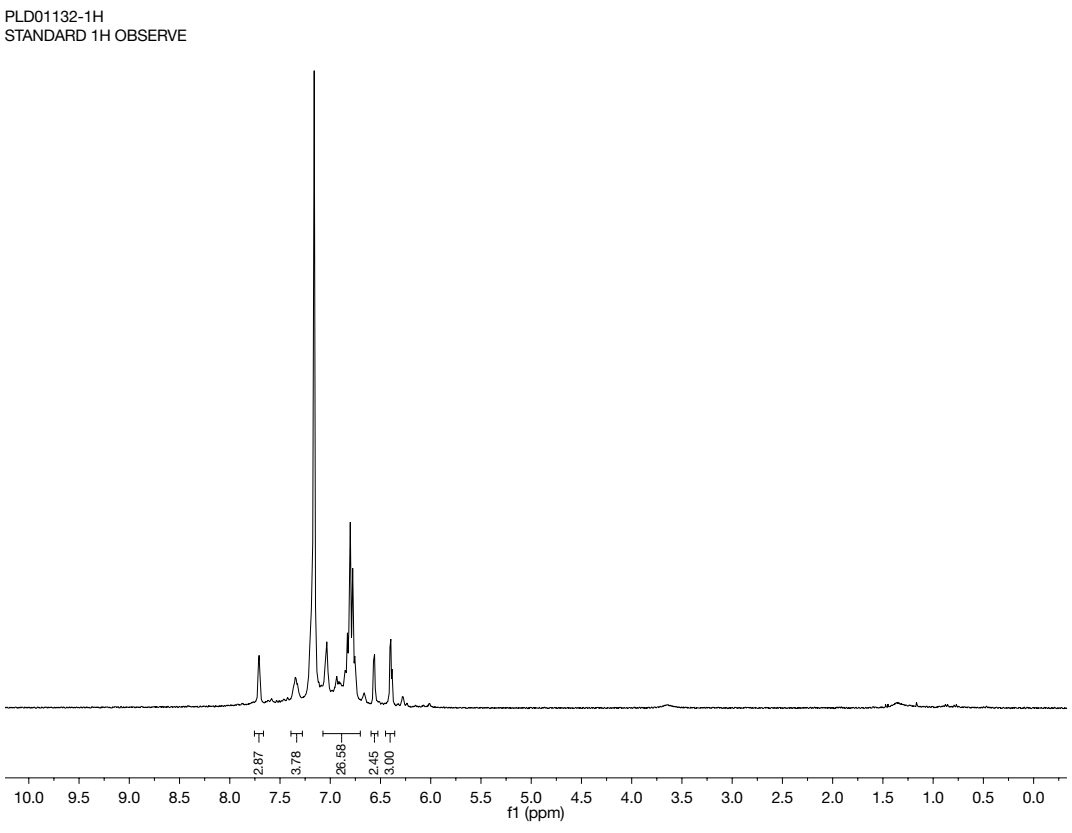

Figure 2.20. ^{1}H NMR of **2.5** in C_6D_6. Taken from PLD01132.

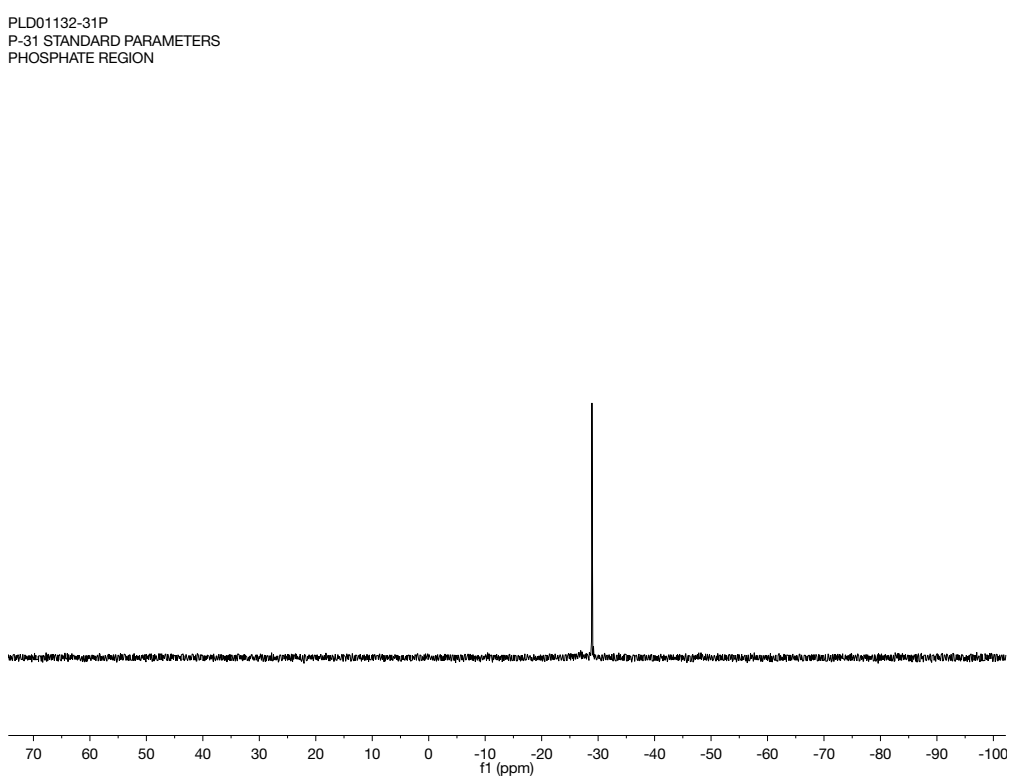

Figure 2.21. ^{31}P NMR of **2.5** in C_6D_6. Taken from PLD01132.

Synthesis of $(NMe_2)Ti((2\text{-}Ph_2P)C_4H_3N)_3$, $(NMe_2)Ti(NP)_3$ (2.6). Solid $(NMe_2)TiCl_3$ (77.0 mg, 0.388 mmol, 1 equiv) and LiNP (300 mg, 1.16 mmol, 3 equiv) were dissolved in benzene and allowed to stir overnight. The reaction quickly turned from pale yellow to an orange, red. The resulting solution was filtered over celite and volatiles were removed *in vacuo*, yielding crude **2.6** as a red powder in 67% yield. ^{1}H NMR (300 MHz, C_6D_6) δ, ppm: 3.00 (s, 6H, methyl); 6.42 (*m*, 3H, pyrrole); 6.575 (*m*, 3H, pyrrole); 6.87-7.0 (*m*, 18H, aryl); 7.25-7.35 (*m*, 15H, aryl). ^{31}P NMR (121 MHz, C_6D_6) δ, ppm: -29 (br).

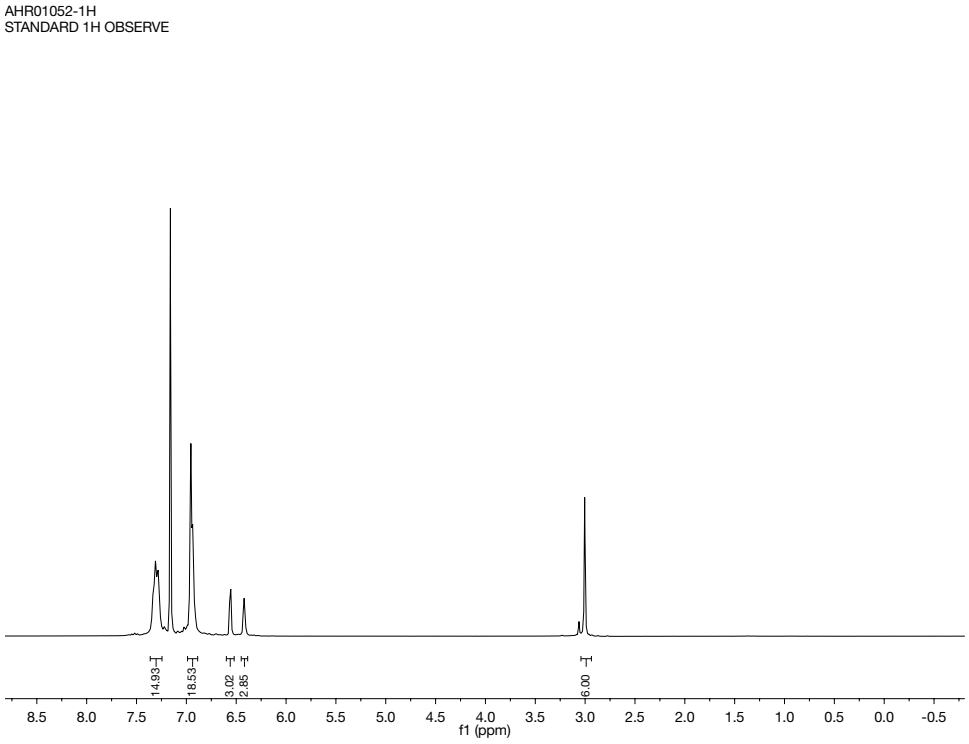

Figure 2.22. ^{1}H NMR of **2.6** in C_6D_6. Taken from AHR01052.

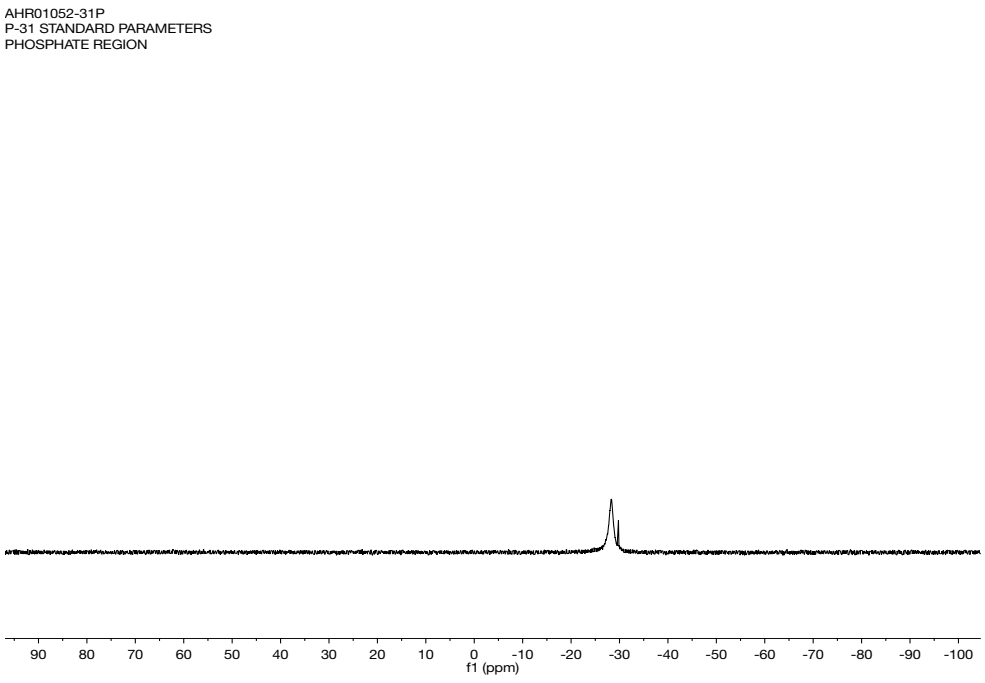

Figure 2.23. ^{31}P NMR of **2.6** in C_6D_6. Taken from AHR01052. H(NP) impurity present.

Table 2.2. Crystal and refinement data for complexes **2.1-2.3**.

	2.1	**2.2**	**2.3**
CCDC Number	997333	997334	997335
Empirical Formula	C_{64} H_{52} N_4 P_4 Zr	$C_{64}H_{52}N_4P_4Ti$	$C_{36}H_{38}N_4P_2Ti$
Formula weight	1092.20	1048.87	636.54
T (K)	173(2)	123(2)	123(2)
a, Å	12.5615(6)	9.7430(11)	14.9946(11)
b, Å	13.7502(7)	16.7613(19)	11.9566(9)
c, Å	18.2508(9)	20.707(2)	18.3905(13)
α, deg	81.9170(10)	106.010(7)	90
β, deg	88.1680(10)	103.249(7)	92.967(1)
γ, deg	69.8650(10)	93.845(7)	90
Volume, Å^3	2929.8(3)	3133.1(6)	3292.7(4)
Z	2	2	4
Crystal System	Triclinic	Triclinic	Monoclinic
Space Group	P-1	P-1	Pc
d_{calc}, g/cm^3	1.238	1.112	1.284
θ Range, deg	1.130 to 27.48	2.298 to 75.039	1.703 to 27.553
μ, mm^{-1}	0.338	2.419	0.388
Abs. Correction	Multi-scan	Multi-scan	Multi-scan
GOF	1.021	1.087	1.008
R_1 ,[a]	R1 = 0.0398	R1 = 0.0531	R1 = 0.0477
wR_2 [b] [I>2σ (I)]	*w*R2 = 0.0896	*w*R2 = 0.1467	*w*R2 = 0.0924

[a] $R_1 = \sum||F_o| - |F_c||/\sum|F_o|$. [b] $wR_2 = [\sum[w(F_o^2-F_c^2)^2]/\sum[w(F_o^2)^2]^{1/2}$.

Table 2.3. Crystal and refinement data for complexes **2.4-2.5**.

	2.4	**2.5**
CCDC Number	-	997336
Empirical Formula	$C_{32}H_{26}Cl_2N_2P_2Ti$ •C_7H_8	$C_{48}H_{39}ClN_3P_3Ti$ •2(C_6D_6)
Formula weight	711.39	1002.37
T (K)	123(2)	123(2)
a, Å	10.8506(3)	9.8417(9)
b, Å	12.1018(3)	13.5795(12)
c, Å	14.4342(4)	19.0352(17)
α, deg	81.317(1)	86.090(4)
β, deg	70.498(1)	81.483(4)
γ, deg	85.361(1)	83.215(4)
Volume, Å^3	1765.22(8)	2495.0(4)
Z	2	2
Crystal System	Triclinic	Triclinic
Space Group	P-1	P-1
d_{calc}, g/cm^3	1.338	1.334
θ Range, deg	3.691 to 72.130	2.350 to 74.917
μ, mm^{-1}	4.534	3.185
Abs. Correction	Multi-scan	Multi-scan
GOF	0.997	1.030
R_1 ,[a]	R1 = 0.0311	R1 = 0.0346
wR_2 [b] [I>2σ (I)]	*w*R2 = 0.1100	*w*R2 = 0.0836

[a] $R_1 = \sum||F_o| - |F_c||/\sum|F_o|$. [b] $wR_2 = [\sum[w(F_o^2-F_c^2)^2]/\sum[w(F_o^2)^2]]^{1/2}$.

Chapter 3

Structure and Bonding of Group 4-Group 10 Heterobimetallics Supported by 2-(diphenylphosphino)pyrrolide Ligands

Reproduced in part with permission from:

Dunn, P. L.; Carlson, R. K.; Gagliardi, L.; Tonks, I. A. Structure and bonding of group 4-nickel heterobimetallics supported by 2-(diphenylphosphino)pyrrolide ligands. *Dalton Trans*. **2016**, *45*, 9892.

and

X-ray Absorption Spectroscopy (XAS) data included with permission from Dr. Sudipta Chatterjee, Dr. Samantha MacMillan and Prof. Kyle Lancaster.

3.1 Overview

The synthesis of a full series of group 4/nickel complexes supported by a 2-(diphenylphosphino)pyrrolide (NP) ligand is reported. Treatment of the homoleptic, 8-coordinate $M(NP)_4$ monometallic precursors with $Ni(COD)_2$ (COD = 1,5-cyclooctadiene) yielded the heterobimetallic complexes $(\kappa^2\text{-NP})M(\mu_2\text{-NP})_3Ni$ (M = Ti, Zr, Hf). Although X-ray crystallographic analysis reveals similarly short metal-metal distances in all three complexes, Theoretical calculations indicate that ZrNi (**3.3**) and HfNi (**3.4**) contain only single Ni→M dative bonds while TiNi (**3.2**) has an additional covalent Ti-Ni π-bond. All three complexes have quasireversible reductions by cyclic voltammetry, and 1-electron chemical reduction of **3.2** by Na(Hg) yields the anion, $[Na][(\kappa^2\text{-NP})Ti(\mu_2\text{-NP})_3Ni]$, **3.5**. X-ray and computational analysis indicate that the 1-electron reduction of **3.2** to **3.5** completely breaks the metal-metal double bond, yielding a formally Ti^{III}-Ni^0 complex. Ti-Ni bonding can also be disrupted by coordination of CO, wherein Ni→CO backbonding effectively outcompetes Ni→Ti dative bonding. Additionally, the synthesis of two Ti-Pd complexes, $(\kappa^2\text{-NP})Ti(\mu_2\text{-NP})_3Pd$ (**3.9**) and $BrTi(\mu_2\text{-NP})_3Pd$ (**3.10**) are also reported.

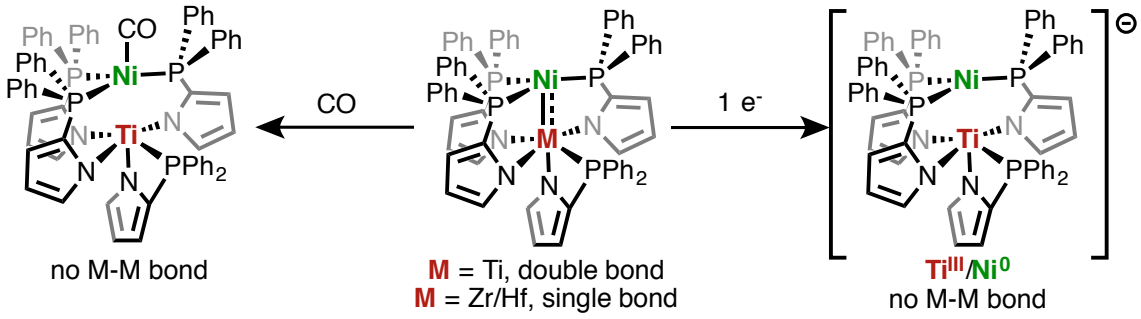

Figure 3.1. Reactivity of a TiNi complex with CO and reductants resulting in Ti-Ni bond cleavage.

3.2 Introduction

There is significant incentive to utilize first row transition metal catalysts based on Fe, Co or Ni instead of their heavier congeners because of their relative earth abundance, cost, and carbon footprint [1-2]. However, an inherent challenge in utilizing first row transition metals is overcoming (or harnessing) their propensity to undergo 1-

electron radical pathways instead of the more easily-controlled 2-electron processes that coincide with many fundamental organometallic reactions. Many successful and novel strategies have been developed to address this challenge, including the use of redox non-innocent ligand scaffolds [20-33] and metal/ligand or metal/metal cooperative reactivity [34-61].

Within the area of metal/ligand or metal/metal cooperativity, two main strategies have been employed. First, various research groups have designed systems in which reactivity occurs on both the metal and the ligand. For example, Milstein coupled ligand aromatization/dearomatization with H_2 oxidative addition with tridentate Ru and Fe pincer complexes to successfully hydrogenate a variety of substrates [34-36]. Noyori performed enantioselective catalytic transfer hydrogenation with Ruthenium diamine complexes where heterolytic H_2 cleavage occurs across the Ru-N bond [37-40]. Parkin reported Ni-B boratrane complexes where the dative Ni→B bond is the site of reactivity, resulting in oxidative addition across the bond [44]. Building upon this, Peters has recently reported several Ni borane complexes that feature cooperative addition of H-H across the Ni-B bond en route to catalytic olefin hydrogenation [45-46], while Thomas has demonstrated diverse cooperative reactivity such as CO_2 activation, hydrosilylation, and E-H and E-E bond activation across trigonally symmetric ZrCo and TiCo heterobimetallics [101-108].

Second, several research groups have exploited M-M bonding to attenuate the electrophilicity of a reacting metal through retrodative interactions. For example, Lu has studied several Ni-M (M = Al, Ga, In) olefin hydrogenation catalysts and found that the strength of H_2 binding and resulting catalytic TOF was impacted by the nature of the Lewis acidic metal [56]. Additionally, Co-M (M=Al, Co) were shown to be active for silylation of N_2, and the identity of the supporting metal affected catalyst activity [58]. Similarly, Nagashima and Michaelis each have carried out catalytic nucleophilic allylic amination reactions with heterobimetallic PdTi complexes. In these amination reactions, a dative Pd→Ti interaction increases the electrophilicity of Pd(η^3-allyl) complexes such that they can undergo attack by weak amine nucleophiles [87-90].

To further investigate cooperative Lewis acidic effects and to investigate the potential role of covalent M-M bonding on fundamental organometallic reactivity, we are

interested in synthesizing early-late transition metal complexes supported by phosphinopyrrolide group 4 metalloligands [131]. While these ligands should impart σ-electronic properties somewhat similar to existing phosphinoamide ligand frameworks [98-100, 132-133], they are much poorer N π-donors, which should allow for stronger M-M interactions between electron-rich late transition metals and electron-poor group 4 metals. Herein we report the synthesis, characterization and electrochemistry of a series of (κ^2-NP)M(μ_2-NP)$_3$Ni complexes (NP = 2-diphenylphosphinopyrrolide; M = Ti, Zr, Hf) and lend insight into how group trends affect bonding in early-late bimetallic complexes.

3.3 Results and Discussion

The homoleptic group 4 complexes M(NP)$_4$ (NP = 2-diphenylphosphinopyrrolide; M = Ti (**2.2**), Zr (**2.1**), Hf (**3.1**)) were synthesized via salt metathesis of MCl$_4$(THF)$_2$ with 4 eq. LiNP (eq. 1). Complexes **2.1** and **2.2** were previously reported via salt metathesis from MCl$_4$; in this case, utilization of the THF adducts gives significantly improved yields for Zr and Hf [131]. In the solid state, **2.1, 2.2,** and **3.1** are all 8-coordinate with κ^2-bound phosphinopyrrolide ligands. However, each of these complexes are fluxional on the NMR timescale: **2.2** displays only a single sharp ^{31}P NMR resonance indicating fast exchange, while **2.1** and **3.1** both have broad ^{31}P NMR resonances indicative of slower exchange. These exchange processes are a function of phosphine ligand decoordination from the high coordination number metal centres [131].

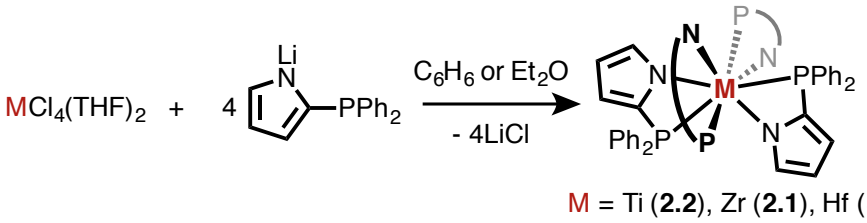

Scheme 3.1. Synthesis of the homoleptic complexes M(NP)$_4$ (M = Ti, Zr, and Hf).

Treatment of **2.1, 2.2,** and **3.1** with Ni(COD)$_2$ (COD = 1,5-cyclooctadiene) affords the heterobimetallic complexes (κ^2-NP)M(μ_2-NP)$_3$Ni (M = Ti (**3.2**), Zr (**3.3**), Hf (**3.4**)) in relatively high yield (Scheme 3.1). While **3.2** could be prepared from treatment with 1 equivalent of Ni(COD)$_2$ at room temperature, both **3.3** and **3.4** required a large excess of Ni(COD)$_2$ (> 5 equiv) and elevated temperatures (90 °C) in order to react. Presumably, the higher reaction temperature is required because the M-P bonds are

significantly less labile (demonstrated by ^{31}P NMR exchange) in the heavier congeners than in Ti, while excess Ni(COD)$_2$ is needed because it decomposes under high temperatures.

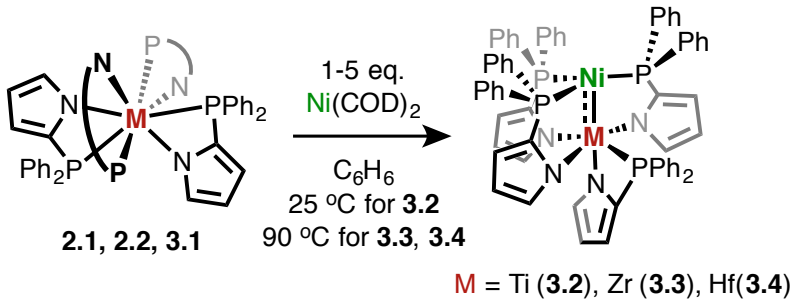

Scheme 3.2. Synthesis of the bimetallic complexes (κ^2-NP)M(μ_2-NP)$_3$Ni (M = Ti (**3.2**), Zr (**3.3**), Hf (**3.4**)).

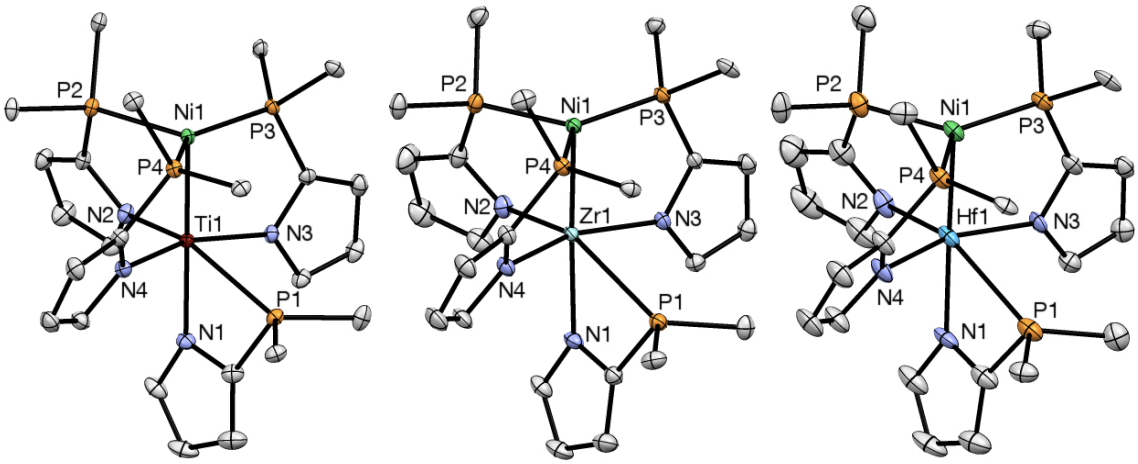

Figure 3.2: Thermal ellipsoid drawings of **3.2** (left), **3.3** (center), and **3.4** (right). Solvent and hydrogen atoms have been removed and phenyl groups have been reduced to the ipso carbon for clarity. Relevant bond distances (Å) and angles (°) are presented in Table 3.1.

Table 3.1. Relevant bond lengths (Å) and angles (°) for **3.2**-**3.4**.

	3.2	**3.3**	**3.4**
M-Ni (Å)	2.2665(5)	2.3724(3)	2.4123(6)
FSR[a]	0.91	0.91	0.93
P-Ni (Å)	2.1906(6)	2.1979(5)	2.1849(10)
	2.2181(6)	2.2160(5)	2.2072(10)
	2.2354(6)	2.2257(5)	2.2171(11)
P-Ni-P (°)	135.91(2)	131.631(19)	131.53(4)
	110.19(2)	110.103(19)	110.61(4)
	112.47(2)	117.840(19)	117.68(4)
M-N (Å)	2.0800(17)	2.1747(14)	2.156(3)
	2.1053(17)	2.1926(13)	2.178(3)
	2.0433(17)	2.2234(13)	2.203(3)
	2.1089(17)	2.2283(13)	2.203(3)
M-P (Å)	2.7224(7)	2.8799(4)	2.8543(11)
Torsional Angle (P-	24.35(5)	30.78(4)	31.60(9)
Ni-M-N) (°)	5.83(5)	3.48(4)	23.99(8)
	30.67(5)	24.17(4)	2.73(8)

[a]FSR = $M_D/\sum(M_c)$: M_D = Metal-metal distance, M_c= Covalent Radii [151]

The structures of **3.2-3.4** are presented in Figure 3.2 and relevant bond lengths and angles can be found in Table 3.1. All three bimetallic compounds are isostructural, containing three phosphinopyrrolide ligands that bridge between the two metals and one phosphinopyrrolide ligand that binds in κ^2-fashion to the group 4 metal center. The geometry about the group 4 metal is pseudooctahedral, while the geometry about Ni is a distorted trigonal pyramidal wherein the group 4 metal occupies the axial site of the pyramid. Interestingly, two of the three bridging phosphinopyrrolide ligands are significantly skewed from the M-Ni vector, although this has no significant effect on M-N or Ni-P bond lengths. The M-P bond of the phosphinopyrrolide that remains κ^2 to the group 4 metal is significantly longer than average for all three complexes, although shorter than the M-P bonds observed in the homoleptic 8-coordinate **2.1**, **2.2**, and **3.1**

[45**]**. Complexes **3.2**-**3.4** are all diamagnetic, and at room temperature display two resonances in the ^{31}P NMR: a broad feature (Ti = 2 ppm, Zr = -9 ppm, Hf = -9 ppm) of integration 3 for the Ni-bound phosphines, and a sharp singlet (Ti = -19.2 ppm, Zr = -29.6 ppm, Hf = -26.6 ppm) that integrates to 1 for the group 4-bound phosphine. Low temperature NMR experiments reveal 3 inequivalent Ni-bound phosphines, as expected based on the solid-state structure: for **3.2** (TiNi), the broad feature at 2 ppm splits into three distinct resonances (Figure 3.3). These resonances consist of two sets of doublets of doublets of doublets (J_{PP} = 11.1 Hz, 44.5 Hz, 92.0 Hz and J_{PP} = 11.1 Hz, 44.5 Hz, 55.6 Hz), which correspond to the two Ni-bound phosphines that are *pseudo-trans* to each other in the distorted trigonal plane; a doublet of doublets (J_{PP} = 55.6 Hz, 92.0 Hz), corresponding to the phosphine *trans* to open space; and a triplet belonging to the titanium bound phosphine (J_{PP} = 11.1 Hz). **3.3** (ZrNi) and **3.4** (HfNi) do not fully decoalesce at low temperature, but the same signal pattern emerges in all three complexes. The source of this fluxional behavior is likely canting/twisting of the NP ligands along the M-Ni vector.

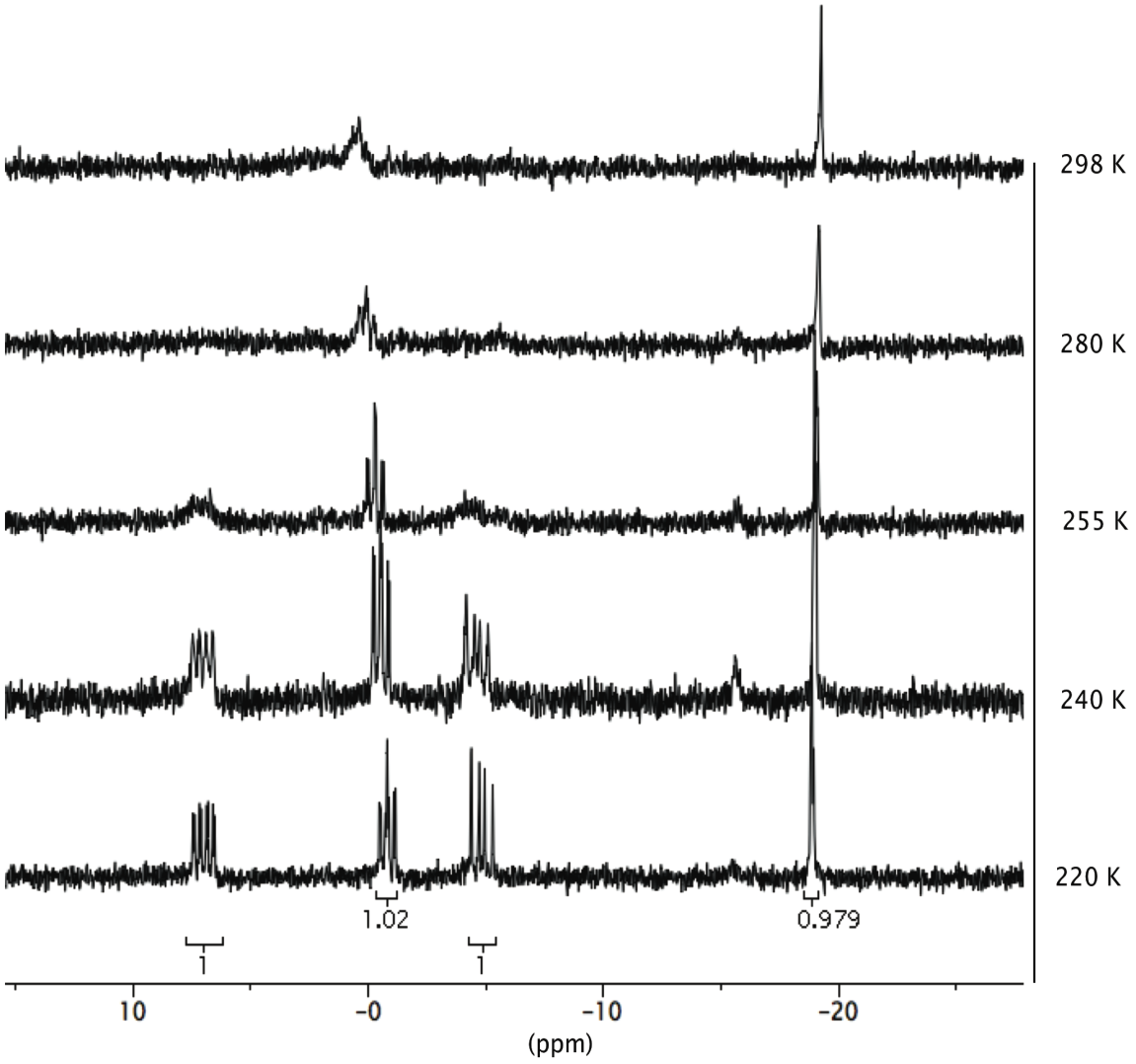

Figure 3.3: Variable temperature ^{31}P NMR spectra of **3.2** showing decoalescence of the 3 inequivalent Ni-bound phosphines at low temperature**.**

All three heterobimetallics possess remarkably short M-Ni bond distances: Ti-Ni 2.2665(5) Å; Zr-Ni 2.3724(3) Å; Hf-Ni 2.4123(6) Å. Although the bonds become longer as the group 4 atomic radius increases, the formal shortness ratio (FSR) increases only slightly down the series, from 0.91 in **3.2** (TiNi) to 0.93 in **3.4** (HfNi) potentially indicating a minor decrease in the strength of M-M bonding down the triad. **3.2** (TiNi) represents the second discrete TiNi bimetallic complex; Lu recently reported a d^{11} TiNi bimetallic complex with a Ti-Ni bond length of 2.4118(7) Å contained in a double-decker

phosphinoamide ligand framework [133]. A CSD search revealed no examples of ZrNi or HfNi complexes containing a metal-metal bond [148].

In order to develop a better understanding of the M-Ni bonding in **3.2-3.4**, DFT and CASSCF calculations were performed. Geometry optimization and frequency calculations were performed using the M06L functional and are in good agreement with crystallographic bond distances (Supplementary Information). CASSCF calculations performed on **3.2** show that the wave function is multiconfigurational and dominated by two configurations. The dominant configuration (72%) is $\sigma^2\pi^2(Ni_{dyz})^2(Ni_{dxy})^2(Ni_{dx2-y2})^2$, containing two Ti-Ni bonding interactions: a σ-bond between the Ti d_{z2} and Ni d_{z2} orbitals, and a π-bond between the Ti d_{xz} and Ni d_{xz} orbitals (Figure 3.4). The second major configuration (11.3%) is similar but contains a double excitation from the Ti-Ni π orbital to π*. The σ-bond is predominantly polarized (94%) on Ni, while the π orbital is more covalent, with 71% of the electron density on Ni. Effective oxidation states can be estimated from the natural orbital occupation numbers and the percentage each atomic orbital of the metals contribute to the molecular orbital. From this analysis, Ti has 3.1 electrons and Ni has 0.9 electrons, and the system is best described as Ti^{III}/Ni^{I}. From DFT natural bond order (NBO) analysis, the Mayer bond order is calculated to be 0.91, approximately a Ti-Ni single bond.

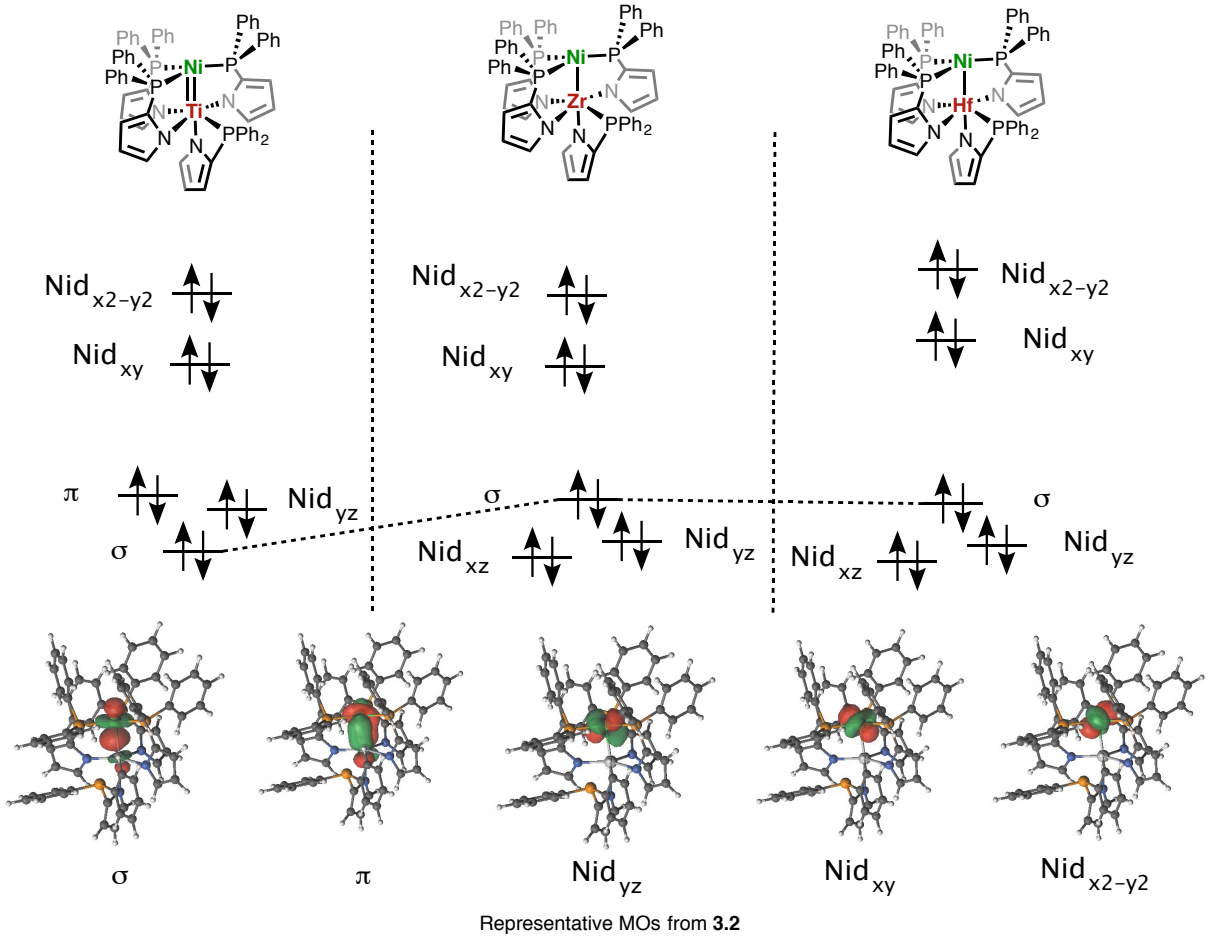

Figure 3.4: Qualitative molecular orbital diagrams taken from M06L energies for **3.2**, **3.3**, and **3.4** (above) and representative molecular orbitals for **3.2** (below).

In contrast, calculations on the Zr and Hf analogues **3.3** and **3.4** indicate that there are *no* M-Ni π interactions, most likely due to poor energy overlap between the two participating orbitals [106, 131]. For both, the dominant configuration is $\sigma^2(Ni_{dxz})^2(Ni_{dyz})^2(Ni_{dxy})^2(Ni_{dx2\text{-}y2})^2$, with a σ-bond between the Zr/Hf d_{z2} and Ni d_{z2} orbitals that is predominantly Ni based (94% for Zr; 93% for Hf). Also unlike the Ti case, there is significantly less orbital occupation on the group 4 metal in **3.3** and **3.4** (approximately 0.2-0.3 electrons), indicating that these are best described as M^{IV}/Ni^0 systems. The Mayer bond orders for **3.3** and **3.4** are 0.78 and 0.70, respectively, suggesting weaker metal-Ni interactions as the metal period increases. Furthermore, since

Ti has better orbital overlap with Ni, there is a larger degree of bonding and covalency in **3.2** than in **3.3** or **3.4**, ultimately yielding a formally Ti^{III}/Ni^{I} bimetallic core in which Ni has effectively reduced the Ti centre [108, 133].

To further examine the effects of introducing a late transition metal into the coordination sphere of group 4 metals, cyclic voltammetry experiments were performed on the monometallic complexes **2.1, 2.2** and **3.1** as well as the corresponding bimetallics **3.2-3.4** (Figure 3.5). Monometallics **2.1, 2.2** and **3.1** each showed one quasi-reversible reduction, and the reduction potential becomes increasingly more negative down the group 4 triad: -0.6 V for **2.2** (Ti); -1.8 V for **2.1** (Zr); - 2.2 V for **3.1** (Hf) *vs*. Fc/Fc^{+}. This trend follows the Pauling electronegativities of the group 4 elements, and the large gap between Ti and Zr is expected; for example, electrochemical studies performed by Laviron with Cp_2MCl_2 (M = Ti, Zr, Hf) revealed reduction potentials of -0.6 V for Ti, -1.5 V for Zr, and -1.9 V for Hf [149-150]. Surprisingly, there were no oxidation events observed within the solvent window for **3.2-3.4**.

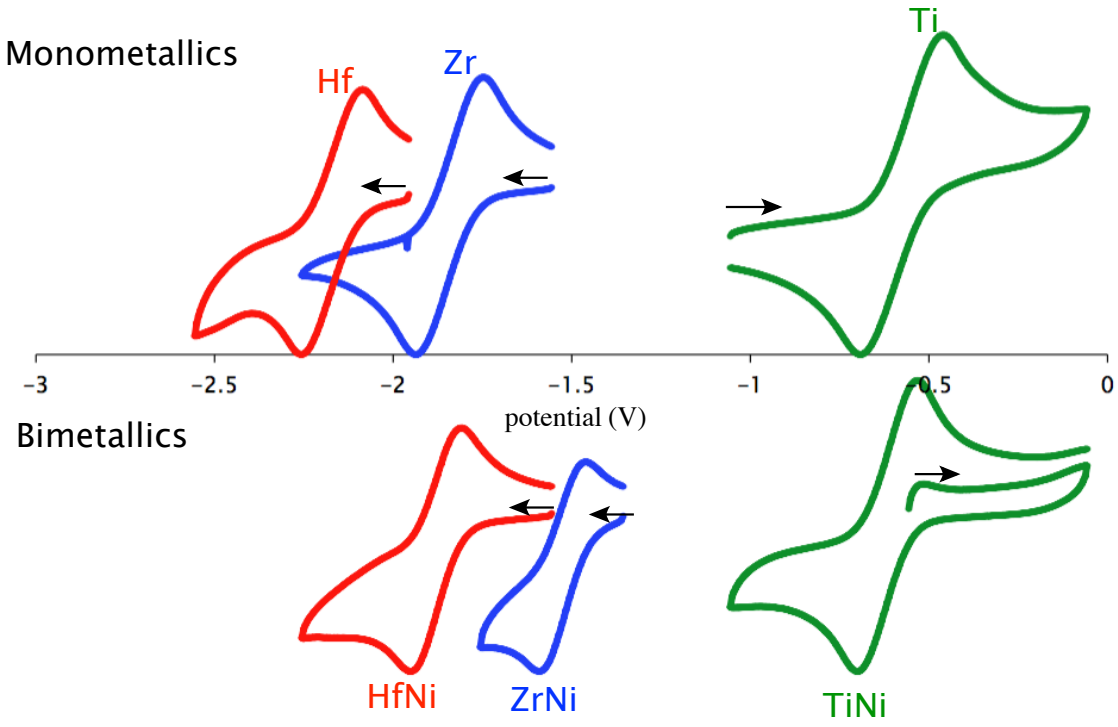

Figure 3.5. Cyclic voltammograms of **2.1**, **2.2**, and **3.1** (top) and **3.2**, **3.3**, and **3.4** (bottom). Potentials are referenced to Fc/Fc^{+}.

Interestingly, addition of a d^{10} Ni center to the coordination environment of Ti, Zr, or Hf has only a small effect on the reduction potential of the bimetallics **3.2-3.4**. Cyclic voltammetry of **3.2-3.4** showed a single quasireversible reduction for each compound. Like the monometallic series, the reduction potentials are increasingly negative down the group 4 triad: -0.6 V for **3.2** (Ti); -1.5 V for **3.3** (Zr); -1.9 V for **3.4** (Hf) *vs.* Fc/Fc^{+}. Because this trend is identical to that observed in the monometallics and because the Ni centre is d^{10}, the electrochemical events observed in **3.2-3.4** are likely the M^{IV}/M^{III} redox couple. The reduction potentials of **3.3** (ZrNi) and **3.4** (HfNi) are 0.3 V *higher* than their monometallic counterparts. In this case, the dramatic change in the group 4 metal coordination environment likely makes reduction more facile: the monometallic complexes are 8-coordinate, formally 16-electron species with 4 dative M-P bonds, whereas the bimetallic complexes are 6-coordinate, formally 12-electron species with only 1 dative M-P and 1 dative M-Ni^{0} bond. Coincidentally, the reduction potential of **3.2** (TiNi) is virtually unshifted with respect to the monometallic **2.2**.

To further investigate the electronic structure of these complexes Ni K-edge XAS data was collected. The Ni K-edge XAS of all group 4-nickel complexes exhibit an intense, well-resolved absorption feature around 8333 eV along with an additional peak at 8335 eV; the latter peak is distinguishable only for complex **3.2**. The first pre-edge maxima appears at 8332.8 eV, 8333.3 eV and 8333.1 eV for complexes **3.2**, **3.3** and **3.4,** respectively (Figure 3.6). The metal K-edge XAS for 2nd and 3rd row transition metals (Zr and Hf) were not recorded due to their broadened K-edge feature. Conventionally, the intense pre-edge features are attributable to dipole allowed 1s → *n*p transitions; relatively low-energy weak pre-edge features (appearing as a shoulder to the intense pre-edge peak) arise due to quadrupole-allowed 1s → (*n-1)*d excitations which are ~2 orders of magnitude weaker than a dipole transition but can gain intensity from *n*p admixture. In addition, excitations to low-lying ligand-based molecular orbitals can also contribute to this spectral region. In this case, no low-energy shoulder in the pre-edge region was observed for all three complexes, which suggests filling of valence vacancies for nickel. Therefore, all complexes likely possess a d^0-d^{10} M^{+4}-Ni^0 closed-shell configuration. Moreover, the overlaying rising edge feature in all these complexes also indicates that the oxidation state of nickel is invariant along the series (Figure 3.6 (top)). There are no spectral features observed that could be assigned to 1s → ligand π* transitions.

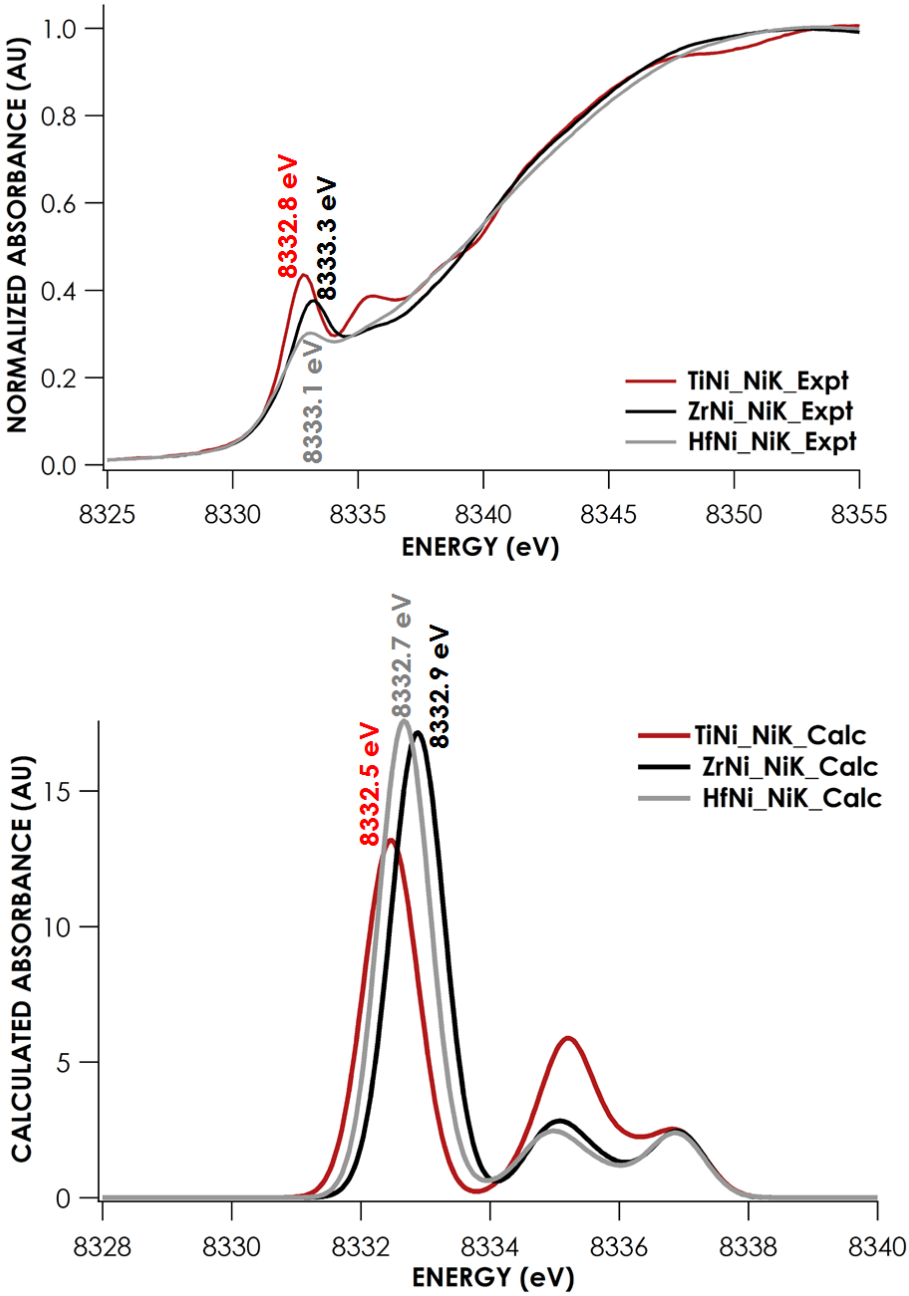

Figure 3.6. Overlaid experimental (top) and calculated (energy corrected) (bottom) K-edge spectra of Ni for heterobimetallic complexes **3.2** (red), **3.3** (black), and **3.4** (grey).

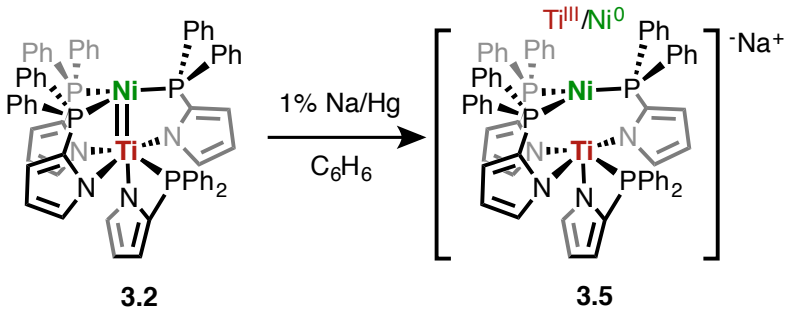

Scheme 3.3. Synthesis of $[Na]^+[(\kappa^2\text{-NP})Ti(\mu_2\text{-NP})_3Ni]^-$, **3.5**, from complex **3.2**

Given the facile reduction of **3.2**, we sought to isolate the reduced species *via* chemical reduction. Reduction of **3.2** with Na(Hg) in benzene leads to the clean formation of the 1-electron reduced anion, $[Na]^+[(\kappa^2\text{-NP})Ti(\mu_2\text{-NP})_3Ni]^-$, **3.5** (Scheme 3.3). The X-ray structure of **3.5** is reported in Figure 3.7. The ligand connectivity of **3.5** is identical to that of **3.2**; however, the Ti-Ni bond distance has dramatically elongated from 2.2665(5) Å to 2.6892(5) Å, giving an FSR (1.08) indicative of complete breakage of the Ti-Ni bond. While the Ni-P bond distances are roughly unchanged in **3.5** from **3.2**, the Ti-N distances are all elongated by 0.02-0.06 Å and the Ti-P distance has elongated by 0.14 Å. The elongated Ti-ligand bond lengths are consistent with a Ti^{III} metal center, yielding a formally Ti^{III}/Ni^0 bimetallic core with little-to-no interaction between the two metals. Similar phosphine elongation has been observed by Wass in isostructural cationic and neutral (2-(Di-t-butylphosphino)phenol)titanocenes where the Ti-P bond length increases from 2.785(2) Å to 2.9067(9) Å upon reduction from Ti^{IV} to Ti^{III} [152-153]. While the d^{11} TiNi core in **3.5** is isoelectronic with Lu's previously-reported TiNi complex $NiTi(N(o\text{-}(NCH_2P^iPr_2)C_6H_4)_3)$ which contains a formal Ti-Ni single bond, the intermetallic distance in **3.5** is significantly (> 0.2 Å) longer and thus any bonding interaction is much weaker [133].

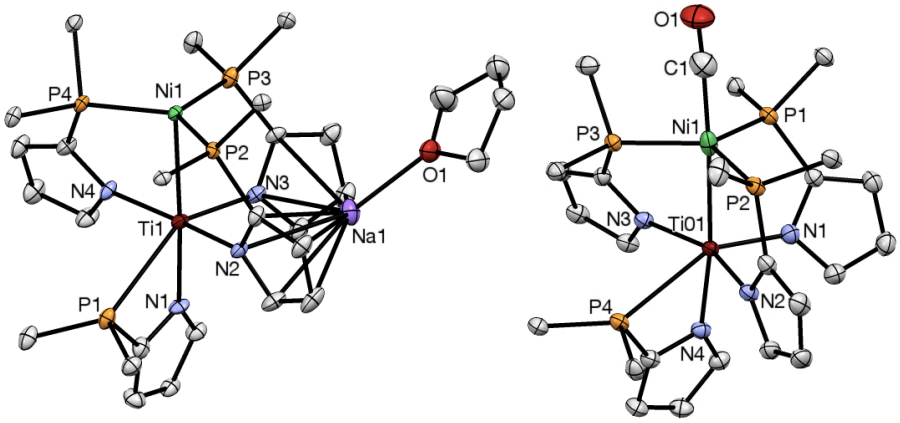

Figure 3.7. Thermal ellipsoid drawings of **3.5** (left) and **3.6** (right). Solvent and hydrogen atoms have been removed and phenyl groups have been reduced to the ipso carbon for clarity. Relevant bond distances (Å) and angles (°) are presented in Table **3.3**.

Table 3.2. Relevant bond lengths (Å) and angles (°) for **3.5-3.8**.

	3.5	**3.6**	**3.7**	**3.8**
M-Ni (Å)	2.6892(5)	2.6136(8)	2.6194(7)	2.6753(5)
FSR[a]	1.08	1.05	1.06	1.03
P-Ni (Å)	2.1651(6)	2.2109(8)	2.2414(8)	2.2407(6)
	2.1810(7)	2.2217(8)	2.2252(7)	2.2327(6)
	2.1898(7)	2.2285(9)	2.2345(7)	2.2329(7)
P-Ni-P (°)	107.36(3)	130.50(3)	112.26	110.08
	129.33(3)	113.26(3)	135.78	133.90
	123.31(3)	114.32(3)	109.31	111.20
Ti-N (Å)	2.098(2)	2.014(2)	2.123(3)	2.142(2)
	2.1068(19)	2.039(2)	2.023(2)	2.163(2)
	2.1263(19)	2.068(2)	2.053(2)	2.245(3)
	2.1390(19)	2.087(2)	2.104(2)	2.201(2)
Ti-P (Å)	2.863(5)	2.7889(9)	2.771(1)	2.8575(8)
Torsion Angle (P-Ni-M-N) (°)	15.49(6)	25.36(7)	21.72	25.09
	24.33(6)	2.77(7)	0.47	0.64
	19.90(6)	31.17(7)	24.96	19.88
Ni-C (Å)	-	1.894(4)	1.906(4)	1.885(3)
C-O (Å)	-	1.211(5)	1.164(5)	1.170(4)

[a]FSR = [a]FSR = $M_D/\sum(M_c)$: M_D = Metal-metal distance, M_c= Covalent Radii [151]

CASSCF calculations were performed on **3.5** to confirm the bonding picture. The dominant configuration, $\sigma^2(Ni_{dxz})^2(Ni_{dyz})^2(Ni_{dxy})^2(Ni_{dx2-y2})^2(Ti_{dxz})^1$, (89%) is consistent with a reduced Ti metal centre and a weak σ-bonding interaction between the Ti and Ni d_{z2} orbitals. As predicted by the X-ray structure, the oxidation state of the system based on orbital occupancy is best described as Ti^{III}/Ni^0. Unlike in **3.2**, Ni_{dxz} and Ti_{dxz} do not form a π-bond and instead have electron density localized on each metal. Consistent with

Ti^{III} being a weaker Lewis acid than Ti^{IV}, the Mayer bond order of 0.43 is significantly lower than that observed in **3.2** (0.91). Remarkably, addition of a single electron into the Ti-Ni bimetallic core has the dual effect of breaking the Ti-Ni π-bond and significantly weakening the dative σ-bond.

Exposure of **3.2** to 1 atm of H_2, ethylene or CO_2 yielded no reactivity by ^{31}P NMR analysis. However, reaction of **3.2** with 1 atm of CO or 1 equivalent of CNXylyl resulted in the reversible formation of a Ni-CO adduct **3.6** or the Ni-CNXylyl adduct **3.7** (Scheme 3.4). The X-ray structures are presented in Figures 3.7 and 3.8. The Ni centre in **3.6** and **3.7** is *pseudo*-trigonal bipyramidal with CO and Ti occupying the axial sites. Much like in **3.5**, the Ni-Ti intermetallic distance has significantly elongated to 2.6136(8) Å (FSR = 1.05) and 2.6194(7) Å (FSR = 1.06), respectively, indicating breakage of the Ni-Ti bond. The C-O bond (1.211(5) Å) is also elongated with respect to free CO, demonstrating that Ni→CO backbonding effectively outcompetes Ni→Ti dative bonding. The ^{31}P NMR spectrum also provides evidence for breakage of the Ni-Ti bond: when compared to **3.2**, **3.6** and **3.7** show a significant sharpening and downfield shift of the broad feature in the ^{31}P NMR associated with the Ni-bound phosphines. The more facile coalescence of the three inequivalent Ni-bound phosphines is a consequence of an *increase* in motion/degrees of freedom about the Ni centre that results from breakage of the Ni-Ti bond. Prolonged exposure of **3.6** to vacuum results in complete reformation of **3.2**. Unsurpsingly, addition of one equivalent of xylyl isocyanide to complex **3.3** also results in formation of Ni-CNR adduct, (κ^2-NP)Zr(μ_2-NP)$_3$Ni(CNXylyl) (**3.8**). Similar to complexes **3.6** and **3.7**, the metal-metal bond is broken as shown by the large increase in intermetallic distance, 2.6753(5) Å (FSR = 1.03). A similar ^{31}P pattern is also observed: the Ni-P resonances sharpen and shift upfield.

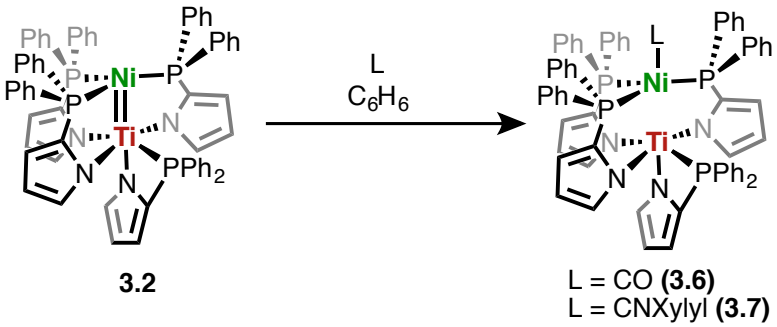

Scheme 3.4. Synthesis of the CO and CNR (R = 2,6 dimethylphenyl) adducts of TiNi

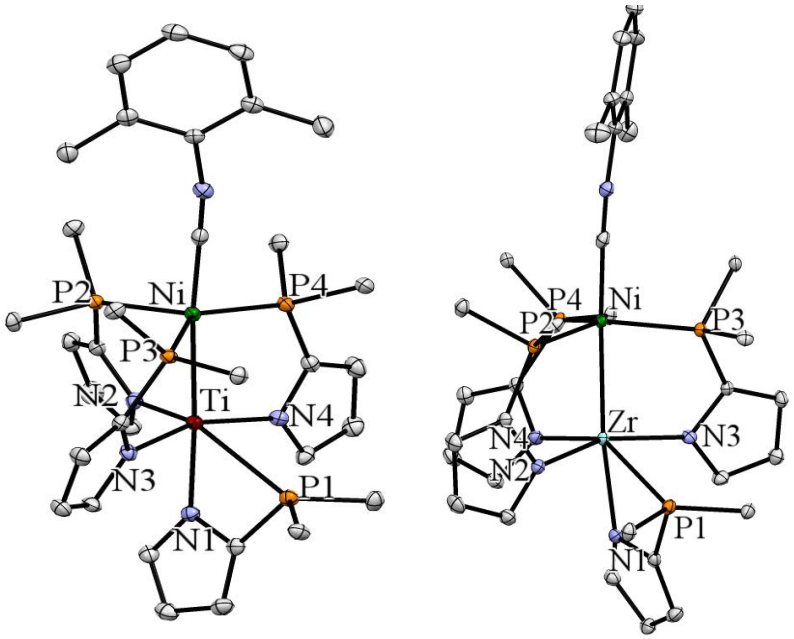

Figure 3.8. 50% thermal ellipsoid drawing of **3.7** and **3.8**. Select phenyl groups have been reduced to the ipso carbon and hydrogen atoms and solvent omitted for clarity.

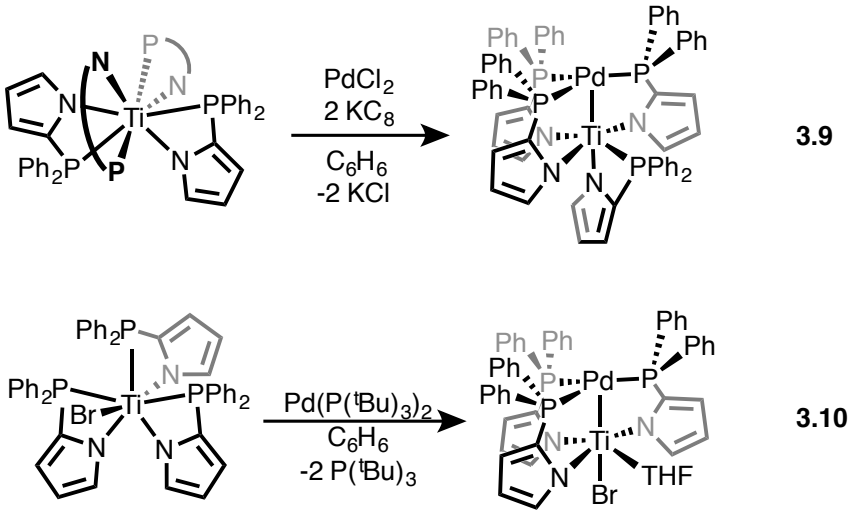

Scheme 3.5: Synthesis of two TiPd complexes supported by phosphinopyrrolides.

To futher investigate the metal-metal bonding between group 4 and group 10 metals, TiPd and TiPt complexes were also targeted. Reduction of $PdCl_2$ by two equivalents of KC_8 in the presence of $Ti(NP)_4$ results in the formation of a new diamagnetic species, (κ^2-NP)Ti(μ_2-NP)$_3$Pd (**3.9**) in moderate yield (Scheme 3.5). **3.9** can also be synthesized from a Pd(0) starting material, Pd(P(^{t}Bu)$_3$)$_2$. **3.9** is isostructural to **3.2**-**3.4**, containing three bridging ligands while the fourth remains bound to Ti in a κ^2 fashion. The Ti-Pd distance is 2.4317(5) Å (FSR = 0.890), consistent with complexes **3.2**-**3.4**. Given the similar bonds in complexes **3.2** and **3.3** where the early metal differs by period, one could also expect similar bonding in **3.2** and **3.9**, where the late metal differs by period. Therefore, we favor a strong sigma bond with minimal pi bonding present.

While utiliziation of ClTi(NP)$_3$ (**2.5**) as a metalloligand for group 10 metals was unsuccessful and yielded a multitude of products *via* ^{31}P; the reaction of BrTi(NP)$_3$ with Pd(P(tbu)$_3$)$_2$ resulted in the formation of new diamagnetic species, Br(THF)Ti(μ_2-NP)$_3$Pd (**3.10**) as confirmed by XRD. Similar to complexes **3.2**-**3.4, 3.10** contains three ligands that bridge the metal centers. The geometry about Pd is a distorted trigonal pyramid where Ti occupies the axial site. The geometry about Ti is a distorted octahedron where the Br atom occupies the axial site, *trans* to Pd, and contains a THF molecule in the equatorial plan. Complexes **3.9** and **3.10** are the second and third TiPd

complexes reported. Nagashima's [(η^3-methallyl)Pd(Ph_2PN^tBu)2$TiCl_2$](OTf) complex contains a much longer Ti-Pd bond, 2.8155(5) Å [60]. This likely stems from the fact that Pd^{II} is a weaker electron donor than Pd^0 and $TiCl_2(Ph_2PN^tBu)$ is a worse acceptor.

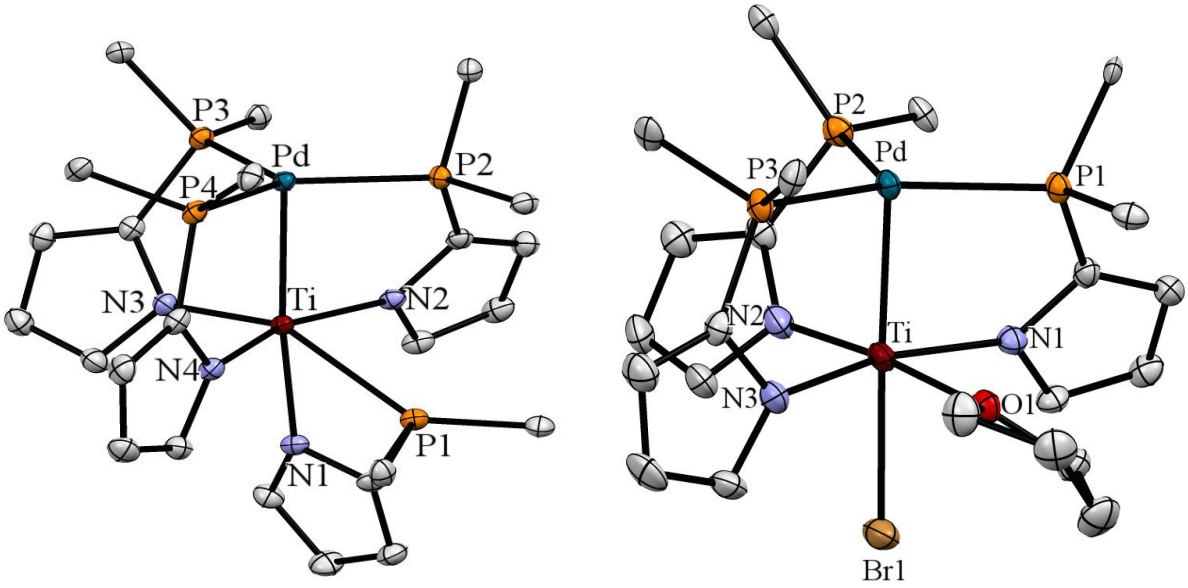

Figure 3.9. 50% thermal ellipsoid drawing of **3.9** and **3.10**. Select phenyl groups have been reduced to the ipso carbon and hydrogen atoms and solvent omitted for clarity.

Table 3.3. Relevant bond lengths (Å) and angles (°) for **3.9-3.11**.

	3.9	**3.10**	**3.11**
Ti-M (Å)	2.4317(5)	2.4165(8)	2.3846(6)
FSR[a]	0.890	0.885	0.96
P-M (Å)	2.3757(7)	2.325(1)	2.1877(7)
	2.3316(6)	2.395(1)	2.1889(8)
	2.3103(5)	2.324(1)	2.1925(7)
P-M-P (°)	115.72	114.17	122.34(5)
	134.24	138.87	116.53(3)
	109.98	106.71	121.07(3)
Ti-N (Å)	2.049(2)	2.076(4)	2.026(2)
	2.067(2)	2.097(4)	2.043(2)
	2.026(2)	2.045(4)	2.053(2)
Ti-P (Å)	2.7637(9)	-	-
Torsion Angle	24.38	24.50	32.45(6)
(P-M-M-N) (°)	3.46	3.26	32.91(7)
	30.19	31.95	36.44(7)

[a]FSR = [a]FSR = $M_D/\sum(M_c)$: M_D = Metal-metal distance, M_c= Covalent Radii [151]

All complexes are extremely water-sensitive. When crystallizing **3.2** or **3.6** in the presence of trace amounts of H_2O (<10 ppm), the oxo-bridged tetrametallic **3.11** often preferentially crystallizes from solution (Scheme 3.5). The X-ray structure of **3.11** is presented in Figure 3.10. In **3.11**, the geometry around Ti is trigonal bipyramidal with O and Ni occupying the axial sites, and the geometry around Ni is trigonal pyramidal. The Ti-Ni bond distance is 2.3846(6) Å, indicative of a single bond (FSR = 0.96). This distance is again elongated with respect to **3.2**, likely due to the presence of a ligand (O) *trans* to Ni and the geometry change about Ti. While we have been unable to intentionally synthesize **3.11** *via* stoichiometric addition of H_2O, this complex raises the

possibility of synthesizing trigonally symmetric structures and molecular wires with the NP framework.

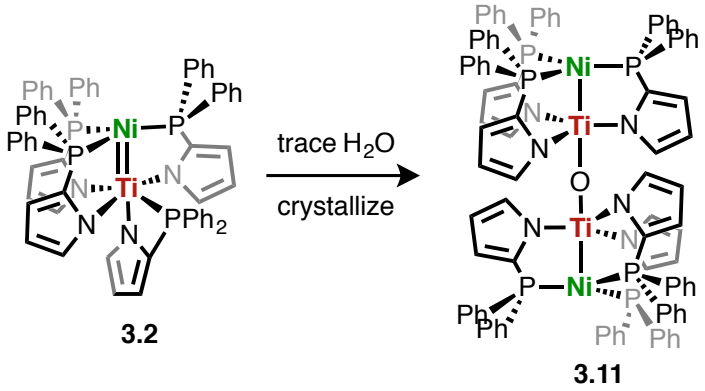

Scheme 3.6. Unintentional synthesis of an oxo bridged dimer.

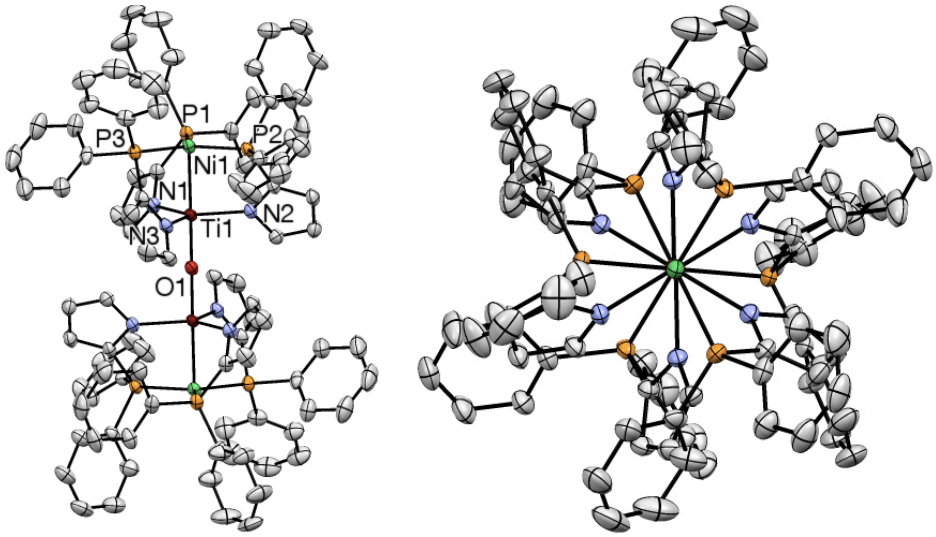

Figure 3.10. Side-on (left) and top-down (right) thermal ellipsoid drawings of **3.11**. Solvent and hydrogen atoms have been removed for clarity. Relevant bond distances (Å) and angles (°) are presented in Table 3.4.

3.4 Conclusions

A complete series of group 4/Ni heterobimetallic complexes based on a 2-(diphenylphosphino)pyrrole ligand scaffold have been synthesized and characterized. X-ray crystallography and computational analysis has revealed that the extent and type of metal-metal bonding in the complexes is dependent on the nature of the group 4 metal. The heavier congeners Zr and Hf are strictly limited to forming strong dative single bonds with Ni, while Ti can form a Ti-Ni double bond through covalent π-bonding.

Reductions of the heterobimetallic complexes take place at the group 4 metal. In the case of Ti, the reduced $[TiNi]^-$ anion was isolated and characterized. Interestingly, addition of a single electron to the bimetallic core completely disrupts the two bonding interactions present in the neutral species: the resulting Ti^{III}/Ni^0 system has no π bonding and a significantly weakened Ti-Ni dative σ-bond.

3.5 Experimental Considerations

General Considerations and Instrumentation. All air- and moisture-sensitive compounds were manipulated in a glovebox under a nitrogen atmosphere. Solvents for air- and moisture-sensitive reactions were vacuum transferred from sodium benzophenone ketyl (THF, Et_2O, pentane, d_6-benzene and d_8-toluene) or predried by passing through activated alumina columns of a SG Water solvent purification system. $Ni(COD)_2$[134], $ZrCl_4(THF)_2$ and $HfCl_4(THF)_2$[135] were prepared according to literature procedure. Cyclic volammetry was conducted using Pine Instruments WaveNow. Analyte solutions were prepared in a THF solution of tetra-n-butylammonium hexafluorophosphate (0.1 M) and referenced to the $FeCp_2/FeCp_2^+$ redox couple. ^1H, ^{13}C and ^{31}P spectra were recorded on Varian INOVA 500 MHz or Bruker Avance III 400 MHz spectrometers. Chemical shifts are reported with respect to residual protio-solvent impurity for ^1H (*s*, 7.16 ppm for C_6D_5H), solvent carbons for ^{13}C (*t*, 128.39 ppm for C_6D_6), and PPh_3 for ^{31}P (*s*, -6 ppm for C_6D_6).

X-ray Crystal Data: General Procedure. Crystals were removed quickly from a scintillation vial to a microscope slide coated with oil. Samples were selected and mounted on the tip of a 0.1 mm diameter glass capillary. Data collection was carried out on a Bruker APEX II CCD diffractometer with a 0.71073 Å Mo Kα source or on a Bruker-AXS D8 Venture diffractometer with a 1.54178 Å Cu Kα source. The structures were solved by direct methods. All non-hydrogen atoms were refined anisotropically. Details regarding refined data and cell parameters are available in Tables 3.5, 3.6, and 3.7.

Synthesis of $Hf(2\text{-}PPh_2)C_4H_3N)_4$, $Hf(NP)_4$ (3.1). Solid Li(NP) (325 mg, 1.26 mmol, 4.5 equiv) was dissolved in 5 mL Et_2O and cooled in a glovebox cold well. Solid

$HfCl_4(THF)_2$ (130.37 mg, 0.28 mmol, 1 equiv) was added to the solution and warmed to room temperature while stirring, resulting in a colorless solution with significant white precipitate. Solvent was removed *in vacuo* and the remaining solid redissolved in benzene. Following filtration over celite and removal of solvent, 245 mg of **3.1** was obtained as a white powder in 74 % yield. X-ray quality crystals were obtained by slow diffusion of pentane into a concentrated benzene solution of **3.1**. ^{1}H NMR (400MHz, C_6D_6) δ, ppm: 6.2–6.6 (*br*, 10H). 6.7–6.82 (*br*, 17H), 6.96–7.03 (*br*, 14H), 7.15–7.25 (*br*, 5H), 7.35 (*br*, 1H), 7.55 (br 1H). ^{13}C NMR (125 MHz, C_6D_6) δ, ppm: 114.0-114.4 (*br*), 117.4-117.6 (*s*), 126.6 (*d*, *br*), 129.1 (*d*), 129.1-129.3 (*br*), 133.2-134.2 (*br*), 135.1 (*d*, *br*), 135.65 (*d*, *br*). ^{31}P NMR (121 MHz, C_6D_6) δ, ppm: -30 to -40 (*br*).

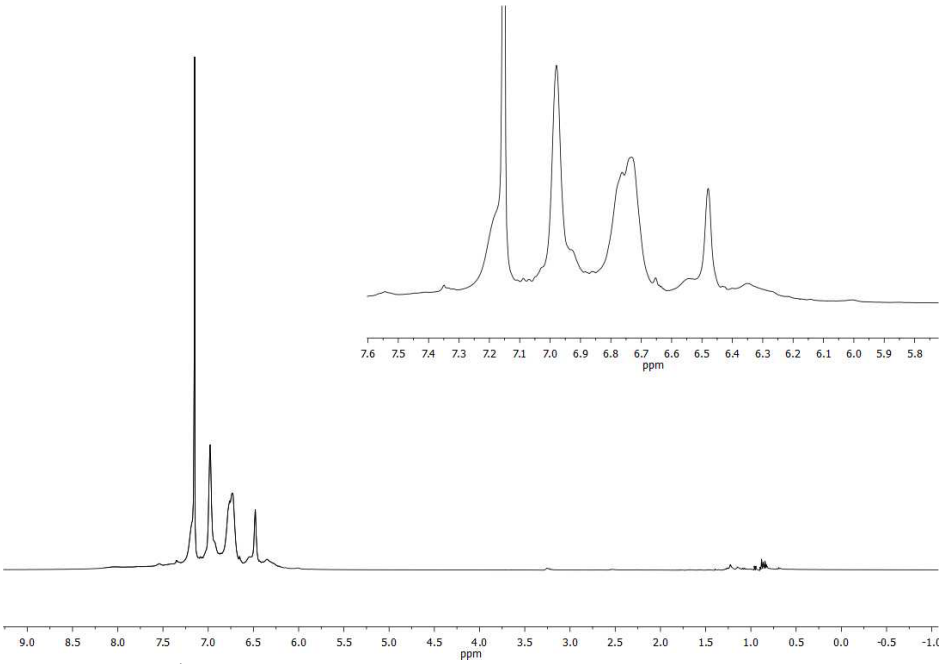

Figure 3.11: ^{1}H NMR of complex **3.1** in C_6D_6. Taken from PLD03118-2.

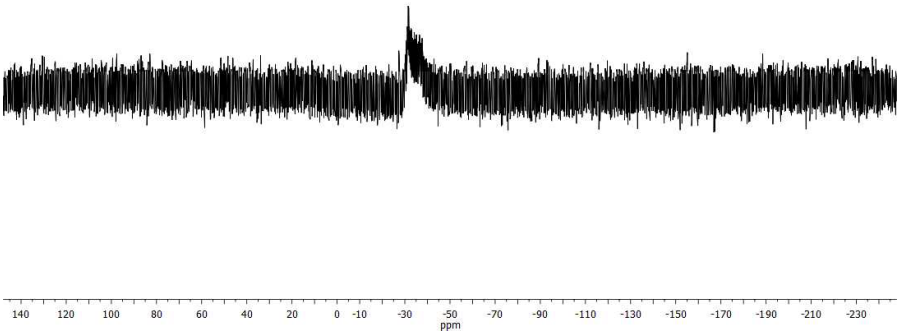

Figure 3.12: ^{31}P NMR of **3.1** in C_6D_6. Taken from PLD03118-2.

Synthesis of (κ^2-NP)Ti(μ_2-NP)$_3$Ni (3.2). Solid **2.2** (250 mg, 0.24 mmol, 1 equiv) and Ni(COD)$_2$ (65.6 mg, 24 mmol, 1 equiv) were added to a 20 mL scintillation vial, dissolved in 5 mL of benzene and stirred overnight. The solution turned from dark red to a dark yellow/orange. Filtration through celite and removal of solvent yielded 198 mg of **3.2** as a dark powder in 75% yield. X-Ray quality crystals were grown from a concentrated benzene solution over the course of days. ^{1}H NMR (400MHz, C_6D_6) δ, ppm: 6.1–6.3 (*br*, 2H). 6.40–7.0 (*br*, 47H), 7.55–7.70 (*br*, 3H), 7.86–7.92 (*br*, 1H), 8.13–8.2 (*br*, 1H). ^{13}C NMR (125 MHz, C_6D_6) δ, ppm: 110.5 (*br*), 111.85 (*d*), 116.5 (*s*), 117.9 (*s*), 118.90 (*s*), 127.85 (*d*), 130.3 (*s*), 131.9 (*br*), 132.2 (*br*) 132.4 (*br*), 133.2 (*br*), 134.0 (*br*), 134.5 (*br*) 135-136.5 (*br*), 137.1 (*s*). ^{31}P NMR (121 MHz, C_6D_6) δ, ppm: 4-0 (*br*, 3P), -19.2 (*s*, 1P).

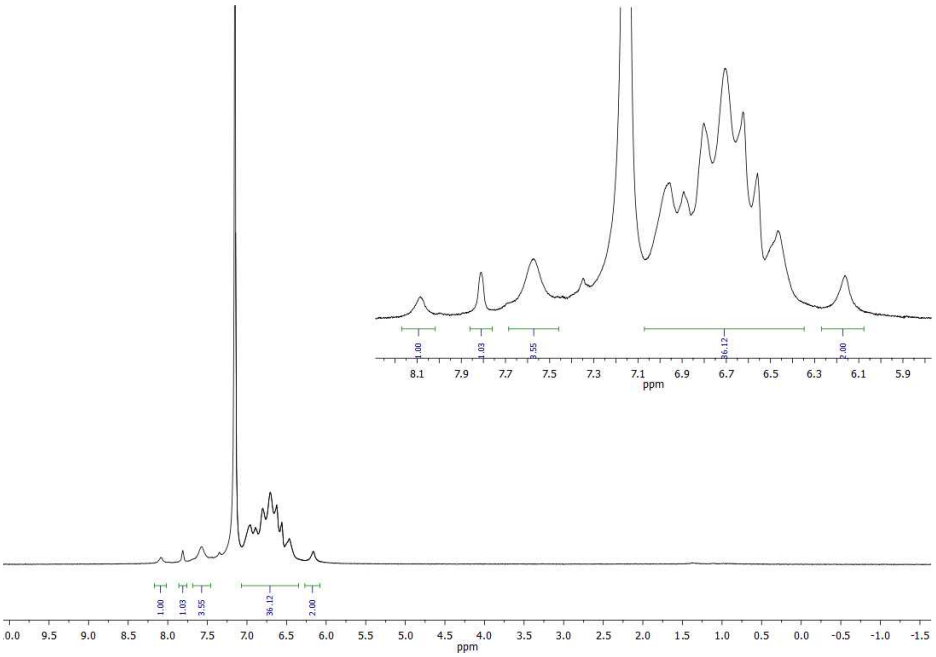

Figure 3.13: ^{1}H NMR of complex **3.2** in C_6D_6. Taken from PLD04047-2.

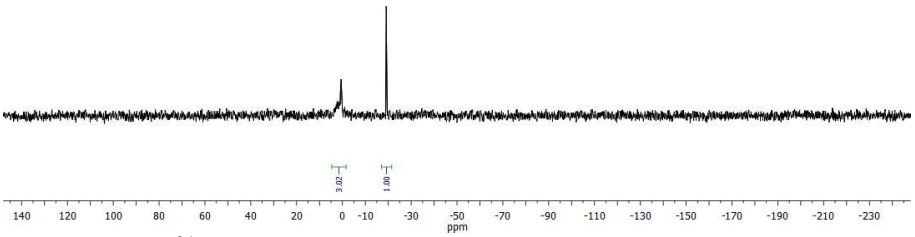

Figure 3.14: ^{31}P NMR of **3.2** in C_6D_6. Taken from PLD04047-2.

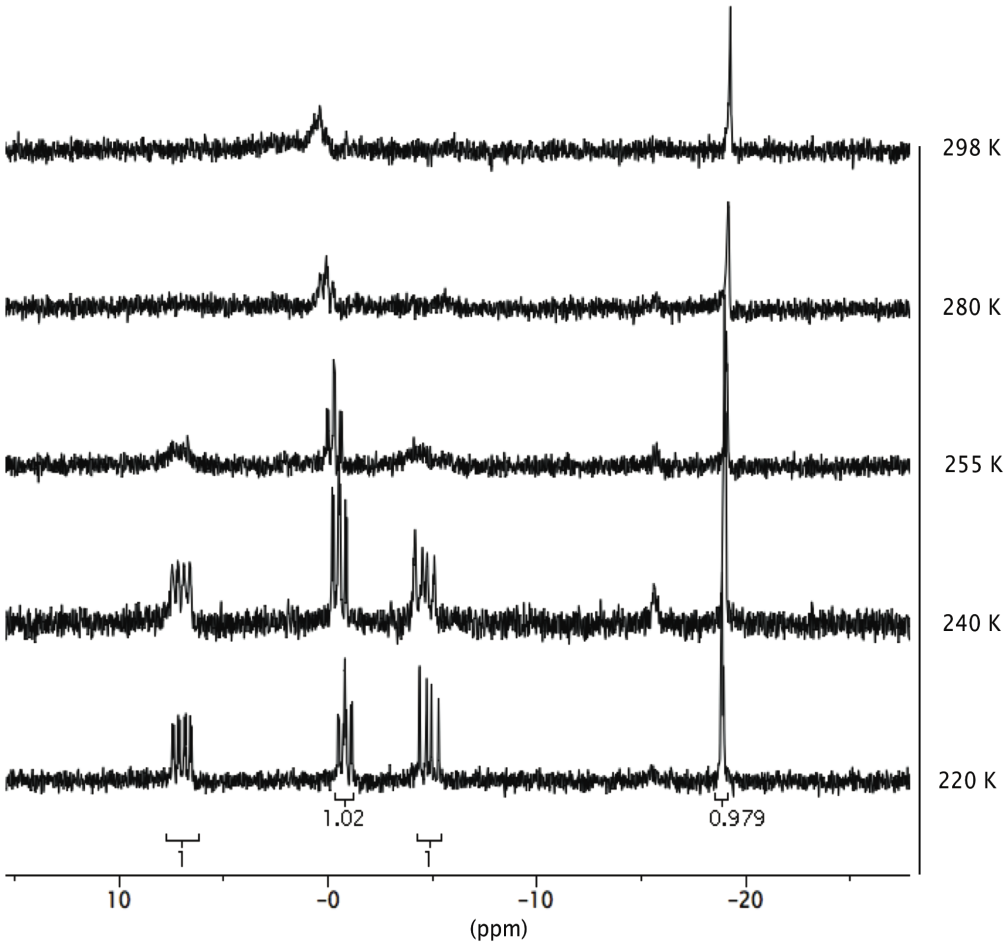

Figure 3.15: Variable temperature ^{31}P NMR of **3.2** in d_8-toluene. Taken from PLD04047-2.

Synthesis of (κ^2-NP)Zr(μ_2-NP)$_3$Ni (3.3). Solid **2.1** (222 mg, 0.20 mmol, 1 equiv) and Ni(COD)$_2$ (523 mg, 0.2 mmol, 10 equiv) were added to a 20 mL scintillation vial and dissolved in toluene, heated to 90 °C and stirred overnight. Filtration through celite and removal of volatiles yielded 145 mg of **5** as a dark red powder in 62% yield. Single crystals were grown from vapor diffusion of pentane into a concentrated benzene solution of **3.3** over the course of days. ^{1}H NMR (400MHz, C_6D_6) δ, ppm: 6.15–6.4 (*br*, 4H), 6.55–6.6 (*s*, 3H), 6.65–7.15 (*br*, 42H), 7.98–8.02 (*m*, 1H). ^{13}C NMR (125 MHz C_6D_6) δ, ppm: 113 (*s*), 113.45 (*d*), 118.5 (*d*), 119.38(*s*), 128.4 (*d*), 128.88 (*d*), 129.17 (*d*), 129.3 (*br*), 133.0 (*br*), 133.15 (*d*), 134.05 (*d*), 134.6 (*d*), 135.15(*br*). ^{31}P NMR (121 MHz, C_6D_6) δ, ppm: -7 to -13 (*br*, 3P), -29.6 (*s*, 1P).

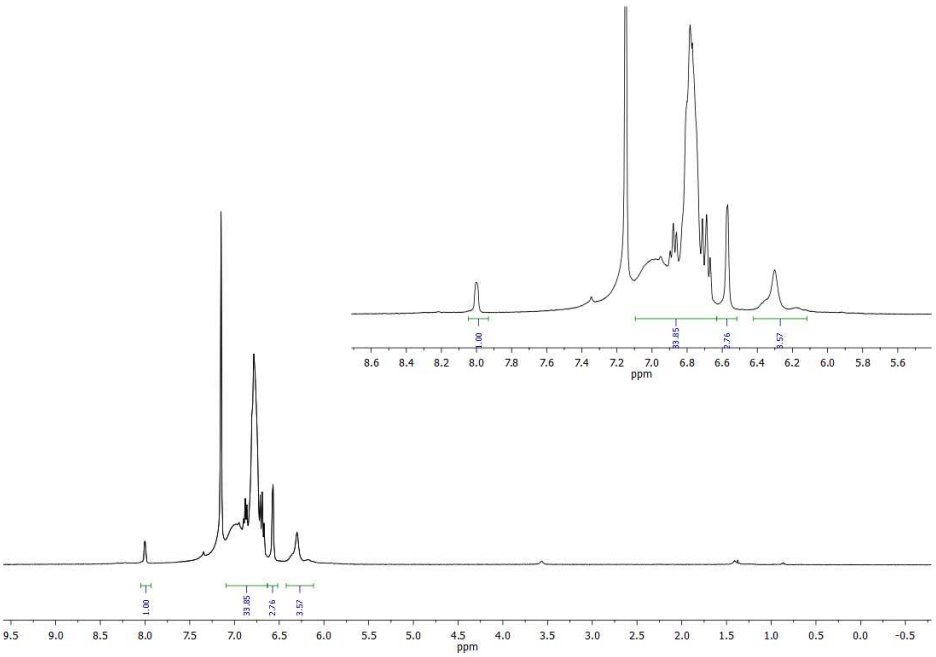

Figure 3.16: ^{1}H NMR of complex **3.3** in C_6D_6. Taken from PLD04045.

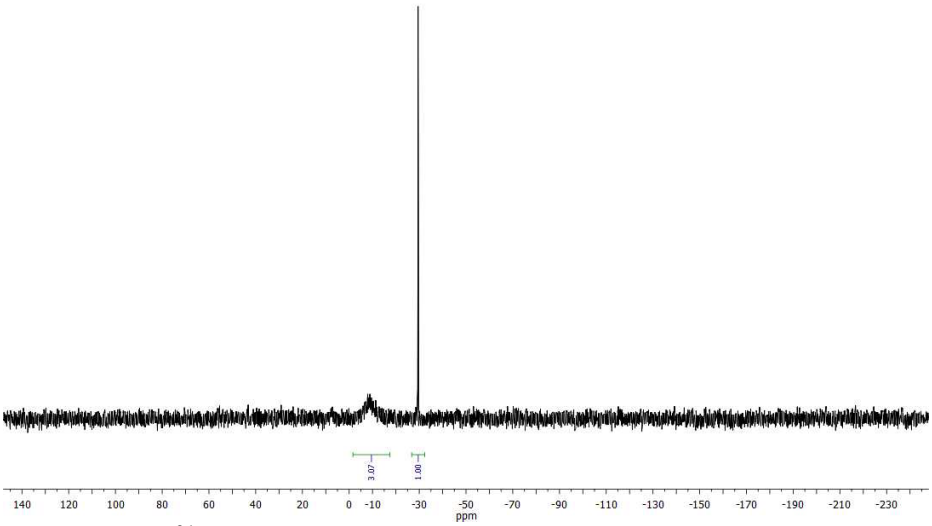

Figure 3.17: ^{31}P NMR of **3.3** in C_6D_6. Taken from PLD04045.

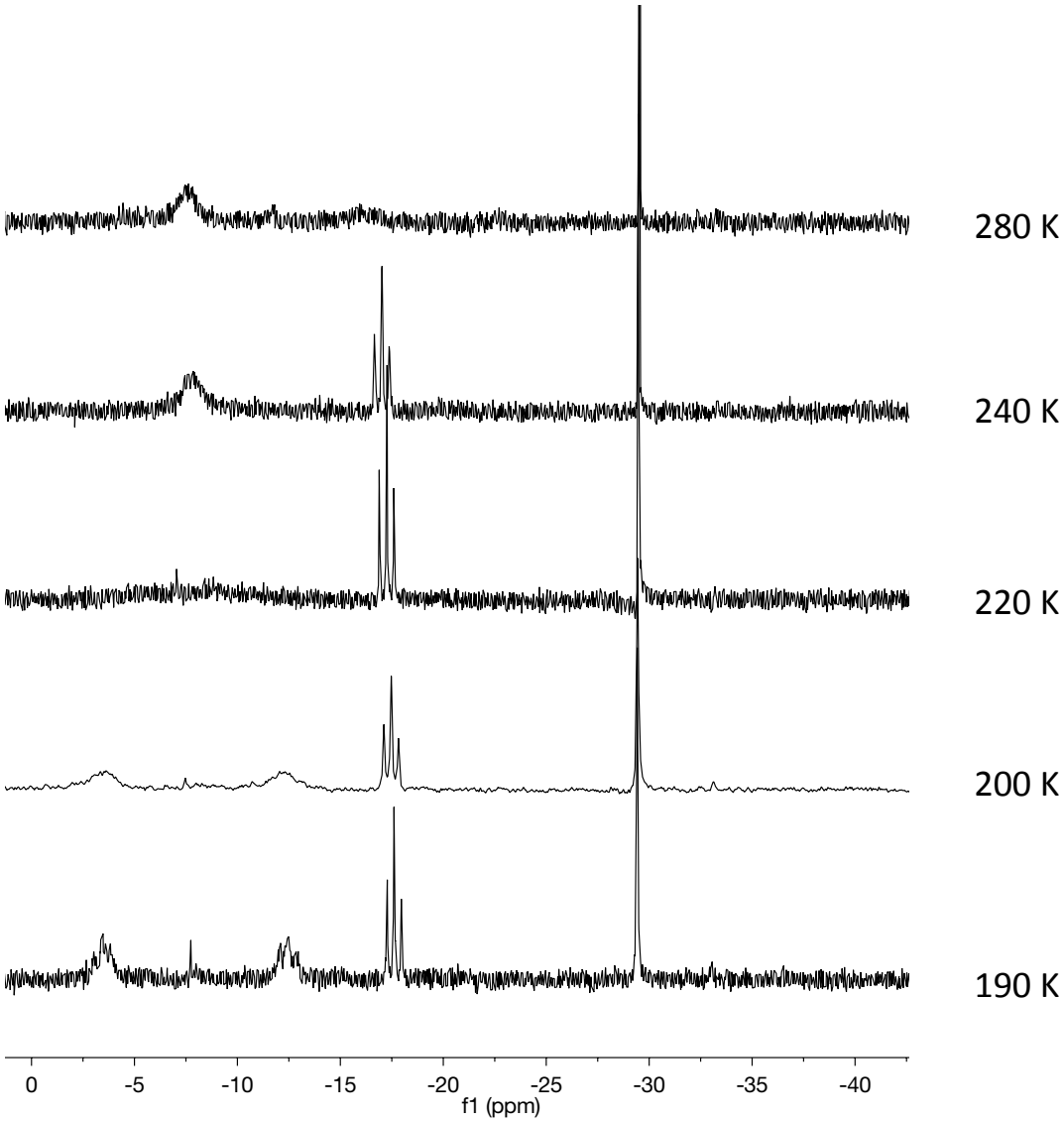

Figure 3.18: Variable temperature ^{31}P NMR of **3.3** in d_8-toluene. Taken from PLD04045.

Synthesis of (κ^2-NP)Hf(μ_2-NP)$_3$Ni (3.4). Solid **3.1** (109 mg, 0.0925 mmol, 1 equiv) and Ni(COD)$_2$ (119 mg, 0.463 mmol, 5 equiv) were added to a 20 mL scintillation vial and dissolved in benzene. The reaction mixture was heated to 90 °C and stirred overnight, resulting in a dark red solution. Following filtration, volatiles were removed *in vacuo*, yielding 76 mg of crude **3.4** in 66% yield. Red crystals of **3.4** were obtained by slow evaporation of pentane into a concentrated benzene solution of **3.4**. ^{1}H NMR (400MHz, C_6D_6) δ, ppm: 6.0–6.45 (*br*, 3H), 6.6–7.15 (*br*, 41H), 8.1–8.13 (*br*, 1H). ^{13}C NMR (125 MHz, C_6D_6) δ, ppm: 113.38 (*br*), 113.8 (*d*), 118.75 (*d*), 119.5 (*br*), 125.9 (*s*), 126.3 (*s*),

127.86 (*d*), 128.85 (*s*), 128.87 (*s*), 133.2 (*d*), 133.78 (*s*), 133.87 (*s*), 135.3 (*s*). ^{31}P NMR (121 MHz, C_6D_6) δ, ppm: -8 to -10 (*br*, 2P), -17 to -19 (*br*, 1P), -26.6 (*s*, 1P).

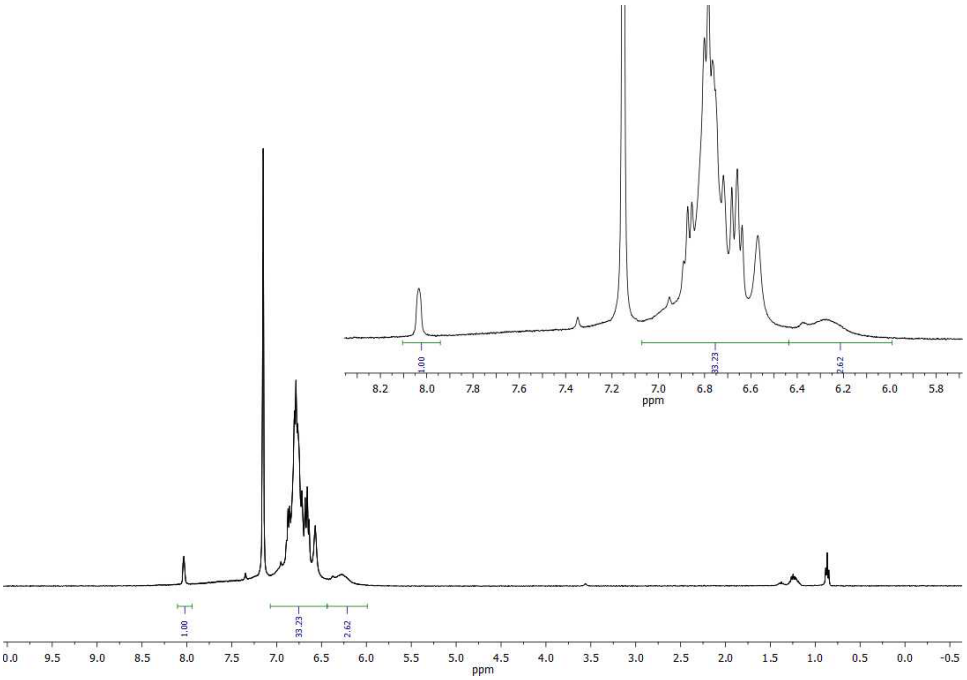

Figure 3.19: ^{1}H NMR of complex **3.4** in C_6D_6. Taken from PLD03118.

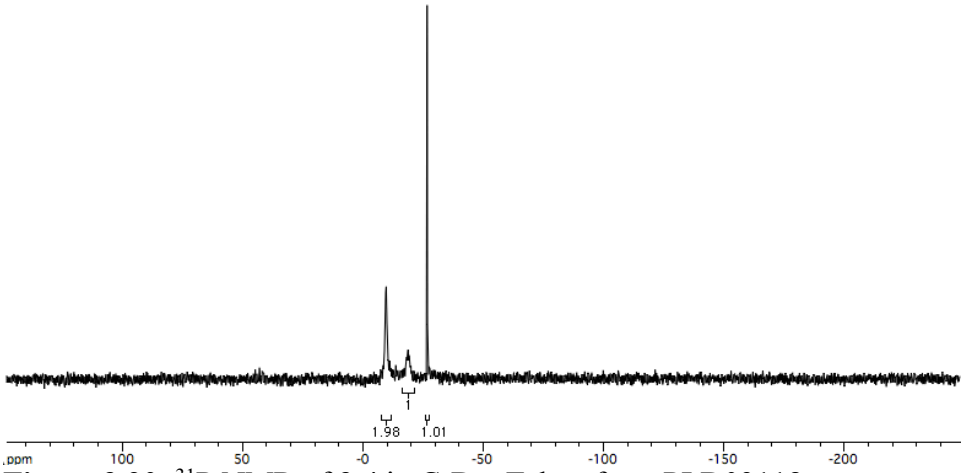

Figure 3.20: ^{31}P NMR of **3.4** in C_6D_6. Taken from PLD03118.

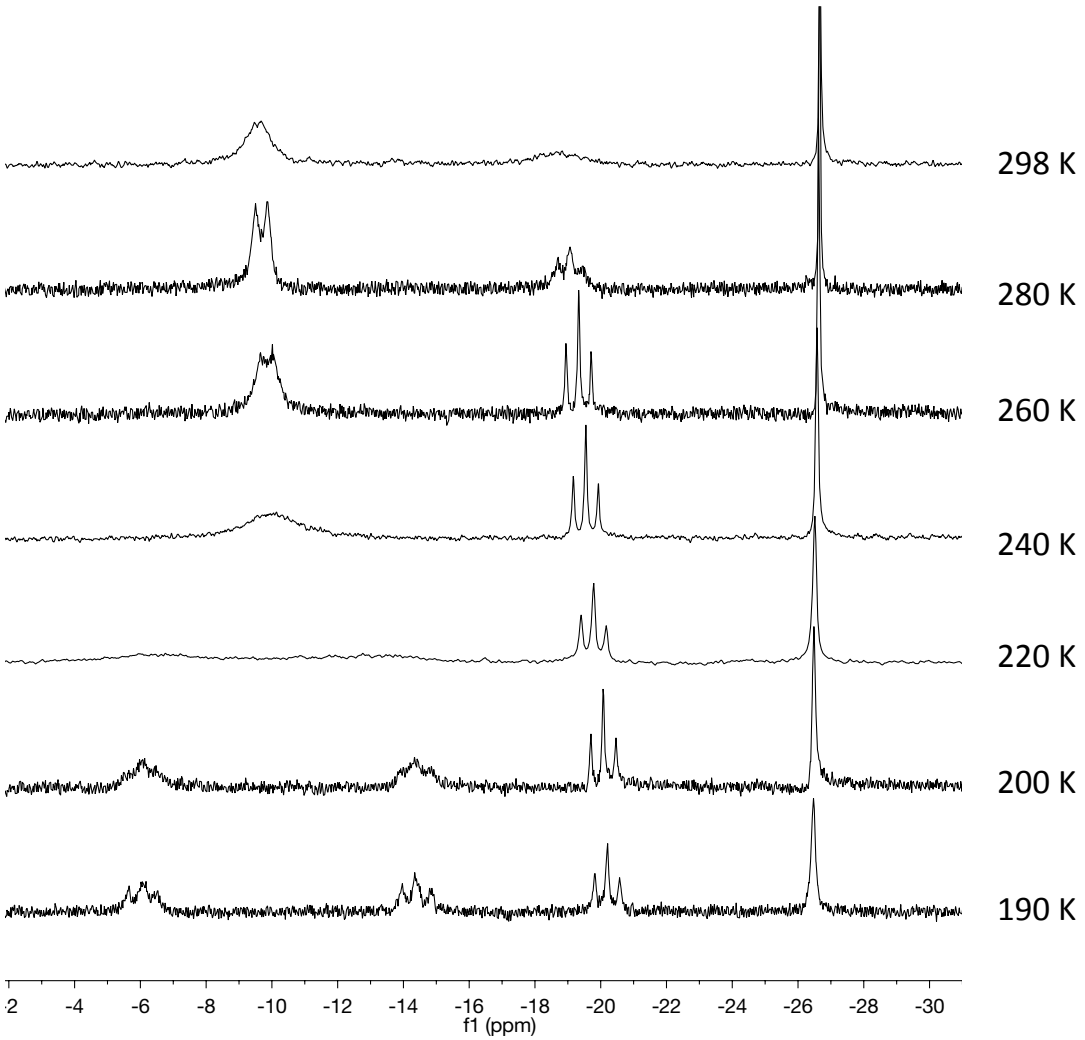

Figure 3.21: Variable temperature ^{31}P NMR of **3.4** in d_8-toluene. Taken from PLD04046.

Synthesis of $[(\kappa^2\text{-NP})Ti(\mu_2\text{-NP})_3Ni]^-[Na]^+$ (3.5). Solid **3.2** (330 mg, 0.3 mmol, 1 equiv) and 1% Na(Hg) (35 mg, 1.5 mmol, 5 equiv) were added to a 20 mL scintillation vial and dissolved in 3 mL benzene and stirred overnight. The solution turned from dark yellow to a dark orange. Following filtration through celite and removal of solvent yielded 220 mg of **3.5** as a powder in 65% yield. X-ray quality crystals were grown from a concentrated benzene solution of **3.5** over the course of days. ^1H NMR (400MHz, C_6D_6) δ, ppm: -3.282 (s), -1.865 (s), 4.273 (s), 4.687 (s), 5.0 to 5.5 (br), 6.0 to 9 (br), 11.840 (s), 14.028 (s), 17.2(br), 23.0 (br), 27.0 (br)

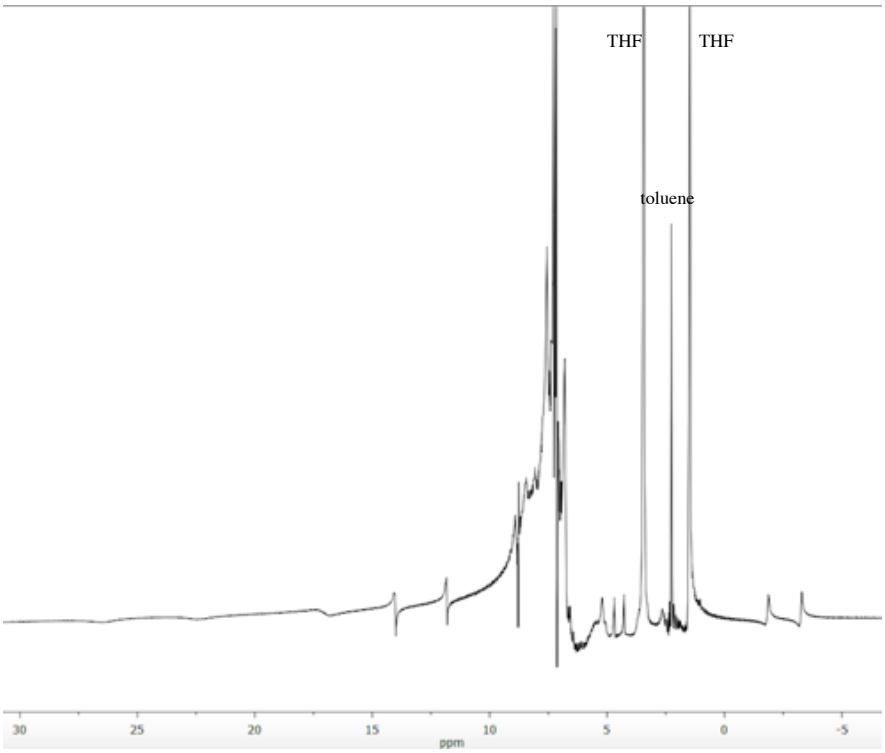

Figure 3.22: ^{1}H NMR of **3.5** in C_6D_6. Taken from PLD04052_THF.

Synthesis of (κ^2-NP)Ti(μ_2-NP)$_3$Ni(CO) (3.6). Solid **3.2** (40 mg, 0.036 mmol, 1 equiv) was dissolved in 0.7 mL of benzene and added to a J Young NMR tube. The J Young tube was attached to a Schlenk line and freeze-pump-thaw degassed three times, followed by addition of approximately 1 atm of CO. ^{31}P NMR confirmed quantitative conversion of the starting material. Single crystals of **3.6** were grown from a concentrated benzene solution layered with pentane over the course of days. Prolonged exposure of **3.6** to vacuum results in regeneration of **3.2**. ^{1}H NMR (300MHz, C_6D_6) δ, ppm: 5.95 (*s*, 2H), 6.25 (*s*, 3H), 6.37 (*t*, 1H), 6.65 (*t*, 3H), 6.8-7.05 (*br*, 28H), 7.12 (*s*, 2 H), 7.33 (*s*, 10H), 7.62 (*s*, 1H). ^{13}C NMR (125 MHz, C_6D_6) δ, ppm: 109.5 (*s*), 111.85 (*d*), 117.25 (*d*), 118.6 (*s*), 127.73 (*d*), 129.925 (*s*), 120.03 (*br*), 129.21 (*s*), 129.5 (*s*), 129.87(*s*), 132.7 (*s*), 133.75 (*s*), 134.4 (*d*), 134.75 (*d*), 135.05 (*d*), 138.25 (*br*), 139.5 (*br*). ^{31}P NMR (121 MHz, C_6D_6) δ, ppm: 6.6 (*s*, 3P), -26 (*s*, 1P).

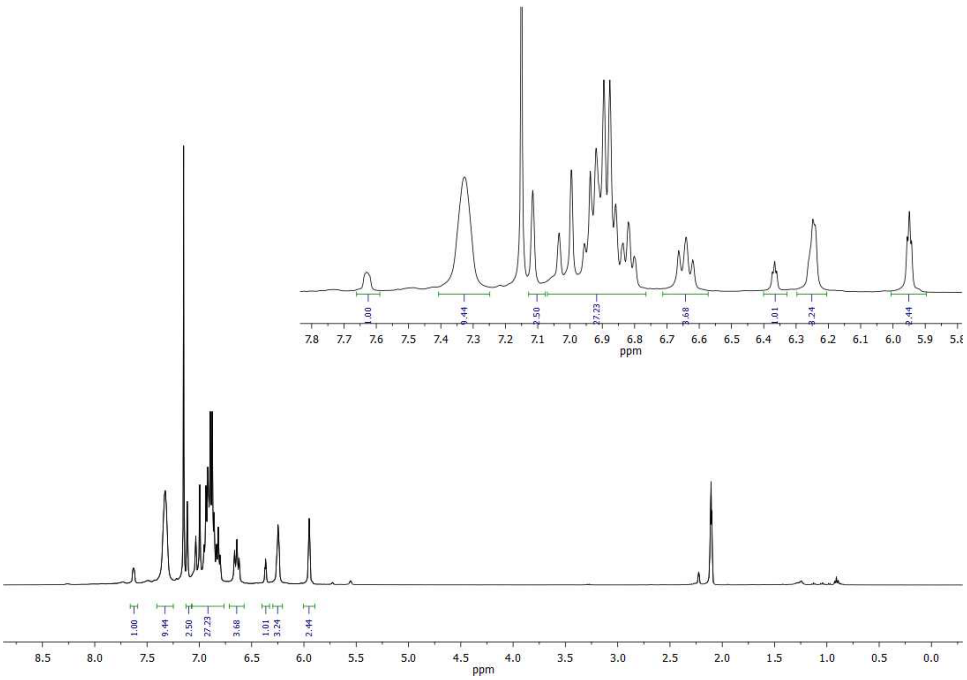

Figure 3.23: ^{1}H NMR of **3.6** in C_6D_6. Taken from PLD04055_2.

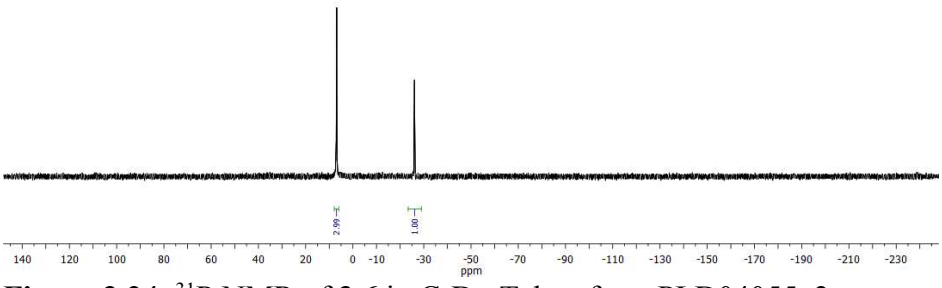

Figure 3.24: ^{31}P NMR of **3.6** in C_6D_6. Taken from PLD04055_2.

Synthesis of (κ^2-NP)Ti(μ_2-NP)$_3$Ni(CNXylyl) (3.7). Solid **3.2** (20 mg, 0.019 mmol, 1 equiv) was dissolved in 0.7 mL of benzene and CNXylyl (2.5 mg, 0.019 mmol, 1 equiv) was added. ^{31}P NMR confirmed quantitative conversion of the starting material. Single crystals of **3.7** were grown from a concentrated benzene solution layered with pentane

over the course of days. ^{1}H NMR (300MHz, C_6D_6) δ, ppm: 1.33 (s, 6H), 6.04 (s, 3H), 6.30-6.55 (m, 9H), 6.73-6.90 (m, 31H), 7.54-7.62 (br, 12H). ^{31}P NMR (121 MHz, C_6D_6) δ, ppm: 6.6 (*s*, 3P), -24.91 (*s*, 1P).

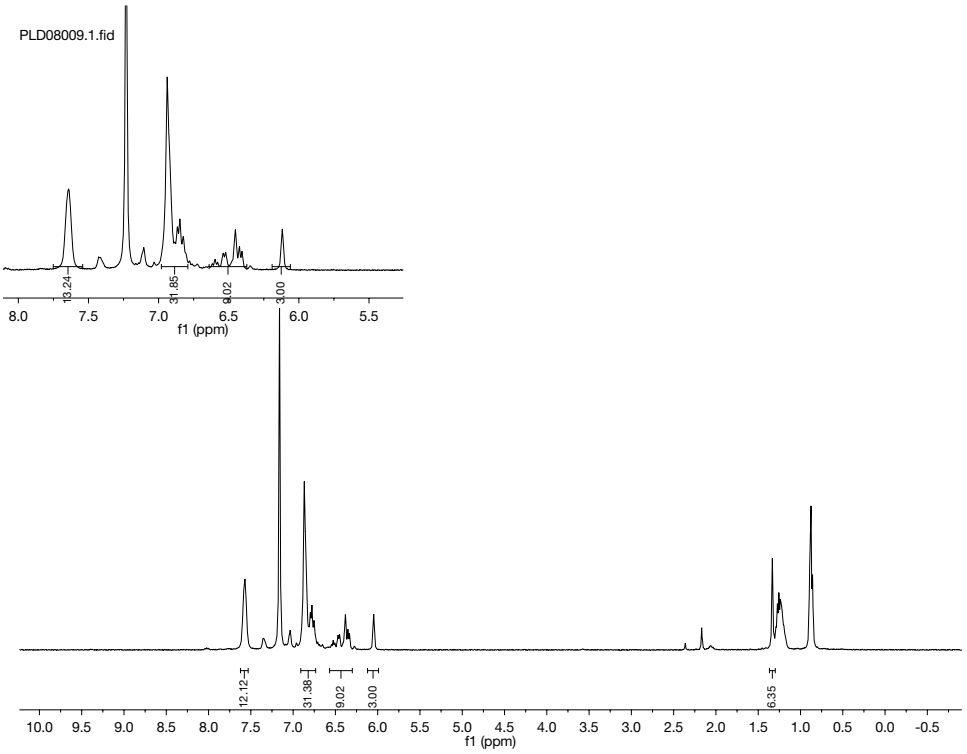

Figure 3.25: ^{1}H NMR of **3.7** in C_6D_6. Taken from PLD08009.

PLD08009.2.fid

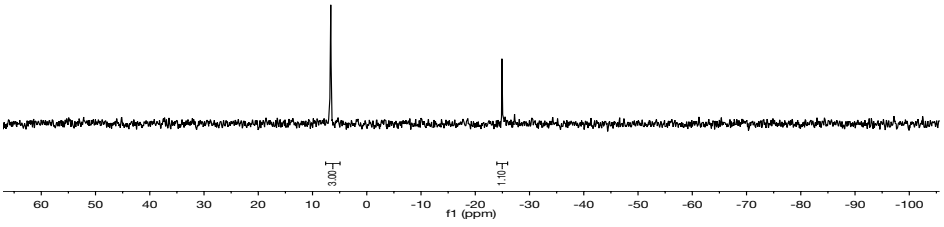

Figure 3.26: ^{31}P NMR of **3.7** in C_6D_6. Taken from PLD08009.

Synthesis of (κ^2-NP)Zr(μ_2-NP)$_3$Ni(CNXylyl) (3.8). Solid **3.3** (20 mg, 0.018 mmol, 1 equiv) was dissolved in 0.7 mL of benzene and and CNXylyl (2.4 mg, 0.018 mmol, 1 equiv) was added. ^{31}P NMR confirmed quantitative conversion of the starting material. Single crystals of **3.8** were grown from a concentrated benzene solution layered with pentane over the course of days. ^{1}H NMR (300MHz, C_6D_6) δ, ppm: 1.42 (s, 6H), 5.90-6.05 (br, 3H), 6.30-7.00 (m, 40H), 7.50-7.70 (br, 12H). ^{31}P NMR (121 MHz, C_6D_6) δ, ppm: 1.75 (*s*, 3P), -32.25 (*s*, 1P).

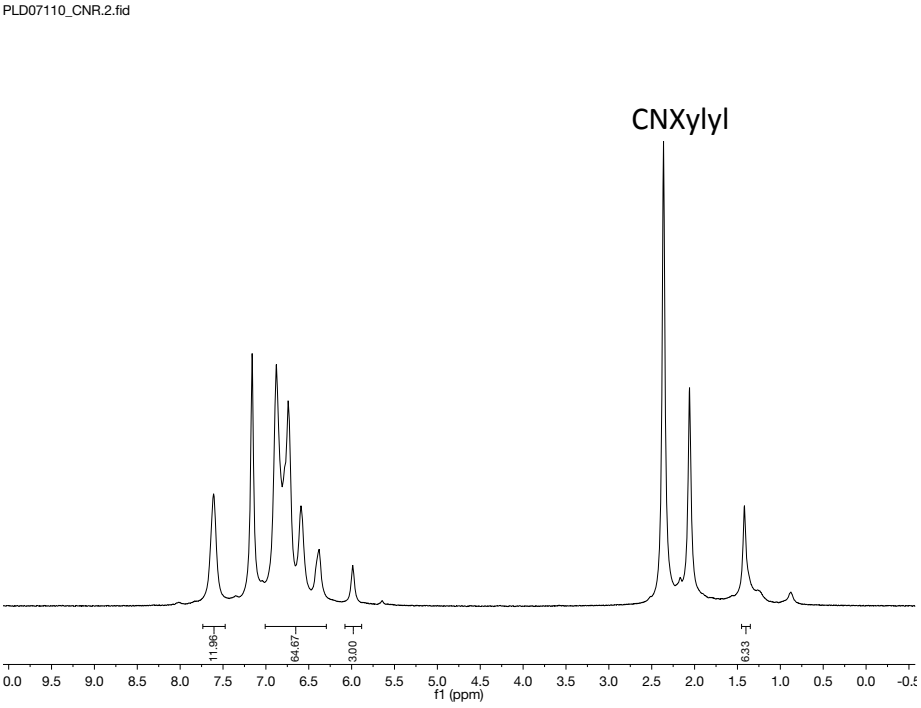

Figure 3.27: ^{1}H NMR of **3.8** in C_6D_6. Taken from PLD07110_CNR. Excess CNXylyl is present. ^{1}H NMR assignments were made by comparison to **3.7.**

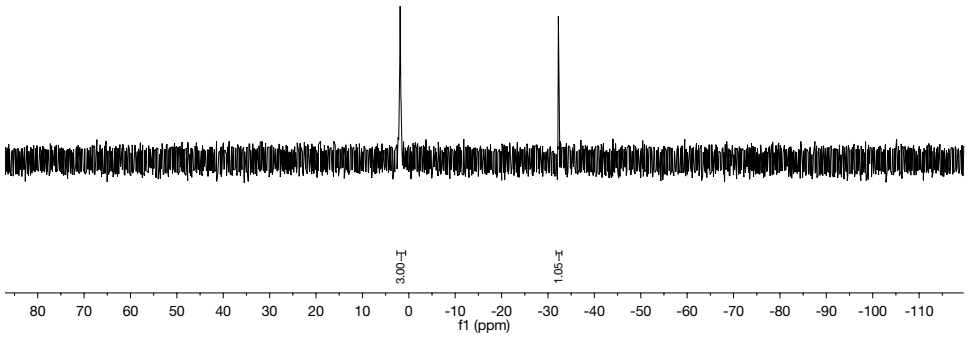

Figure 3.28: ^{31}P NMR of **3.8** in C_6D_6. Taken from PLD07110_CNR.

Synthesis of (κ^2-NP)Ti(μ_2-NP)$_3$Pd (3.9). Solid **2.2** (250 mg, 0.238 mmol, 1 equiv) and $PdCl_2$ (642.26 mg, 0.238 mmol, 1 equiv) and KC_8 (65 mg, 0.476 mmol, 2 equiv) were added to a 20 mL scintillation vial, dissolved in 5 mL of benzene and stirred overnight. Filtration through celite and removal of solvent yielded crude **3.9** as a dark red powder. X-Ray quality crystals were grown by slow evaporation of pentane into a concentrated benzene solution of **3.9** over the course of days. ^{1}H NMR (300MHz, C_6D_6) δ, ppm: 5.9-6.0 (br, 2H, ar), 6.2-6.4 (br, 6H, ar), 6.60-7.00 (br, 42H, ar), 7.35-7.41 (br, 2H, ar), 7.7 to 8.2 (br, 5H, ar). ^{31}P NMR (121 MHz, C_6D_6) δ, ppm: -24 to -22 (br, 1P), 0 to 1.5 (br, 1P), 2 to 4 (br, 2P).

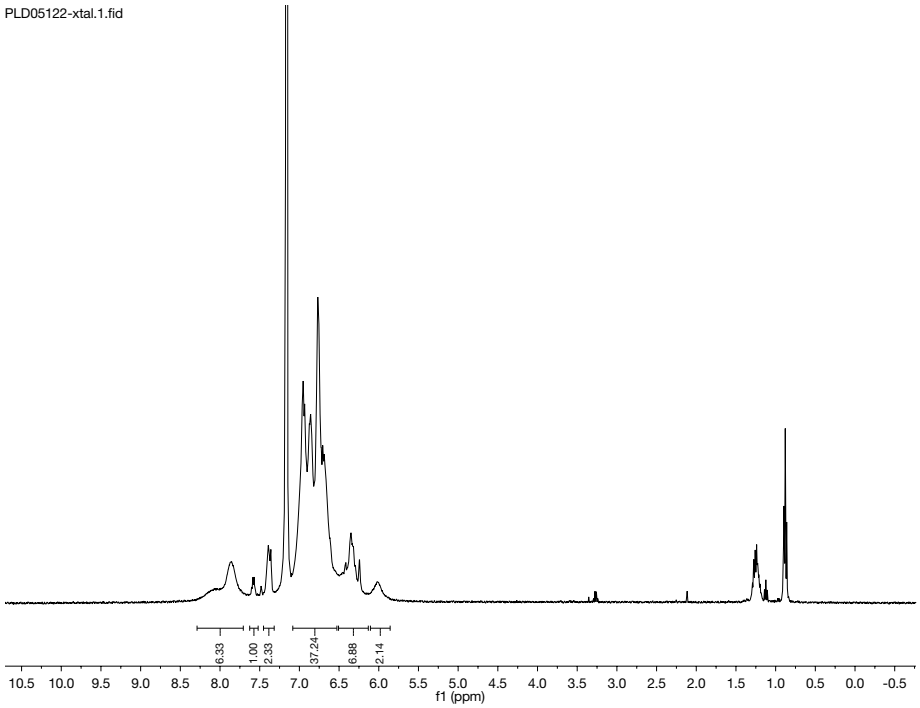

Figure 3.29: ^{1}H NMR of **3.9** in C_6D_6. Taken from PLD05122.

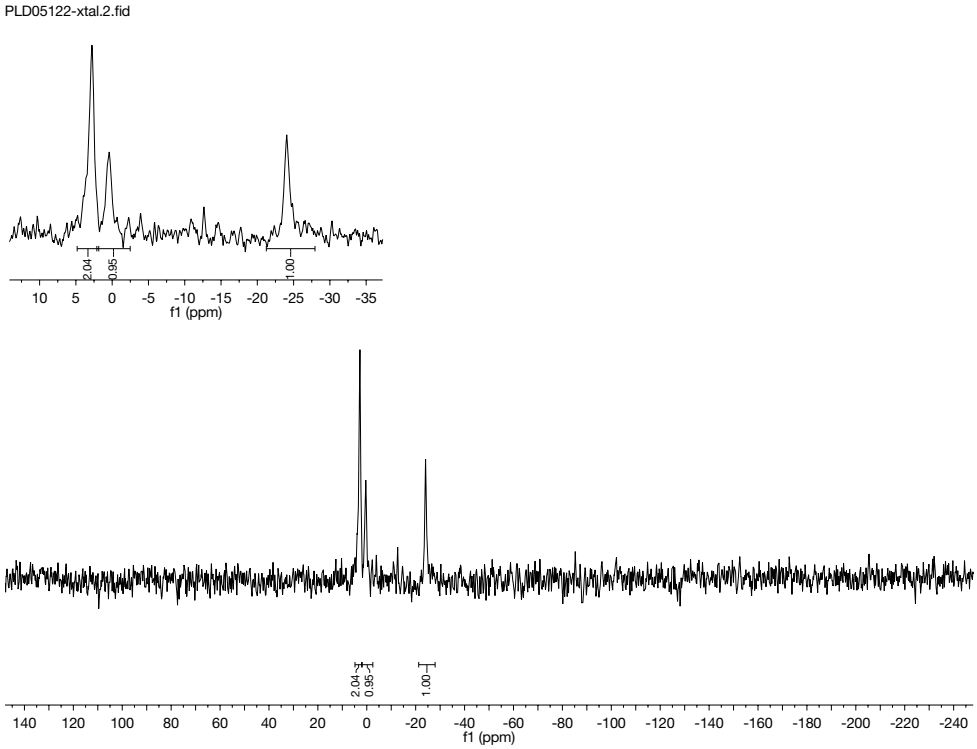

Figure 3.30: ^{31}P NMR of **3.9** in C_6D_6. Taken from PLD05122.

Synthesis of Br(THF)Ti(μ_2-NP)$_3$Pd (3.10). Solid BrTi(NP)$_3$ (55 mg, 0.063 mmol, 1 equiv) and Pd(P(tbu)$_3$)$_2$ (32 mg, 0.063 mmol, 1 equiv) were added to a 20 mL scintillation vial, dissolved in 5 mL of benzene and stirred overnight. Volatiles were removed *in vacuo*. Single crystals of 3.10 were grown by slow evaporation of pentane into a concentrated THF solution of **3.10**. ^{1}H NMR (300MHz, C_6D_6) δ, ppm: 1.3-1.4 (br, 4H, THF), 3.5-3.7 (br, 4H, THF), 6.14-6.17 (br, 3H, aryl), 6.32-6.37 (br, 3H, aryl), 6.83-6.95 (br, 19H, aryl), 7.29-7.38 (br, 12H, aryl), 8.453 (br, 3H, aryl). ^{31}P NMR (121 MHz, C_6D_6) δ, ppm: 2.58 (br, 3P).

PLD07139.1.fid

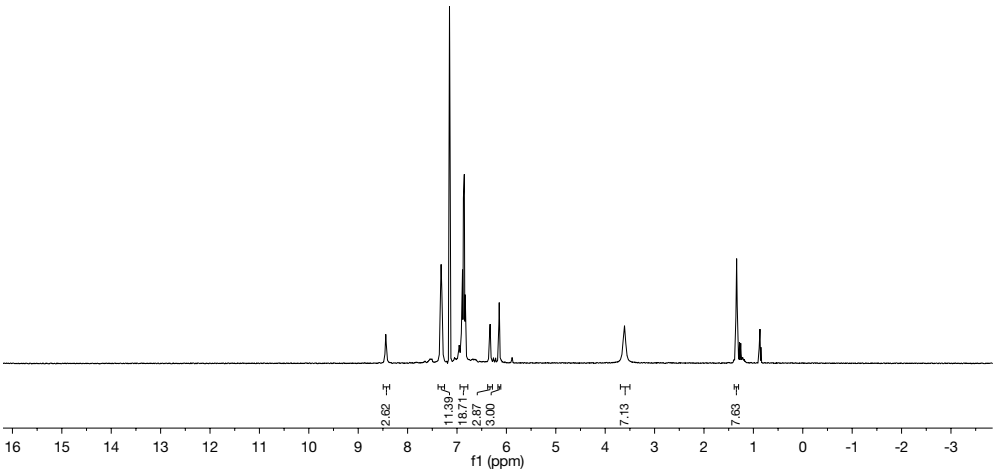

Figure 3.31: ^{1}H NMR of **3.10** in C_6D_6. Taken from PLD07139.

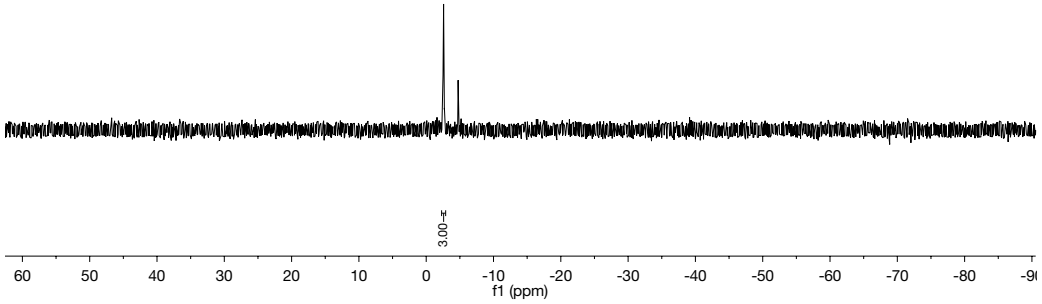

Figure 3.32: ^{31}P NMR of **3.10** in C_6D_6. Taken from PLD07139. Unidentified impurty at ~ -5 ppm.

Computational Details

DFT: All density functional theory (DFT) calculations were performed with the Gaussian 09 program package[136]. The structures were optimized with the M06-L functional and 6-311G+(d) basis sets for Ti, Ni, N, and P, 6-31G(d) for C, 6-31G for H and Def2-TZVP with effective core potentials for Zr and Hf[137-141]. Frequency calculations were performed to confirm structures were local minima. Natural bond order analysis was performed on the optimized structures to estimate the Mayer bond order[142].

CASSCF/CASPT2 Calculations: All the complete active space self-consistent-field (CASSCF) and complete-active-space second-order perturbation theory (CASPT2)

calculations were performed with the MOLCAS 7.8 package [143-145]. These calculations were performed on the M06L optimized structures. The relativistic all-electron ANO-RCC basis sets were used on all atoms in the complexes [146]. Specifically, ANO-RCC-VTZP basis sets were used for Hf, Zr, Ti, and Ni atoms, ANO-RCC-VDZP basis sets for N and P atoms, and ANO-RCC minimal basis sets were used for C and H atoms. Scalar-relativistic effects were included with the Douglas-Kroll-Hess Hamiltonian up to the second-order [147]. In addition, reduction of the four center 2-electron integrals to effective three center integrals via auxiliary basis sets were accomplished with the RICD approximation. For the CASPT2 calculations, an imaginary level shift of 0.2 a.u. was used to prevent the occurrence of intruder states. For the anion, the active space choice was 11 3d electrons in 12 orbitals, corresponding to the five doubly occupied Ni 3d orbitals and one singly occupied Ti 3d orbital and a set of corresponding set of correlating orbitals for a total of 12 orbitals. For the neutral species, the active space was 10 electrons in 12 orbitals, corresponding to the five doubly occupied Ni 3d orbitals, a set of 4d correlating orbitals for each doubly occupied orbital, plus two other M=Ti, Zr, or Hf 3d orbitals for sigma and pi bonding.

XAS:

Sample preparation, measurements and data analysis:

Solid samples for X-ray spectroscopic analysis were prepared in an inert-atmosphere glove box. For Ni K-edge measurements, the solid samples were finely ground using an agate mortar and pestle with BN into a homogeneous mixture comprising 10% w/w photoabsorbing metal. These mixtures were pressed into 1 mm Al spacers and sealed with 38 μm Kapton tape. Ni K-edge XAS spectra were obtained at the Stanford Synchrotron Radiation Lightsource (SSRL) at beamline 7-3 under ring conditions of 3 GeV and 500 mA. A Si(220) double-crystal monochromator was used for energy selection. Spectra were collected in transmission mode with X-rays detected by ionization chambers immediately downstream and upstream of the sample. A Ni foil and a third ionization chamber upstream of the sample were used for internal energy calibration, assigning the first inflection point of the Ni foil scan to 8331.6 eV. Samples

were maintained at 10 K in an Oxford liquid He flow cryostat. Data were collected from 8010 to 8730 eV for all the complexes. Multiple scans were measured and averaged with SIXPACK software package. No spectral changes due to photo-damage were observed after multiple scans for these complexes. A smooth pre-edge background was removed from each averaged spectrum by fitting a Gaussian normalization to the pre-edge region followed by subtraction from the entire spectrum. Data were normalized to post-edge jumps of 1.0 above E_0= 8350 eV in SIXPACK by applying a quadratic normalization to produce the final spectra. The final processed spectra were plotted using Igor Pro 6.37.

Computational details

Density functional theory (DFT) calculations were performed to directly correlate X-ray spectroscopy to electronic structure. All electronic structure and spectroscopic calculations were performed using version 3.03 of the ORCA computational chemistry package. Geometry optimizations were carried out starting from crystal structure coordinates and were performed using the BP86 functional, the zeroth-order regular approximation for relativistic effects (ZORA) as implemented by van Wüllen and scalar relativistically recontracted Ahlrich's def2-TZVP(-f)(def2-TZVP(-f)-ZORA) basis set. Solvation was 85odeled using the conductor like screening model (COSMO) using a dielectric of 9.08 (CH_2Cl_2). Constrained optimization were applied during geometry optimization where the bulky phenyl rings were replaced with H-atoms and only the positions of the H-atoms were optimized keeping the molecule skeleton fixed. Ni K-edge XAS spectra were calculated using time dependent density functional theory (TDDFT) calculations with geometry optimized coordinates utilizing B3LYP functional, the CP(PPP) basis set on Ni using an integration grid accuracy of 7, and the def2-TZVP(-f)-ZORA basis set on all other atoms. Error in core potential energetics were evaluated by plotting the calculated XAS peak energies against experimental peak energies. These fits were used to shift the calculated spectra for comparison to experiment. All molecular orbital images were generated using UCSF Chimera package. The molecular orbitals were plotted at an isolevel of 0.03 au.

Table 3.4. Crystal and refinement data for complexes **3.1**-**3.4**.

	3.1	**3.2**	**3.3**	**3.4**
CCDC Number	1450732	1450733	14507734	14507735
Empirical Formula	$C_{64}H_{52}N_4P_4Hf$	$C_{64}H_{52}N_4P_4TiNi$	$C_{64}H_{52}N_4P_4ZrNi$ • C_6H_6	$C_{64}H_{52}N_4P_4HfNi$ • C_6H_6
Formula weight	1179.47	1107.59	1229.01	1316.34
T (K)	123(2) K	123(2) K	150(2) K	123(2) K
a, Å	9.7556(11)	12.772(2)	11.2579(5)	11.2134(3)
b, Å	16.9397(19)	14.5023(16)	23.6880(9)	23.6739(5)
c, Å	21.120(3)	14.5023(16)	23.6877(9)	22.8293(5)
α, deg	106.175(2)	93.11	90	90
β, deg	103.058(1)	92.3180(10)	102.7780(10)	103.8260(10)
γ, deg	93.195(1)	92.3180(10)	90	90
Volume, Å^3	3290.1(6)	2677.9(6)	5900.5(4)	5884.8(2)
Z	2	2	4	4
Crystal System	Triclinic	Triclinic	Monoclinic	Monoclinic
Space Group	P-1	P-1	P2(1)/c	P2(1)/c
d_{calc}, g/cm^3	1.209	1.374	1.384	1.486
θ Range, deg	2.32 to 28.85	3.05 to 72.64	2.728 to 72.155	2.73 to 72.24
μ, mm^{-1}	1.747	3.186	3.227	4.946
Abs. Correction	Multi-scan	Multi-scan	Multi-scan	Multi-scan
GOF	1.033	1.108	1.020	1.039
R_1 ,[a]	$R1$ = 0.0384	R1 = 0.0383	R1 = 0.0275	$R1$ = 0.0377
wR_2 [b] [I>2σ (I)]	$wR2$ = 0.0947	wR2 = 0.0970	wR2 = 0.0703	$wR2$ = 0.0891

[a] $R_1 = \sum||F_o| - |F_c||/\sum|F_o|$. [b] $wR_2 = [\sum[w(F_o^2-F_c^2)^2]/\sum[w(F_o^2)^2]]^{1/2}$.

Table 3.5. Crystal and refinement data for complexes **3.5-3.7**.

	3.5	**3.6**	**3.7**
CCDC Number	1450736	1450737	1841644
Empirical Formula	$NaC_{64}H_{52}N_4P_4TiNi \bullet (OC_4H_8)$	$C_{65}H_{52}N_4O_1P_4TiNi$	$C_{73}H_{61}N_5P_4TiNi$
Formula weight	1202.68	1229.01	1238.71
T (K)	123(2)	123(2)	100(2)
a, Å	14.5006(3)	11.6014(16)	24.6916(7)
b, Å	14.7943(3)	12.1966(16)	12.2857(4)
c, Å	16.1167(3)	21.545(3)	22.9164(11)
α, deg	98.340(1)	75.265(6)	90
β, deg	107.470(1)	76.711(6)	121.179(1)
γ, deg	94.600(1)	67.796(6)	90
Volume, $Å^3$	3234.93(11)	2699.0(6)	5947.6(4)
Z	2	2	4
Crystal System	Triclinic	Triclinic	Monoclinic
Space Group	P-1	P-1	Cc
d_{calc}, g/cm^3	1.235	1.397	1.383
θ Range, deg	2.92 to 72.190	3.99 to 72.470	2.409 to 28.737
μ, mm^{-1}	2.749	3.190	0.608
Abs. Correction	Multi-scan	Multi-scan	Multi-scan
GOF	1.034	1.053	1.083
R_1 ,[a]	*R*1 = 0.0447	R1 = 0.0627	R1 = 0.0339
wR_2 [b] [I>2σ (I)]	*w*R2 = 0.1102	*w*R2 = 0.1220	*w*R2 = 0.0913

[a] $R_1 = \sum||F_o| - |F_c||/\sum|F_o|$. [b] $wR_2 = [\sum[w(F_o^2-F_c^2)^2]/\sum[w(F_o^2)^2]]^{1/2}$.

Table 3.6. Crystal and refinement data for complexes **3.8-3.11**.

	3.8	**3.9**	**3.10**	**3.11**
CCDC Number	1841641	1841642	1841643	1450738
Empirical Formula	$C_{73}H_{61}N_5P_4ZrNi$	$C_{64}H_{52}N_4P_4TiPd$	$C_{52}H_{47}N_3P_3OTiPd$	$C_{84}H_{78}N_6O_1P_6Ti$ Ni • $2(C_6H_6)$
Formula weight	1282.06	1155.25	1057.01	2043.02
T (K)	100(2)	123(2)	100(2)	123(2)
a, Å	24.8362(6)	11.7290(3)	11.9549(5)	20.6085(9)
b, Å	12.2804(3)	12.1410(3)	19.1065(10)	22.0874(9)
c, Å	22.9910(5)	21.3980(5)	20.1421(11)	22.0874(9)
α, deg	90	75.272(1)	90	90
β, deg	121.554(1)	76.943(1)	90	90
γ, deg	90	67.567(1)	90	90
Volume, $Å^3$	5975.5(3)	2695.52(12)	4600.8(4)	10053.9(7)
Z	4	2	4	4
Crystal System	Monoclinic	Triclinic	Orthorhombic	Orthorhombic
Space Group	Cc	P-1	P2(1)2(1)2(1)	Pbca
d_{calc}, g/cm^3	1.425	1.423	1.526	1.350
θ Range, deg	2.4075 to 30.182	4.018 to 72.109	2.723 to 26.233	2.92 to 73.86
μ, mm^{-1}	0.646	5.424	1.580	3.055
Abs. Correction	Multi-scan	Multi-scan	Multi-scan	Multi-scan
GOF	1.012	1.027	0.998	1.037
R_1 ,[a]	$R1 = 0.0384$	$R1 = 0.0308$	$R1 = 0.0383$	R1 = 0.0523
wR_2 [b] [I>2σ (I)]	$wR2 = 0.0800$	$wR2 = 0.0753$	$wR2 = 0.0836$	wR2 = 0.1462

[a] $R_1 = \sum||F_o| - |F_c||/\sum|F_o|$. [b] $wR_2 = [\sum[w(F_o^2-F_c^2)^2]/\sum[w(F_o^2)^2]]^{1/2}$.

Chapter 4

Synthesis and Characterization of Triply-Bonded Titanium-Iron Complexes Supported by 2-(diphenylphosphino)pyrrolide Ligands

Reproduced with permission from:

Dunn, P. L.; Carlson, R. K.; Tonks, Synthesis and Characterization of Triply-Bonded Titanium-Iron Complexes Supported by 2-(diphenylphosphino)pyrrolide Ligands. *Inorg. Chim. Acta* **2017**, 460, 43.

4.1 OVERVIEW

The synthesis of several titanium-iron multiply bonded complexes supported by a 2-(diphenylphosphino)pyrrolide (NP) ligand is reported. Treatment of the homoleptic, 8-coordinate $Ti(NP)_4$ monometallic precursors with $FeCl_2$ and KC_8 yielded the tetragonally-symmetric heterobimetallic complex $Ti(\mu_2\text{-}NP)_4Fe$, **4.1**. X-ray crystallographic analysis reveals a short metal-metal distance (2.021(2) and 2.028(2) Å for two independent molecules in the asymmetric unit) consistent with a Fe-Ti triple bond. Theoretical calculations also indicate 3 bonding interactions. Further reduction of **4.1** by 2 electrons with KC_8 results in the isolation of the dianion, $[K_2][(\kappa^1\text{-}NP)Ti(\mu_2\text{-}NP)_3Fe]$, **4.2**, where one phosphine arm has decoordinated from Fe, and the Fe-Ti triple bond has shortened to 1.9474(7) Å. This shortening results from the local ligand field change about Fe from tetragonal to trigonal, which allows for significantly better orbital overlap with Ti.

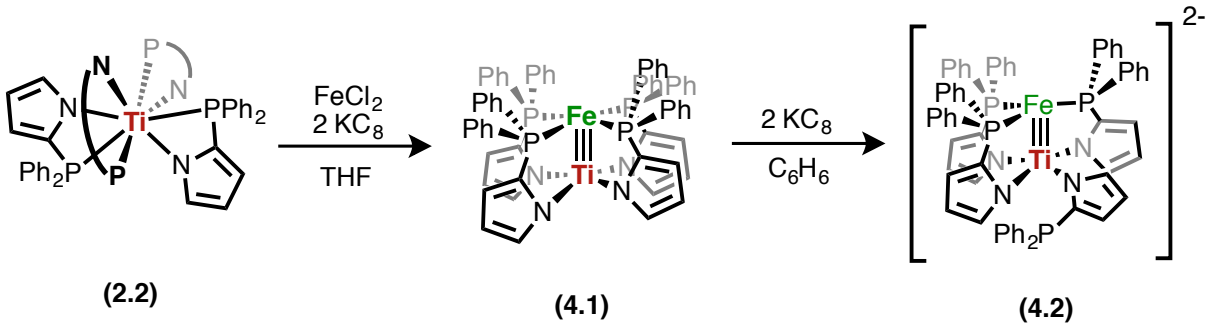

Figure 4.1. Synthesis of titanium-iron bimetallic complexes.

4.2 INTRODUCTION

Metal-metal bonds between two first row transition metals have received significant recent attention owing to their potential utility as catalysts for multielectron transformations relevant to small molecule activation. Additionally, bonds between metals play important roles in both natural enzymatic systems[154-155] and heterogeneous processes[156-159], making the study of metal-metal bonding an important tool for understanding and improving these systems. Recent seminal work by Lu and Thomas has involved using bifunctional, hard-soft ligands to construct several heterobimetallic frameworks that can support diverse classes of trigonally-symmetric

heterobimetallic transition metal cores [50-59, 98-118]. A number of factors dictate the extent of metal-metal bonding in these complexes: for example, as the metal center periods become more disparate, orbital overlap decreases resulting in a loss of delta then pi bonding; while addition of more than 10 total electrons into the metal-metal manifold typically results in a population of metal-metal antibonding orbitals, decreasing the effective bond order [108, 133]. In a trigonally symmetric system, the d_{yz} and d_{xz} orbital pair and d_{x2-y2} and d_{xy} pair are each degenerate, allowing for formation of up to 5 bonds (two pi and two delta orbitals, in addition to d_{z2} sigma bonding), making it an ideal symmetry to observe periodic trends in bonding. We recently reported the synthesis of a series of pseudo-trigonal MNi (M= Ti, Zr, Hf) complexes supported by phosphinopyrrolides, where, due to symmetry constraints, only two bonding interactions can occur instead of three (from idealized trigonal geometry), illustrating how the extent of metal-metal bonding can be further manipulated by deviation from idealized metal geometries [163]. Additionally, Nagashima and Michaelis have carried out catalytic nucleophilic allylic amination reactions with low-symmetry 'boat' shaped heterobimetallic MTi (M=Ni, Pd, Pt) complexes [87-90]. Despite the prevalence of trigonally symmetric species, there are few examples of bimetallics displaying tetragonal symmetry that contain two different first row transition metals, akin to the tetragonal lantern complexes such as Cotton's $[Re_2Cl_8]^{2-}$ complex [165-166]. A tetragonal environment, in contrast to a trigonal symmetry, significantly destabilizes d_{x2-y2} due to metal-ligand antibonding interactions, and allows only for a maximum of 4 bonding interactions.

To further investigate cooperative Lewis acidic effects, impact of symmetry on heterobimetallic metal-metal bonding and to investigate the potential role of covalent M-M bonding on fundamental organometallic reactivity, we are interested in synthesizing tetragonally-symmetric early-late transition metal complexes supported by phosphinopyrrolide group 4 metalloligands. Herein we report the synthesis and characterization of $Ti(\mu_2\text{-NP})_4Fe$ (NP = 2-diphenylphosphinopyrrolide) and the doubly reduced dianion $K_2Ti(\mu_2\text{-NP})_4Fe$ and lend insight into metal-metal bonding in early-late bimetallic complexes.

4.3 Results and Discussion

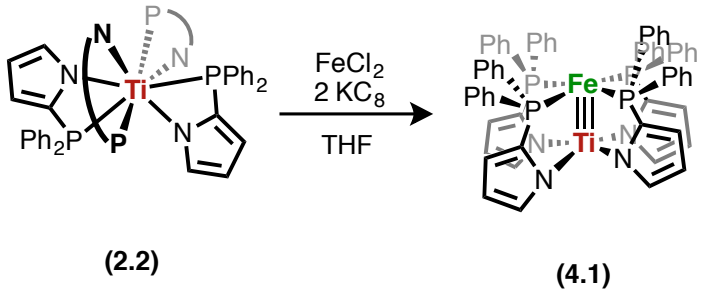

(2.2) **(4.1)**

Scheme 4.1. Synthesis of bimetallic TiFe complexes **4.1**.

The homoleptic titanium complex, $Ti(NP)_4$ (**2.2**) (NP = 2-diphenylphosphinopyrrolide), has been previously synthesized and characterized[131]. Treatment of **2.2** with 1 equivalent of $FeCl_2$ and two equivalents of KC_8 leads to the formation of the diamagnetic **4.1** (Scheme 4.1). The solid-state structure of **4.1** is presented in Figure 4.2 and selected bond lengths and angles can be found in Table 4.1. Complex **4.1** crystallizes in the P_{4CC} space group with two molecules in the asymmetric unit and where the ligands are symmetrically equivalent. All phosphinopyrrolide ligands are used to bridge the metal center giving it a *pseudo*-C_4 symmetry down the metal-metal axis. The Fe center is rigorously square pyramidal with Ti occupying the apical position of the square pyramid (< PFeP (°) = 89.991(1) and 89.998(1) and < PFeTi (°) = 90.71(5) and 90.15(5)), and the Fe center is ~0.03 Å out of the phosphine plane. The Ti center is *pseudo* square pyramidal, with the Ti sitting ~ 0.42 Å above the N_4 plane. Ti-N distances in the two molecules of the asymmetric unit are 2.093(4) and 2.075(5) Å, and the Fe-P bond lengths are 2.3655(12) and 2.3705(13) Å. At room temperature in a chloroform solution, **4.1** contains a single resonance by ^{31}P NMR consistent with the C_4-symmetric solid-state structure.

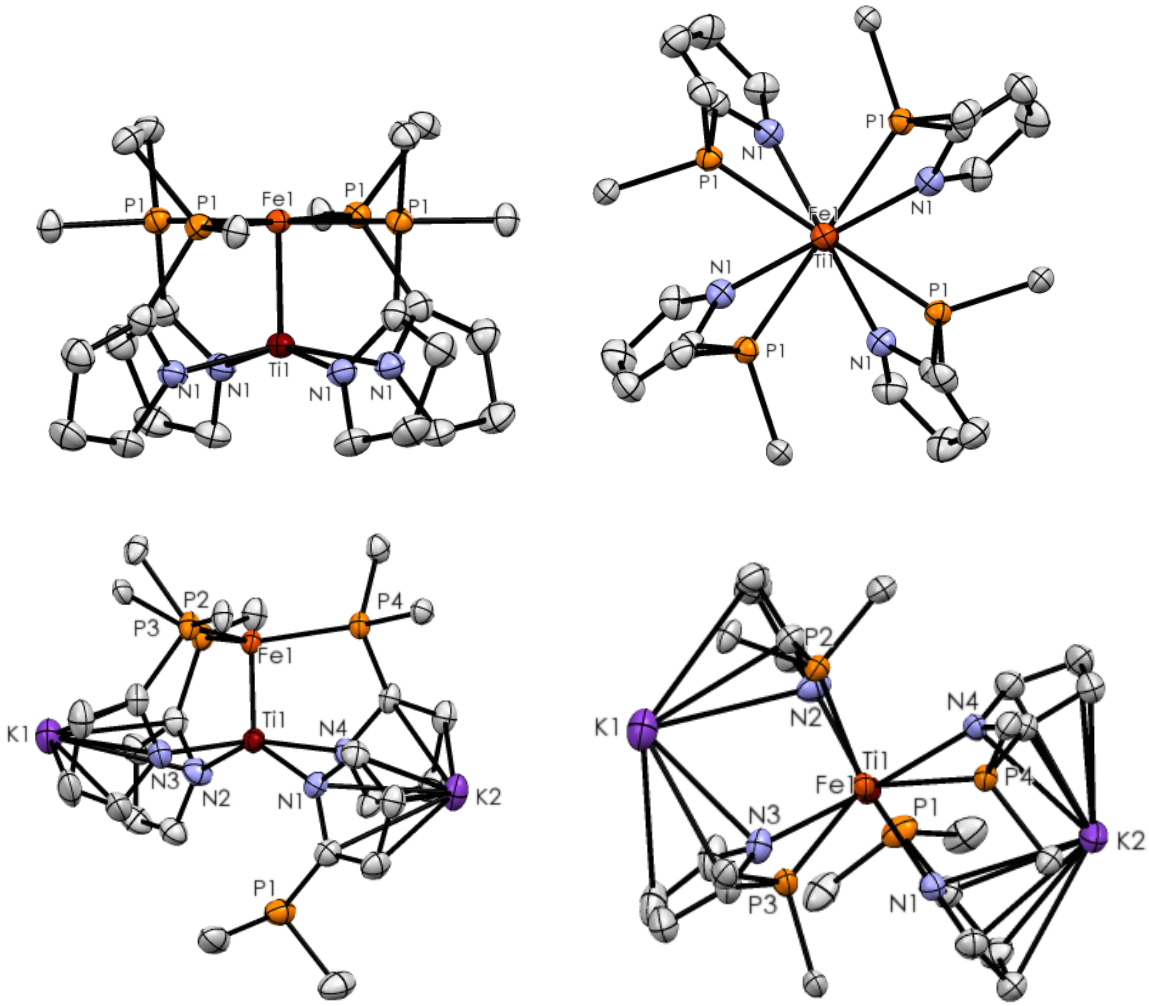

Figure 4.2. Thermal ellipsoid drawing of **4.1** (top) and **4.2** (bottom). Solvent and Hydrogen atoms have been removed and the phosphine phenyl rings reduced to the *ipso* carbons for clarity. Selected bond distances and angles are provided in Table 4.1.

Table 4.1. Relevant bond lengths (Å) and angles (°) for **4.1** and **4.2**.

	4.1[b]	**4.2**
Ti-Fe (Å)	2.021(2)	1.9474(7)
	2.028(2)	
FSR[a]	0.81	0.78
P-Fe (Å)	2.3655(12)	2.2286(9)
	2.3705(13)	2.1936(9)
		2.203(1)
P-Fe-P (°)	89.991(1)	106.87(3)
	89.998(1)	119.05(4)
		129.91(4)
Ti-N (Å)	2.093(4)	2.206(3)
	2.075(5)	2.146(3)
		2.187(3)
		2.195(3)
Torsional Angle (P-	26.21(13)	7.05(9)
Fe-Ti-N) (°)	27.45(14)	27.57(7)
		25.16(8)

[a]FSR = $M_D/\sum(M_c)$: M_D = Metal-metal distance, M_c= Covalent Radii [151].

[b]Values given for both molecules in the asymmetric unit.

The independent molecules in the asymmetric unit of complex **4.1** feature remarkably short Fe-Ti distances of 2.028(2) and 2.021(2) Å (FSR = 0.81) indicative of a Ti-Fe triple bond. From DFT calculations using M06-L, the molecular orbitals (MOs) of **4.1** indicate three metal-metal bonding molecular orbitals: a σ bond between the Ti and Fe d_{z2} orbitals and two degenerate π bonds formed from the d_{xz} and d_{yz} orbitals (Figure 4.3) [151]. NBO calculations predict a Mayer bond order of 1.48, slightly less than a double bond, resulting from significant polarization of the π symmetry orbitals to Fe.

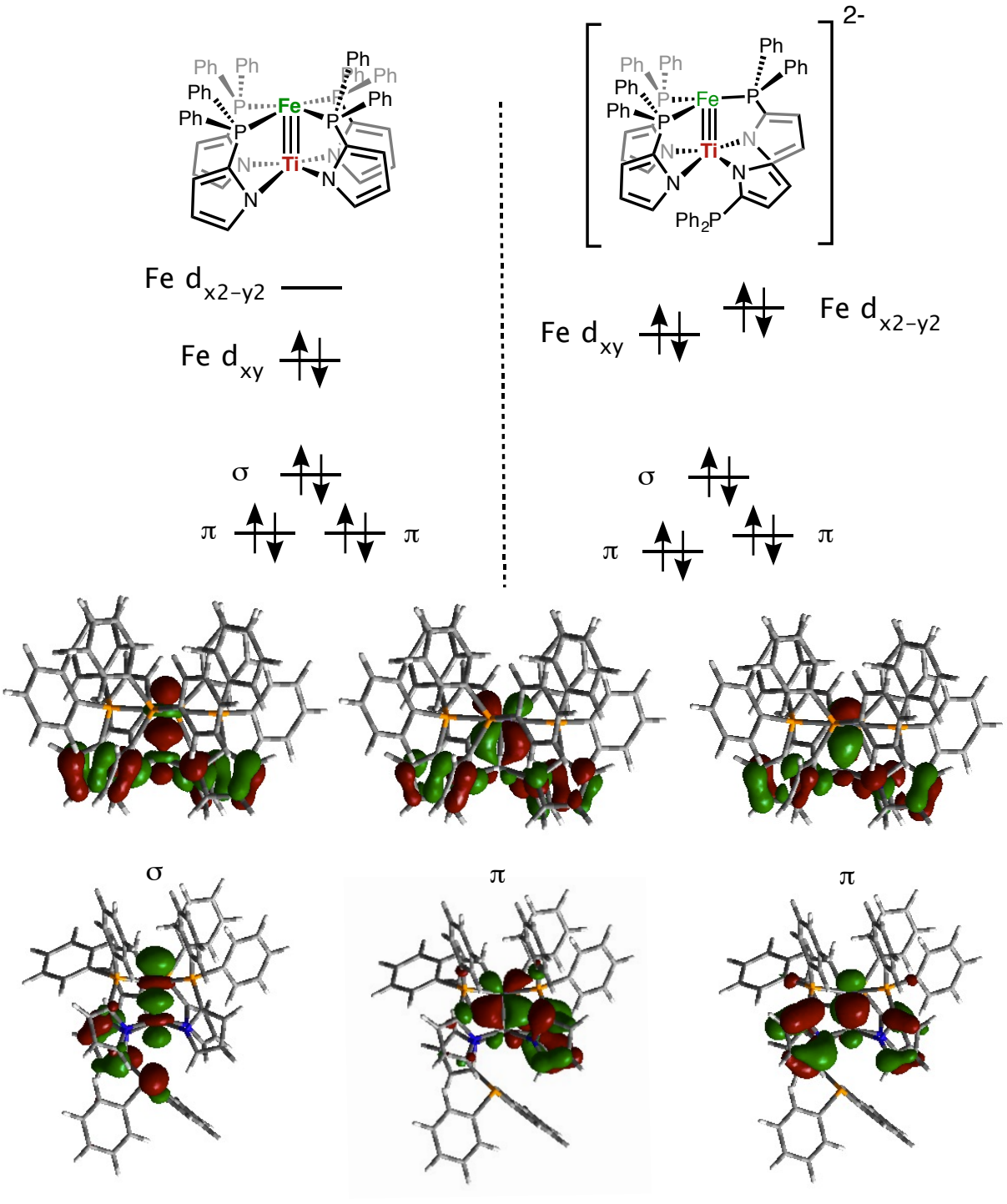

Representative MOs from **4.1** (top) and **4.2** (bottom)

Figure 4.3. Qualitative molecular orbital diagram and bonding molecular orbitals computed from M06-L calculations for complexes **4.1** and **4.2**.

Further reduction of **4.1** with 2 equivalents of KC_8 allowed for the isolation of doubly reduced complex **4.2**, K_2TiFe (Figure 4.1). Complex **4.2** is diamagnetic and contains three resonances that integrate 2:1:1 by ^{31}P NMR: a multiplet, triplet (J_{pp} = 60 Hz) and singlet. The solid-state structure of **4.2** is presented in Figure 4.3 and selected bond lengths and angles can be found in Table 4.1. Interestingly, only 3 phosphinopyrrolides bridge the two metal centers, rendering the geometry around iron *pseudo*-trigonal pyramidal. The fourth pyrrolide ligand remains bound to Ti through the nitrogen atom, while the phosphine is unbound and approximately 3.5 Å away from Ti. The multiplet corresponds to the two pseudo-trans phosphines, the triplet corresponds to the phosphine trans from the vacant coordination site and the singlet is the unbound phosphine arm, consistent with the pattern expected from the solid-state structure. Phosphine decoordination is due to the increased d-electron count at Fe: if one assumes that **4.1** is an 16-electron d^8 Fe center, addition of electrons into the d manifold would populate the d_{x2-y2} orbital and cause ligand dissociation from the Fe square plane. The K^+ countercations each remain tightly bound between two pyrrole aryl π systems further confirming a dianionic complex.

The Fe-P bond lengths in **4.2** have contracted by greater than 0.15 Å to ~2.208 Å, while the Ti-N distances have lengthened by ~0.1 Å to ~2.18 Å. The shortening of the Fe-P bond distances is likely due to increased Fe-P backbonding by the reduced Fe species, since the complex is now formally dianionic and only 3 phosphines now compete for backdonation [170]. The large increase in the Ti-N bond distances indicates that at least one of the two reductive events is Ti-based [108]. The Ti-Fe distance has shortened by 0.08 Å to 1.9469(8) Å (FSR = 0.78), while the Fe has been pulled below the P_3 plane by ~ 0.26 Å. This distortion from planarity is most likely caused by the increased Ti-Fe bond strength, as well as the relaxed geometric constraints imposed by 3 bridging ligands instead of 4.

Similarly to **4.1**, the MOs from DFT calculations on **4.2** also show three Ti-Fe bonding molecular orbitals. In contrast to **4.1**, the trigonal geometry at Fe breaks the degeneracy of the two π bonding orbitals, although they remain close in energy. Similarly, the nonbonding Fe d_{x2-y2} orbital has been significantly lowered in energy on

account of the ligand field change from tetragonal to trigonal. NBO calculations indicate a Mayer bond order of 1.83, significantly higher than **4.2** and is in agreement with the shorter FSR observed in the solid-state structure. It is interesting that nominal population of a nonbonding orbital (Fe d_{x2-y2}) results in an increase in the Ti-Fe bond strength in **4.2**. This can be rationalized from a simple increase in the Lewis basicity of the reduced Fe center, which should result in decreased polarization of the π bonding Ti-Fe orbitals. The Mulliken charges for **4.2** increase by about 0.5 electrons for Fe and decrease by about 1 electron for Ti compared to **4.1**. This qualitative behavior correlates with the shorter Fe-Ti distance and suggests better Fe to Ti electron donation.

The d^{10} complex **4.2** presents an interesting contrast to the previously-reported d^{10} complex, $(\kappa^2\text{-NP})Ti(\mu_2\text{-NP})_3Ni$ **(3.2)**. This Ti/Ni complex contains a Ti-Ni double bond that is strongly polarized toward Ni, while the filled Ni d_{yz} orbital remains disengaged from π bonding. Thus, the bonding is significantly *stronger* in the TiFe analogue compared to TiNi. This periodic trend is expected based on previous results observed by Thomas and Lu [133, 162] which showed that M-M bonding and orbital overlap among first row transition metals increases as the difference in group number between the two metals decreases. Another difference between **4.2** and the TiNi complex is that the 4th phosphine arm remains decoordinated in **4.2**, while it binds to Ti in TiNi. This observation is also consistent with Fe being a more effective donor than Ni: the more electron-rich Ti center in TiFe **4.2** is less prone to phosphine coordination than TiNi. For further comparison, Lu recently reported a d^9 $N_4Ti^{IV}P_3Fe^{I-}$ complex supported by a heptadentate *tris*(amide)amine scaffold [162]. In Lu's complex, the Ti-Fe bond is 2.0636(7) Å, longer than that found in d^8 **4.1** and d^{10} **4.2**, indicating that the electron-poor Ti pyrrolide with no *trans* ligand may form stronger bonds than the π-donating amide framework that has an apical amine donor.

4.4 Conclusions

An early-late, titanium-iron, tetragonally symmetric bimetallic complex supported by a phosphinopyrrolide ligand has been synthesized and characterized. X-ray crystallographic and computational analysis shows a metal-metal triple bond consisting of a sigma and two pi interactions. Further reduction by two electrons results in the isolation of the dianion, K_2TiFe, where one ligand arm has decoordinated from iron and

the metal-metal bond has shortened to 1.9474(7) Å. In this instance, additional electrons into the metal-metal bonding manifold cause ligand dissociation rather than weakening of the metal-metal bond. In fact, the change from tetragonal to pseudo-trigonal symmetry serves to increase the bond order.

4.5 EXPERIMENTAL CONSIDERATIONS

General Considerations and Instrumentation. All air- and moisture-sensitive compounds were manipulated in a glovebox under a nitrogen atmosphere. Solvents for air- and moisture-sensitive reactions were vacuum transferred from sodium benzophenone ketyl (THF, Et_2O, pentane, and d_6-benzene) or predried by passing through activated alumina columns of a SG Water solvent purification system. $FeCl_2$ was purchased from Aldrich and dried at 100 °C overnight under vacuum before use. KC_8 was prepared according to literature procedure [167]. ^{1}H, ^{13}C and ^{31}P spectra were recorded on Varian INOVA 500 MHz or Bruker Avance III 400 MHz spectrometers. Chemical shifts are reported with respect to residual protio-solvent impurity for ^{1}H (*s*, 7.16 ppm for C_6D_5H), solvent carbons for ^{13}C (*t*, 128.39 ppm for C_6D_6), and PPh_3 for ^{31}P (*s*, -6 ppm for C_6D_6).

X-ray Crystal Data: General Procedure. Crystals were removed quickly from a scintillation vial to a microscope slide coated with oil. Samples were selected and mounted on the tip of a 0.1 mm diameter glass capillary. Data collection was carried out on a Bruker APEX II CCD diffractometer with a 0.71073 Å Mo Kα source or on a Bruker-AXS D8 Venture diffractometer with a 1.54178 Å Cu Kα source. The structures were solved by direct methods. All non-hydrogen atoms were refined anisotropically. Details regarding refined data and cell parameters are available in Table 4.2.

Computational Details

DFT: All density functional theory (DFT) calculations were performed with the Gaussian 09 program package [136]. The structures were optimized with the M06-L functional and 6-311G+(d) basis sets for Ti, Fe, N, and P, 6-31G(d) for C, 6-31G for H [137-141]. Frequency calculations were performed to confirm structures were local

minima. Natural bond order (NBO) analysis was performed on the optimized structures to estimate the Mayer bond order [142].

Synthesis of Ti(2-PPh_2)$C_4H_3N)_4Fe$, Ti(μ_2-NP)$_4$Fe (4.1). Solid $Ti(NP)_4$ (175 mg, 0.167 mmol, 1 equiv) and $FeCl_2$ (20.8 mg, 0.167 mmol, 1 equiv) were dissolved in 3 mL THF and cooled to -35 °C. KC_8 (45 mg, 0.334 mmol, 2 equiv) was added and the solution allowed to stir for two hours while warming to room temperature. Solvent was removed *in vacuo* and the remaining solid redissolved in benzene, filtered through celite and pumped to dryness leaving 120 mg of crude 2 as a red/orange powder. 30 mg of crystals (16% yield) were obtained by slow diffusion of pentane into a concentrated benzene solution of crude **4.1**. ^{1}H NMR ($CDCl_3$) δ, ppm: 4.86-4.96 (4H, br, pyrrole), 5.92-6.03 (4H, br, aryl), 6.08-6.16 (4H, t, pyrrole), 6.26-6.33 (4H, d, aryl), 6.43-6.49(4H, br, aryl), 6.55-6.61(4H, br, aryl), 6.62-6.69(4H, t, aryl), 6.69-6.76(4H, t, aryl), 6.76-6.85 (8H, m, pyrrole and aryl), 6.85-6.92 (4H, br, aryl), 7.08-7.16 (4H, br, aryl) 7.23-7.27 (4H, br, aryl). ^{13}C NMR ($CDCl_3$) δ, ppm: 111.7, 118.7, 126.5, 126.9, 126.9, 126.9, 128.6, 129.2, 130.0, 131.2, 132.4, 132.8, 135.1. ^{31}P NMR ($CDCl_3$) δ, ppm: 12.1 (4P, s). Anal calcd (%) for $C_{64}H_{52}N_4P_4TiFe$: C 69.33 H 5.09 N 5.05 Found: C 70.17 H 5.27 N 4.83.

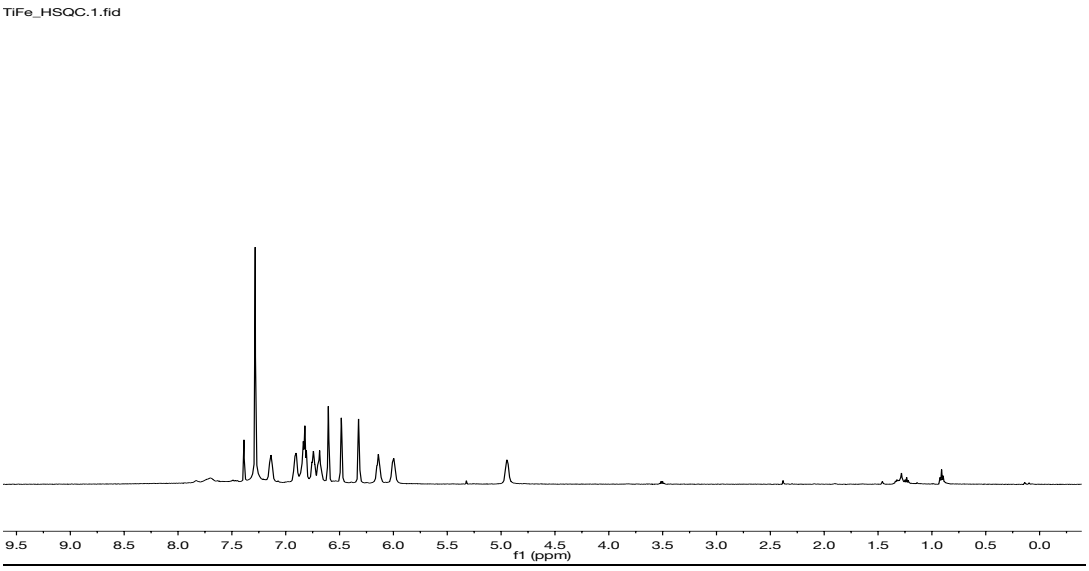

Figure 4.4: ^{1}H NMR of **4.1** in $CDCl_3$. Taken from PLD04153.

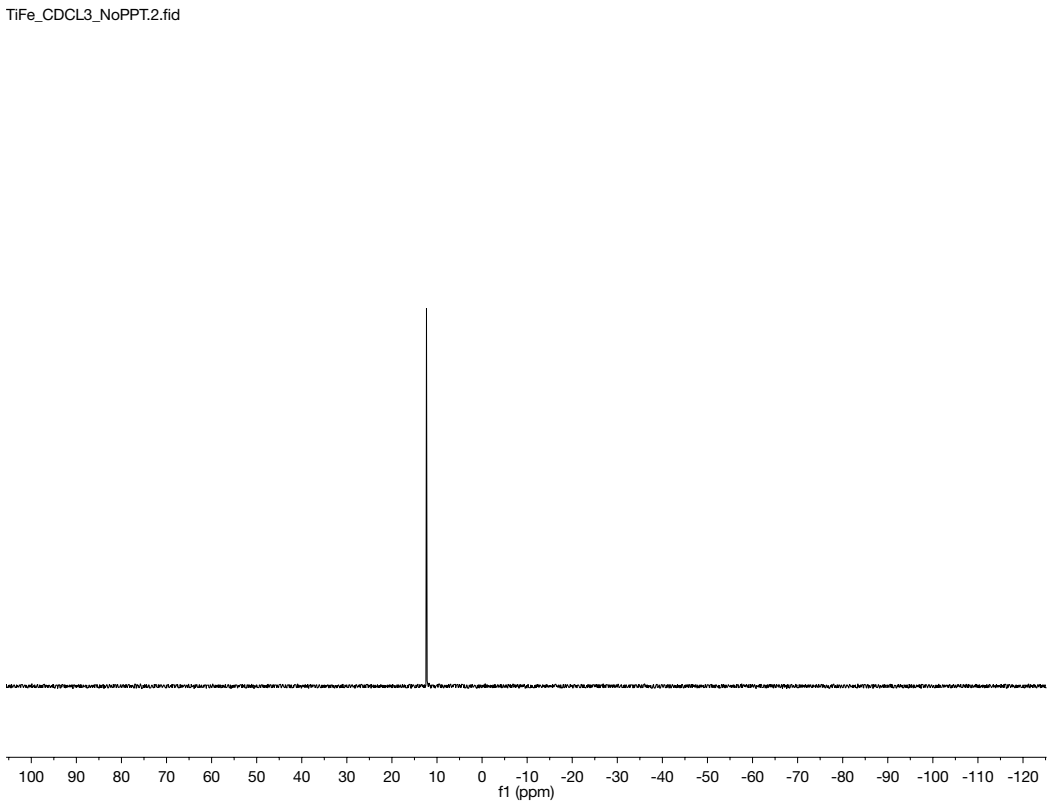

Figure 4.5: ^{31}P NMR of **4.1** in $CDCl_3$. Taken from PLD04153.

Synthesis of $[K_2][Ti((2\text{-}PPh_2)C_4H_3N)_4Fe]$, $[K_2][(\kappa^1\text{-}NP)Ti(\mu_2\text{-}NP)_3Fe]$ (4.2). Solid $Ti(NP)_4Fe$ **4.1** (20 mg, 0.018 mmol, 1 equiv) is dissolved in benzene and solid KC_8 (5 mg, 0.036 mmol, 2 equiv) added. The reaction is allowed to stir for approximately ten minutes and then filtered giving a dark red solution. 5 mg (23%) of X-ray quality crystals were obtained by slow diffusion of pentane into a concentrated benzene solution of **4.2**. ^{1}H NMR (C_6D_6) δ, ppm: 5.83-5.85 (1H, br), 5.98-5.96 (1H, br), 6.24-6.45(3H, br), 6.54-6.56(1H, br), 6.57-7.14 (36H, br), 7.29-7.43(5H, br), 7.84-8.0(3H, br), 8.19-8.29(2H, br). ^{31}P NMR (C_6D_6) δ, ppm: 26.5 (2P, t), 15.5 (1P, t) -31.8 (1P, s). Satisfactory elemental analysis was not obtained for this molecule because it decomposes over time during solvent removal *in vacuo*.

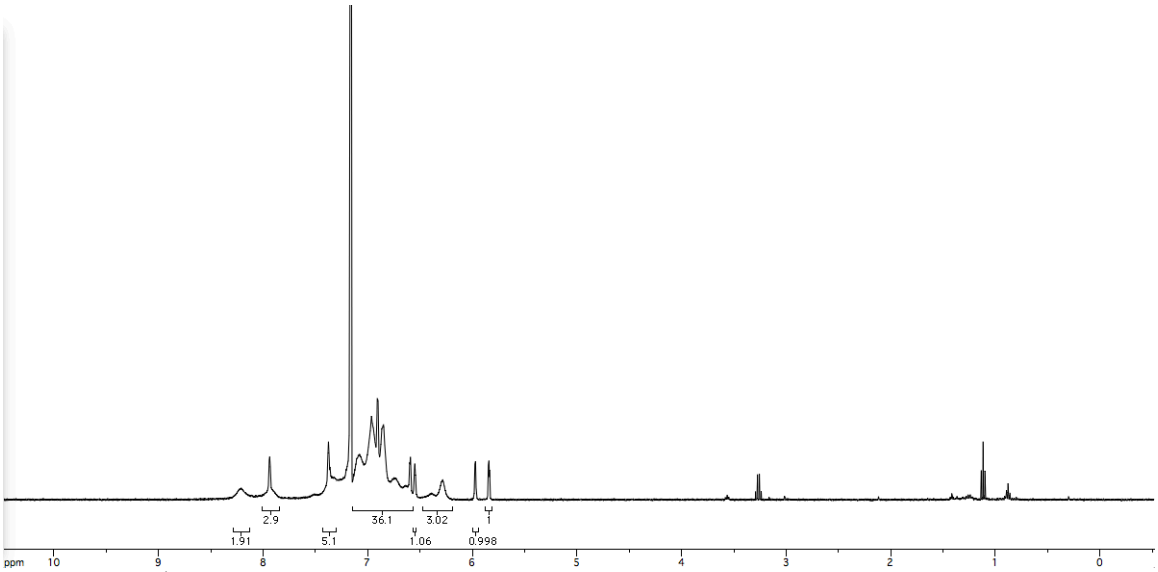

Figure 4.6: ^{1}H NMR of **4.2** in C_6D_6. Taken from PLD05098.

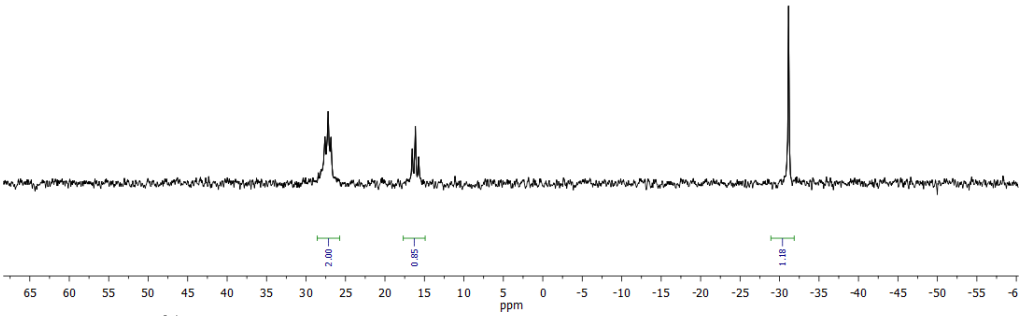

Figure 4.7: ^{31}P NMR of **4.2** in C_6D_6. Taken from PLD05098.

Table 4.2. Crystal and refinement data for complexes **4.1** and **4.2**.

	4.1	**4.2**
CCDC Number	1496978	1496979
Empirical Formula	$C_{64}H_{52}FeN_4P_4Ti$ • $2(C_6H_6)$	$C_{64}H_{52}FeN_4P_4TiK_2$ • $2(C_6H_6)$
Formula weight	1108.75	1185.91
T (K)	123(2)	123(2)
a, Å	18.0499(4)	17.3366(6)
b, Å	18.0499(4)	12.4623(5)
c, Å	21.9628(6)	33.0415(13)
α, deg	90	90
β, deg	90	91.670(2)
γ, deg	90	90
Volume, Å^3	7155.5(3)	7135.7(5)
Z	4	4
Crystal System	Tetragonal	Monoclinic
Space Group	P_{4cc}	$P_{21(n)}$
d_{calc}, g/cm^3	1.316	1.247
θ Range, deg	4.03 to 72.18	2.67 to 72.110
μ, mm^{-1}	1.316	4.809
Abs. Correction	Multi-scan	Multi-scan
GOF	1.048	1.071
R_1 ,[a]	$R1$ = 0.0466	$R1$ = 0.0607
wR_2 [b] [I>2σ (I)]	$wR2$ = 0.0923	$wR2$ = 0.1502

[a] $R_1 = \sum||F_o| - |F_c||/\sum|F_o|$. [b] $wR_2 = [\sum[w(F_o^2-F_c^2)^2]/\sum[w(F_o^2)^2]]^{1/2}$.

Chapter 5

Synthesis, Characterization, and Reactivity of a Trimetallic $TiNi_2$ Complex

5.1 OVERVIEW

The synthesis and reactivity of a trimetallic $TiNi_2$ complex supported by 2-diphenylphosphinopyrrolide (NP) ligands is reported. Treatment of $Ti(NP)_4$ with excess $Ni(COD)_2$ at 90 °C results in incorporation of two Ni atoms into the ligand framework and formation of $Ti(NP)_4Ni_2$ (**5.1**). Single crystal diffraction of complex **5.1** reveals close contacts between all metal centers: one short Ni-Ni bond (2.369(1) Å, FSR = 1.03) bond, one short Ti-Ni (2.289(1) Å, FSR = 0.93) bond and one long Ti-Ni bond (2.634(1) Å, FSR = 1.07). In solution the nickel centers are equivalent *via* ^{31}P NMR spectroscopy. We further explored the dynamics of this complex with a variety of L (L = isocyanide and alkyne) donors and found that depending on the nature of the L type ligand, the Ni-Ni bond can be broken. Finally, reactivity studies have shown complex **5.1** to be capable of cleaving the N=N double bond in benzo[c]cinnoline. The resulting product, **5.7,** has been characterized structurally and spectroscopically, and the mechanistic implications are discussed in the context of metal-metal cooperativity.

5.2 INTRODUCTION

Multi-electron transformations are relevant to numerous biological and industrial processes such as N_2 reduction [171]. In biological systems, redox processes often take place at enzyme-based metal clusters allowing for multiple centers to participate in the redox event. This observation led to the polynuclear hypothesis: the idea that multiple metal centers can work in conjunction to enhance redox reactivity for small molecule activation [74]. Indeed, synthetic analogues have been prepared and have shown remarkable redox reactivity. For example, Johnson has used a pentanuclear nickel cluster to perform carbon atom abstraction from ethylene [172]. Trinuclear ruthenium complexes have also been demonstrated to selectively cleave strong C=C double bonds [173] as well as perform azobenzene cleavage [174]. Similarly, other trinuclear species have been shown to perform multielectron transformations such as N_2 cleavage [175].

In attempt to better stabilize and control the geometry of these highly reactive clusters, a number of polydentate ligands have been designed. Betley has synthesized polydentate amine based ligand scaffolds capable of supporting various multimetallic clusters. Not only do these species exhibit an enhanced redox profile, but a triiron cluster was able to perform the two and four electron reductions of various nitrene donors by

utilizing the cooperative effects of the iron centers [74,176]. Agapie constructed cluster complexes based on substituted arenes that can support multiple metal centers and where these centers can be electronically tuned and work cooperatively to reduce small molecules such as NO [177-179]. Murray has designed a tris(β-diketiminate) cyclophane ligand capable of supporting a trimetallic hydride cluster and reported CO_2 insertion chemistry [180].

With such a rich reactivity profile demonstrated by these multinuclear systems, we were excited to discover our previously characterized metalloligand $Ti(NP)_4$ is capable of supporting two nickel centers, resulting in a trimetallic $TiNi_2$ cluster. While there are a limited number of multimetallic Ni systems in the literature, these complexes have shown a rich reactivity profile. Agapie has published the synthesis of a $LNi^{I}Ni^{I}(u2\text{-}Cl)_2$ (L = 1,4-bis(2-(diisopropylphosphino)phenyl)benzene) complex containing a metal-metal bond (2.3658(2) Å (FSR = 1.03) [181-183]. Using this framework, cooperative oxidative addition processes were studied. Reaction of this starting material with phenyl Grignard results in the formation of biphenyl, likely stemming from the product of double transmetallation, $LNi^{I}Ni^{I}(Ph)_2$. However this product could not be isolated. Reaction with *o*,*o*'- biphenyl Grignard affords the biphenyl complex $LNi^{I}Ni^{I}$(biphenyl), where two transmetallation events have taken place (Figure 5.1). Treatment with CO or *gem*-dichloroalkanes results in the formation of fluorenone or fluorene, respectively, laying the groundwork for a bimetallic cross-coupling catalyst.

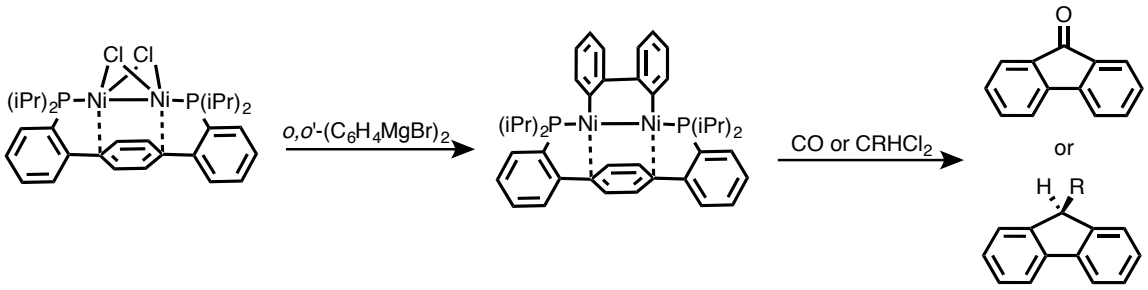

Figure 5.1: Reactivity of a dinickel system support by phosphino arene ligand.

Uyeda has recently synthesized a dinickel moiety supported by a naptheridinediimine framework which features a metal-metal single bond of 2.496(1) Å (FSR = 1.09) and can occupy numerous redox states ranging from $LNi^{0}Ni^{I}$ to $LNi^{I}Ni^{II}$. This complex has shown remarkable reactivity stemming from the two nickel centers

ability to react in a cooperative fashion, resulting in regioselective alkyne trimerization, Paulson-Khand cyclizations, hydrosilylation, carbene transfer type chemistry, and nitrene coupling (Figure 5.2) [184-192].

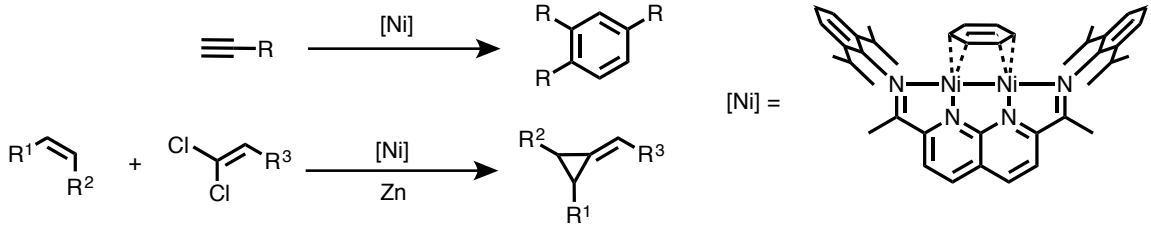

Figure 5.2: Catalytic trimerization and reductive cyclopropanation by Uyeda's Ni_2 complex.

Accordingly, we report the four electron cleavage of the N=N double bond in benzo[c]cinnoline by a trimetallic $TiNi_2$ complex and discuss the mechanistic implications as it relates to metal-metal cooperativity.

5.3 Results and Discussion

Treatment of the metalloligand $Ti(NP)_4$ (**2.2**) with 1 equivalent of $Ni(COD)_2$ yields the heterobimetallic TiNi lantern complex **3.2** [163]. Treatment of **2.2** with excess $Ni(COD)_2$ at 90°C results in a second metallation event, cleanly yielding a new heterotrimetallic $Ti(\mu_2\text{-}NP)_4Ni_2$ complex, **5.1**, in modest (32%) yield (Scheme 5.1). The solid-state structure of **5.1** is presented in Figure 5.3. Complex **5.1** is asymmetric in the solid state, with three phosphines bound to Ni1 and only one to Ni2. This low-coordinate Ni2 is stabilized by an η^2-π interaction with a neighboring phenyl group of the Ni1 bound phosphine. The Ni-Ni distance is short, 2.369(1) Å (FSR = 1.03), while the Ti-Ni distances are asymmetric with one long (2.634(1) Å FSR = 1.07) and one short (2.289(1) Å FSR = 0.93) [149]. There are a limited number of formally Ni(0)-Ni(0) bimetallic complexes in the literature that feature short metal-metal bonds. These complexes are typically supported by bridging ligands that are strong π acceptors such as CO, alkynes, nitriles, or isocyanides. For example, the Ni-Ni bond in $Ni_2(dppm)_2(CNMe)_3$ is 2.572(1) Å, where both dppm ligands bridge the metal centers [193]. The Ni-Ni bond distance in **5.1** is more in line with Ni(1)-Ni(1) complexes such as Agapie's Ni_2Cl_2 supported by a bisphosphino arene that has a Ni-Ni distance of 2.366 Å[183]. We ascribe this complex

to only contain one titanium-nickel bond, similar to the dative bond in the bimetallic TiNi, and a dative Ni-Ni bond, from the electron rich P_3Ni to electron deficient P_1Ni. The overall bonding is best described as a pull-pull interaction, where the Ti center pulls electron density from P_1Ni, which in turn pulls electron density from P_3Ni. For reference, the bimetallic **3.2** contains a Ti-Ni double bond (2.2665(5) Å FSR = 0.91) and the axially-ligated CO species TiNiCO contains no metal-metal bond (2.6136(8) Å FSR = 1.05). Despite the asymmetry in the solid state, **5.1** appears fluxional in C_6D_6 solution, showing only 2 broad ^{31}P NMR signals in a 1:1 ratio, indicating facile phosphine exchange between the two Ni centers. Cooling the sample to -90°C results in broadening of the peaks into the baseline.

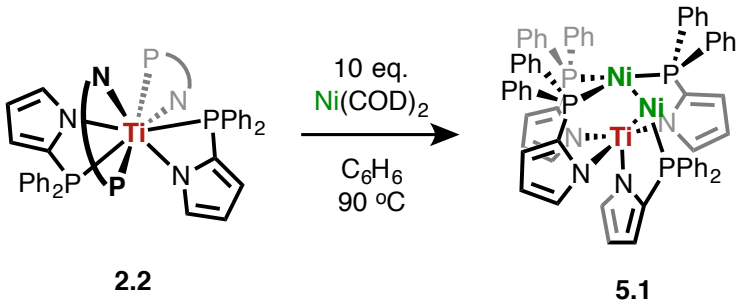

Scheme 5.1. Synthesis of a trimetallic $TiNi_2$ complex, **5.1**.

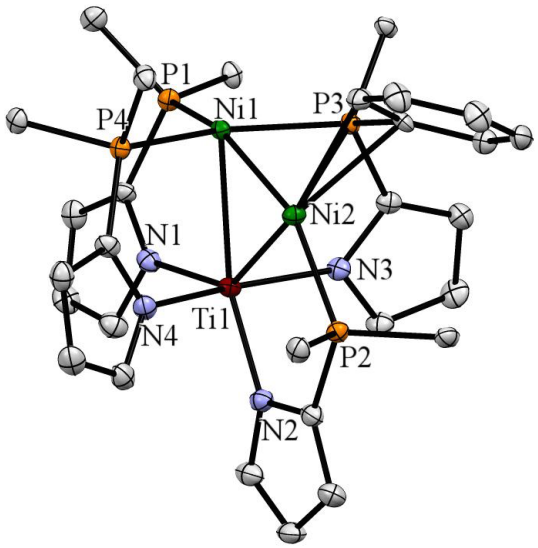

Figure 5.3. 50% thermal ellipsoid drawing of **5.1**. Select phenyl group have been reduced to the ipso carbon and hydrogen atoms omitted for clarity.

To probe the ability of the metals within the trimetallic $TiNi_2$ core to react either cooperatively or independently, **5.1** was reacted with several simple donor ligands. Reaction of **5.1** with PhCCPh at 90°C resulted in the quantitative formation of the bridging alkyne complex, $Ti(NP)_4Ni_2(PhCCPh)$ (**5.2**). Complex **5.2** maintain the same triangular trimetallic core while binding the alkyne perpendicular to the nickel-nickel bond, resulting in two equivalent nickel centers. The C-C bond length of the alkyne increased from 1.194(4) Å to 1.328(4) Å and shows deviation from planarity due to backbonding from the two adjacent Ni(0) centers. The Ni-Ni bond length increased to 2.5273(6) Å in complex **5.2.** While the Ti-Ni distances are more symmetric than the parent structure with values of 2.5319(6) Å and 2.4152(6) Å (FSR = 1.023 and 0.977). Garcia published a series dinuclear nickel complexes supported by dippe (diisopropylphosphinoethane) containing different bridging fluorinated alkynes with much longer Ni-Ni distances (2.8566(9) Å) and significantly more activated alkynes, C-C 1.368(7) Å [194]. This shows the electron withdrawing effects of the proximal Ti center. The Ni-P distances of **5.2** are also slightly elongated from the parent structure, most likely a result of less backbonding due to the presence of a strong π acceptor ligand.

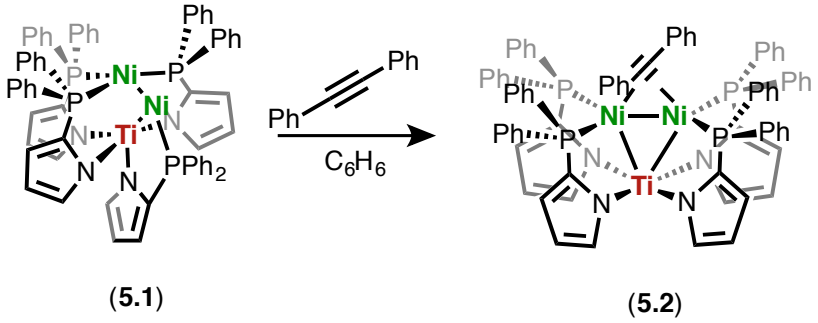

Scheme 5.2. Synthesis of a diphenylacetylene adduct of $TiNi_2$.

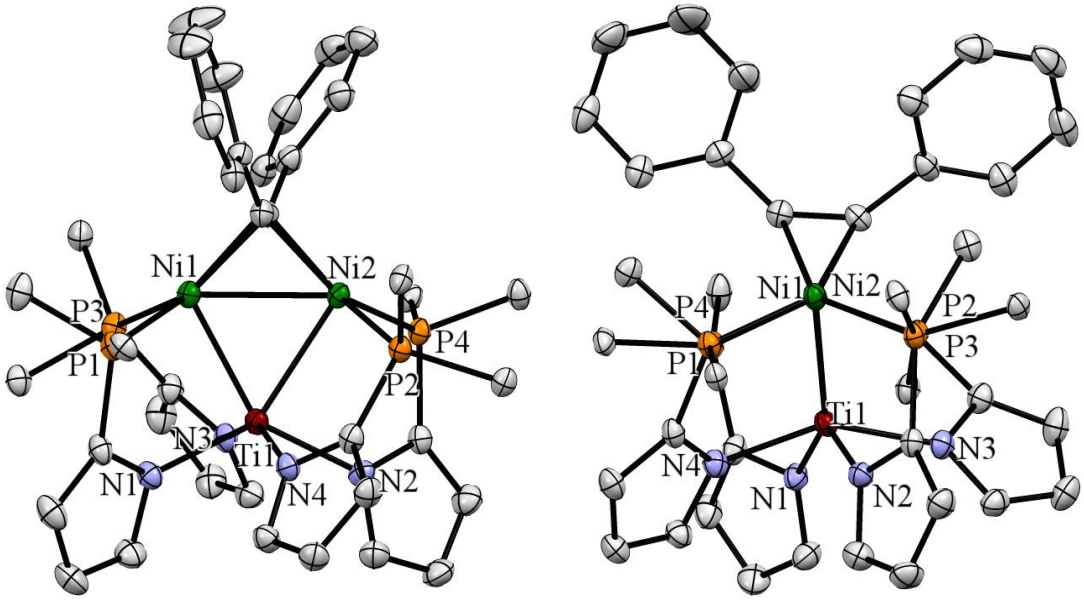

Figure 5.4. 50% thermal ellipsoid drawings of **5.2** with side-on (left) and front (right) views**.** Select phenyl group have been reduced to the ipso carbon and hydrogen atoms omitted for clarity.

In contrast, reaction of **5.1** with 2 equivalents of CN^tBu breaks apart the trimetallic core, yielding $Ti((\mu_2\text{-}NP)_2Ni(CN^tBu))_2$ (**5.3**) in quantitative yield. The trimetallic core has been split by coordination of one isocyanide to each Ni, resulting in complete cleavage of the Ni-Ni interaction as shown by the ~4 Å Ni-Ni distance. The Ni centers are equivalent by NMR and XRD, and are ligated by two phosphines and a bridging pyrrolide (Ti-N = 2.104(2) and 2.103(2) Å, Ni-N 2.070(2) and 2.061(2) Å) giving a pseudo trigonal bipyramidal Ni that is capped by an isocyanide. The Ti-Ni distances are 2.4749(6) Å and 2.4754(6) Å (FSR = 1.005), consistent with a single bond.

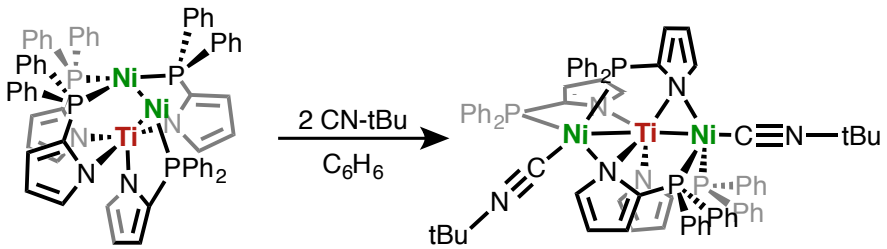

Scheme 5.3. Synthesis of isocyanide adducts of $TiNi_2$ resulting in Ni-Ni bond cleavage.

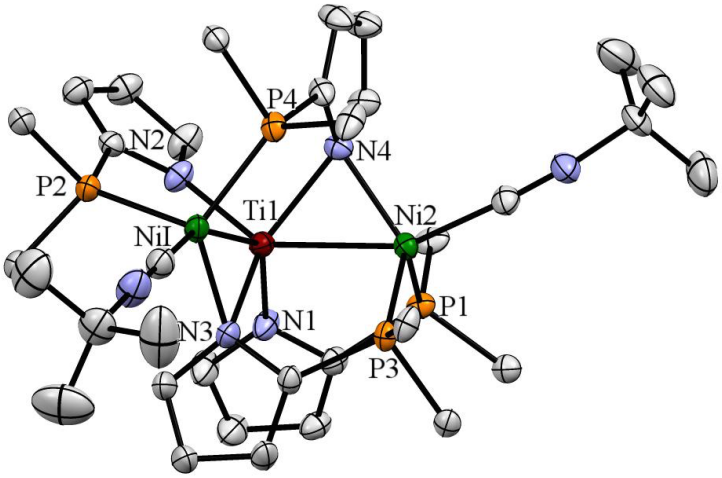

Figure 5.5. 50% thermal ellipsoid drawing of **5.3**. Select phenyl group have been reduced to the ipso carbon and hydrogen atoms omitted for clarity.

Table 5.1. Relevant bond lengths (Å) for **5.1**, **5.2**, **5.3**, and **5.5**.

	5.1	**5.2**	**5.3**	**5.5**
Ti-Ni (Å)	2.634(1)	2.5319(6)	2.4749(6)	3.065(1)
	2.289(1)	2.4152(6)	2.4754(6)	2.805(1)
Ni-Ni	2.369(1)	2.5273(6)	-	2.3583(7)
P-Ni (Å)	2.186(1)	2.2450(8)	2.1880(9)	2.166(1)
	2.162(2)	2.2530(8)	2.2176(9)	2.226(1)
	2.184(2)	2.2796(9)	2.2155(9)	2.235(1)
	2.203(1)	2.2413(8)	2.1832(8)	
Ti-N (Å)	2.098(4)	2.075(2)	2.104(2)	1.915(3)[a]
	1.977(4)	2.088(2)	2.103(2)	2.018(3)
	2.132(5)	2.051(2)	2.075(2)	2.085(4)[b]
	2.099(5)	2.057(3)	2.074(2)	2.113(4)
				2.146(4)
C-C (Å)	-	1.328(4)	-	-
Ni-N	-	-	2.070(2)	1.920(4)
			2.061(2)	1.837(3)

[a]Ti-amido. [b]Ti-imine.

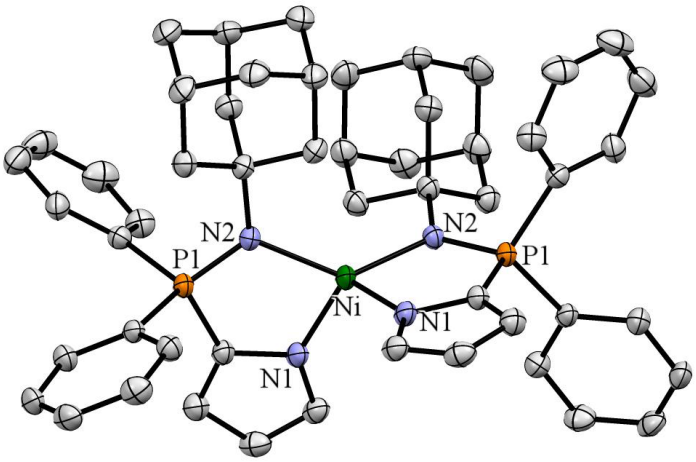

Figure 5.6: 50% thermal ellipsoid drawing of **5.4**. Select phenyl group have been reduced to the ipso carbon and Hydrogen atoms omitted for clarity.

We next sought to react **5.1** with various nitrene donors in order to probe its ability to perform multielectron transformations. Azobenzene did not react, and attempts at catalytic nitrene transfer with azides resulted in isolation of an oxidized phosphine complex, $Ni(NP(Ph)_2NAd)_2$ (**5.4**) (Figure 5.6**)**. However, reaction of **5.1** with benzo[c]cinnoline resulted in the isolation of complex **5.5**. Complex **5.5** contains the benzo[c]cinnoline moiety however the N-N bond has been completely cleaved resulting in a phospinimide (P=N: 1.631(3) Å) and a μ^3-imido that facially caps all three metal centers (Ti-N: 1.915(3) Å, Ni-N: 1.837(3) Å and 1.920(4) Å). Additionally, one NP ligand completely migrated from titanium to chelate across the nickel centers. While the triangular metal-metal core is maintained, the Ti-Ni distances have elongated significantly (Ti-Ni: 3.065(1) Å and 2.805(1) Å) and a short nickel-nickel contact is maintained (Ni-Ni: 2.3583(7) Å). At room temperature, the ^{31}P NMR consists of only a single resonance with a number of underlying broad features. Cooling the sample reveals two sets of 1:1:1:1 resonances in a ~2:1 ratio, consistent with two species, each containing 4 inequivalent phosphines. Importantly, each species contains a singlet shifted significantly downfield due to phosphine oxidation. Based on P-P coupling constants, we tentatively assign the major species to be similar to the crystal structure (where only the phosphines coordinated to Ni1 are coupling), while the minor species,

containing a large P-P coupling constant (J_{PP} = 155.82 Hz) likely has *trans*-phosphines on the same metal center. The nature of this species is ambiguous, but based upon successful elemental analysis and similar ^{31}P NMRs we propose that they are structural isomers. Heating to 100 °C and cooling to -100 °C revealed no interchange between the two species.

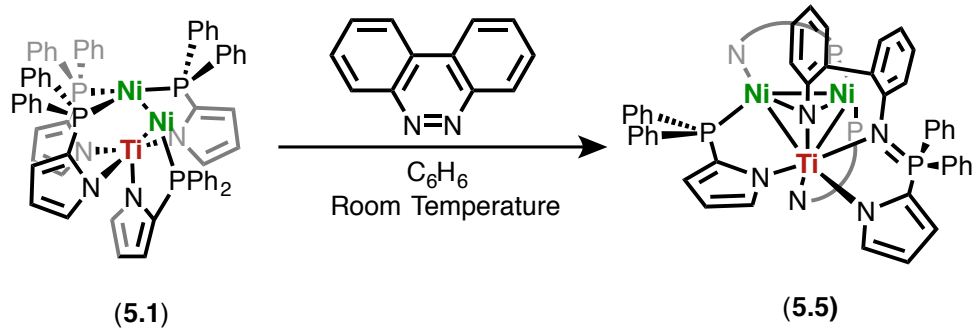

(**5.1**) (**5.5**)

Scheme 5.4: Synthesis of complex **5.5** from the reaction of $TiNi_2$ with benzo[c]cinnoline.

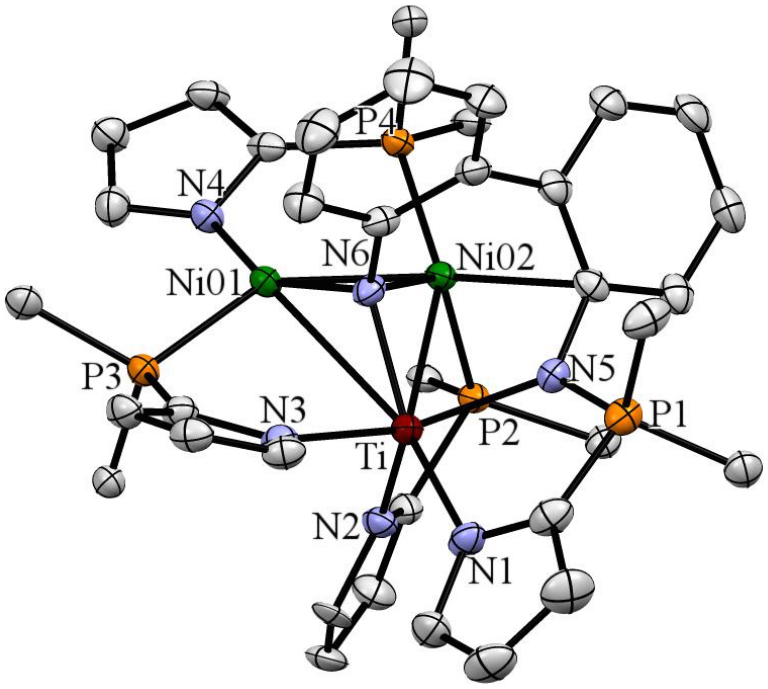

Figure 5.7. 50% thermal ellipsoid drawing of **5.5**. Select phenyl group have been reduced to the ipso carbon and hydrogen atoms omitted for clarity.

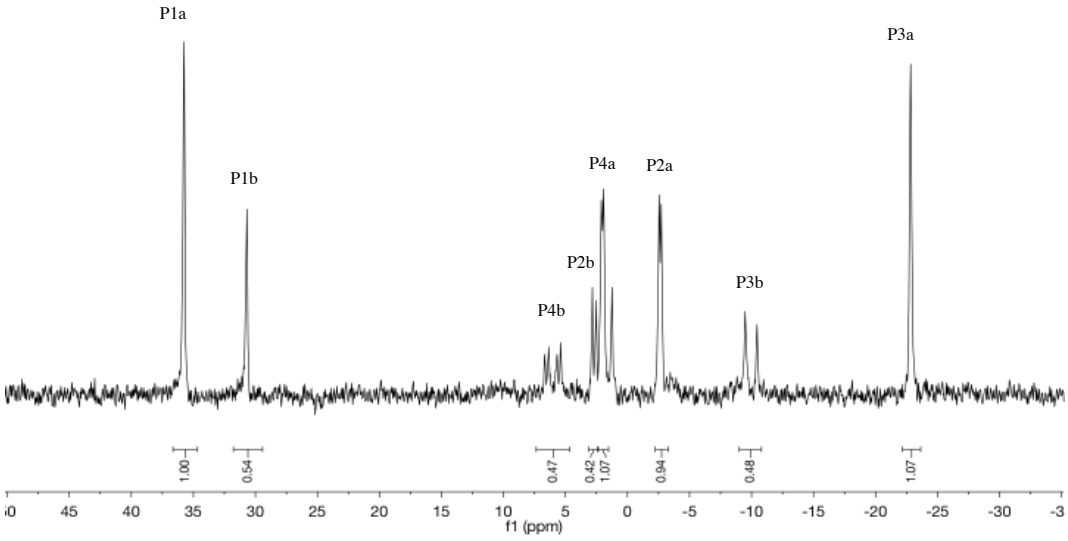

Figure 5.8: Low temperature ^{31}P NMR of **5.5** showing the two isomeric species.

N-N double bond cleavage reactions have received significant attention due to their relation with N_2 reduction. These types of transformation are most often reported at early transition metal centers, where the metals are significantly more reducing and formation of strong metal-ligand pi bonds acts as a thermodynamic driving force [195-208]. Additionally, these metals can occupy a large range of oxidation states that can provide the requisite electrons to facilitate these types of transformations at a single metal center. There are significantly less reports of these reactions that utilize late transition metals and those that do typically involve multiple centers to provide the necessary electrons [209-211]. There are no literature reports of N-N cleavage reactions featuring nickel.

The Holland group has reported azobenzene cleavage with dimeric iron hydrides supported by β-diketiminate ligands and studied the associated reaction kinetics [211]. Based on their findings they propose azo coordination to the dimer to form an L-type adduct. Rate determining reductive elimination of H_2 (both a negative $\Delta S^{\pm}$ and inverse

KIE were observed) then provides the electrons necessary to cleave the N-N bond. DFT calculations indicate the μ-η^2:η^2 binding of azobenzene is ~5 kcal/mol lower in energy than the μ-η^1:η^1 mode. Therefore, azobenzene likely rotates before undergoing N-N bond cleavage (Figure 5.9). Interestingly, benzo[c]cinnoline is not cleaved under these reaction conditions, instead resulting in isolation of L-type adducts.

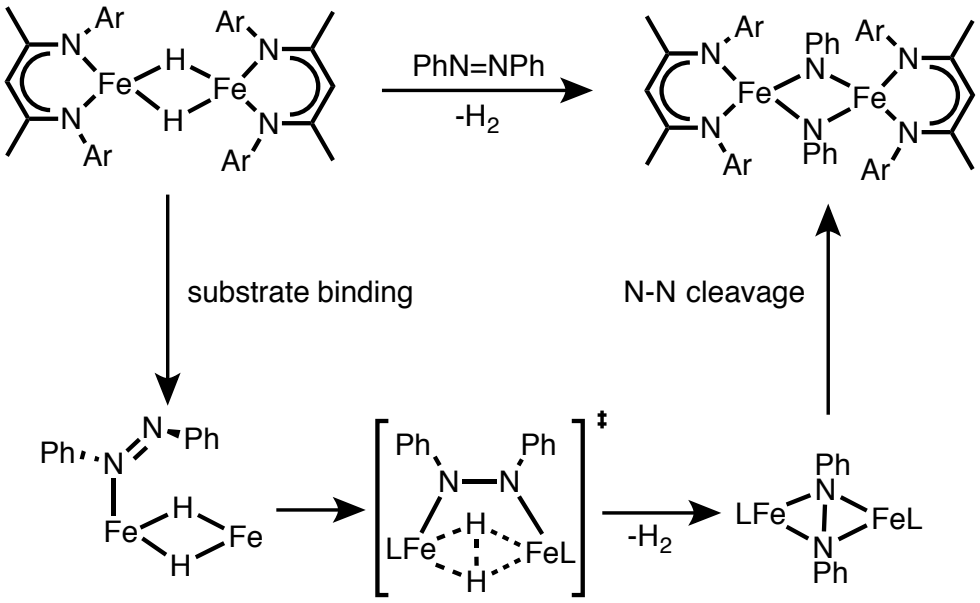

Figure 5.9: Mechanism of azobenzene cleavage by dimeric Fe complexes.

Accordingly, we postulate that the formation of **5.5** proceeds *via* substrate coordination across the nickel centers, similar to complex **5.2**. This adduct, which most likely contains a moderately activated N=N bond, can then proceed through two different pathways: (1), complete N-N bond cleavage resulting in two equivalent P_2Ni(II) imido fragments, followed by phosphine oxidation and subsequent ligand rearrangement; or (2), N-N bond breakage could be a concerted process with phosphine oxidation circumventing the dinickeldiimido intermediate (Figure 5.10). While we have been unable to isolate the presumed dinickel diimido intermediate or the L type adduct, we still favor this pathway for a number of reasons. First, bisphosphine nickel imidos in similar geometries have been synthesized and shown to be stable [212-213], imido group transfers to phosphines observed from late transition metals typically proceed through a discrete, preformed metal-imido intermediate [214], and lastly, bisphosphine nickel azo complexes have no reported cleavage reactivity. Additionally, control experiments with

3.2 have shown no reaction with benzo[c]cinnoline at room temperature, indicating both nickel centers are necessary for reactivity.

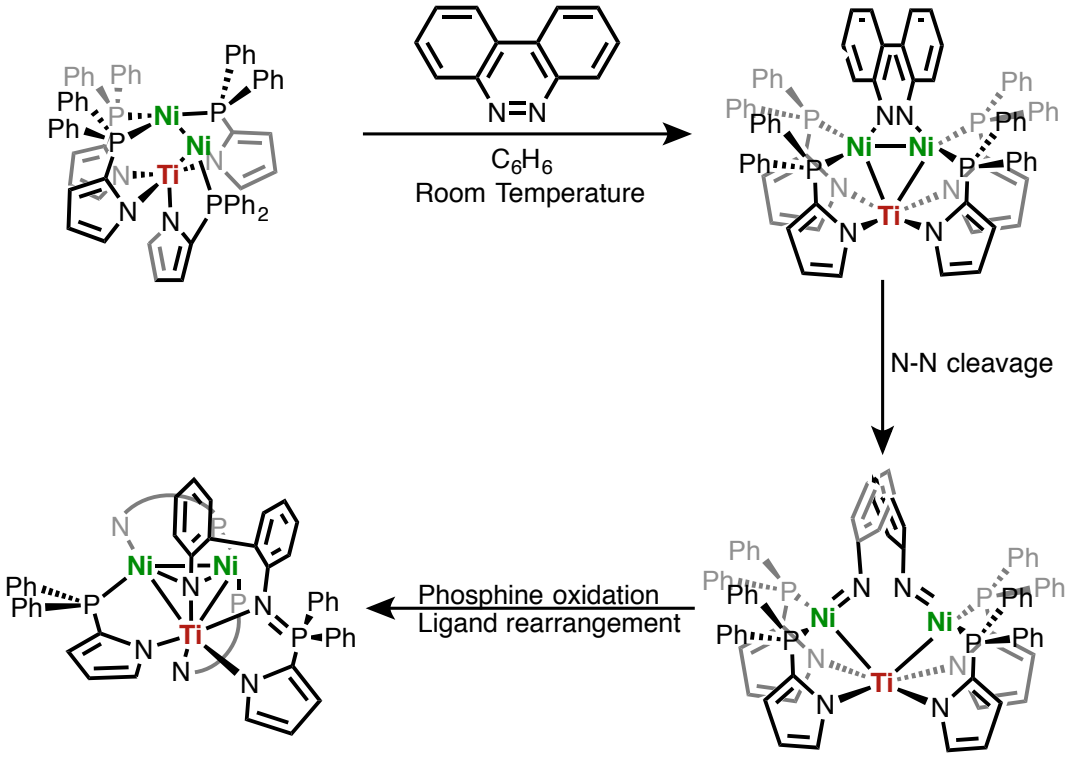

Figure 5.10. Proposed mechanism for the cleavage of benzo[c]cinnoline by complex **5.1**.

5.4 Conclusion

In summary, we report the synthesis of a trimetallic $TiNi_2$ complex supported by phosphinopyrrolides. The complex contains three short intermetallic distances but only contains two significant bonding interactions: a Ni-Ni bond and a dative Ti-Ni bond. The Ni-Ni bond can be manipulated by the presence of L type donors. In the case of diphenylacetylene coordination across the two Ni centers is observed, while addition of two equivalents of t-butyl isocyanide breaks apart the trimetallic core. Reaction of this complex with benzo[c]cinnoline results in the formal four electron cleavage of the N-N double bond. We favor a mechanism where the nickel centers work in a cooperative fashion to generate a dinickel diimido intermediate. This intermediate decomposes via phosphine oxidation and subsequent ligand rearrangement.

5.5 EXPERIMENTAL CONSIDERATIONS

General Considerations and Instrumentation. All air- and moisture-sensitive compounds were manipulated in a glovebox under a nitrogen atmosphere. Solvents for air- and moisture-sensitive reactions were vacuum transferred from sodium benzophenone ketyl (THF, Et_2O, pentane, d_6-benzene and d_8-toluene) or predried by passing through activated alumina columns of a SG Water solvent purification system. $Ti(NP)_4$ and $Ni(COD)_2$ was prepared according to literature procedure [131, 134]. ^1H and ^{31}P spectra were recorded on Varian INOVA 500 MHz or Bruker Avance III 400 MHz spectrometers. Chemical shifts are reported with respect to residual protio-solvent impurity for ^1H (*s*, 7.16 ppm for C_6D_5H) and PPh_3 for ^{31}P (*s*, -6 ppm for C_6D_6).

X-ray Crystal Data: General Procedure. Crystals were removed quickly from a scintillation vial to a microscope slide coated with oil. Samples were selected and mounted on the tip of a 0.1 mm diameter glass capillary. Data collection was carried out on a Bruker APEX II CCD diffractometer with a 0.71073 Å Mo Kα source or on a Bruker-AXS D8 Venture diffractometer with a 1.54178 Å Cu Kα source. The structures were solved by direct methods. All non-hydrogen atoms were refined anisotropically. Details regarding refined data and cell parameters are available in Tables 5.2 and 5.3.

Synthesis of $Ti((2\text{-}Ph_2P)C_4H_3N)_4Ni_2$, $Ti(NP)_4Ni_2$ (5.1).

Solid $Ti(NP)_4$ (**2.2**) (540 mg, 0.515 mmol, 1 equiv) was dissolved in 10 mL benzene and $Ni(COD)_2$ (1417 mg, 5.15 mmol, 10 equiv) was added. The solution was refluxed at 90°C overnight. The dark solution was then allowed to cool and filtered over celite (Caution! The reduced Ni black fumes upon contact with air). Volatiles were removed to leave a black, oily residue, which was taken up in THF and layered with pentane. The solution was cooled to -35°C and allowed to crystallize. The resulting black crystals were washed thoroughly with pentane and dried to give 192 mgs (32% yield) of **5.1**. The product can be further purified from a benzene/pentane mixture. ^1H NMR (300MHz, C_6D_6) δ, ppm: 6.45-6.52 (4H, br), 6.60-6.93 (32H, br) 6.93-7.13 (16H, br). ^{31}P NMR

(121 MHz, C_6D_6) δ, ppm: -5.0 to -8.0 (br, 2P), -15.0 to -18.0 (br, 2P). Satisfactory elemental analysis could not be obtained due to incomplete combustion.

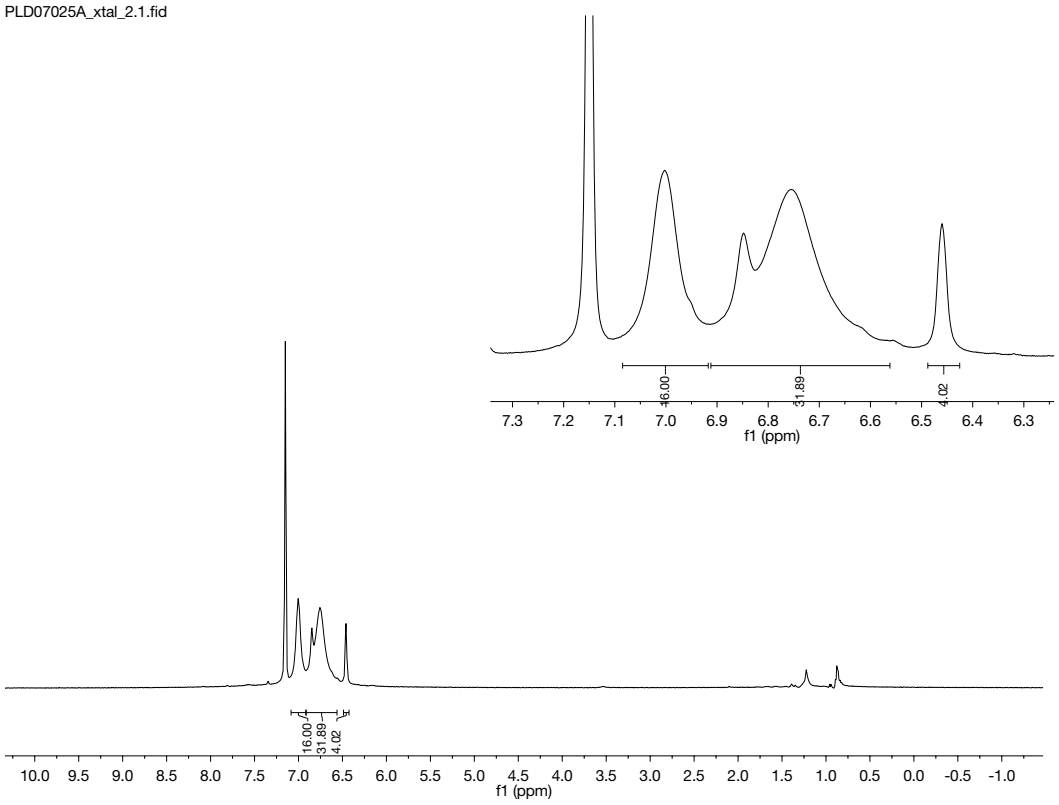

Figure 5.11: ^{1}H NMR of **5.1** in C_6D_6. Taken from PLD07025.

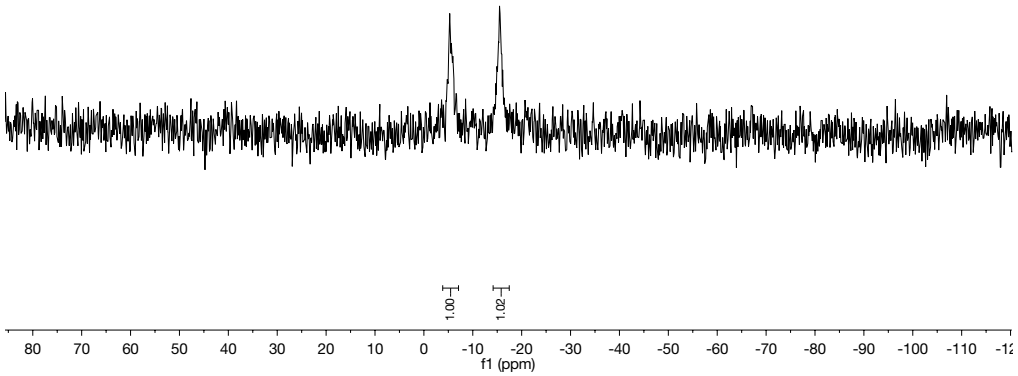

Figure 5.12: ^{31}P NMR of **5.1** in C_6D_6. Taken from PLD07025.

Synthesis of Ti(NP)$_4$Ni$_2$(PhCCPh) 5.2.

Solid Ti(NP)$_4$Ni$_2$ (**5.1**) (30 mg, 0.026 mmol, 1 equiv) was dissolved in 0.5 mL C_6D_6 and diphenylacetylene (4.6 mg, 0.026 mmol, 1 equiv) was added. The solution was warmed to 90°C or allowed to sit in solution for approximately 3 days. Reaction progress can be monitored *via* ^{31}P NMR. The solution was then layered with pentane and allowed to sit. The resulting dark crystals were washed with pentane and dried to give crystalline **5.2** (quantitative by NMR). ^{1}H NMR (300MHz, C_6D_6) δ, ppm: 5.75-5.86 (br, 4H), 6.25-6.95 (m, 58H). ^{31}P NMR (121 MHz, C_6D_6) δ, ppm: -1.10 (q, J_{pp} = 12.01 Hz) Elemental Analysis: Calculated: C, 69.68; H, 4.65; N, 4.17. Found: C, 69.60; H, 5.02; N, 3.89.

PLD07015.1.fid

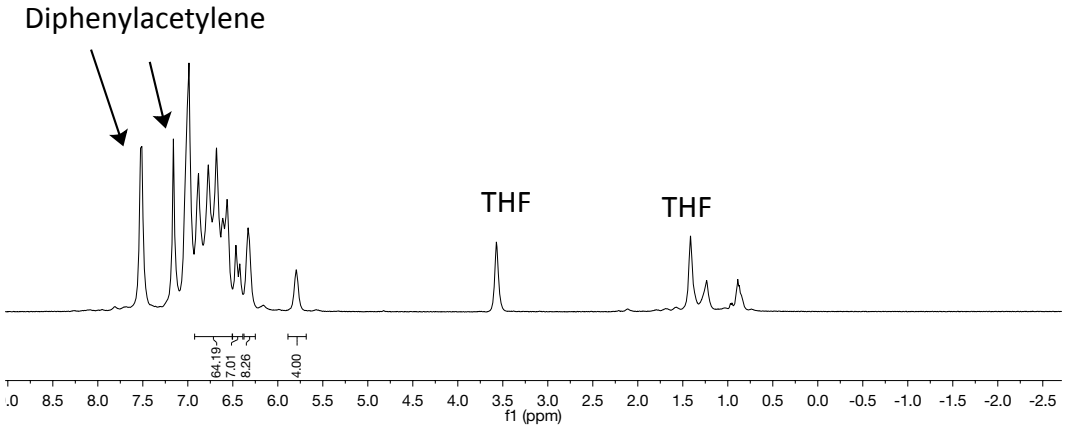

Figure 5.13: ^{1}H NMR of **5.2** in C_6D_6. Contains THF and diphenylacetylene impurities. Taken from PLD07015.

PLD07015.2.fid

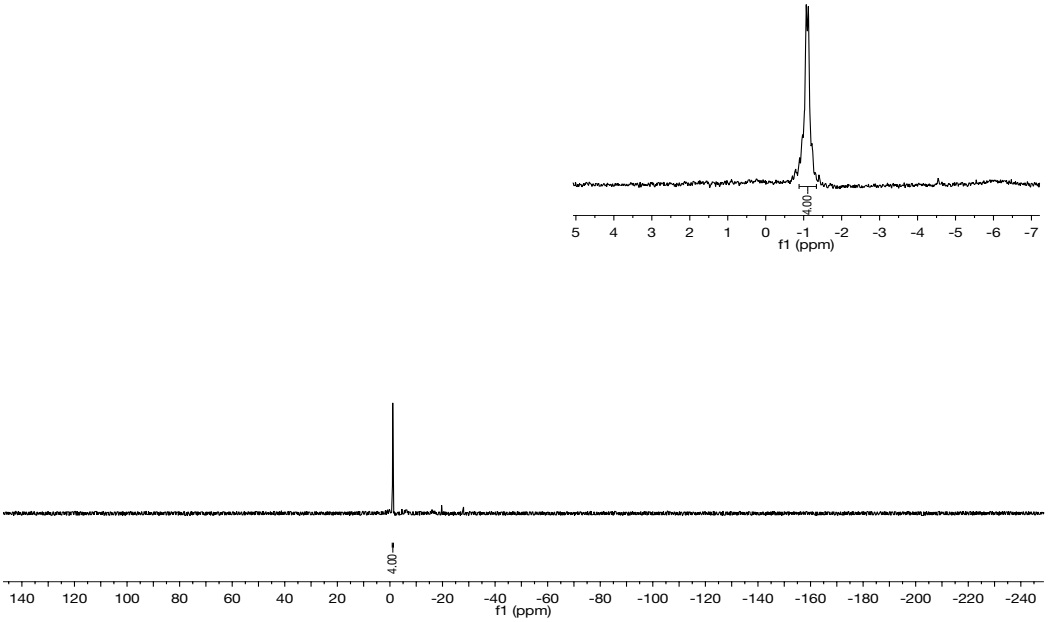

Figure 5.14: ^{31}P NMR of **5.2** in C_6D_6. Taken from PLD07015.

Synthesis of $Ti((NP)_2Ni(CN\text{-}tBu))_2$ (5.3)

Solid $Ti(NP)_4Ni_2$ (**5.1**) (30 mg, 0.026 mmol, 1 equiv) was dissolved in 0.5 mL benzene and t-butyl isocyanide was added (4.3 mg, 0.052 mmol, 2 equiv). The solution was layered with pentane and allowed to crystallize. The resulting crystals were washed with pentane and dried to give crystalline **5.3** (quantitative by NMR). ^{1}H NMR (300MHz, C_6D_6) δ, ppm: 1.01-1.05 (s, 18H), 6.31 (m, 2H), 6.39-6.41 (m, 6H), 6.56-6.62 (m, 9H), 6.66-6.71 (m, 3H), 6.77-6.81(m, 2H), 6.86-6.93(m, 5H), 6.98-7.05 (m, 7H), 7.07-7.13 (m, 5H), 7.44-7.52 (m, 6H), 7.54-7.58 (s, 2H), 7.80-7.88 (m, 4H). ^{31}P NMR (121 MHz, C_6D_6) d, ppm: -6.62 (δ, J_{pp} = 11.73 Hz, 4P). Satisfactory elemental analysis could not be obtained due to decomposition under vacuum.

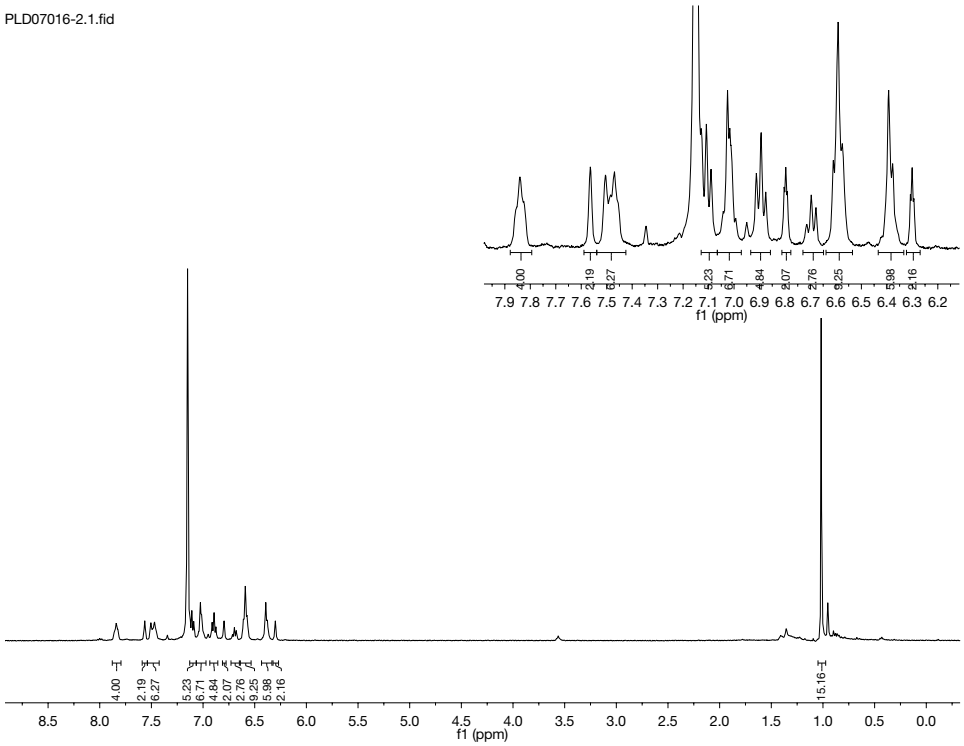

Figure 5.15: ^{1}H NMR of **5.3** in C_6D_6. Taken from PLD07016.

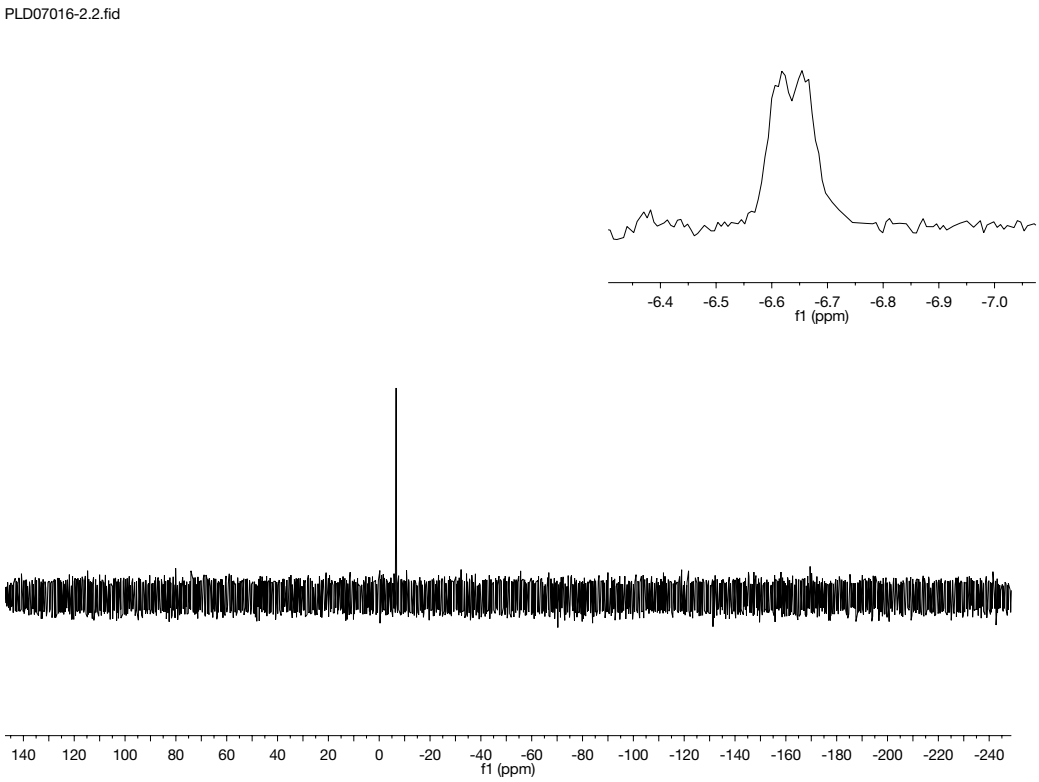

Figure 5.16: ^{31}P NMR of **5.3** in C_6D_6. Taken from PLD07016.

Synthesis of $Ti(NP)_4Ni_2$(benzo[c]cinnoline) (5.5)

Solid $Ti(NP)_4Ni_2$ (62 mg, 0.026 mmol, 1 equiv) was dissolved in 0.5 mL benzene and benzo[c]cinnoline (12 mg, 0.026 mmol, 1 equiv) was added. The solution was stirred for four hours and then layered with pentane and allowed to crystallize. The resulting crystals were washed to pentane and dried to give 46 mg (64% yield) of **5.5**. ^1H NMR (300MHz, C_6D_6) δ, ppm: 5.2 (m, 1H), 5.63 (m, 1H), 5.70 (m, 1H), 6.00 (m, 1H), 6.03 (m, 1H), 6.06 (m, 2H), 6.13-6.50 (br m, 24H), 6.50-6.58 (m, 2H), 6.60- 7.15 (br m, 90H), 7.19-7.45 (m, 8H), 7.57-7.67 (m, 5H), 7.80-7.84 (br, 1H), 7.89-7.98 (m, 5H), 8.32-8.38 (m, 3H), 9.64 (m, 1H). ^{31}P NMR (121 MHz, C_6D_6) δ, ppm: Species A: -23.5 (s, 1P), -2.655(d, J_{pp} = 23.42 Hz, 1P), 1.99 (d, J_{pp} = 23.42 Hz, 1P), 35.75 (s, 1P). Species B: -9.96 (d, J_{pp} = 155.82 Hz, 1P), 2.66 (d, J_{pp} = 49.7 Hz, 1P), 6.01 (dd, J_{pp} = 155.82, 49.7 Hz, 1P), 30.7 (s, 1P). Elemental Analysis: Calculated: C, 67.79; H, 4.49; N, 6.24. Found: C, 67.81; H, 4.51; N, 5.97.

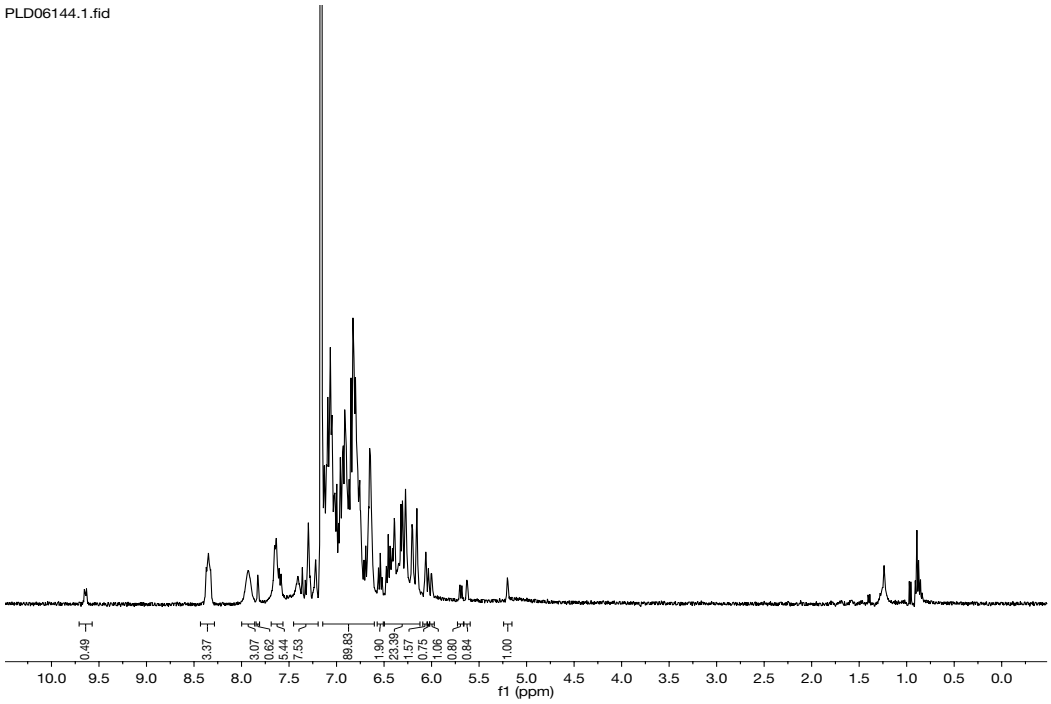

Figure 5.17: ^{1}H NMR of **5.5** in C_6D_6. Taken from PLD06144.

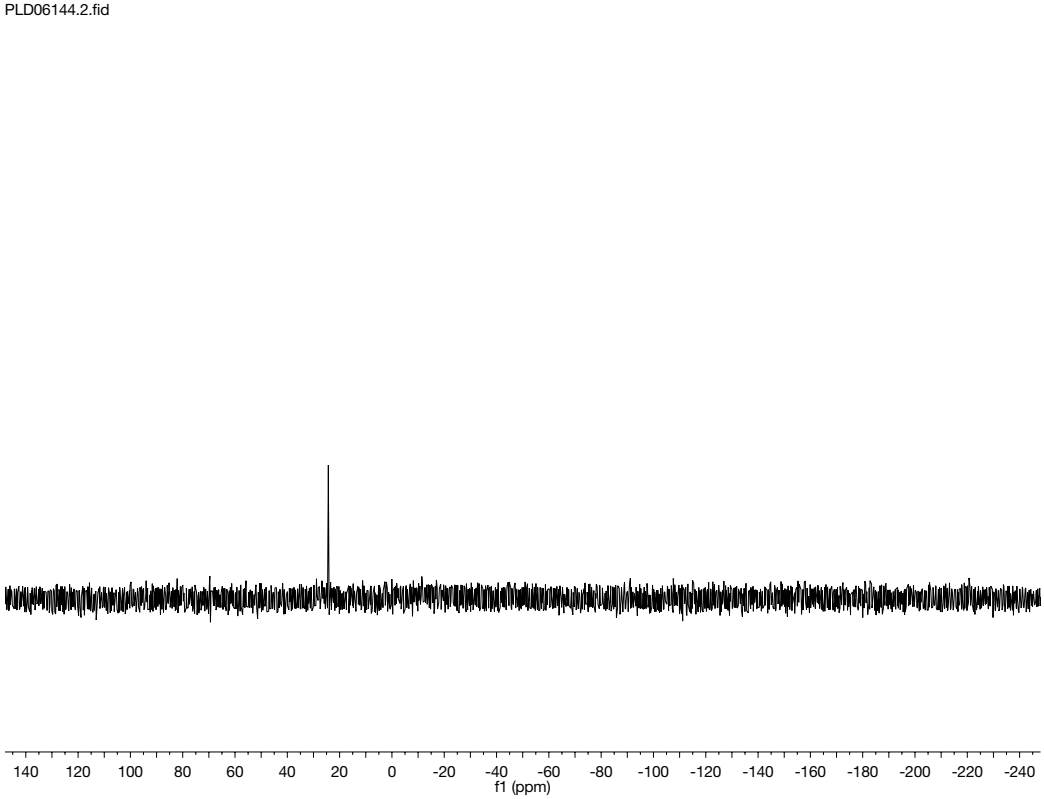

Figure 5.18: ^{31}P NMR of **5.5** at room temperature in d_8-toluene. Taken from PLD06144.

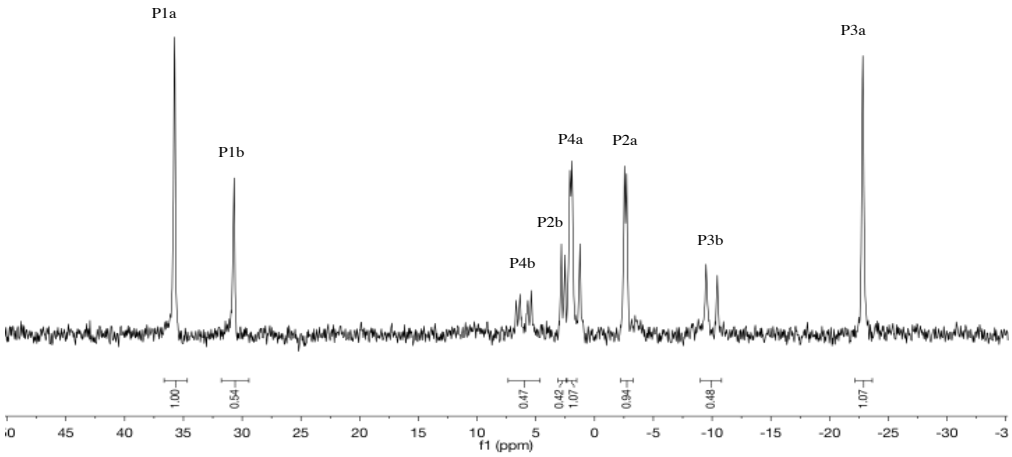

Figure 5.19: ^{31}P NMR of **5.5** at –70 °C in d_8-toluene showing two species each containing four inequivalent phosphines. Taken from PLD06146.

Table 5.2. Crystal and refinement data for complexes **5.1-5.3**.

	5.1	**5.2**	**5.3**
CCDC Number	1841829	1841830	1841833
Empirical Formula	$C_{64}H_{52}N_4P_4TiNi_2$	$C_{78}H_{62}N_4P_4TiNi_2$	$C_{74}H_{70}N_6P_4TiNi_2$
Formula weight	1166.23	1400.81	1332.49
T (K)	123(2)	123(2)	123(2)
a, Å	21.9511(7)	13.8348(4)	25.2271(10)
b, Å	10.8767(3)	23.1240(6)	13.1700(6)
c, Å	24.5495(8)	20.3199(5)	19.5170(8)
α, deg	90	90	90
β, deg	113.911(1)	96.1600(10)	90.277(1)
γ, deg	90	90	90
Volume, Å^3	5358.3	6463.1(3)	6479.2(5)
Z	4	4	4
Crystal System	Monoclinic	Monoclinic	Monoclinic
Space Group	Cc	P2(1)/n	P2(1)/c
d_{calc}, g/cm^3	1.446	1.440	1.366
θ Range, deg	4.032 to 72.142	3.685 to 72.240	2.584 to 30.4805
μ, mm^{-1}	3.540	3.037	0.841
Abs. Correction	Multi-scan	Multi-scan	Multi-scan
GOF	1.049	1.014	1.096
R_1 ,[a]	$R1$ = 0.0504	$R1$ = 0.0467	$R1$ = 0.0509
wR_2 [b] [I>2σ (I)]	$wR2$ = 0.1350	$wR2$ = 0.1161	$wR2$ = 0.1577

[a] $R_1 = \sum||F_o| - |F_c||/\sum|F_o|$. [b] $wR_2 = [\sum[w(F_o^2-F_c^2)^2]/\sum[w(F_o^2)^2]]^{1/2}$.

Table 5.3. Crystal and refinement data for complexes **5.4** and **5.5**.

	5.4	**5.5**
CCDC Number	1841831	1841832
Empirical Formula	$C_{52}H_{56}N_4P_2Ni$ • C_6H_6	$C_{76}H_{60}N_6P_4TiNi_2$ • C_6H_6
Formula weight	935.75	1424.54
T (K)	123(2)	123(2)
a, Å	16.9487(18)	12.474(2)
b, Å	17.9432(18)	27.079(5)
c, Å	16.1747(15)	21.510(3)
α, deg	90	90
β, deg	106.472(5)	101.459(5)
γ, deg	90	90
Volume, Å^3	4717.1(8)	7121(2)
Z	4	4
Crystal System	Monoclinic	Monoclinic
Space Group	C2/c	P2(1)/n
d_{calc}, g/cm^3	1.318	1.329
θ Range, deg	2.5145 to 26.460	2.2405 to 26.2385
μ, mm^{-1}	0.524	0.772
Abs. Correction	Multi-scan	Multi-scan
GOF	1.042	1.063
R_1 ,[a]	R1 = 0.0477	R1 = 0.0674
wR_2 [b] [I>2σ (I)]	wR2 = 0.1260	wR2 = 0.1524

[a] $R_1 = \sum||F_o| - |F_c||/\sum|F_o|$. [b] $wR_2 = [\sum[w(F_o^2-F_c^2)^2]/\sum[w(F_o^2)^2]]^{1/2}$.

Chapter 6

Synthesis and Characterization of Group 5 – Group 9/10 Early-Late Bimetallic Complexes Supported by 2-(diphenylphosphino)pyrrolide Ligands

6.1 Overview

The synthesis of $M(\kappa^2\text{-NP})_4$ and $M(\kappa^2\text{-NP})_3Cl_2$ (M= Nb, Ta and NP = 2-diphenylphosphinopyrrolide) metalloligands and their corresponding early – late bimetallics is reported. Treatment of $M(\kappa^2\text{-NP})_3Cl_2$ (M = Nb, Ta) precursors with group 9 and 10 metals resulted in clean formation of the heterobimetallic complexes $Cl_2M(\mu_2\text{-NP})_3M'$ (MM' = NbPd (**6.5**), TaNi (**6.6**), TaPd (**6.7**)) or $Cl_2M(\mu_2\text{-NP})_3M'Cl$ (MM' = NbRh (**6.8**), NbIr (**6.9**), TaRh (**6.10**), TaIr (**6.11**)). Each set of complexes is isostructural and contains three ligands that bridge the metal centers. The d^{10} or d^8 complexes are all diamagnetic and X-ray crystallographic analysis reveals similarly short metal-metal distances, ranging from 2.2979(5) Å to 2.4366(2) Å. Despite similar bonding metrics, treatment with an L type donor (2,6 xylyl isocyanide) reveals differential reactivity. While complexes **6.6**, **6.7**, **6.9**, and **6.11** all bind the isocyanide at the late metal, ligand rearrangements are observed in **6.6**. Complex **6.7** binds the isocyanide in the axial position while equatorial binding is observed in **6.9** and **6.11**. All isocyanide adducts maintain close metal-metal contacts *via* XRD.

6.2 Introduction

Pioneered by Cotton's characterization of a quadruple bond in $[Re_2Cl_8]^{2-}$, the study of metal-metal bonds has received significant attention over the past 50 years [215-217]. While initial studies focused heavily on homobimetallic complexes [218], advances in ligand design have enabled the study of metal-metal bonding in early-late heterobimetallic complexes. Development of hard, soft bifunctional ligands (often bearing hard oxygen/nitrogen and soft phosphorous donors) by the Wolczanski, Nagashima, Lu, and Thomas groups have utilized stepwise metallations resulting in a plethora of early-late bimetallic complexes containing strong metal-metal bonds [31, 87-90, 108, 133]. From these series of complexes, a couple of trends have emerged: metal-metal bonding is strongest when the total d-electron count is ten, and bond strength decreases as the metal centers become more disparate. For example, Lu reported a series of Cr-M (M = Mn, Fe, Co, and Ni) complexes supported by a 'double-decker' $N((o\text{-}C_6H_4)NCH_2P(^iPr)_2)$ ligand in a trigonal framework. As the apical metal is varied from

Mn > Fe > Co > Ni the bond order decreases from a quintuple bond in CrMn to a single bond in Cr-Ni [112].

Despite these significant synthetic efforts, many bimetallic combinations of the transition metal block remain underexplored. While there are many examples of early-late bimetallic complexes featuring group 5/group 9 or 10 metals, most of these complexes contain bridging ligands (e.g. imidos, hydrides, alkylidenes, or carbonyls) and long metal-metal distances (FSR > 1.1) [78-79, 220]. The presence of bridging ligands often forces close contact between metal centers and convolutes the bonding picture, making it difficult to extract meaningful trends. In fact, there are relatively few examples of metal-metal bonds in early-late bimetallic complexes featuring group 5 metals. Lu has synthesized a series V-M (M = Fe, Co, and Ni) complexes that feature multiple metal-metal bonds in the cases of Fe and Co [162], while Thomas has made both VM (M = Fe, Co, Ni, and Cu) and NbFe bimetallic complexes that also contain strong metal-metal bonds [118, 160, 221]. Surprisingly, Thomas' NbFe complex was the first report of a metal-metal bond in an early-late bimetallic complex containing Nb.

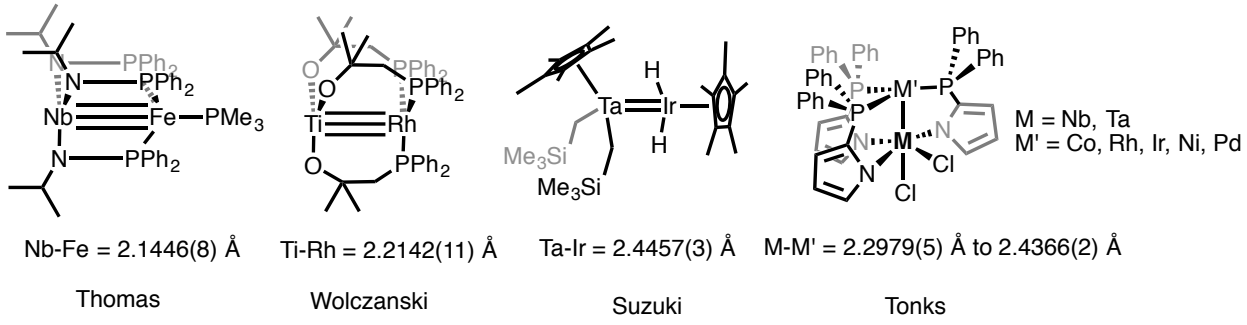

Figure 6.1: Select examples complexes containing strong metal-metal bonds featuring group 5 or group 9/10 metals.

We have previously described the ability of phosphinopyrrolide ligands to facilitate metal-metal bonding in group 4-group 10 bimetallic complexes and sought to expand our efforts to the group 5 triad [163, 219]. Herein, we report the synthesis of two different types of Nb and Ta metalloligands and their successful coordination to group 9 and 10 metals. These complexes, which contain strong metal-metal bonds, are some of the first examples of these elemental pairings.

6.3 Results and Discussion

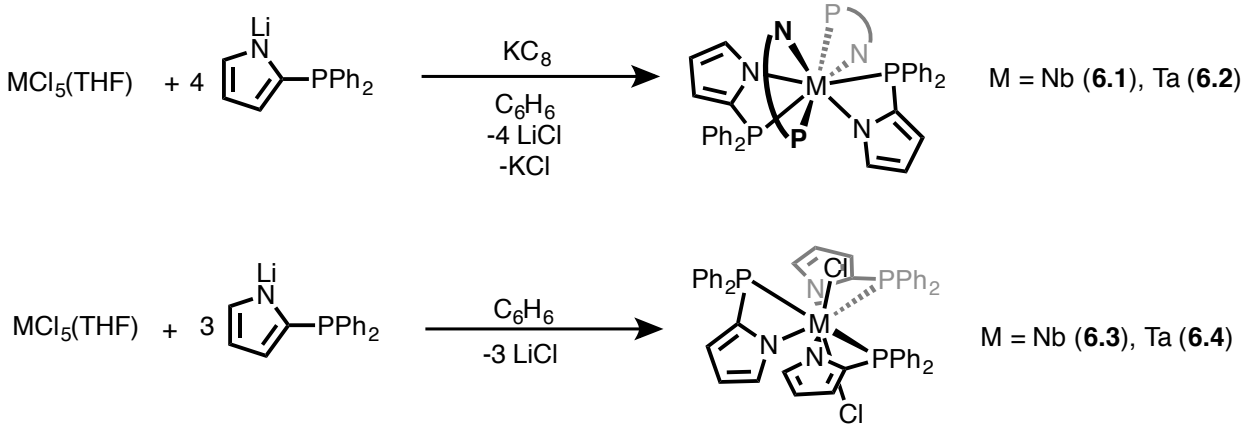

Scheme 6.1: The synthesis of homo- and heteroleptic Nb and Ta complexes.

The homoleptic group 5 complexes M(κ^2-NP)$_4$ (M = Nb (**6.1**) and Ta (**6.2**)) can be synthesized from the corresponding pentahalide complexes, $MCl_5(THF)$, four equivalents of Li(NP), and one equivalent of reductant in moderate yield (Scheme 6.1). Single crystal diffraction reveals that both complexes are 8 – coordinate in the solid state, similar to the group 4 M(κ^2-NP)$_4$ complexes (M = Ti, Zr, Hf) we have previously prepared. Using the method as described in Chapter 2, intersecting trapezoid angles of 85.06° and 85.13° are obtained for complexes **6.1** and **6.2**, respectively, indicating that both are best described as distorted dodecahedrons [125-126]. The structures of **6.1** and **6.2** are presented in Figure 6.2 and relevant bond lengths can be found in Table 6.1. Attempts to synthesize pentavalent M(κ^2-NP)$_5$ or M(κ^2-NP)$_4$Cl complexes resulted in intractable mixtures of products from which M(κ^2-NP)$_4$ complexes were crystallized. Presumably the high coordination number induces a reductive event.

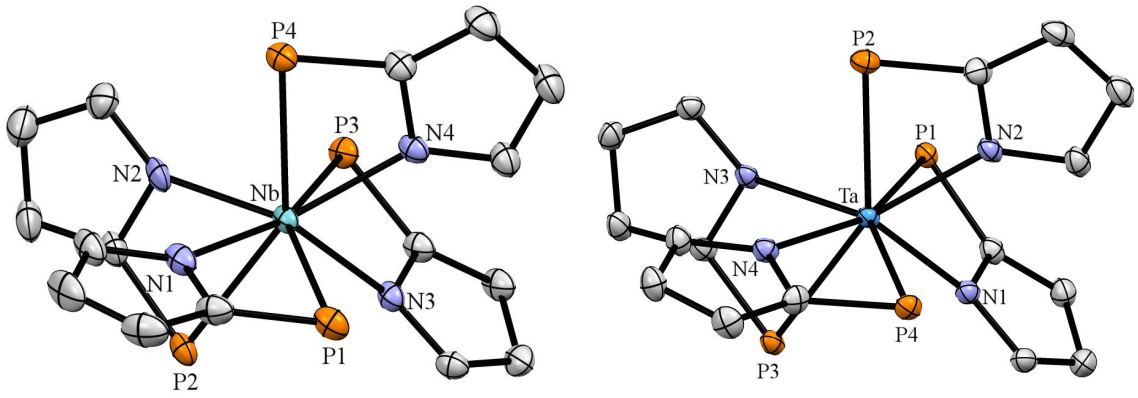

Figure 6.2. 50% thermal ellipsoid drawing of **6.1** (left) and **6.2** (right). Phenyl groups, hydrogen atoms and solvent omitted for clarity.

However, the M^V trisubstituted complexes, $M(\kappa^2\text{-NP})_3Cl_2$ (M = Nb (**6.3**), Ta (**6.4**)) can be synthesized from $MCl_5(THF)$ and three equivalents of Li(NP) in high yield (Scheme 6.1). Similar to **6.1** and **6.2**, **6.3** and **6.4** are 8-coordinate in the solid state, containing three NP ligands that are bound κ^2 to the metal center. The ^{31}P NMR of these diamagnetic compounds consists of two resonances in a 2:1 ratio, consistent with the solid-state structure where two phosphines are equivalent and related by a mirror plane. The structures of **6.3** and **6.4** are presented in Figure 6.3 and relevant bond lengths can be found in Table 6.1.

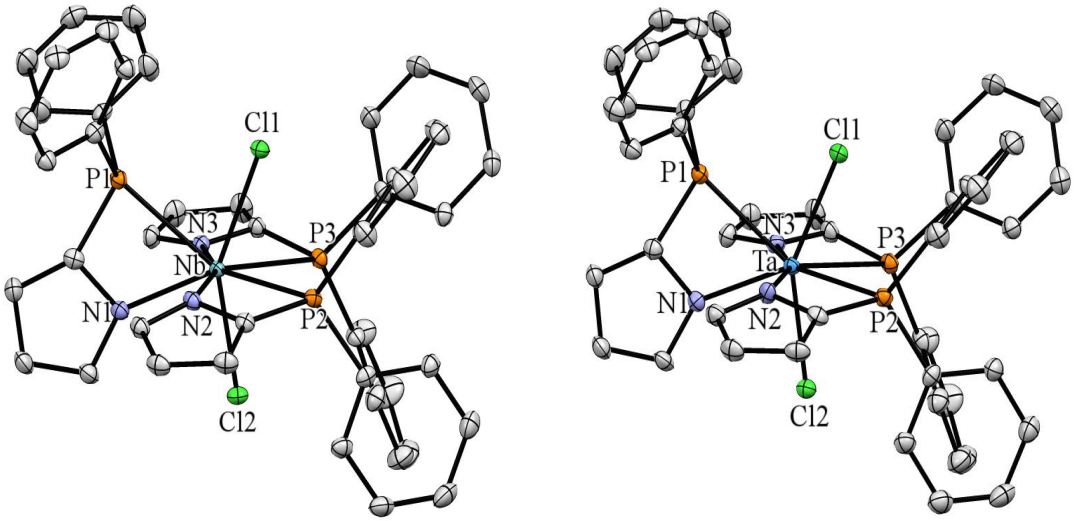

Figure 6.3. 50% thermal ellipsoid drawing of **6.3** (left) and **6.4** (right). Hydrogen atoms and solvent omitted for clarity.

Table 6.1. Relevant bond lengths (Å) for **6.1**-**6.4**.

	6.1	**6.2**	**6.3**	**6.4**
M-N(Å)	2.194(3)	2.188(2)	2.201(2)	2.113(3)
	2.194(3)	2.201(2)	2.160(2)	2.189(3)
	2.210(2)	2.185(2)	2.121(2)	2.154(3)
	2.183(2)	2.217(2)		
M-P (Å)	2.7356(8)	2.7570(6)	2.6644(5)	2.667(1)
	2.7526(8)	2.7143(7)	2.7618(5)	2.768(1)
	2.7745(8)	2.7654(6)	2.7480(5)	2.749(1)
	2.7297(8)	2.7100(7)		
M-Cl (Å)	-	-	2.3923(5)	2.383(1)
			2.4464(5)	2.430(1)

Treatment of **6.3** and **6.4** with $Ni(COD)_2$ (COD = 1,5-cyclooctadiene) or $Pd(P(^tBu)_3)_2$ affords the heterobimetallic complexes $Cl_2M(\mu_2\text{-}NP)_3M'$ (MM' = NbPd (**6.5**), TaNi (**6.6**), TaPd (**6.7**)) in moderate yield (Scheme 6.2). The structures of **6.5**-**6.7**

are presented in Figure 6.4 and relevant bond lengths and angles can be found in Table 6.2. All three bimetallic compounds are isostructural, containing three phosphinopyrrolide ligands that bridge between the two metals. The geometry about the group 5 metal is pseudooctahedral, while the geometry about the late TM is a distorted trigonal pyramidal wherein the group 5 metal occupies the axial site of the pyramid. Complexes **6.5-6.7** are diamagnetic, and at room temperature display two resonances in the ^{31}P NMR: a doublet and triplet corresponding to two equivalent *trans* phosphines and a *cis* phosphine, consistent with the crystal structures. In the case of complex **6.6**, two broad features are observed in a 2:1 ratio, consistent with a fluxional species. Single crystal diffraction reveals close contacts between metal centers: (**6.5**) NbPd 2.4068(4) Å (FSR = 0.918), **(6.6**) TaNi: 2.2979(5) Å (FSR = 0.92), and (**6.7**) TaPd 2.4189(6) Å (FSR = 0.923) [149]. Metallations with $Pt(P(^tBu)_3)_2$ were unsuccessful even at elevated temperatures and resulted in decomposition of the Pt starting material as noted by free $P(^tBu)_3$ in solution. Attempts to synthesize $Cl_2Nb(\mu_2\text{-}NP)_3Ni$ were also unsuccessful, resulting in crystalline samples containing products of ligand decomposition: ring-opened pyrroles.

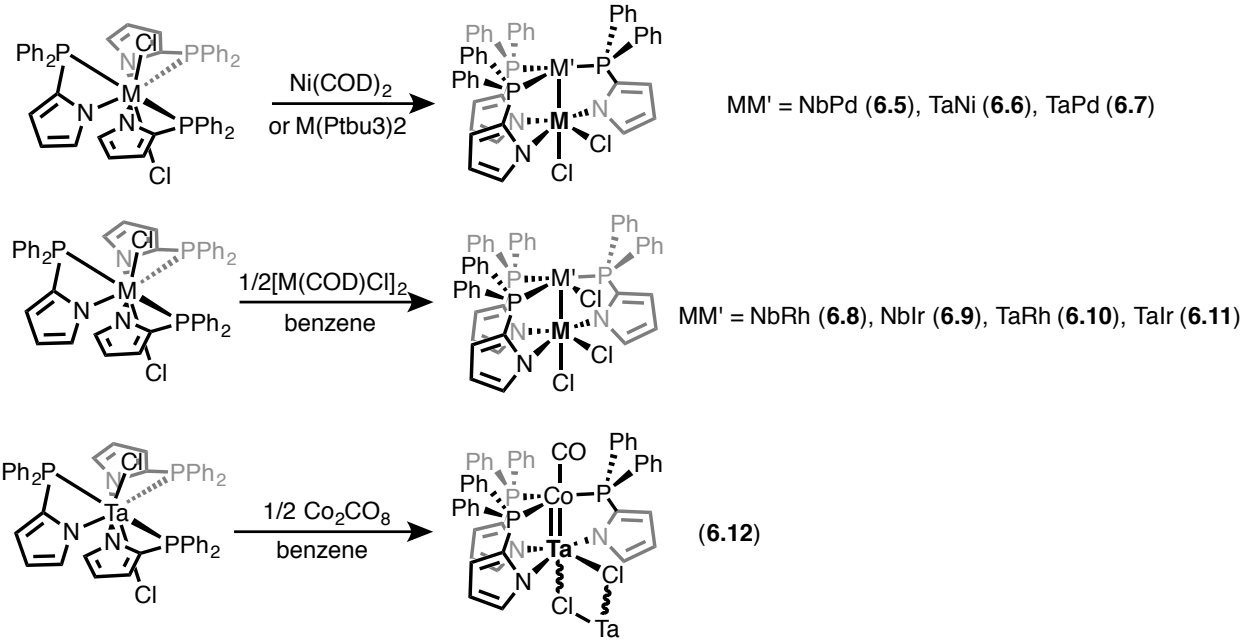

Scheme 6.2. Synthesis of group 5 – group 9/10 bimetallic complexes.

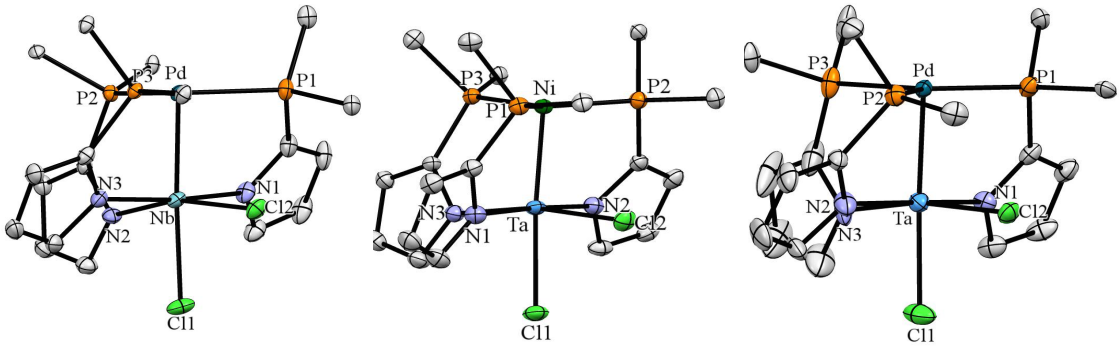

Figure 6.4. 50% thermal ellipsoid drawing of **6.5** (left), **6.6** (center), and **6.7** (right). Phenyl groups have been truncated to the ipso carbon, and hydrogen and solvent atoms have been removed for clarity. Selected bond lengths and angles can be found in Table 6.2.

Table 6.2. Relevant bond lengths (Å) and angles (°) for **6.5**-**6.7**.

	6.5 NbPd	**6.6 TaNi**	**6.7 TaPd**
M-M(Å)	2.4068(4)	2.2979(5)	2.4189(6)
FSR[a]	0.919	0.922	0.923
P-M (Å)	2.3638(7)	2.249(1)	2.389(2)
	2.3957(7)	2.239(1)	2.416(2)
	2.3712(8)	2.221(1)	2.385(3)
P-M-P (°)	127.70	123.13	112.98
	109.49	106.81	115.49
	129.73	129.17	131.53
M-N (Å)	2.097(2)	2.111(3)	2.110(6)
	2.148(2)	2.140(4)	2.10(1)
	2.157(3)	2.135(4)	2.132(6)
M-Cl (Å)	2.3731(7)	2.396(1)	2.369(2)
	2.3949(9)	2.375(1)	2.358(3)
Torsional Angle (P-	26.74	22.98	30.82
M-M-N) (°)	5.16	11.60	4.43
	30.28	29.08	21.14

[a]FSR = $M_D/\sum(M_c)$: M_D = Metal-metal distance, M_c= Covalent Radii [151]

Analogous metallations with group 9 starting materials were performed. Treatment of **6.3** and **6.4** with half an equivalent of $[MCl(COD)]_2$ (M = Rh, Ir) precursors afforded the heterobimetallic complexes $Cl_2M(\mu_2\text{-}NP)_3M'Cl$ (MM' = NbRh (**6.8**), NbIr (**6.9**), TaRh (**6.10**), TaIr (**6.11**)) in good yield. The structures of **6.8**-**6.11** are presented in Figure 6.6 and relevant bond lengths and angles can be found in Table 6.3. All four heterobimetallic compounds are isostructural, containing three phosphinopyrrolide ligands that bridge between the two metals, resulting in a P_3MCl square-pyramidal d^8 center and a d^0 octahedral group 5 center. Similar to the group 10 complexes, these species are diamagnetic and by ^{31}P NMR contain resonances of a doublet and triplet in a 2:1 ratio (NbIr: J_{PP} = 12.77 Hz and TaIr: J_{PP} = 12.66 Hz). In the case of Rh, a doublet of triplets and doublet of doublets is observed (TaRh: J_{PP} = 20.12 Hz, J_{RhP} = 140.91 Hz, 104.96 Hz and NbRh: J_{PP} = 19.63 Hz, J_{RhP} = 144.14, 105.82 Hz) (Figure 6.5). All four complexes contain short metal-metal bond distances: (**6.8**) NbRh: 2.3649(3) Å (0.913), (**6.9**) NbIr: 2.3973(6) Å (0.921), (**6.10**)TaRh: 2.4238(5) Å (0.93), (**6.10**) TaIr: 2.4366(2) Å (0.936) consistent with the formation of a metal-metal bond.

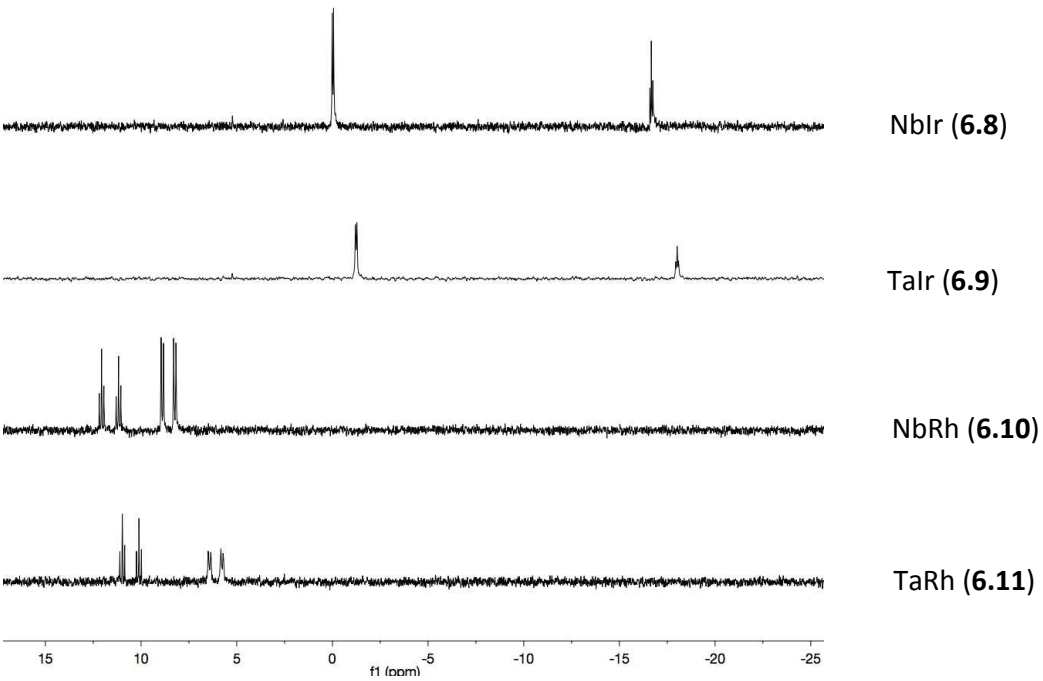

Figure 6.5: ^{31}P NMR of $Cl_2M(\mu_2\text{-}NP)_3M'Cl$ complexes (MM' = NbRh (**6.8**), NbIr (**6.9**), TaRh (**6.10**), TaIr (**6.11**)).

Table 6.3. Relevant bond lengths (Å) and angles (°) for **6.8-6.11**.

	6.8 NbRh	**6.9 NbIr**	**6.10 TaRh**	**6.11 TaIr**
M-M (Å)	2.3649(3)	2.3973(6)	2.4238(5)	2.4366(2)
FSR[a]	0.913	0.921	0.936	0.936
M-P (Å)	2.3286(8)	2.319(1)	2.346(2)	2.362(2)
	2.3808(6)	2.375(2)	2.302(1)	2.402(1)
	2.4276(9)	2.420(2)	2.406(2)	2.305(1)
P-M-P (°)	94.55	92.45	91.84	91.95
	92.62	94.12	92.81	93.56
M-N (Å)	2.135(2)	2.151(5)	2.141(4)	2.136(4)
	2.153(3)	2.144(7)	2.128(3)	2.128(3)
	2.124(2)	2.142(7)	2.108(5)	2.142(3)
Group 5 - Cl (Å)	2.3624(8)[b]	2.368(1)[b]	2.356(1)[b]	2.370(1)[b]
	2.4442(7)	2.432(2)	2.408(2)	2.408(1)
Group 9 - Cl (Å)	2.3209(8)	2.334(2)	2.320(1)	2.338(1)
Torsional Angle (P-	25.52	18.82	25.64	19.69
M-M-N) (°)	21.86	25.05	25.62	22.49
	19.16	26.08	26.61	23.74

[a]FSR = $M_D/\sum(M_c)$: M_D = Metal-metal distance, M_c= Covalent Radii [151]. [b]Equitorial chloride.

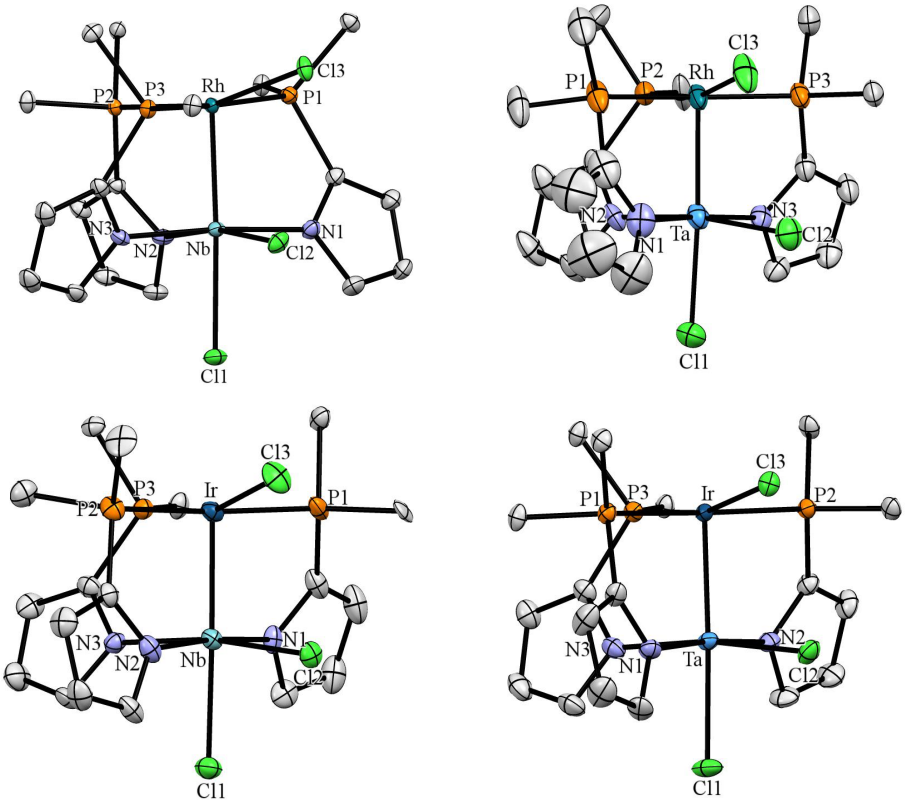

Figure 6.6. 50% thermal ellipsoid drawings of **6.8** (top left), **6.9** (top right), **6.10** (bottom left), and **6.11** (bottom right**)**. Hydrogen atoms and solvent have been removed and phenyl groups have been truncated to the ipso carbon for clarity. Selected bond lengths and angles can be found in Table 6.3.

Heterobimetallic complexes containing cobalt were also targeted. Reaction of **6.4** with 0.5 equivalents of $Co_2(CO)_8$ resulted in the isolation of heterobimetallic complex $[ClTa(\mu_2\text{-}NP)_3Co(CO)]_2$ (**6.12**). In complex **6.12** all three NP ligands bridge the metal centers resulting in a trigonal bipyramidal Co center and an octahedral Ta center. A single CO ligand remains bound to Co. Complex **6.12** exists as a dimer in the solid state, where the equatorial Cl bridges to the vacant axial site on an adjacent Ta center. This is borne out in the bond lengths where the axial Cl bond length is significantly longer (2.8529(6) Å vs. 2.4657(5) Å). **6.12** is d^{10} and diamagnetic, containing two resonances by ^{31}P in a 2:1 ratio, consistent with the crystal structure. The Ta-Co bond is short: 2.3451(3) Å (FSR = 0.938). Presumably, a transmetallation and electron transfer event

has occurred resulting in the formally d^1 Ta center. The Lu group has synthesized LVCo (L = N(*o*-(NCH_2P-$^iPr_2$)C_6H_4)$_3$) complexes in two oxidation states. Both the neutral LV(III)Co(0) and the cationic LV(III)Co(I) complexes contain short metal-metal bonds, 2.1234(4) Å (FSR = 0.89) and 1.9791(6) Å (FSR = 0.83), respectively [162]. Single crystal and computational analysis correlate to a double bond in the neutral and triple bond in the cationic complex. Based on these distances we ascribe **6.12** to contain a formal double bond.

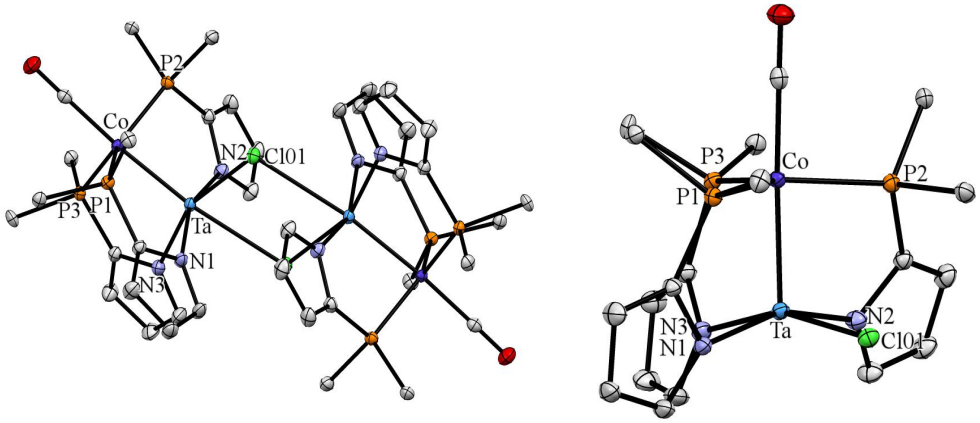

Figure 6.7. 50% thermal ellipsoid drawing of complex **6.12** in dimeric (left) and truncated form (right). Hydrogen atoms have been removed and phenyl groups have been truncated to the ipso carbon for clarity.

Next, we decided to probe the coordination chemistry of these complexes by simple L type ligand addition. Addition of 1 equivalent of CNR (R = 2,6 dimethylphenyl) to complexes **6.6, 6.7, 6.9** and **6.11** resulted in coordination of the isocyanide to the late TM center and formation of complexes **6.13-6.16** in quantitative yield *via* ^{31}P NMR (Scheme 6.3). For the group 10 complexes, **6.13** and **6.14,** two different geometries are observed. In the case of **6.13**, the isocyanide coordinates to Ni and induces a ligand rearrangement where one NP ligand has migrated to the Ta center giving (κ^2-NP)ClTa(μ_2-NP)$_2$(μ_2-Cl)Ni(CNR) (**6.13**). No ligand rearrangement is observed in the Pd congener giving Cl_2Ta(μ_2-NP)$_3$Pd(CNR) (**6.14**). This is similar to the group 4-Ni complexes, **3.6**, **3.7**, and **3.8**.

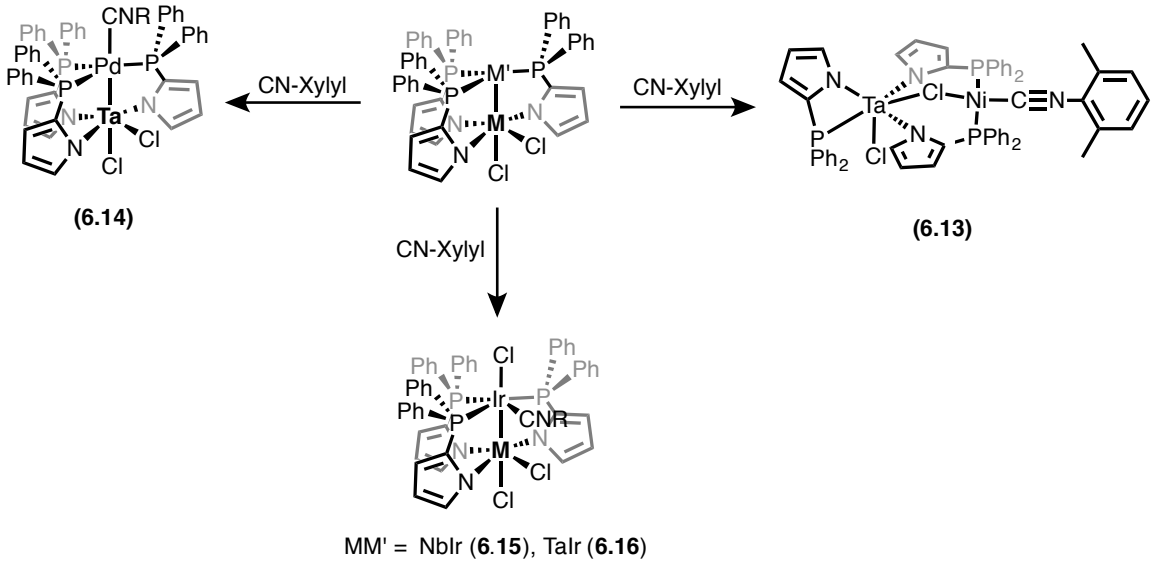

Scheme 6.3. Synthesis of isocyanide adducts of group 5 / group 9-10 bimetallic complexes.

Complex **6.13** consists of three isomers *via* ^{31}P NMR in a ~ 4:2:1 ratio: a doublet and triplet (J_{PP} = 9.03 Hz), three doublets of doublets (J_{PP} = 74.27, 24.98, and 2.65 Hz) and a doublet of doublets and two doublets (J_{PP} = 95.98 and 4.00 Hz), respectively (Figure 6.8). Each isomer contains a single resonance shifted upfield, consistent with a Ta bound phosphine. The nature of these closely related species is ambiguous but likely arises from twisting/canting of the NP ligands or the position of the Ta bound NP ligand and bridging chloride. The ^{31}P NMR of **6.14** consists of two broad peaks in a 2:1 ratio. The solid-state structures of **6.13** and **6.14** can be found in Figure 6.9 and relevant bond lengths and angles can be found in Table 6.5. The metal-metal bonds in **6.13** and **6.14** are slightly elongated compared to the parent bimetallics by ~0.24 Å to 2.5354(3) Å (FSR = 1.017) in **6.13** and by ~0.13 Å to 2.5509(6) Å (FSR = 0.973) in **6.14**. This contrasts with our previous reported group 4-Ni series where coordination of an axial ligand (CO or isocyanide) breaks apart the metal-metal bond. In the case of **6.13**, the short metal-metal distance is likely a function of the bridging chloride; however, **6.14** does not contain any bridging ligands. Additionally, **6.14** does not contain any first row metals, which are known to be more sensitive to changes in ligand environment. This is result of stronger metal-metal and weaker metal-ligand interactions [108].

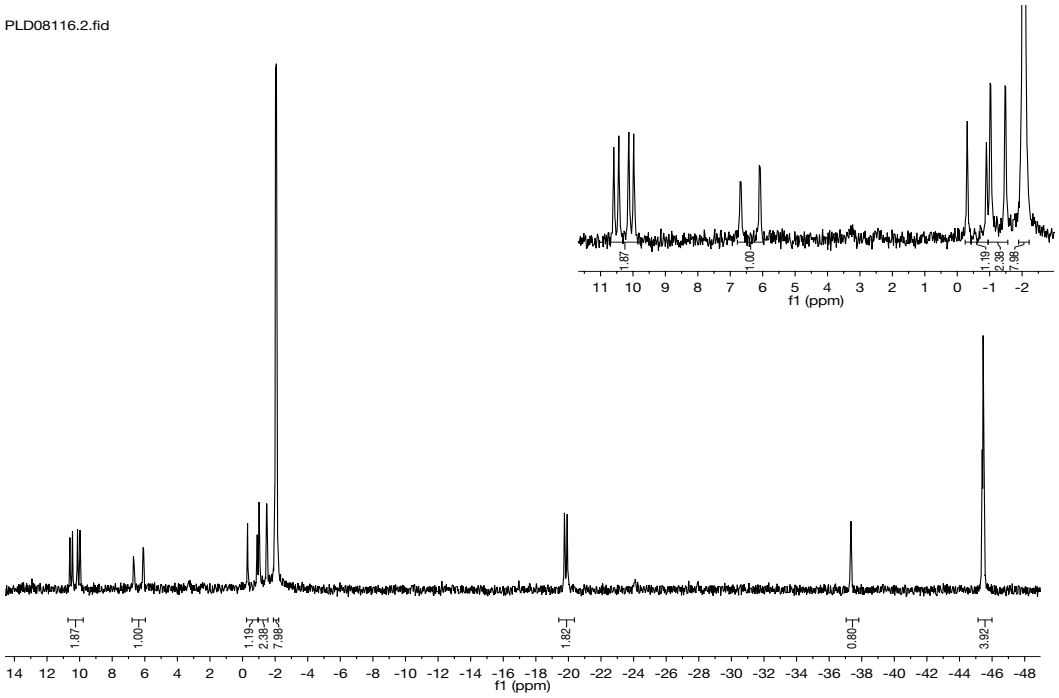

Figure 6.8: ^{31}P NMR of **6.13** showing three isomeric species.

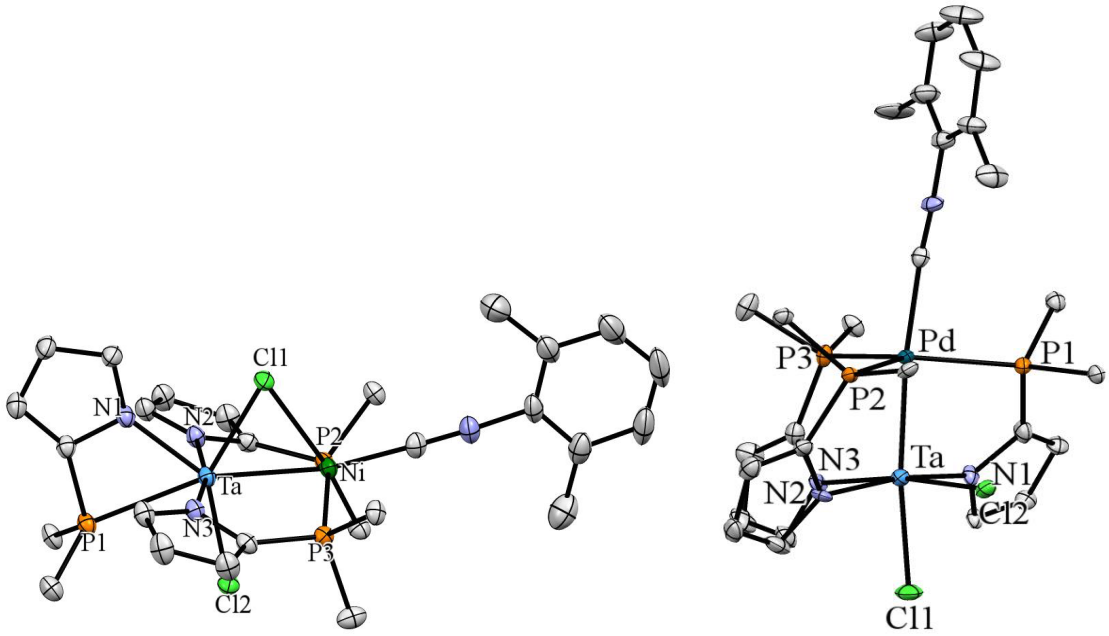

Figure 6.9: 50% thermal ellipsoid drawings of **6.13** (left) and **6.14** (right**)**. Hydrogen atoms and solvent have been removed and phenyl groups have been truncated to the ipso carbon for clarity. Selected bond lengths and angles can be found in Table 6.5.

For the group 9 complexes, equatorial coordination of CNXylyl is observed giving complexes $Cl_2M(\mu_2\text{-}NP)_3Ir(CNXylyl)Cl$ (MM' = NbIr (**6.15**) and TaIr (**6.16**)) (Scheme 6.3). These complexes are isostructural and diamagnetic. The ^{31}P NMR of both species consists of a broad resonance and triplet in a 2:1 ratio (NbIr: J_{PP} = 21.87 Hz, TaIr: J_{PP} = 21.52 Hz). Both peaks have shifted significantly upfield compared to the parent bimetallic. The solid-state structures of **6.15** and **6.16** can be found in Figure 6.10 and relevant bond lengths and angles can be found in Table 6.5. Surprisingly, the iridium bound chloride ligand has migrated to the axial position to allow the isocyanide to coordinate in the sterically crowded equatorial plane. Similar to **6.13** and **6.14,** the metal-metal bond lengths have increased in **6.15** by ~ 0.11 Å to 2.5064(3) Å (FSR = 0.963) and in **6.16** by ~ 0.095 Å to 2.5316(3) Å (FSR = 0.973).

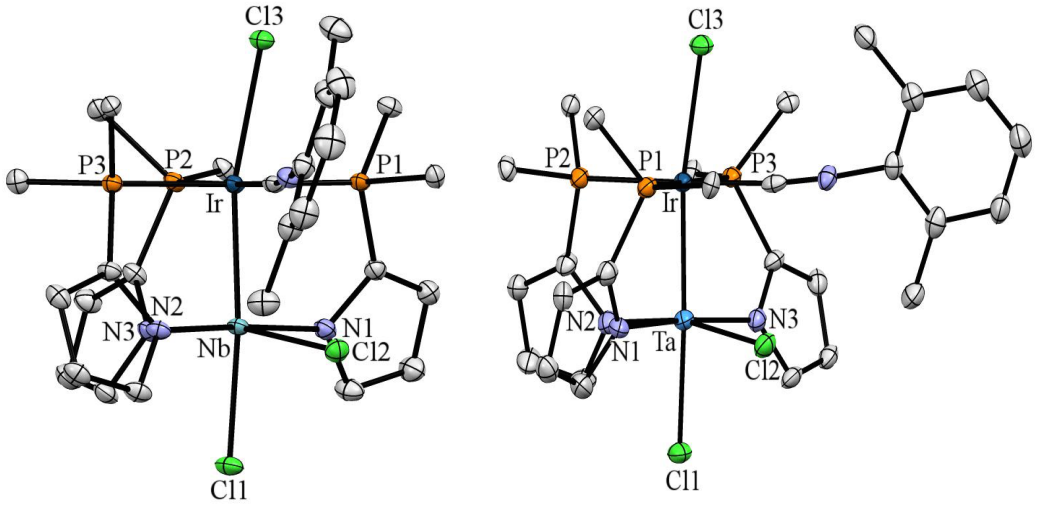

Figure 6.10: 50% thermal ellipsoid drawings of **6.15** (left) and **6.16** (right**)**. Hydrogen atoms and solvent have been removed and phenyl groups have been truncated to the ipso carbon for clarity. Selected bond lengths and angles can be found in Table 6.5.

Table 6.4. Relevant bond lengths (Å) and angles (°) for **6.13-6.16**.

	6.13 **TaNi(CNXylyl)**	**6.14** **TaPd(CNXylyl)[b]**	**6.15** **NbIr(CNXylyl)**	**6.16** **TaIr(CNXylyl)**
M-M(Å)	2.5354(3)	2.5509(6)	2.5064(3)	2.5316(3)
FSR[a]	1.017	0.973	0.963	0.973
P-M (Å)	2.2068(6)	2.390(2)	2.3852(8)	2.383(2)
	2.1917(7)	2.382(2)	2.3764(7)	2.372(1)
		2.379(2)	2.4210(7)	2.405(1)
P-M-P (°)	143.11	110.69	91.96	91.43
		112.02	94.62	95.25
		135.04		
M-N (Å)	2.101(2)	2.126(5)	2.134(3)	2.114(4)
	2.096(2)	2.132(5)	2.137(2)	2.133(6)
	2.149(2)	2.093(5)	2.146(3)	2.134(4)
M-Cl (Å)	2.4371(5)	2.363(1)[c]	2.3814(7)[c]	2.381(2)[c]
	2.4439(6)	2.434(2)	2.4551(9)	2.452(1)
M-Cl (Å)	2.3518(5)	-	2.6208(8)	2.609(1)
Torsional Angle (P-	20.32	31.13	21.17	24.05
M-M-N) (°)	20.59	7.10	21.07	17.65
		19.80	22.82	21.96
M-C (Å)	1.874(3)	2.164(6)	2.014(3)	2.006(7)
C-N (Å)	1.159(3)	1.176(8)	1.147(4)	1.150(9)

[a]FSR = $M_D/\sum(M_c)$: M_D = Metal-metal distance, M_c= Covalent Radii [151]. [b]Values given for one of two molecules in the asymmetric unit. [C]equatorial Cl.

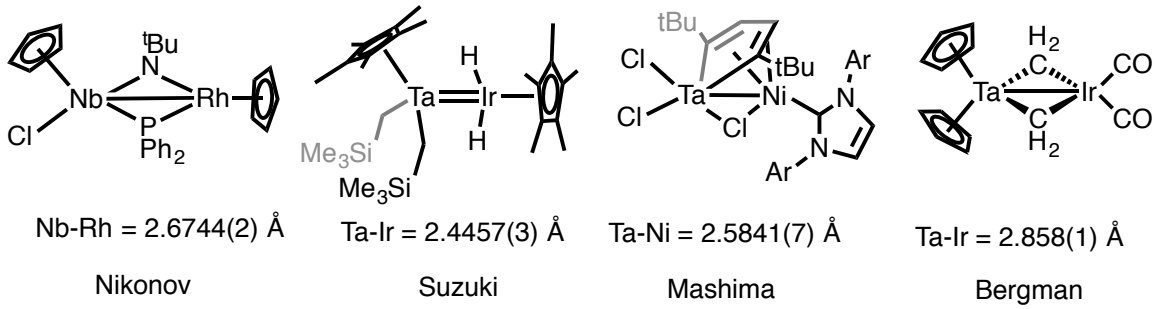

Figure 6.11: Selected example of bimetallic complexes containing group 5 metals.

A 2018 search of the CDC revealed a limited number of discrete bimetallic complexes containing Nb or Ta paired with group 9 or 10 metals [222]. There are no crystallographically characterized bimetallic complexes that contain the metal-metal pairings of NbPd or NbIr. Various research groups have utilized imidos, phosphides, methylenes, or metallocyclopentadienes to bridge the two transition metal centers together. Bergman has used methylene bridges derived from $Cp_2Ta(CH_2)(CH_3)$ to synthesize TaPd, TaCo, and TaIr complexes that feature two methylene bridges and metal-metal contacts that range from 2.7 Å to 2.8 Å depending on the metal pairing. The TaIr complexes have been utilized for ethylene hydrogenation and hydrosilylation chemistry [222-223, 233-235]. Mashima has reported TaNi, TaRh, and TaIr complexes derived from tantalocyclopentadienes, where the metallocycle π donates into the late metal center, which in turn has a dative interaction to Ta [224]. Nikonov linked Nb to Rh using imidos and phosphide bridges [228-229] and in an additional report linked Ta to Rh using phosphides [230] and investigated their reactivity for the hydrosilylation of acetophenone. Suzuki has published a number of TaIr complexes that feature unsupported metal-metal bonds. The parent complex was synthesized *via* salt metathesis and contains a short metal-metal bond: 2.4457(3) Å (FSR = 0.939). This distance is quite similar to the metal-metal distance in **6.11**, and DFT calculations show two bonding interactions.

In contrast to the above examples that contain Nb or Ta, much more work has been performed utilizing first row transition metals. The Lu group has synthesized a LVNi (L = $N(o\text{-}(NCH_2P\text{-}^iPr_2)C_6H_4)_3$) complex that contains a short metal-metal distance

[162]. The metal-metal bond in LVNi is 2.4873(14) Å (FSR = 1.05) and significantly longer than that of complex **6.6**, most likely stemming from the fact that Ta(V) is a stronger Lewis Acid than V(III). The Thomas group has synthesized a (XylylNP(^{i}Pr)$_2$)V(XylylNP(^{i}Pr)$_2$)$_2$NiI complex that has a metal-metal bond length of 2.6417(17) Å (FSR = 1.11) [160]. In this case, the presence of an axial iodide ligand most likely disrupts strong metal-metal bonding. The metal-metal bond length in complex **6.6** is more similar to our previously published group 4 – Ni series, (κ^2-NP)M(μ_2-NP)$_3$Ni (M = Ti, Zr, and Hf), that contain bond lengths of 2.2665(5) Å (FSR = 0.91), 2.3724(3) Å (FSR = 0.91) and 2.4123(6) Å (FSR = 0.93), respectively [163]. Comparison of **6.5** and **6.7** to (κ^2-NP)Ti(μ_2-NP)$_3$Pd (**3.9**) and Br(THF)Ti(μ_2-NP)$_3$Pd (**3.10**) also reveal similar bonding metrics. (κ^2-NP)Ti(μ_2-NP)$_3$Pd and BrTi(μ_2-NP)$_3$Pd contain bond lengths of 2.4317(5) Å (FSR = 0.89) and 2.4342(9) Å (FSR = 0.885), respectively.

The Thomas group has synthesized CrM (M = Rh and Ir) from Cr(^{i}PrNP(^{i}Pr)$_2$)$_3$ and [MCl(COD)]$_2$ (M = Rh, Ir), however these complexes undergo a metathesis event generating ClCr(^{i}PrNP(^{i}Pr)$_2$)$_2$M(^{i}PrNP(^{i}Pr)$_2$) (M = Rh, Ir) complexes that contain long metal-metal bonds (CrRh: 2.6095(3) Å (FSR = 1.07) and CrIr: 2.6064(4) Å (FSR = 1.06)) [226]. These complexes adopt boat shaped configurations similar to TiM (M = Ni, Pd, and Pt) species synthesized by the Nagashima group [60]. The Lu group has synthesized RhM (M = Al and Ga) complexes that contain dative Rh-M bonds (AlRh: 2.5400 Å (FSR = 0.97) and GaRh: 2.5003(7) Å (FSR = 0.95)) [209]. In these complexes the late TM chloride also resides above the square plane due to steric crowding. Perhaps the best comparison of complexes **6.7**-**6.11** is a TiRh complex supported by alkoxyphosphines synthesized by Wolczanski. Reduction of ClTi(OMe$_2$Ch$_2$PPh$_2$)$_3$RhCl resulted in the formation of trigonally symmetric Ti(OMe$_2$Ch$_2$PPh$_2$)$_3$Rh complex, which contains a short metal-metal bond, 2.2142(11) Å (FSR = 0.86) [83]. The bond in this formally Ti(III)Rh(0) complex is best described as a covalent σ bond with two dative π interactions from Rh to Ti.

Complexes **6.5-6.7** and **6.8-6.11** are two sets of isostructural complexes that contain similarly short metal-metal bonds (Table 6.4). These molecules are some of the

first examples of bimetallic complexes containing these metal-metal pairings, allowing for further evaluation of periodic effects on metal-metal bonding. Closer inspection of the bond lengths in complexes **6.5-6.7** and **6.8-6.11** reveals only minor trends: Nb forms slightly shorter bonds than Ta. Interestingly, changing from the 1st to 2nd row transition metal does not seem to affect the degree of bonding: TaNi and TaPd have similar FSRs. One might expect metals of the same row to have stronger bonds, however 4d-4d, 5d-4d and 4d-5d combinations all show similar metrics. Surprisingly, changing from group 9 to group 10 does not affect the degree of metal-metal bonding (TaCo/TiNi, NbPd/TaPd, and TaRh/TaIr all have similar FSRs). Examination of M-N, M-Cl, and M-P distances also reveals similar metrics. If stronger M-M bonds were present, a change in other bond metrics might be observed to compensate for the electronic differences.

These results contrast with observations from the Lu group, where their isostructural Cr-M (M = Mn, Fe, Co, and Ni) series shows a decrease in bond order across the periodic table. For example, the metal-metal distance in CrCo is, on average, 2.140 Å (FSR = 0.92) and CrNi is 2.4105(7) Å (FSR = 1.04) [108, 112, 133]. There are a number of possible explanations for this discrepancy. Higher d electron counts (CrCo is d^{12} and CrNi is d^{13}) can cause a decrease in bond order (all complexes in this work are d^{10} or d^8 so antibonding orbitals will never be populated). Another possible explanation is that π bonding might not be a significant contributor to the bonding in complexes **6.5-6.11**. This is similar to our group 4-10 series, where limited π bonding is present in the case of TiNi, but does not significantly affect the metal-metal distance [163]. If no π bonding is present, then each complex would only contain a metal-metal σ bond and similar effective bond orders would be expected. Lastly, since these complexes mostly consist of 4d and 5d metals, which contain larger orbitals that have better overlap and strong bonding interactions, the π bonding present may be less susceptible to change as the metal centers become more disparate, leading to similar effective bond orders.

Table 6.5. Metal-metal distances, Spin States, and FSRs of Heterobimetallic Complexes

Late TM	Compound	**Core**	**d e-count**	**D_{M-M}, (Å)**	**FSR**	**S**
Ni	$Cl_2Ta(\mu_2\text{-}NP)_3Ni$ **(6.6)**	$(TaNi)^{5+}$	10	2.2979(5)	0.922	0
	$(\kappa^2\text{-}NP)Hf(\mu_2\text{-}NP)_3Ni$ **(3.4)**	$(HfNi)^{4+}$	10	2.4123(6)	0.93	0
	$VNi(N(o\text{-}(NCH_2P\text{-}^iPr_2)C_6H_4)_3)$	$(VNi)^{3+}$	12	2.4873(14)	1.05	1
	$(XylylNP(^iPr)_2)V(XylylNP(^iPr)_2)_2NiI$	$(VNi)^{4+}$	11	2.6417(17)	1.11	1/2
	$TiNi(N(o\text{-}(NCH_2P\text{-}^iPr_2)C_6H_4)_3)$	$(TiNi)^{3+}$	11	2.4118(7)	0.98	1/2
Pd	$Cl_2Nb(\mu_2\text{-}NP)_3Pd$ **(6.5)**	$(NbPd)^{5+}$	10	2.4068(4)	0.919	0
	$Cl_2Ta(\mu_2\text{-}NP)_3Pd$ **(6.7)**	$(TaPd)^{5+}$	10	2.4189(6)	0.923	0
	$(\kappa^2\text{-}NP)Ti(\mu_2\text{-}NP)_3Pd$ **(3.9)**	$(TiPd)^{4+}$	10	2.4165(8)	0.885	0
	$Br(THF)Ti(\mu_2\text{-}NP)_3Pd$ **(3.10)**	$(TiPd)^{4+}$	10	2.4342(9)	0.891	0
	$[(\eta^3\text{-methallyl})Pd(Ph_2PN^tBu)_2TiCl_2]$	$(TiPd)^{6+}$	8	2.8155(5)	1.08	0
Rh	$Cl_2Nb(\mu_2\text{-}NP)_3RhCl$ **(6.8)**	$(NbRh)^{5+}$	8	2.3649(3)	0.913	0
	$Cl_2Ta(\mu_2\text{-}NP)_3RhCl$ (**6.10)**	$(TaRh)^{5+}$	8	2.4238(5)	0.936	0
	$Ti(OMe_2CH_2PPh_2)_3Rh$	$(TiRh)^{3+}$	10	2.2142(11)	0.86	0
	$ClCr(^iPrNP(iPr)_2)_2Rh(^iPrNP(^iPr)_2)$	$(CrRh)^{3+}$	11	2.6095(3)	1.07	3/2
	$GaRhCl(N(o\text{-}(NCH_2P\text{-}^iPr_2)C_6H_4)_3)$	$(GaRh)^{3+}$	8	2.5003(7)	0.95	0
Ir	$Cl_2Nb(\mu_2\text{-}NP)_3IrCl$ (**6.9)**	$(NbIr)^{5+}$	8	2.3973(6)	0.921	0
	$Cl_2Ta(\mu_2\text{-}NP)_3IrCl$ (**6.11)**	$(TaIr)^{5+}$	8	2.4366(2)	0.936	0
	$ClCr(^iPrNP(^iPr)_2)_2Ir(^iPrNP(^iPr)_2)$	$(CrIr)^{3+}$	11	2.6064(4)	1.06	3/2
Co	$[ClTa(\mu_2\text{-}NP)_3Co(CO)]_2$ (**6.12)**	$(TaCo)^{4+}$	10	2.3451(3)	0.938	0
	$CoV(N(o\text{-}(NCH_2P\text{-}^iPr_2)C_6H_4)_3)$	$(VCo)^{3+}$	11	2.1234(4)	0.89	1/2
	$[CoV(N(o\text{-}(NCH_2P\text{-}^iPr_2)C_6H_4)_3)][BPh_4]$	$(VCo)^{4+}$	10	1.9791(6)	0.83	0
	$(t\text{-}BuN{=})Ta(^iPrNPPh_2)_3CoI$	$(TaCo)^{6+}$	8	3.0388(3)	-	1

6.4 CONCLUSIONS

Synthesis of $M(NP)_4$ and $M(NP)_3Cl_2$ (M= Nb, Ta and NP = 2-diphenylphosphino pyrrolide) metalloligands complexes were achieved in good yields from $MCl_5(THF)$ starting materials. All monometallic complexes are 8-coordinate in the solid state with all ligands bound κ^2 to the metal center. Reaction with zero-valent group 10 starting materials resulted in complexes of the form $Cl_2M(NP)_3M$ (MM' = NbPd (**6.5**), TaNi (**6.6**), and TaPd (**6.7**)). While reaction with group 9 starting materials resulted in $Cl_2M(NP)_3M'Cl$ (MM' = NbRh (**6.8**), NbIr (**6.9**), TaRh (**6.10**), and TaIr (**6.11**)) complexes. All complexes reported are isostructural, diamagnetic, and contain short metal-metal distances (FSR < 1.00), resulting from dative, late-to-early metal-metal bonds. Surprisingly, all metal-metal combinations have similar FSRs, although Nb tends to form slightly shorter bonds than Ta. Addition of L type ligands (isocyanides) to TaNi (**6.13**), TaPd (**6.14**), NbIr (**6.15**), and TaIr (**6.16**) resulted in coordination to the late metal center and slightly elongated metal-metal bonds. In the case of TaNi ligand rearrangements are observed, while TaPd does not undergo any structural changes. NbIr and TaIr both bind the isocyanide in the equatorial plane of the Ir center.

6.5 EXPERIMENTAL CONSIDERATIONS

General Considerations and Instrumentation. All air- and moisture-sensitive compounds were manipulated in a glovebox under a nitrogen atmosphere. Solvents for air- and moisture-sensitive reactions were vacuum transferred from sodium benzophenone ketyl (THF, Et_2O, pentane, d_6-benzene and d_8-toluene) or predried by passing through activated alumina columns of a SG Water solvent purification system. $Ni(COD)_2$, KC_8, $TaCl_5(THF)$ and $NbCl_5(THF)$ were prepared according to literature procedure [167, 237-238]. $Co_2(CO)_8$, $Pd(P(^tBu)_3)_2$, $[Rh(COD)Cl]_2$, and $[Ir(COD)Cl]_2$ were purchased from Strem Chemicals and used without further purification. ^1H, ^{13}C and ^{31}P spectra were recorded on Varian INOVA 500 MHz or Bruker Avance III 400 MHz spectrometers. Chemical shifts are reported with respect to residual protio-solvent impurity for ^1H (*s*, 7.16 ppm for C_6D_5H), solvent carbons for ^{13}C (*t*, 128.39 ppm for C_6D_6), and PPh_3 for ^{31}P (*s*, -6 ppm for C_6D_6).

Synthesis of Nb((2-Ph_2P)C_4H_3N)$_4$, Nb(NP)$_4$ (6.1). Solid $NbCl_5$(THF) (84 mg, 0.245 mmol, 1 equiv) was dissolved in 5 mL benzene and Li(NP) (253 mg, 0.98 mmol, 4 equiv) and KC_8 (33 mg, 0.245 mmol, 1 equiv) were added as solids. The solution turns dark immediately and was allowed to stir for 30 minutes. Following this, the mixture was filtered over celite and volatiles were removed *in vacuo*. 85 mg (31 % yield) of crystalline **6.1** was grown by slow evaporation of pentane into a concentrated benzene solution of **6.1.** ^{1}H NMR (300MHz, C_6D_6) δ, ppm: 4.5 to 5.65 (br), 5.65 to 6.2 (br), 6.7 to 7.1 (br), 7.2 to 7.5 (br), 7.8 to 9.5 (br).

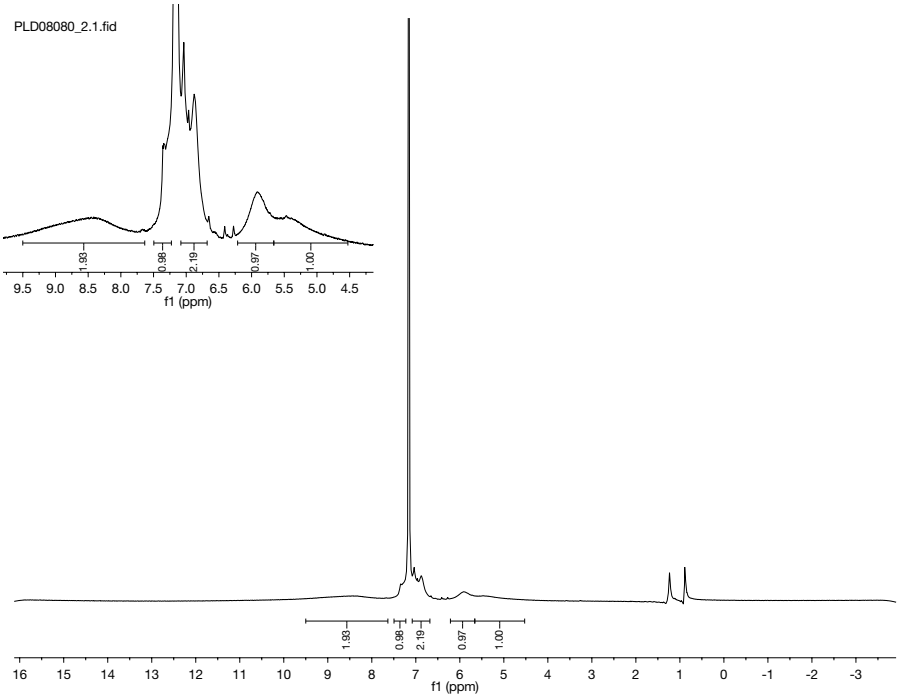

Figure 6.12: ^{1}H NMR of **6.1** in C_6D_6. Taken from PLD08080.

Synthesis of Ta((2-Ph_2P)C_4H_3N)$_4$, Ta(NP)$_4$ (6.2). Solid $TaCl_5$(THF) (76 mg, 0.176 mmol, 1 equiv) was dissolved in 5 mL benzene and Li(NP) (181 mg, 0.71 mmol, 4 equiv) and KC_8 (24 mg, 0.176 mmol, 1 equiv) were added as solids. The dark solution immediately was allowed to stir for 30 minutes. Following this, the mixture was filtered over celite and volatiles were removed *in vacuo*. Dark yellow single crystals of **6.2** were grown by slow evaporation of pentane into a concentrated benzene solution of **6.2**. ^{1}H NMR (300MHz, C_6D_6) δ, ppm: 5.8 to 6.1 (br), 6.2 to 6.45 (br), 6.85 to 7.15 (br), 7.3 to

7.7 (br), 7.8 to 8.1 (br), 8.5 to 9.0 (br).

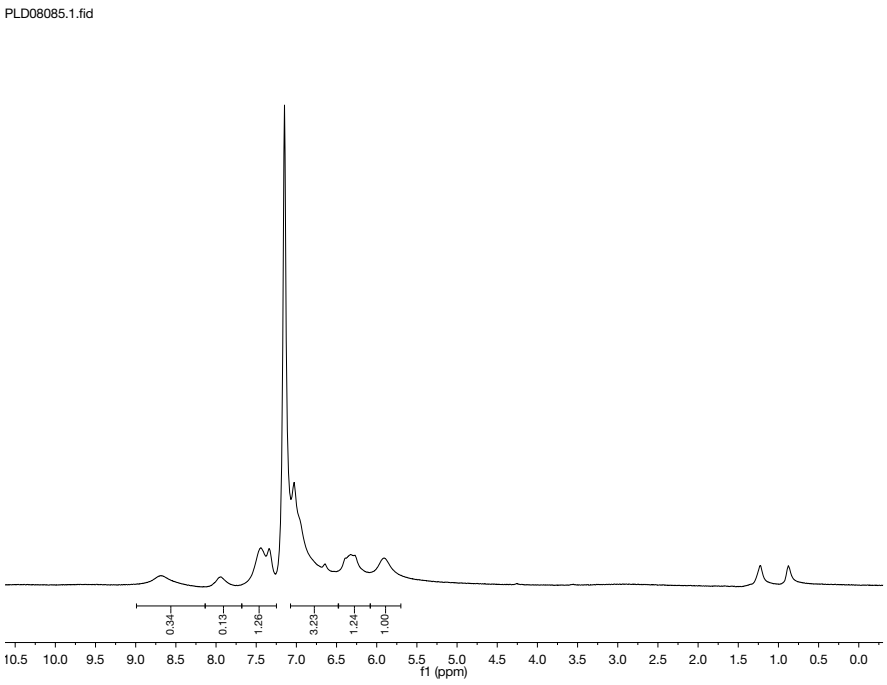

Figure 6.13: ^{1}H NMR of **6.2** in C_6D_6. Taken from PLD08085.

Synthesis of Nb((2-Ph$_2$P)C$_4$H$_3$N)$_3$Cl$_2$, Nb(NP)$_3$Cl$_2$ (6.3).

Solid $NbCl_5$(THF) (284 mg, 0.830 mmol, 1 equiv) was dissolved in 5 mL benzene and Li(NP) (640 mg, 2.49 mmol, 3 equiv) was added as a solid. The solution immediately turns a dark red and was allowed to stir for 30 minutes. The mixture was filtered over celite and volatiles were removed *in vacuo* to yield 660 mg of a dark red powder in 87% yield. Single crystals of **6.3** were grown by slow evaporation of pentane into a concentrated benzene solution of **6.3**. ^{1}H NMR (300MHz, C_6D_6) δ, ppm: 5.89-5.91 (br, 2H), 6.30-6.33 (br, 2H), 6.49-6.52 (br, 2H), 6.76-7.06 (m, 20H)), 7.23-7.24 (br, 1H), 7.33-7.36 (br, 1H), 7.54-7.58 (br, 4H), 7.68-7.79 (br, 8H), 8.46-8.54 (br, 1H). NMR (125 MHz, C_6D_6) d, ppm: 113.2 (br), ^{31}P NMR (121 MHz, C_6D_6) δ, ppm: -21.57 (s, 2P), -12.35 (s, 1P). Elemental Analysis: Calculated: C, 63.04; H, 4.30; N, 4.59. Found: C, 61.25; H, 4.43; N, 4.14.

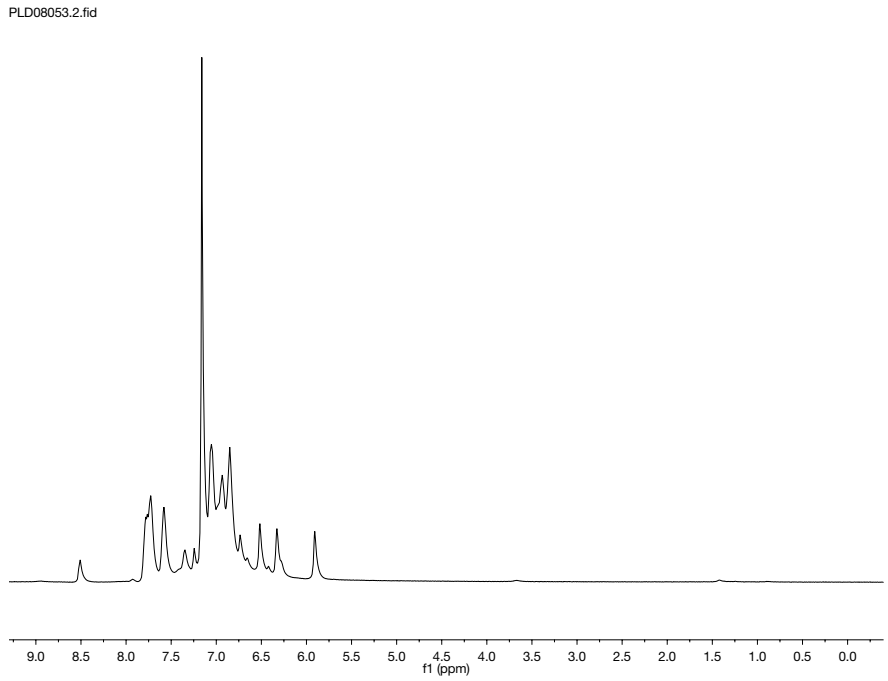

Figure 6.14: ^{1}H NMR of **6.3** in C_6D_6. Taken from PLD08053.

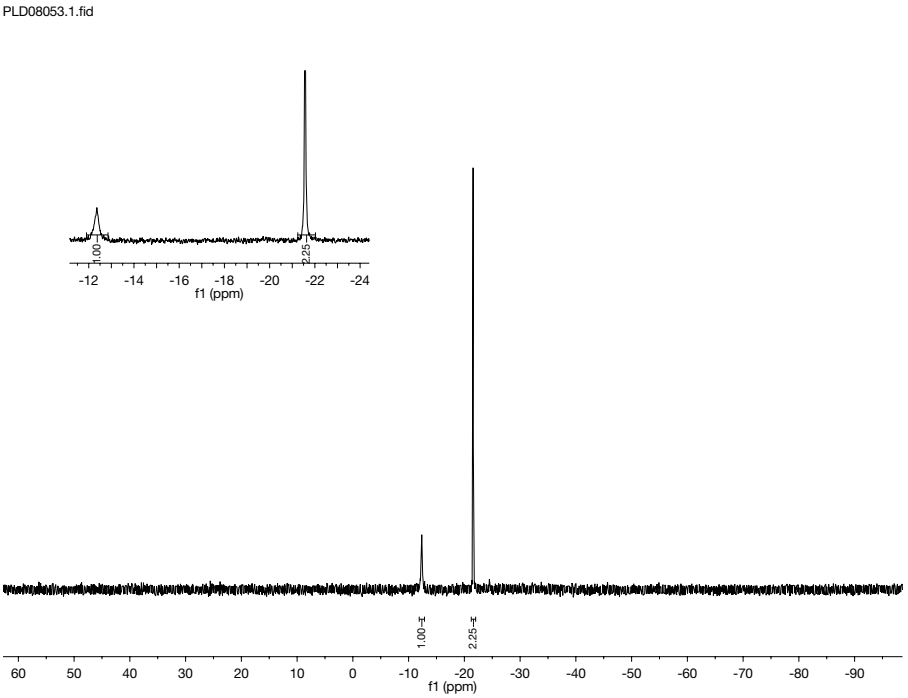

Figure 6.15: ^{31}P NMR of **6.3** in C_6D_6. Taken from PLD08053.

Synthesis of $Ta((2\text{-}Ph_2P)C_4H_3N)_3Cl_2$, $Ta(NP)_3Cl_2$ (6.4).

Solid $TaCl_5(THF)$ (287 mg, 0.667 mmol, 1 equiv) was dissolved in 5 mL benzene and Li(NP) (514 mg, 2.00 mmol, 3 equiv) was added as a solid. The solution immediately turns a yellow/orange and is allowed to stir for 30 minutes. The mixture is filtered over celite and volatiles were removed *in vacuo* to yield 621 mg of a yellow-orange powder in 93% yield. Single crystals of **6.4** were grown by slow evaporation of pentane into a concentrated benzene solution of **6.4**. ^{1}H NMR (300MHz, C_6D_6) δ, ppm: 5.95-5.99 (br, 2H), 6.33-6.38 (br, 2H), 6.50- 6.55 (br, 2H), 6.65-6.70 (br, 1H, aryl), 6.8 to 7.10 (br, 19H, aryl), 7.20-7.24 (br, 1H), 7.32-7.38 (br, 1H), 7.55-7.63 (br, 4H), 7.71-7.82 (br, 8H, aryl), 8.46-8.52 (br, 1H, aryl). ^{31}P NMR (121 MHz, C_6D_6) δ, ppm: -17.75 (s, 2P), -8.39 (s, 1P). Elemental Analysis: Calculated: C, 57.50; H, 3.92; N, 4.19. Satisfactory elemental analysis could not be obtained due to incomplete combustion.

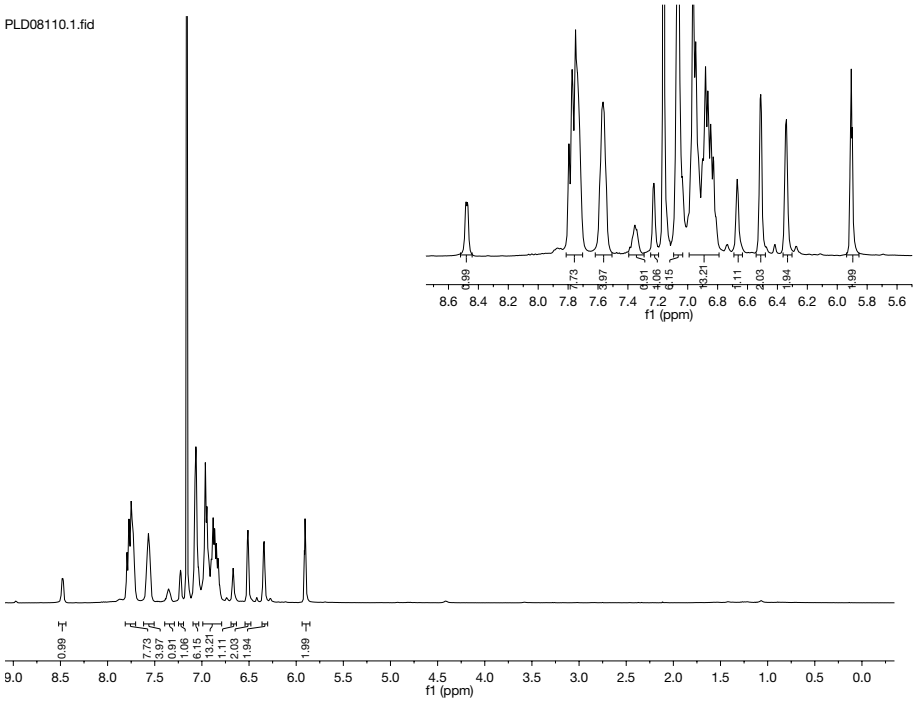

Figure 6.16: ^{1}H NMR of **6.4** in C_6D_6. Taken from PLD08110.

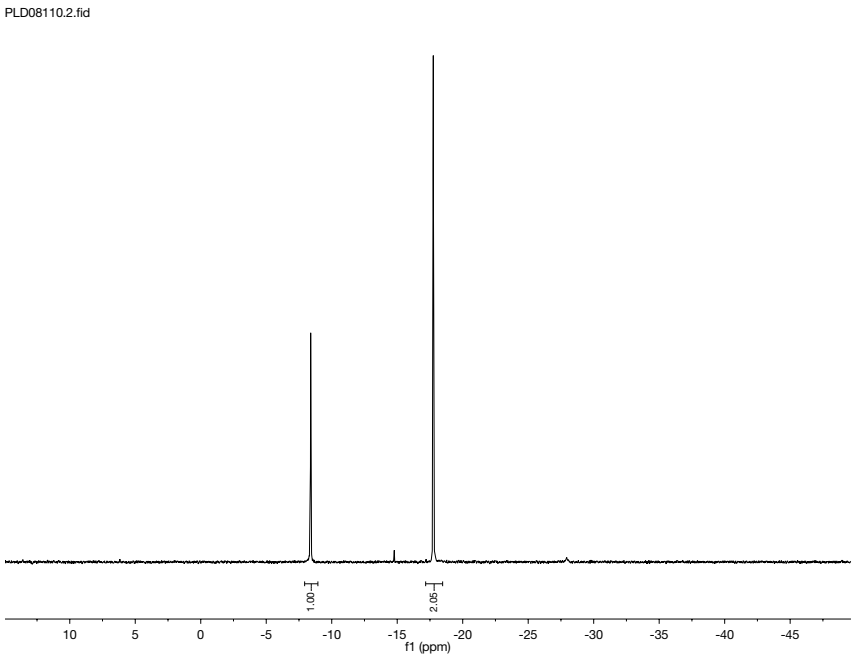

Figure 6.17: ^{31}P NMR of **6.4**. Taken from PLD08110.

Synthesis of Nb((2-Ph_2P)C_4H_3N)$_3Cl_2Pd$, Nb(NP)$_3Cl_2Pd$ (6.5).

Solid $NbCl_2NP_3$ (227 mg, 0.248 mmol, 1 equiv) was dissolved in 2.5 mL benzene and $Pd(P(tbu_3)_2$ (127 mg, 0.248 mmol, 1 equiv) was added. The solution was stirred for 30 minutes then 2.5 mL of THF was added. Single crystals of **6.5** were grown by slow evaporation of pentane into a concentrated 50:50 benzene/THF solution of **6.5.** However, examination of the bulk material revealed no detectable product *via* ^{31}P NMR. Therefore ^{1}H and ^{31}P NMR data cannot be provided at this time.

Synthesis of Ta((2-Ph_2P)C_4H_3N)$_3Cl_2Ni$, Ta(NP)$_3Cl_2Ni$ (6.6).

Solid $TaCl_2NP_3$ (300 mg, 0.299 mmol, 1 equiv) was dissolved in 4 mL benzene and $Ni(COD)_2$ (83 mg, 0.299 mmol, 1 equiv) was added. The solution was stirred for 30 minutes then reduced to half volume under vacuum and filtered over a fine frit to yield 240 mg of pure **6.6**, as a dark powder in 75% yield. Single crystals of **6.6** were grown by vapor diffusion of pentane into a concentrated 50:50 benzene/THF solution of **6.6**. ^{1}H NMR (300MHz, C_6D_6) δ, ppm: NMR. 6.3 to 7.15 (br, 22H), 7.60 to 7.95 (br, 3H), 8.1 to

8.3 (br, 1H), 8.6-9.3 (br, 1H). ^{31}P NMR (121 MHz, C_6D_6) δ, ppm: -14.2 to -12.0 (br, 1P), -8.5 to -7.0 (br, 2P).

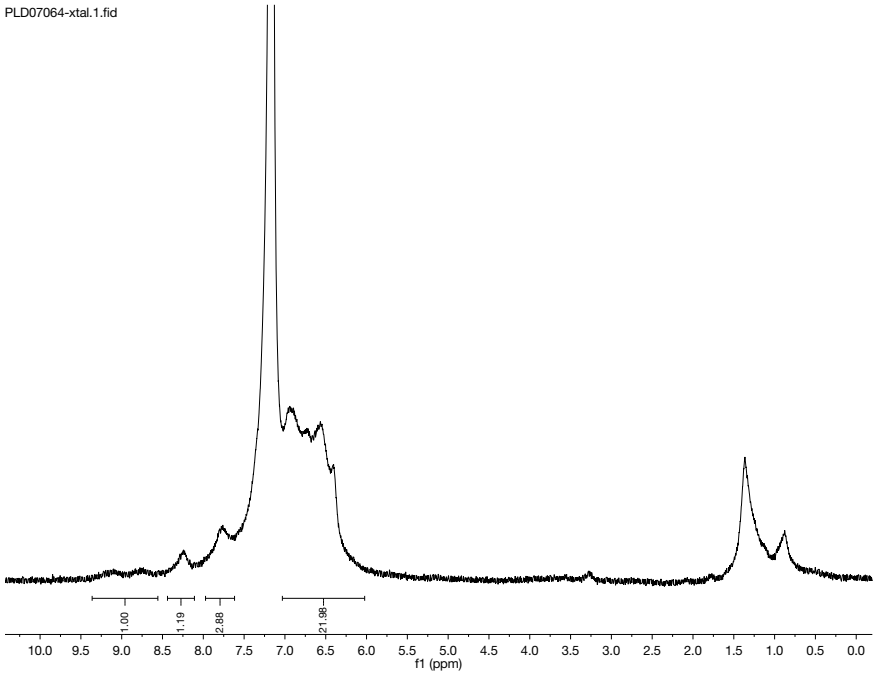

Figure 6.18: ^{1}H NMR of **6.6** in C_6D_6. Taken from PLD07064.

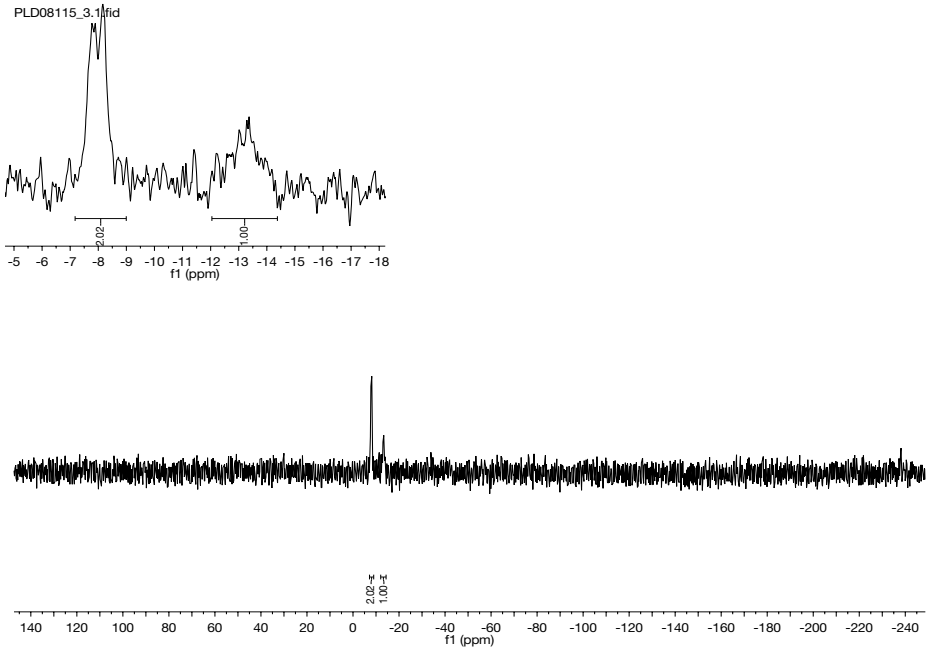

Figure 6.19: ^{31}P NMR of **6.6** in C_6D_6. Taken from PLD07064.

Synthesis of $Ta((2\text{-}Ph_2P)C_4H_3N)_3Cl_2Pd$, $Ta(NP)_3Cl_2Pd$ (6.7).

Solid $TaCl_2NP_3$ (207 mg, 0.206 mmol, 1 equiv) was dissolved in 2.5 mL benzene and $Pd(P(tbu_3)_2$ (105 mg, 0.206 mmol, 1 equiv) was added. The solution was stirred for 30 minutes then 2.5 mL of THF was added. **6.7** was isolated as a dark powder by slow evaporation of pentane into a concentrated 50:50 benzene/THF solution of crude **6.7**. The solution was filtered over a fine frit and washed with pentane and dried to give 125 mg (54% yield) of **6.7** as a dark powder. Single crystals were grown by slow evaporation of pentane into a concentrated benzene solution of **6.7**. ^{1}H NMR (300MHz, C_6D_6) δ, ppm: 6.05 (br, 2H), 6.18 (br, 2H), 6.29 (br, 2H), 6.65-7.10 (m, 30H), 7.55-7.65 (br, 4H), 7.77-7.83 (br, 2H), 8.52 – 8.56 (br, 1H). ^{31}P NMR (121 MHz, C_6D_6) δ, ppm: -6.48 (t, 1P, J_{PP} = 83.32), 2.84 (d, 2P, J_{PP} = 83.32). Elemental Analysis: Calculated: C, 51.98; H, 3.54; N, 3.79. Found: C, 52.58; H, 4.54; N, 3.59.

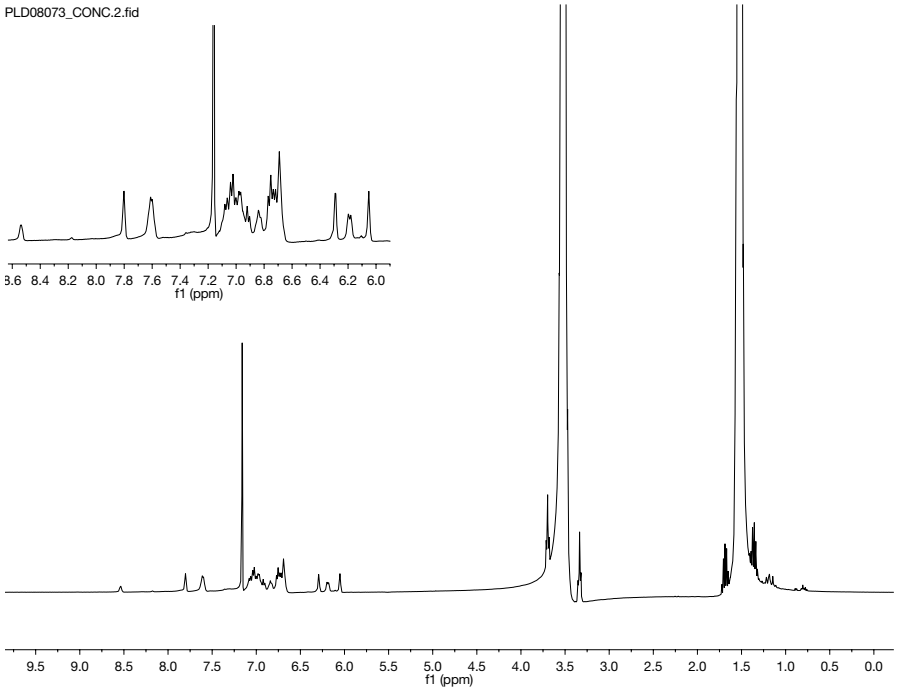

Figure 6.20: ^{1}H NMR of **6.7** in 50:50 THF/C_6D_6. Taken from PLD08073.

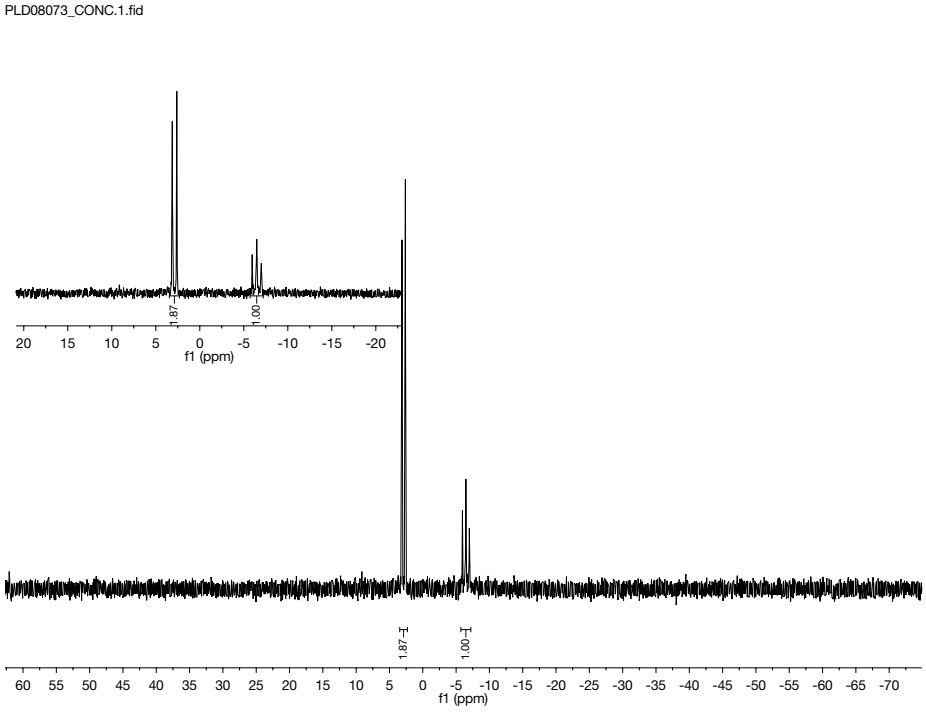

Figure 6.21: ^{31}P NMR of **6.7** in 50:50 THF/C_6D_6. Taken from PLD08073.

Synthesis of Nb((2-Ph$_2$P)C$_4$H$_3$N)$_3$Cl$_2$RhCl, Nb(NP)$_3$Cl$_2$RhCl (6.8).

Solid $NbCl_2NP_3$ (166 mg, 0.181 mmol, 1 equiv) was dissolved in 2.5 mL benzene and $[Rh(COD)Cl]_2$ (45 mg, 0.091 mmol, 1/2 equiv) was added. The solution was stirred for 30 minutes then 2.5 mL of THF was added. **6.8** was isolated as a powder by slow evaporation of pentane into a concentrated 50:50 benzene/THF solution of crude **6.8**. The solution was filtered over a fine frit and washed with pentane and dried to give 80 mg (42% yield) of **6.8** as a red/brown powder. Single crystals were grown by slow evaporation of pentane into a concentrated benzene solution of **6.8**. ^{1}H NMR (300MHz, C_6D_6) δ, ppm: 5.94-5.95 (s, 1H), 6.07-6.12 (3H, m), 6.32-6.33 (2H, m), 6.37-6.43 (4H, m), 6.56-6.59 (m, 4H), 6.64-6.68 (8H, m), 6.85-6.93 (m, 4h), 7.08-7.10 (6H, m), 7.66-7.70 (4H, m), 8.05-8.08 (s, 2H), 8.40-8.43 (m, 1H). ^{31}P NMR (121 MHz, C_6D_6) δ, ppm: 11.62 (dt, J_{PP} = 19.63 Hz, J_{RhP} = 144.14 Hz, 1P), 8.56 (dd, J_{PP} = 19.63, J_{RhP} = 105.82, 2P). Elemental Analysis: Calculated: C, 54.60; H, 4.01; N, 3.98. Satisfactory elemental analysis could not be obtained due to imcomplete combustion.

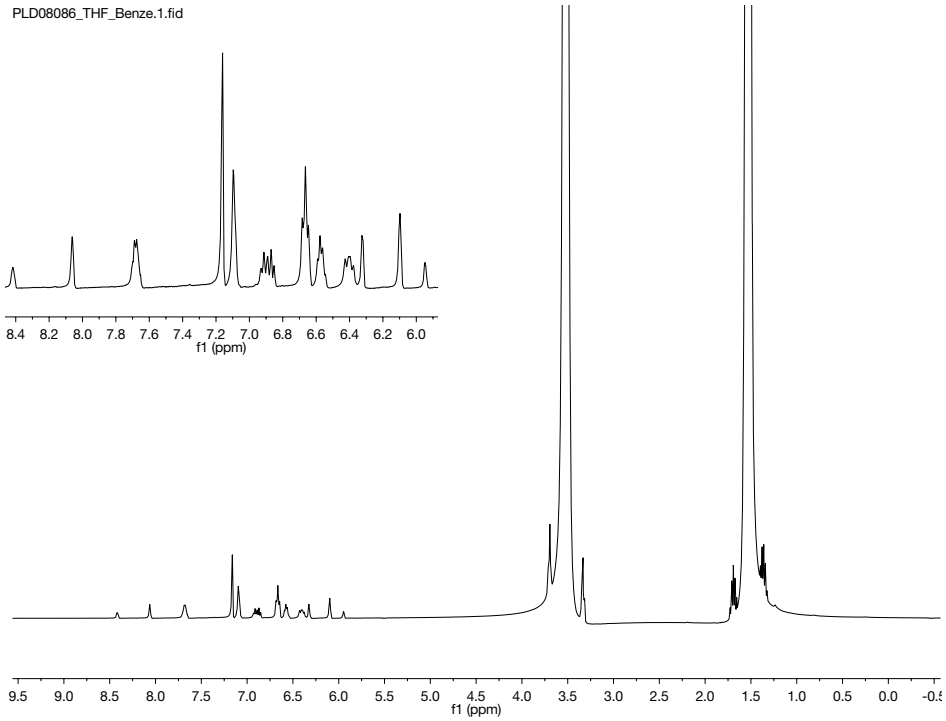

Figure 6.22: ^{1}H NMR of **6.8** in 50:50 THF/C_6D_6. Taken from PLD08086.

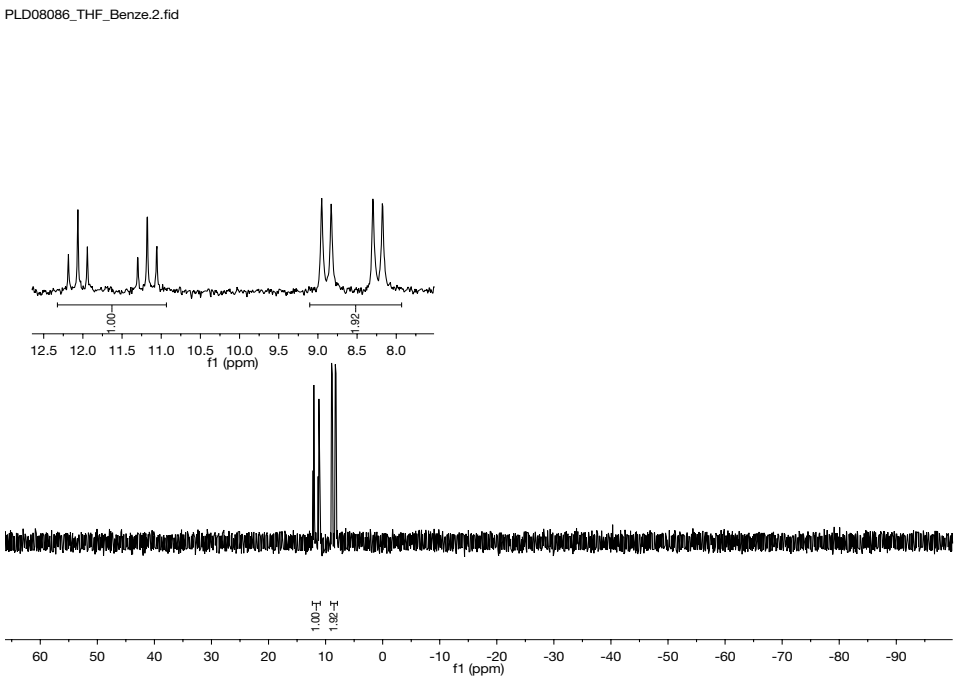

Figure 6.23: ^{31}P NMR of **6.8** in 50:50 THF/C_6D_6. Taken from PLD08086.

Synthesis of $Nb((2\text{-}Ph_2P)C_4H_3N)_3Cl_2IrCl$, $Nb(NP)_3Cl_2IrCl$ (6.9).

Solid $NbCl_2NP_3$ (210 mg, 0.228 mmol, 1 equiv) was dissolved in 2.5 mL benzene and $[Ir(COD)Cl]_2$ (77 mg, 0.114 mmol, 1/2 equiv) was added. The solution is allowed to stir for 30 minutes then 2.5 mL of THF was added. **6.9** was isolated as a powder by slow evaporation of pentane into a concentrated 50:50 benzene/THF solution of **6.9**. The solution was filtered over a fine frit and washed to pentane and dried to give 160 mg (61% yield) of **6.9**. Single crystals were grown by slow evaporation of pentane into a concentrated benzene solution of **6.9**. ^{1}H NMR (300MHz, C_6D_6) δ, ppm: 5.95 (m, 1H), 6.10-6.12 (m, 2H), 6.15-6.17 (m, 1H), 6.30-6.32 (m, 2H), 6.28-6.40 (br, 3H), 6.46-6.57 (br, 4H), 6.59-6.73 (br, 7H), 6.85-6.94 (m, 5H), 7.09-7.12 (m, 7H), 7.59-7.65 (m, 4H), 8.08-8.11 (m, 2H), 8.43-8.45 (m, 1H). ^{31}P NMR (121 MHz, C_6D_6) δ, ppm: -16.70 (t, J_{PP} = 12.77 Hz, 1P), -0.03 (d, J_{PP} = 12.77 Hz, 2P). Elemental Analysis: Calculated: C, 50.47; H, 3.44; N, 3.68. Found: C, 50.01; H, 3.57; N, 3.98.

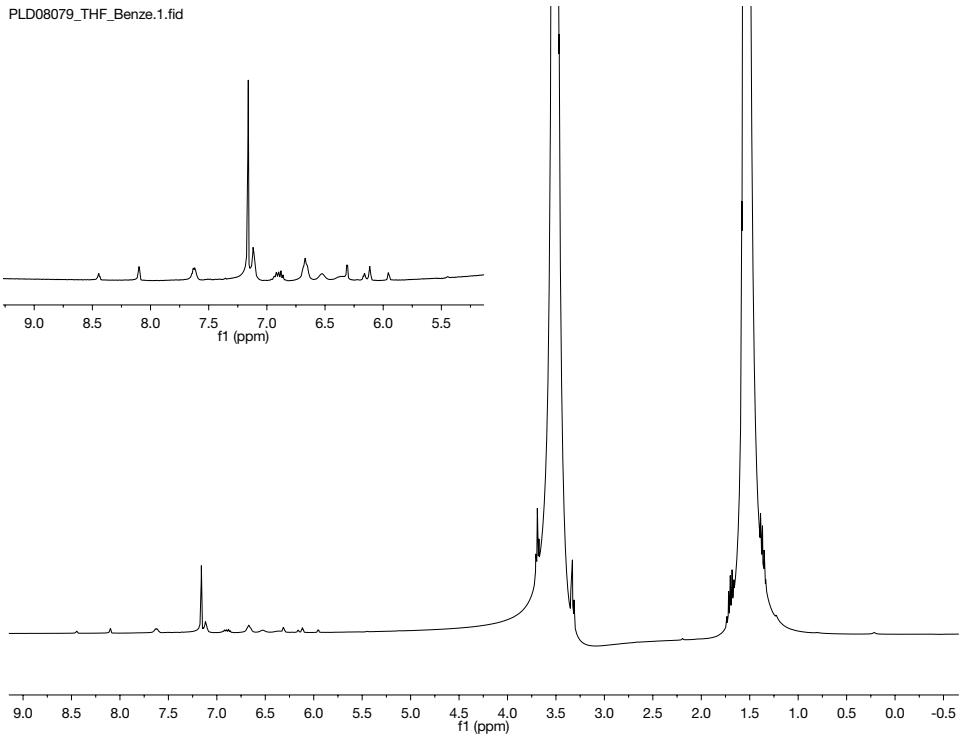

Figure 6.24: ^{1}H NMR of **6.9** in 50:50 THF/C_6D_6. Taken from PLD08079.

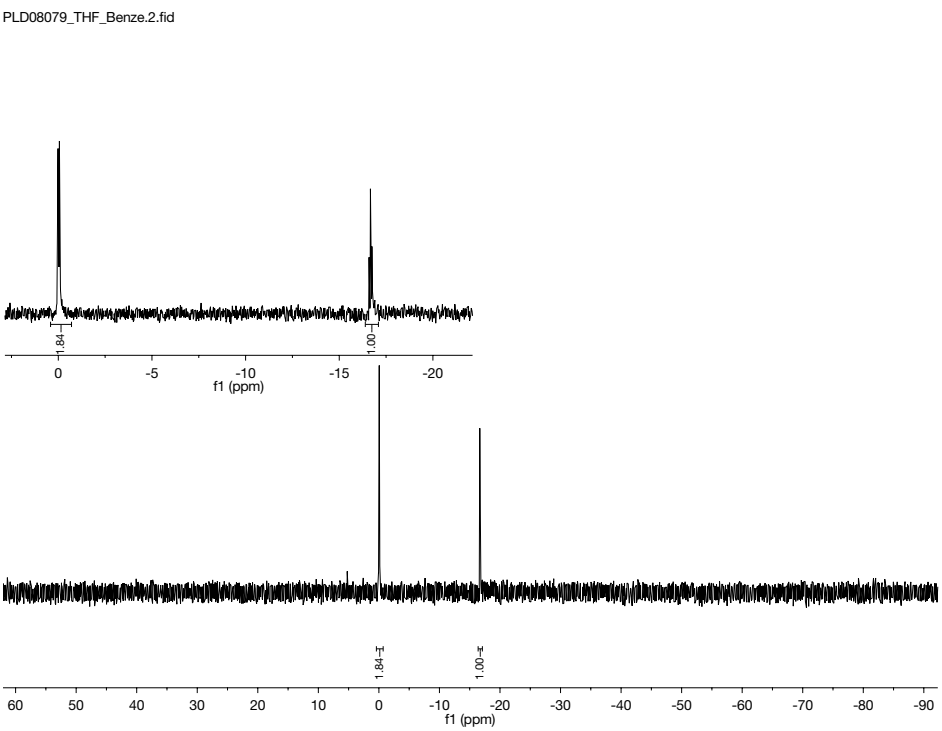

Figure 6.25: ^{31}P NMR of **6.9** in 50:50 THF/C_6D_6. Taken from PLD08079.

Synthesis of Ta((2-Ph_2P)C_4H_3N)$_3Cl_2RhCl$, Ta(NP)$_3Cl_2RhCl$ (6.10).

Solid $TaCl_2NP_3$ (147 mg, 0.146 mmol, 1 equiv) was dissolved in 5 mL benzene and $[Rh(COD)Cl]_2$ (36 mg, 0.073, 1/2 equiv) was added. The solution is allowed to stir for 30 minutes then 2.5 mL of THF was added. Single crystals were grown by slow evaporation of pentane into a concentrated 50:50 benzene/THF solution of crude **6.10.** The resulting yellow/orange crystals were washed to pentane and dried to give 160 mg (x % yield) of **6.10**. ^{1}H NMR (300MHz, C_6D_6) δ, ppm: 5.87-5.90 (s, 1H), 6.03-6.06 (br, 1H), 6.10-6.14 (br, 2H), 6.31-6.35 (br, 2H), 6.77-6.89 (br, 4H), 6.55-6.68 (br, 12H), 6.77-6.89 (m, 4H), 7.03-7.11 (br, 6H), 7.71-7.79 (br, 4H), 8.17-8.21 (br, 2H), 8.47-8.51 (br, 1H). ^{31}P NMR (121 MHz, C_6D_6) δ, ppm: 10.54 (dt, J_{PP} = 20.90, J_{RhP} = 140.37, 1P), 6.09 (dd, J_{PP} = 20.90, J_{RhP} = 105.78, 2P). Elemental Analysis: Calculated: C, 50.53; H, 3.45; N, 3.66. Found: C, 51.44; H, 4.26; N, 3.15.

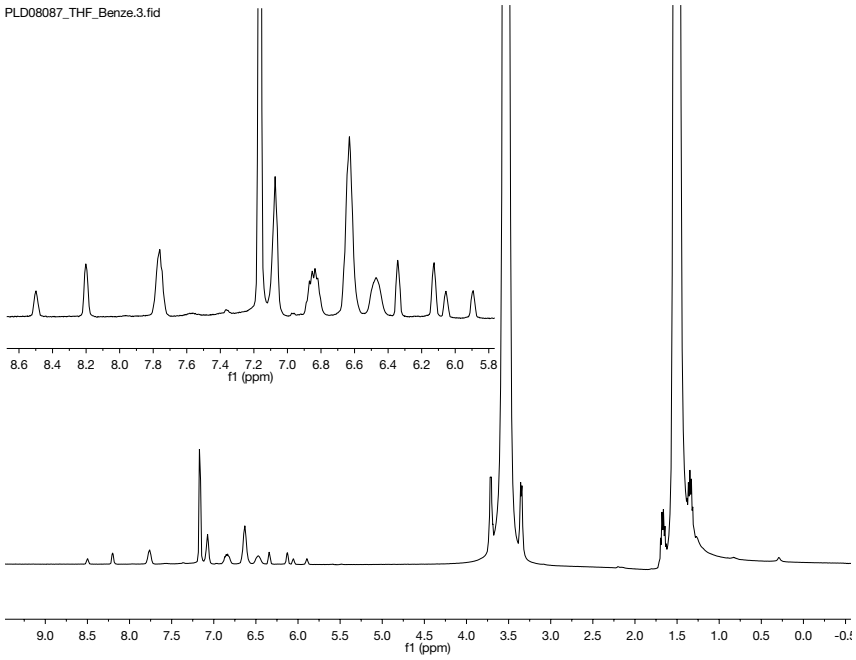

Figure 6.26: ^{1}H NMR of **6.10** in 50:50 THF/C_6D_6. Taken from PLD08087.

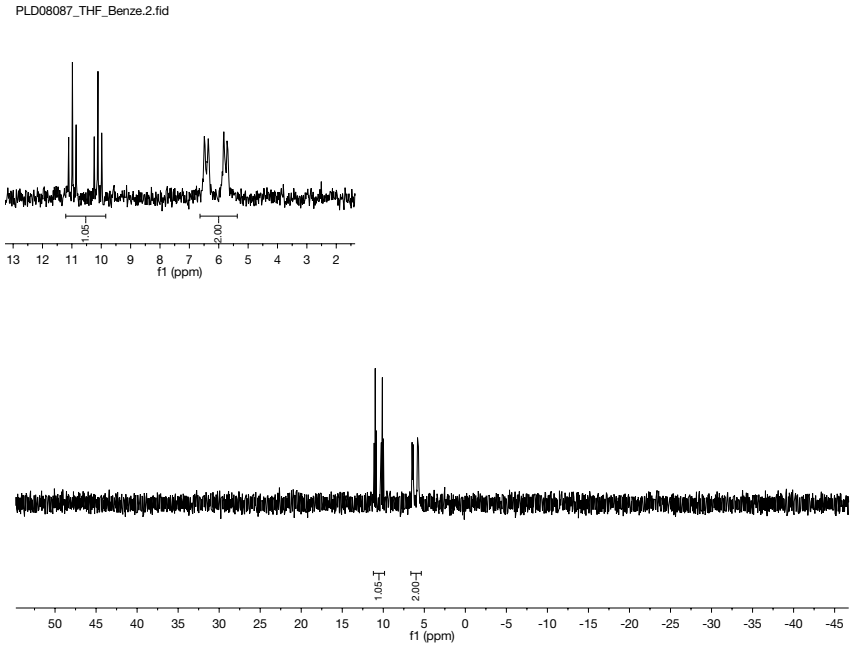

Figure 6.27: ^{31}P NMR of **6.10** in 50:50 THF/C_6D_6. Taken from PLD08087.

Synthesis of Ta((2-Ph_2P)C_4H_3N)$_3Cl_2IrCl$, Ta$(NP)_3Cl_2IrCl$ (6.11).

Solid $TaCl_2NP_3$ (181 mg, 0.180 mmol, 1 equiv) was dissolved in 2.5 mL benzene and $[Ir(COD)Cl]_2$ (60.5 mg, 0.090, 1/2 equiv) was added. The solution was allowed to stir for 30 minutes then 2.5 mL THF was added. Single crystals were grown by slow evaporation of pentane into a concentrated 50:50 benzene/THF solution of crude **6.11.** The resulting yellow/orange crystals were washed to pentane and dried to give 100 mg (45 % yield) of **6.11**. ^{1}H NMR (300MHz, C_6D_6) δ, ppm: 5.91 (m, 1H), 6.10-6.13 (br, 3H), 6.32 (m, 2H) 6.37-6.45 (br, 3H), 6.51-6.60 (br, 4H), 6.70-6.60 (br, 8H), 6.84-6.92 (m, 5H), 7.08-7.13 (m, 7H), 7.64-7.69 (m, 4H), 8.19 (m, 2H), 8.49 (m, 1H). ^{31}P NMR (121 MHz, C_6D_6) δ, ppm: -1.25 (d, J_{pp} = 12.13 Hz, 2P), -18.03 (t, J_{pp} = 12.13, 1P). Elemental Analysis: Calculated: C, 46.86; H, 3.20; N, 3.42. Found: C, 48.62; H, 4.05; N, 2.75.

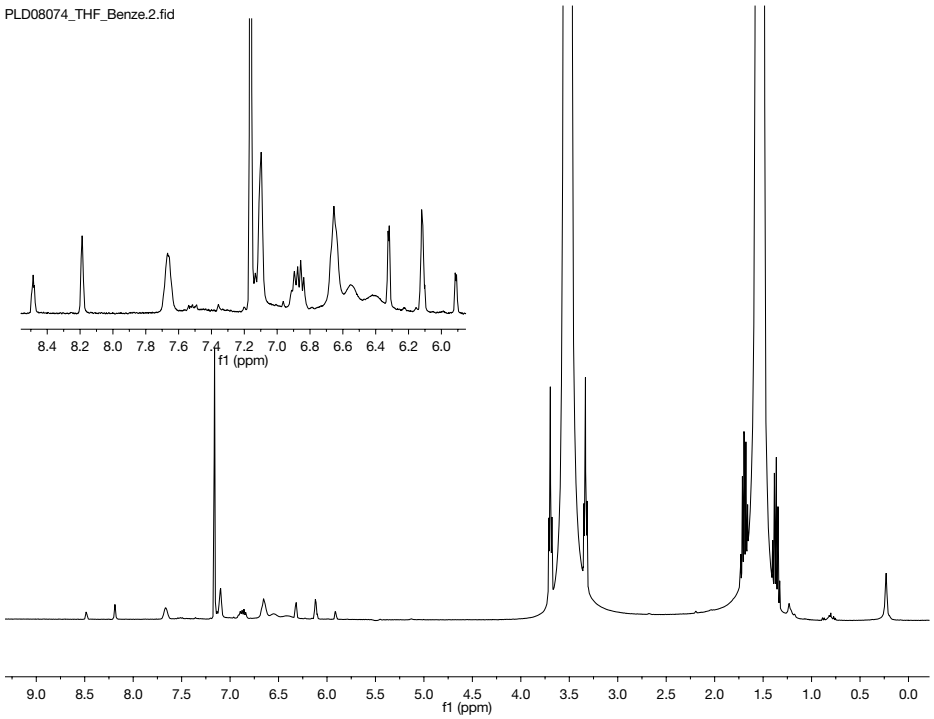

Figure 6.28: ^{1}H NMR of **6.11** in 50:50 THF/C_6D_6. Taken from PLD08074.

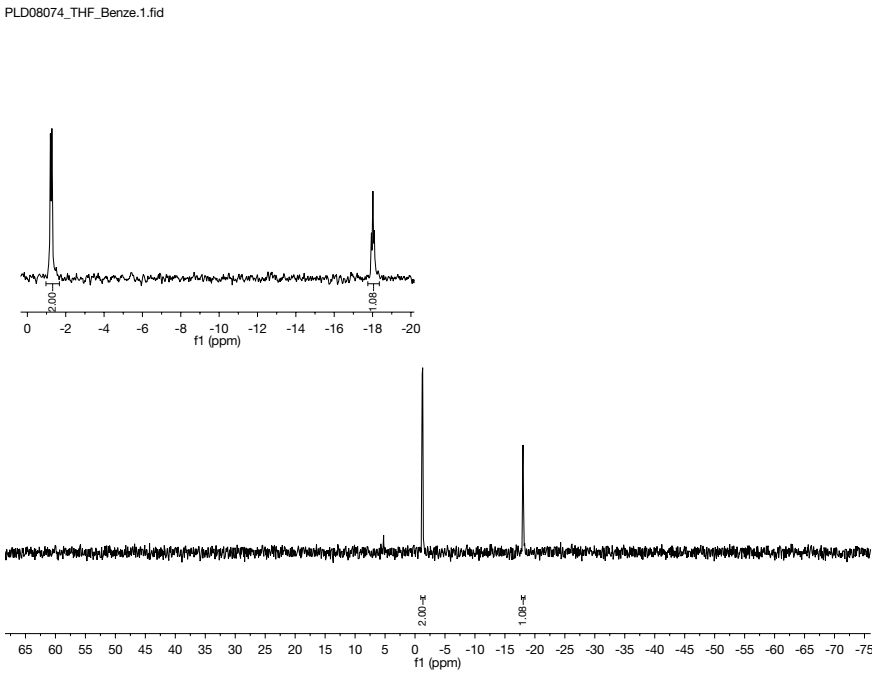

Figure 6.29: ^{31}P NMR of **6.11** in 50:50 THF/C_6D_6. Taken from PLD08074.

Synthesis of Ta((2-Ph_2P)C_4H_3N)$_3$ClCo, Ta(NP)$_3$ClCo (6.12).

Solid $TaCl_2NP_3$ (163 mg, 0.162 mmol, 1 equiv) was dissolved in 5 mL benzene and $Co_2(CO)_8$ (26 mg, 0.081 mmol, 1/2 equiv) was added. Single crystals were grown by slow evaporation of pentane into a concentrated benzene solution of crude **6.12**. Satisfactory ^{1}H data cannot be provded at this time. ^{31}P NMR (121 MHz, C_6D_6) δ, ppm: -17.88 (s, 2P), -8.50 (s, 1P).

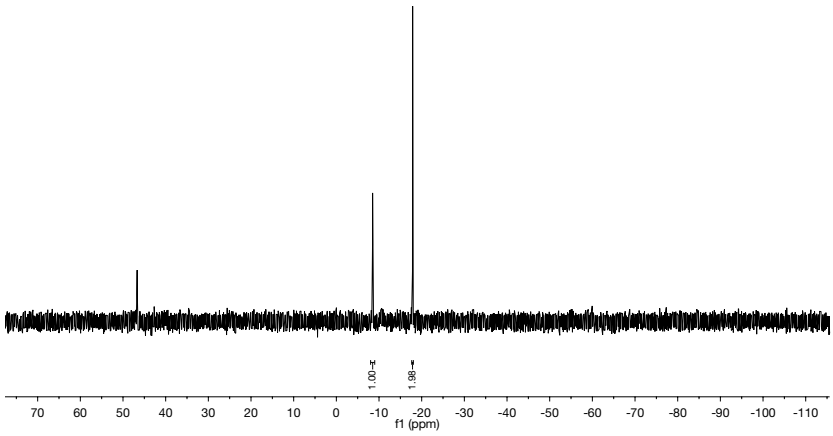

Figure 6.30: ^{31}P NMR of **6.12** in C_6D_6. Taken from PLD07092.

Synthesis of Ta((2-Ph_2P)C_4H_3N)$_3Cl_2$Ni(CN(C_8H_9), Cl_2Ta(NP)$_3$Ni(CNXylyl) (6.13).

Solid Cl_2Ta(NP)$_3$Ni (**6.6**) (20 mg, 0.018 mmol, 1 equiv) was dissolved in 1 mL of a 50:50 THF/C_6D_6 solution and xylyl isocyanide was added (2.5 mg, 0.018 mmol, 1 equiv) . The solution was layered with pentane and allowed to crystallize. The resulting crystals were washed with pentane and dried to give crystalline **6.13** (quantitative by NMR). ^{1}H NMR (300MHz, C6D6) δ, ppm: 5.40-5.60 (m, 7H), 5.60-5.70 (br, 1H), 5.80-5.95 (br, 12H), 5.95-6.05 (br, 1H), 6.20-7.10 (m, 148H), 7.20-8.10 (m, 79H), 8.40-8.60 (br, 5H), 8.86-8.98 (br, 1H), 9.18-9.30 (br, 3H). ^{31}P NMR (121 MHz, C6D6) δ, ppm: Species A: -45.45 (t, J_{PP} = 9.03 Hz, 1P), -2.05 (d, J_{PP} = 9.03 Hz, 2P). Species B: -37.33 (d, J_{PP} = 4.00 Hz, 1P), -0.59 (d, J_{pp} = 95.98 Hz, 1P), 6.39 (dd, J_{PP} = 95.98, 4.00 Hz, 1P). Species C: -19.84 (dd, J_{PP} = 25.38, 2.65 Hz, 1P), -1.26 (dd, J_{PP} = 74.37, 2.65 Hz, 1P), 10.28 (dd, J_{PP} = 74.37, 24.57 Hz, 1P).

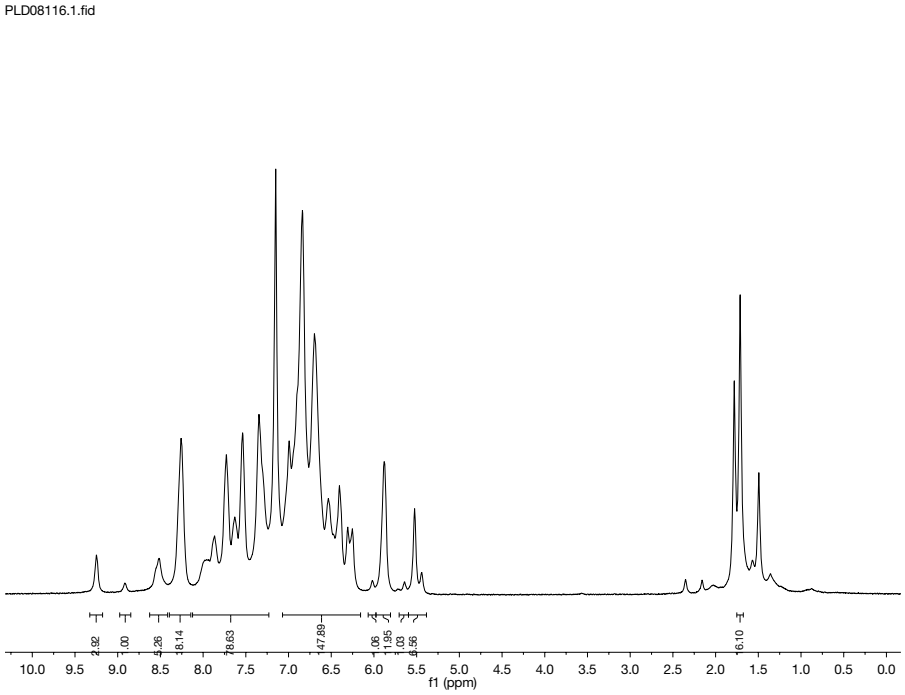

Figure 6.31: ^{1}H NMR of **6.13** in C_6D_6. Taken from PLD08116.

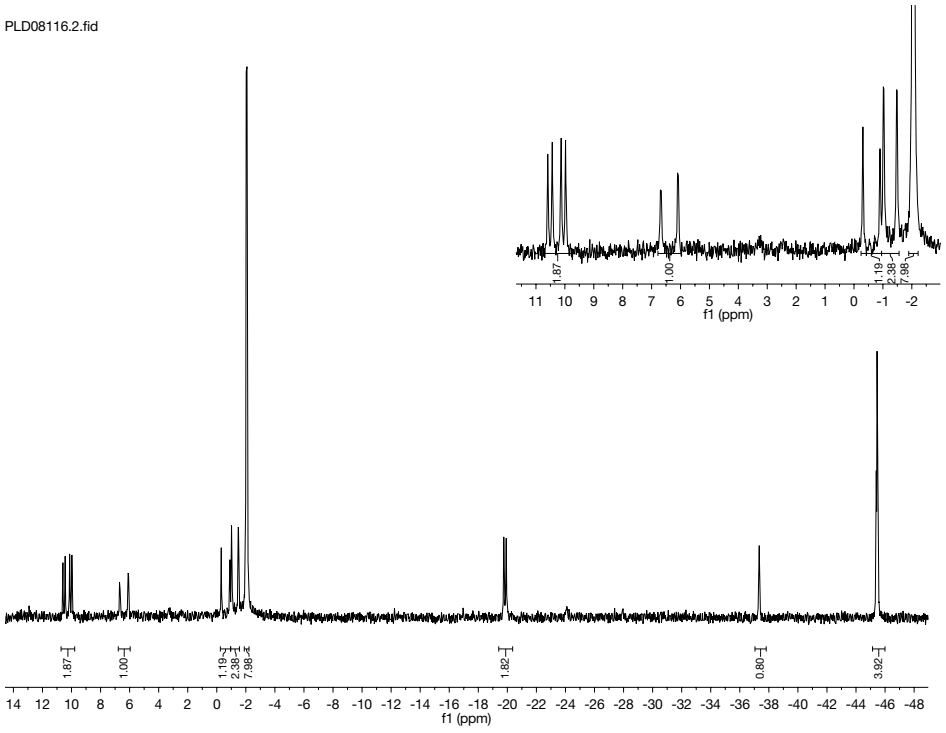

Figure 6.32: ^{31}P NMR of **6.13** in C_6D_6. Taken from PLD08116.

Synthesis of Ta((2-Ph_2P)C_4H_3N)$_3Cl_2$Pd(CN(C_8H_9), Cl_2Ta(NP)$_3$Pd(CNXylyl) (6.14).

Solid Cl_2Ta(NP)$_3$Pd (**6.7**) (20 mg, 0.018 mmol, 1 equiv) was dissolved in 1 mL of a 50:50 THF/C_6D_6 solution and xylyl isocyanide was added (2.36 mg, 0.018 mmol, 1 equiv) . The solution was layered with pentane and allowed to crystallize. The resulting crystals were washed with pentane and dried to give crystalline **6.14** (quantitative by NMR). Satisfactory ^{1}H data cannot be provided at this time. ^{31}P NMR (121 MHz, C_6D_6) δ, ppm: -6 to -4 (br, 2P), 9.66 (d, J_{PP} = 66.79 Hz, 2P).

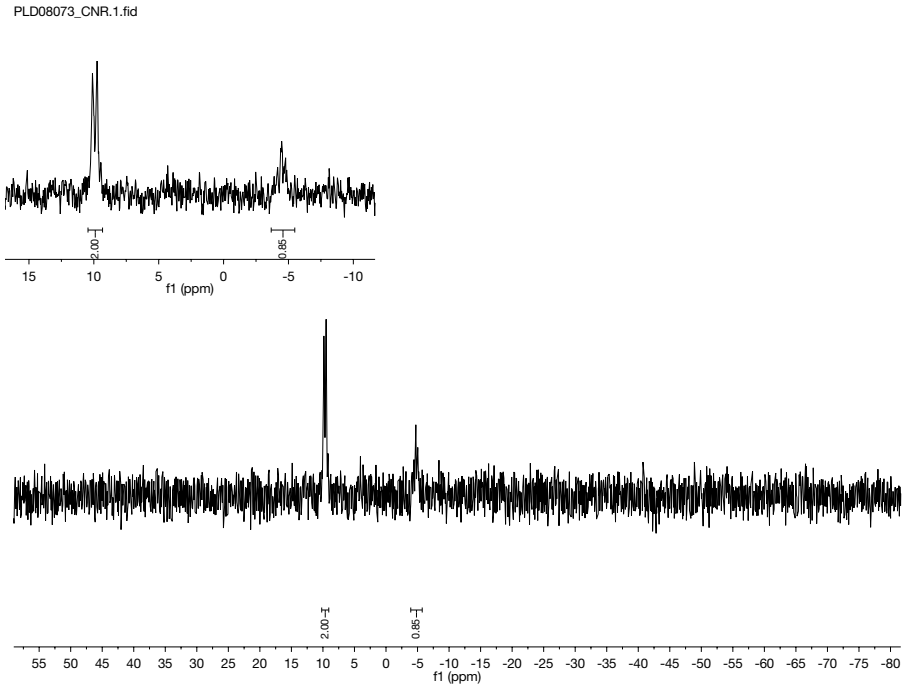

Figure 6.33: ^{31}P NMR of **6.14** in C_6D_6. Taken from PLD08073_CNR.

Synthesis of $Nb((2\text{-}Ph_2P)C_4H_3N)_3Cl_2IrCl(CN(C_8H_9))$, $Cl_2Nb(NP)_3IrCl(CNXylyl)$ (6.15).

Solid $Cl_2Nb(NP)_3IrCl$ (**6.9**) (20 mg, 0.0175 mmol, 1 equiv) was dissolved in 1 mL of a 50:50 THF/C_6D_6 solution and xylyl isocyanide was added (2.30 mg, 0.0175 mmol, 1 equiv). The solution was layered with pentane and allowed to crystallize. The resulting crystals were washed with pentane and dried to give crystalline **6.15** (quantitative by NMR). ^{1}H NMR (300MHz, C_6D_6) δ, ppm: 1.885 (s, 6H), 5.97-6.00 (m, 1H), 6.11-6.13 (m, 1H), 6.16-6.19 (m, 2H), 6.23-6.26 (m, 2H), 6.57-6.63 (m, 6H), 6.68-6.90 (m, 17H), 7.25-7.50 (br, 6H), 7.90-7.96 (m, 4H), 8.16-8.19 (m, 2H), 8.42-8.46 (m, 1H). ^{31}P NMR (121 MHz, C_6D_6) δ, ppm: -34.12 (t, J_{PP} = 21.87 Hz, 1P), -30.5 to -29 (br, 2P).

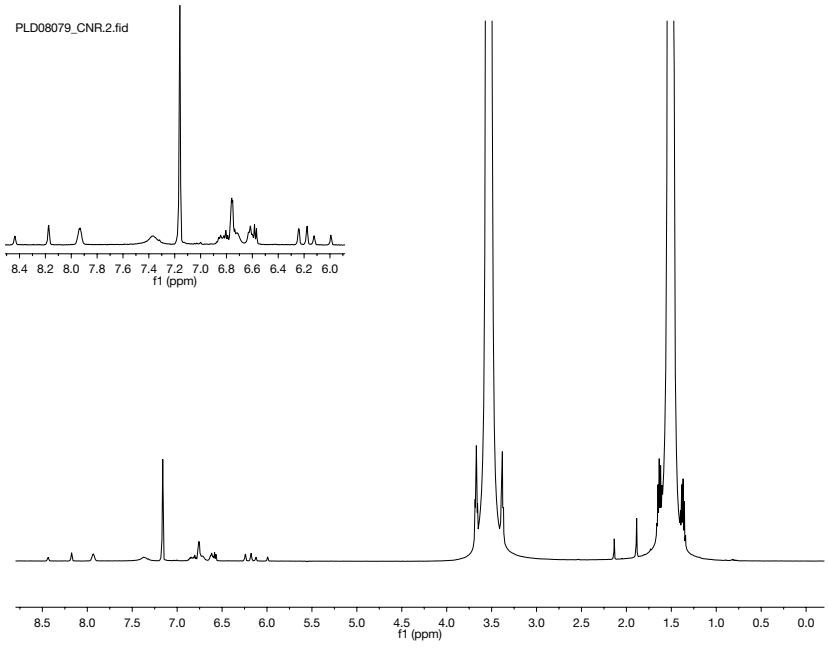

Figure 6.34: NMR of **6.15** in 50:50 THF/C_6D_6. Taken from PLD08079_CNR.

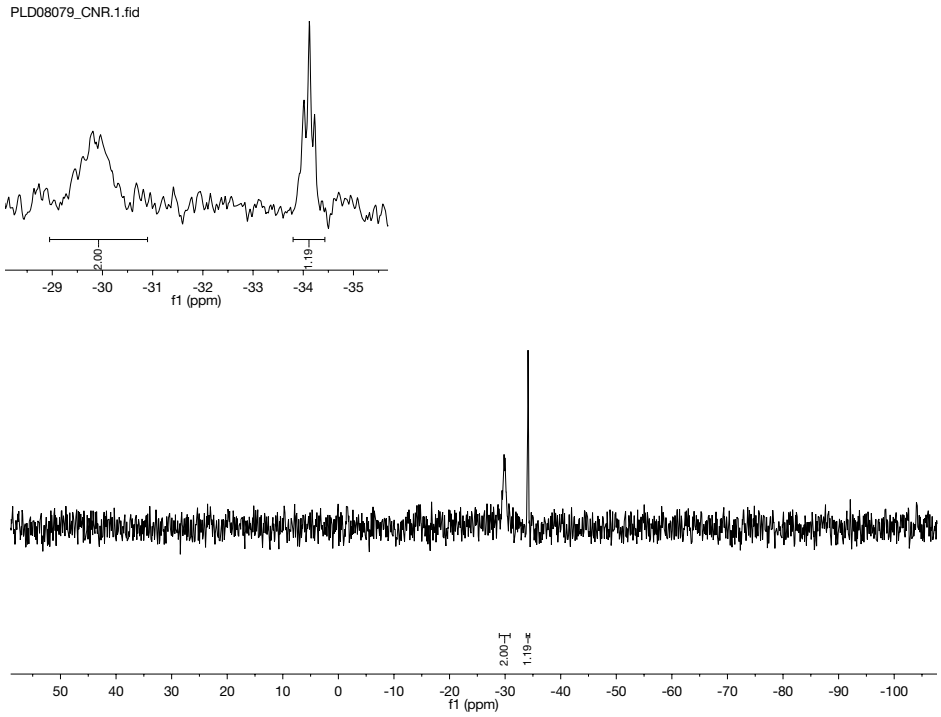

Figure 6.35: ^{31}P NMR of **6.15** in 50:50 THF/C_6D_6. Taken from PLD07079_CNR.

Synthesis of Ta((2-Ph_2P)$C_4H_3N)_3Cl_2$IrCl(CN(C_8H_9), Cl_2Ta(NP)$_3$IrCl(CNMesityl) (6.16). Solid Cl_2Ta(NP)$_3$IrCl (**6.11**) (20 mg, 0.016 mmol, 1 equiv) was dissolved in 1 mL of a 50:50 THF/C_6D_6 solution and xylyl isocyanide was added (2.13 mg, 0.016 mmol, 1 equiv). The solution was layered with pentane and allowed to crystallize. The resulting crystals were washed with pentane and dried to give crystalline **6.16** (quantitative by NMR). ^{1}H NMR (300MHz, C_6D_6) δ, ppm: 1.85 (s, 6H), 6.01-6.03 (m, 1H), 6.11-6.15 (m, 3H), 6.18-6.21 (m, 2H), 6.57-6.60 (m, 6H), 6.69-6.73 (m, 4H), 6.75-6.85 (m, 12H), 7.18-7.23 (br, 4H), 7.28-7.41 (br, 3H), 7.89-7.95 (m, 4H), 8.19-8.22 (m, 2H), 8.49-8.50 (m, 1H). ^{31}P NMR (121 MHz, C_6D_6) δ, ppm: -35.26 (t, J_{PP} = 21.54 Hz, 1P), -32.25 to -31.0 (br, 2P).

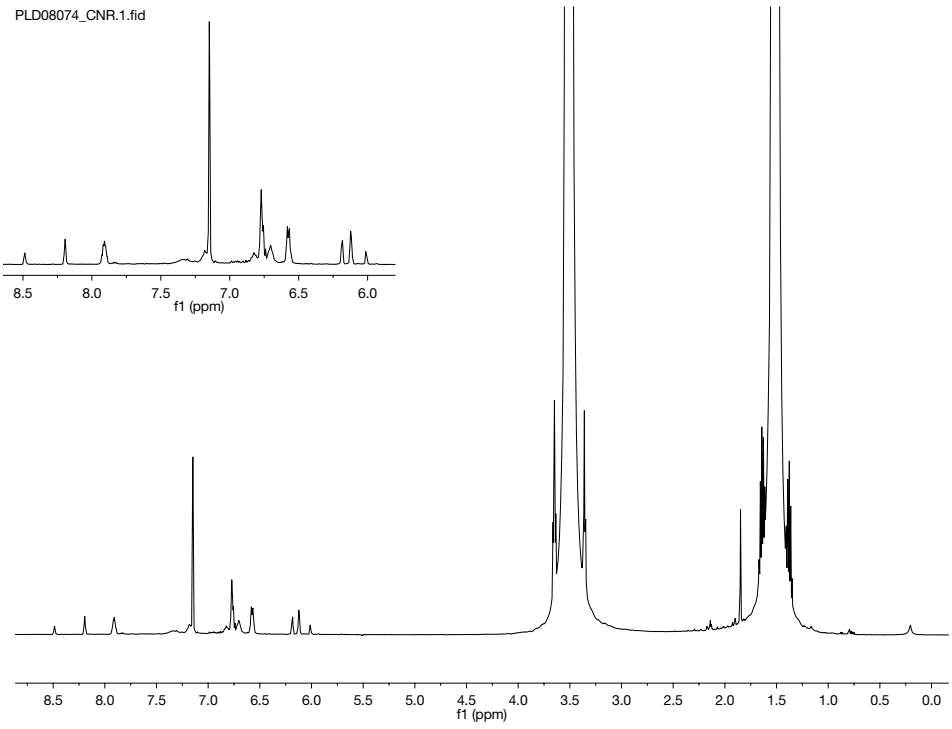

Figure 6.36: ^{1}H NMR of **6.16** in 50:50 THF/C_6D_6. Taken from PLD08074_CNR.

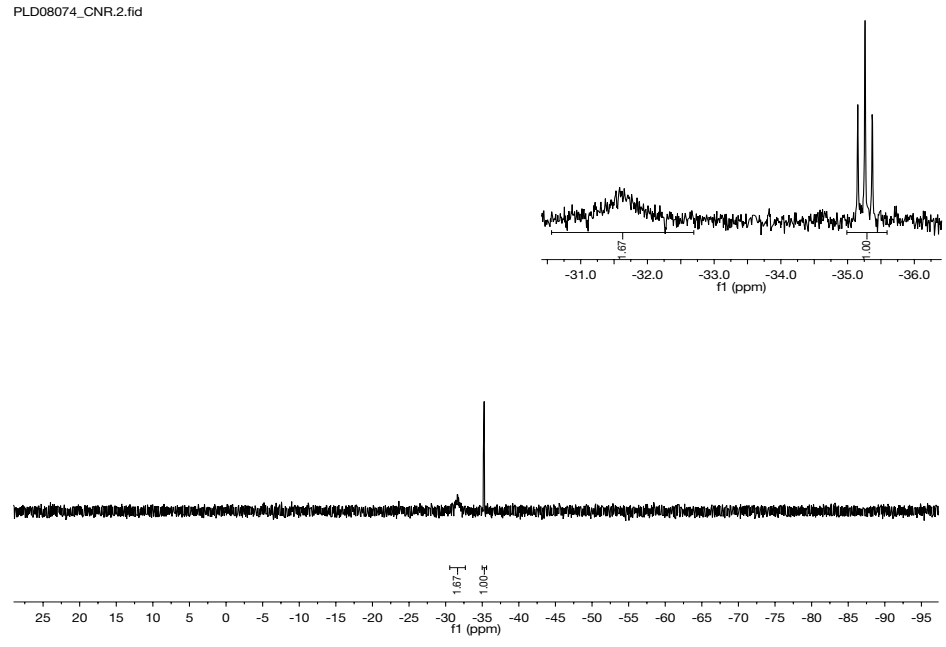

Figure 6.37: ^{31}P NMR of **6.16** in 50:50 THF/C_6D_6. Taken from PLD07074_CNR.

X-ray Crystal Data: General Procedure. Crystals were removed quickly from a scintillation vial to a microscope slide coated with oil. Samples were selected and mounted on the tip of a 0.1 mm diameter glass capillary. Data collection was carried out on a Bruker APEX II CCD diffractometer with a 0.71073 Å Mo Kα source or on a Bruker-AXS D8 Venture diffractometer with a 1.54178 Å Cu Kα source. The structures were solved by direct methods. All non-hydrogen atoms were refined anisotropically. Details regarding refined data and cell parameters are available in Tables 6.6-6.9.

Table 6.6. Crystal and refinement data for complexes **6.1-6.4**.

	6.1	**6.2**	**6.3**	**6.4**
CCDC Number	1842033	1842027	1842032	1842024
Empirical Formula	$C_{64}H_{52}N_4P_4Nb$	$C_{64}H_{52}N_4P_4Ta$	$C_{48}H_{39}N_3P_3Cl_2Nb$	$C_{48}H_{39}N_3P_3Cl_2Ta$
Formula weight	1093.89	1260.04	914.54	1002.58
T (K)	100(2)	100(2)	100(2)	100(2)
a, Å	12.1794(5)	12.2400(3)	14.9780(6)	15.0010(13)
b, Å	13.1172(5)	12.9995(4)	16.4049(5)	16.3582(12)
c, Å	35.6622(15)	35.964(1)	16.7474(6)	16.7487(13)
α, deg	90	90	90	90
β, deg	90.419(2)	91.449(1)	92.870(1)	92.923(3)
γ, deg	90	90	90	90
Volume, $Å^3$	5697.2(4)	5720.5(3)	4109.9(3)	4104.6(6)
Z	4	4	4	4
Crystal System	Monoclinic	Monoclinic	Monoclinic	Monoclinic
Space Group	P2(1)/c	P2(1)/c	P2(1)/n	P2(1)/n
d_{calc}, g/cm^3	1.275	1.463	1.478	1.622
θ Range, deg	2.5455 to 29.935	2.2885 to 30.490	2.434 to 30.497	2.248 to 30.534
μ, mm^{-1}	0.366	2.081	0.579	2.965
Abs. Correction	Multi-scan	Multi-scan	Multi-scan	Multi-scan
GOF	1.068	1.062	1.080	1.179
R_1 ,[a]	$R1$ = 0.0686	$R1$ = 0.0303	$R1$ = 0.0363	$R1$ = 0.0408
wR_2 [b] [I>2σ (I)]	$wR2$ = 0.1372	$wR2$ = 0.0667	$wR2$ = 0.0926	$wR2$ = 0.1237

[a] $R_1 = \sum||F_o| - |F_c||/\sum|F_o|$. [b] $wR_2 = [\sum[w(F_o^2-F_c^2)^2]/\sum[w(F_o^2)^2]]^{1/2}$.

Table 6.7. Crystal and refinement data for complexes **6.5-6.8.**

	6.5	**6.6**	**6.7**	**6.8**
CCDC Number	1842034	1842023	1842026	1842035
Empirical Formula	$C_{48}H_{39}N_3P_3Cl_2NbPd$ • C_6H_6	$C_{48}H_{39}N_3P_3Cl_2TaNi$ • $3(C_6H_6)$	$C_{48}H_{39}N_3P_3Cl_2TaPd$	$C_{48}H_{39}N_3P_3Cl_3NbRh$ • C_6H_6 • $2(C_4H_8O)$
Formula weight	1099.05	1295.60	1108.98	1275.22
T (K)	100(2)	100(2)	100(2)	100(2)
a, Å	9.76500	12.5097(3)	23.2731(19)	11.1203(5)
b, Å	15.56000	23.6118(6)	11.6716(7)	18.1202(10)
c, Å	16.65200	18.9624(5)	19.2249(14)	27.6749(15)
α, deg	79.0700	90	90	90
β, deg	76.0700	94.487(1)	125.576(2)	90
γ, deg	72.9600	90	90	90
Volume, $Å^3$	2328.538	5620.0(2)	4247.4(5)	5576.6(5)
Z	2	4	4	4
Crystal System	Triclinic	Monoclinc	Monoclinic	Orthorhombic
Space Group	P-1	P2(1)/n	Cc	P2(1)2(1)2(1)
d_{calc}, g/cm^3	1.568	1.531	1.734	1.519
θ Range, deg	2.296 to 30.388	2.367 to 28.949	2.7835 to 28.269	2.366 to 30.440
μ, mm^{-1}	0.892	2.506	3.276	0.779
Abs. Correction	Multi-scan	Multi-scan	Multi-scan	Multi-scan
GOF	1.040	1.072	1.122	1.057
R_1 ,[a]	$R1 = 0.0446$	$R1 = 0.0497$	$R1 = 0.0346$	$R1 = 0.0359$
wR_2 [b] [I>2σ (I)]	$wR2 = 0.0986$	$wR2 = 0.1058$	$wR2 = 0.1116$	$wR2 = 0.0851$

[a] $R_1 = \sum||F_o| - |F_c||/\sum|F_o|$. [b] $wR_2 = [\sum[w(F_o^2-F_c^2)^2]/\sum[w(F_o^2)^2]]^{1/2}$.

Table 6.8. Crystal and refinement data for complexes **6.9-6.12.**

	6.9	**6.10**	**6.11**	**6.12**
CCDC Number	1842031	1842029	1842025	1842036
Empirical Formula	$C_{48}H_{39}N_3P_3Cl_3NbIr$	$C_{48}H_{39}N_3P_3Cl_3TaRh$	$C_{48}H_{39}N_3P_3Cl_3TaIr$ • $2(C_4H_8O)$	$C_{48}H_{39}N_3P_3ClTaCo$
Formula weight	1142.21	1140.95	1374.46	1054.07
T (K)	100(2)	100(2)	100(2)	100(2)
a, Å	20.6618(6)	11.82400	11.9034(7)	11.98600
b, Å	13.1650(4)	11.96200	15.5335(10)	12.26600
c, Å	20.4394(9)	19.99500	27.7150(19)	16.24200
α, deg	90	74.6100	90	87.2600
β, deg	117.215(1)	85.0200	98.146(2)	82.4300
γ, deg	90	61.3200	90	62.7700
Volume, $Å^3$	4944.3(3)	2389.383	5072.8(6)	2194.553
Z	4	2	4	2
Crystal System	Monoclinic	Tricliinic	Monoclinic	Triclinic
Space Group	Cc	P-1	P2(1)/c	P-1
d_{calc}, g/cm^3	1.535	1.586	1.800	1.663
θ Range, deg	2.323 to 30.490	2.4765 to 30.357	2.374 to 30.482	2.241 to 33.127
μ, mm^{-1}	3.214	2.937	5.075	3.212
Abs. Correction	Multi-scan	Multi-scan	Multi-scan	Multi-scan
GOF	1.061	1.080	1.084	1.056
R_1 ,[a]	$R1 = 0.0385$	$R1 = 0.0488$	$R1 = 0.0355$	$R1 = 0.0322$
wR_2 [b] [I>2σ (I)]	$wR2 = 0.0954$	$wR2 = 0.1351$	$wR2 = 0.0734$	$wR2 = 0.0728$

[a] $R_1 = \sum||F_o| - |F_c||/\sum|F_o|$. [b] $wR_2 = [\sum[w(F_o^2-F_c^2)^2]/\sum[w(F_o^2)^2]]^{1/2}$.

Table 6.9. Crystal and refinement data for complexes **6.13-6.15.**

	6.13	**6.14**	**6.15**	**6.15**
CCDC Number	1842030	1842028	1843043	1842022
Empirical Formula	$C_{57}H_{48}Cl_2N_4P_3TaNi$ •2(C_4H_8O)	$C_{57}H_{48}Cl_2N_4P_3TaPd$	$C_{57}H_{48}Cl_3N_4P_3NbIr$ • (C_6H_6) • (C_4H_8O)	$C_{57}H_{48}Cl_3N_4P_3TaIr$ •2(C_6H_6) • (C_4H_8O)
Formula weight	1336.66	1240.16	1423.60	1589.75
T (K)	123(2)	100(2)	100(2)	100(2)
a, Å	11.37200	35.502(3)	12.22900	12.2652(8)
b, Å	16.44400	37.018(2)	17.22700	15.9047(10)
c, Å	16.66900	30.510(2)	18.84800	18.3995(12)
α, deg	96.7300	90	121.6700	66.156(2)
β, deg	90.8100	90	95.8200	80.491(2)
γ, deg	92.2100	90	94.3100	86.035(2)
Volume, Å^3	3062.406	40097(5)	3323.101	3237.8(4)
Z	2	32	2	2
Crystal System	Triclinic	Orthorhombic	Triclinic	Triclinic
Space Group	P-1	Fdd2	P-1	P-1
d_{calc}, g/cm^3	1.450	1.643	1.423	1.631
θ Range, deg	2.355 to 36.350	2.543 to 28.271	2.290 to 30.580	2.440 to 28.233
μ, mm^{-1}	2.305	2.786	2.408	3.998
Abs. Correction	Multi-scan	Multi-scan	Multi-scan	Multi-scan
GOF	1.100	1.037	1.064	1.031
R_1 ,[a]	R_1 = 0.0408	R1 = 0.0456	R1 = 0.0388	R1 = 0.0406
wR_2 [b] [I>2□(I)]	wR2 = 0.1055	wR2 = 0.0928	wR2 = 0.0835	wR2 = 0.1051

[a] $R_1 = \sum||F_o| - |F_c||/\sum|F_o|$. [b] $wR_2 = [\sum[w(F_o^2-F_c^2)^2]/\sum[w(F_o^2)^2]]^{1/2}$.

Chapter 7

Synthesis and Characterization of Group 6 Metalloligands and Homo- and Heterobimetallic Complexes Supported by 2-(diphenylphosphino)pyrrolide Ligands

7.1 OVERVIEW

The homoleptic group 6 complexes, $Cr(\kappa^2\text{-NP})_3$ (**7.1**), $Cr(\mu\text{-NP})_2(\mu\text{-PN})_2Cr$ (**7.2**), $Mo(\kappa^2\text{-NP})_4$ (**7.3**), and $W_2(\mu_2\text{-NP})_4$ (**7.4**) were synthesized via salt metathesis (NP = 2-diphenylphosphinopyrrolide). $Cr(\mu_2\text{-NP})_2(\mu_2\text{-NP})_2Cr$ (**7.2)** and $W_2(\mu_2\text{-NP})_4$ (**7.4)** both feature short metal-metal distances, 2.0011(7) Å (FSR = 0.85) and 2.2432(2) Å (FSR = 0.86), respectively. These distances are consistent with the formation of metal-metal triple bonds. The heteroleptic complexes $W(=Ntolyl)(\kappa^2\text{-NP})(\kappa^1\text{-NP})$ (**7.5**), $Mo(\kappa^2\text{-NP})_2(\kappa^2\text{-NPNtolyl})$ (**7.6**), and $Mo(=NDipp)(\kappa^2\text{-NP})(\kappa^2\text{-NPNDipp})$ (**7.7**) were also synthesized via salt metathesis from their corresponding imido precursor. $Mo(\kappa^2\text{-NP})_2(\kappa^2\text{-NPNtolyl})$ and $Mo(=NDipp)(\kappa^2\text{-NP})(\kappa^2\text{-NPNDipp})$ both contain phosphinimides, the product of N-P bond formation, as shown by short P-N bond lengths. Treatment of $W(=Ntolyl)(\kappa^2\text{-NP})(\kappa^1\text{-NP})$ with late metal carbonyls results in formation of the heterobimetallic complexes $(\kappa^2\text{-NP})W(=NTolyl)(\mu_2\text{-NP}_2(\mu_2\text{-CO})Co(CO)_2$ (**7.8**) and $(\kappa^2\text{-NP})W(=Ntolyl)(\mu_2\text{-NP})_2Fe(CO)_3$ (**7.10**).

7.2 INTRODUCTION

Bimetallic complexes of the group 6 metals exhibit some of the strongest metal-metal bonds discovered, containing up to quadruple, quintuple, and even sextuple bonds [239-246]. The group 6 metals are ideally situated to form these strong interactions because their typical oxidation states give an ideal electron count (d^8 or d^{10}). Metal-metal bonds are strongest when the electron count is ten. They decrease in strength due to removal of electrons from bonding orbitals or due to population of metal-metal antibonding orbitals. These group 6 bimetallic complexes typically contain two to four anionic, bidentate (LX) ligands giving metal oxidation states ranging from d^{10} M(I)M(I) to d^8 M(II)M(II) (M = Cr, Mo, or W), resulting in occupation of only metal-metal bonding orbitals. This has resulted in a plethora of group 6 bimetallic complexes that contain strong metal-metal bonds.

While there are numerous examples of complexes that contain both a group 6 metal and a late TM center, there are significantly fewer that contain short metal-metal distances and still fewer that contain formal metal-metal bonds. Many of these examples contain bridging ligands (e.g. imidos, hydrides, alkylidenes, or carbonyls) and close metal-metal contacts that arise from the geometric constraints of the bridging ligand [78-

79]. Recently, hard/soft bifunctional ligands have found application in linking two different transition metal centers, resulting in a numerous complexes that contain strong metal-metal bonds [83, 108, 133, 163, 219]. Notably, the Lu group has synthesized a series of CrM (M = Mn, Fe, Co, and Ni) complexes that contain strong metal-metal bonds, including a quintuple bond in the case of CrMn [112]. Similarly, the Thomas group has synthesized CrM (M = Fe, Co, Cu) complexes where CrFe contains a triple bond [247].

Accordingly, we are interested in investigating mid-late heterobimetallic complexes containing group 6 metals. We have previously demonstrated that our phosphinopyrrolide ligand framework is capable of supporting metal-metal bonding in early-late bimetallic complexes containing group 4 and 5 metals [163, 219]. Herein we report the synthesis of a variety of group 6 complexes and their application as metalloligands to late metal carbonyls.

7.3 Results and Discussion

To synthesize the desired heterobimetallic complexes, group 6 $M(\kappa^2\text{-NP})_3$ and $M(\kappa^2\text{-NP})_4$ (M = Cr, Mo, W) species were targeted. Treatment of $CrCl_3$ with 3 equivalents of Li(NP) resulted in formation of a monometallic octahedral Cr complex, $Cr(\kappa^2\text{-NP})_3$ (**7.1**) (Scheme 7.1). This dark green, d^3 species contains four broadened resonances *via* ^{1}H NMR, consistent with a paramagnetic metal center. All Cr-N and Cr-P bond lengths are equivalent (Table 7.1). Treatment of $CrCl_2$ with 2 equivalents of Li(NP) resulted in the formation of bimetallic species $Cr(\mu_2\text{-NP})_2(\mu_2\text{-NP})_2Cr$ (**7.2**). All four ligands bridge the metal centers and adopt a head to tail configuration resulting in *trans* phosphines. This formally Cr(II)Cr(II), d^8 complex is diamagnetic and contains a short metal-metal distance, 2.0011(7) Å (FSR = 0.85), consistent with a triple bond. The ^{31}P NMR consists of a single broad resonance ranging from 0 to 3 ppm. The formation of this complex likely arises from the dimerization of $Cr(\kappa^2\text{-NP})_2$ to form the more stable metal-metal bonded species. The structures of **7.1** and **7.2** are presented in Figures 7.1 and 7.2, respectively, and relevant bond lengths can be found in Table 7.1.

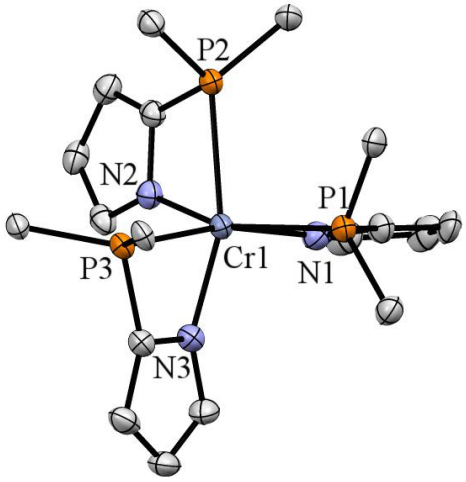

Figure 7.1. 50% thermal ellipsoid drawing of **7.1.** Phenyl groups have been reduced to the ipso carbon and hydrogen atoms and solvent omitted for clarity.

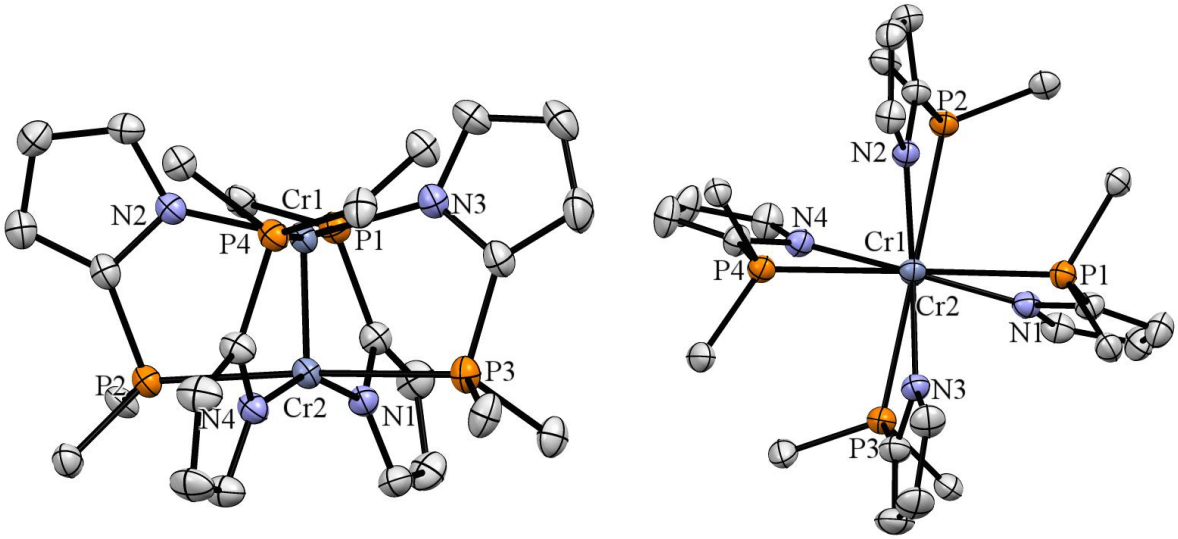

Figure 7.2. 50% thermal ellipsoid drawings of **7.2** top down (right) and side on (left). Phenyl groups have been reduced to the ipso carbon and hydrogen atoms and solvent omitted for clarity.

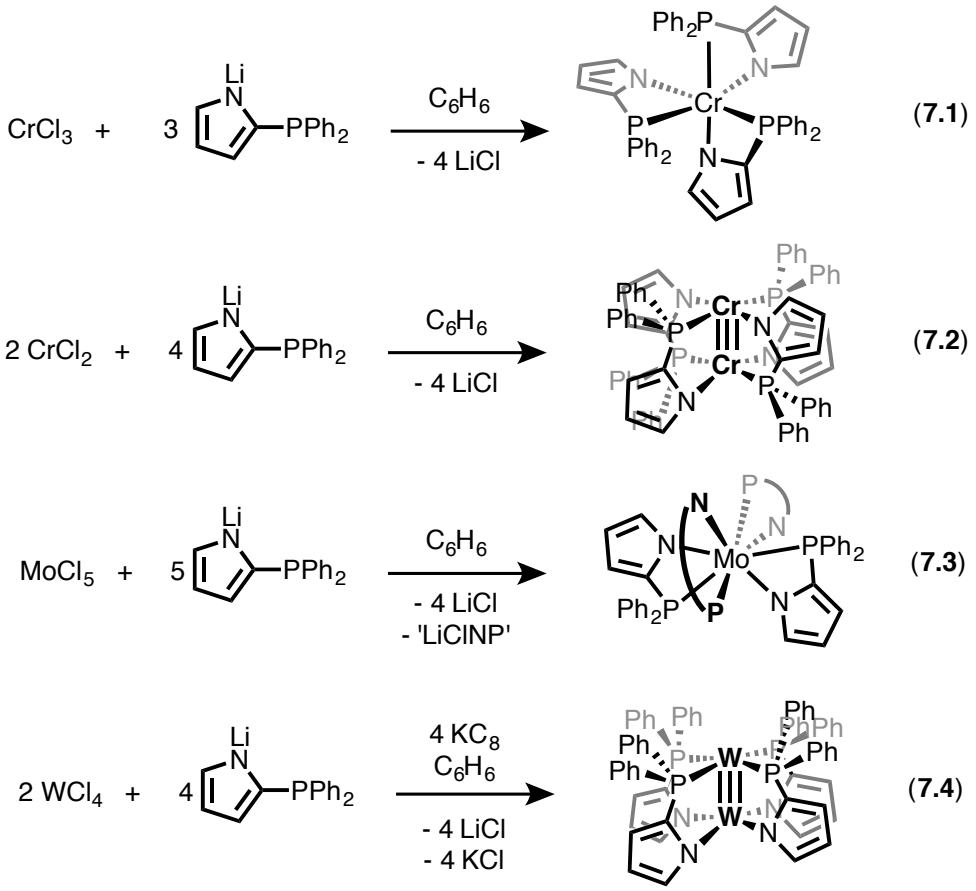

Scheme 7.1: Synthesis of mono- and bimetallic homoleptic complexes of the group 6 metals.

Molybdenum metalloligands were also targeted. Treatment of $MoCl_3$ with three equivalents of Li(NP) resulted in a color change to orange, consistent with the formation of a new species. However, attempts to crystallize this paramagnetic complex, presumably Mo(κ^2-NP)$_3$, were unsuccessful. In contrast to this, reaction of $MoCl_5$ and five equivalents of Li(NP) resulted in isolation of the paramagnetic species, Mo(κ^2-NP)$_4$ (**7.3**) (Scheme 7.2). With this structure in hand, the stoichiometric synthesis was performed. Treatment of $MoCl_4(THF)_2$ with four equivalents of Li(NP) yielded a diamagnetic product that contains three resonances *via* ^{31}P. Oddly, this unidentified product can be obtained more cleanly by treatment of two equivalents of $MoCl_4$(THF) with four equivalents of Li(NP) and four equivalents of KC_8. The nature of this species is amibiguous, but likely contains three NP ligands, two Mo centers, and other ancillary ligands. Despite this, treatment of $MoCl_5$ with five equivalents of Li(NP) remains a

reliable procedure to isolate **7.3.** In the solid state **7.3** contains four κ^2 ligands and using the same method as described in Chapter 2, intersecting trapezoids have an angle of 84.17° indicating that **7.3** is best described as distorted dodecahedron [125-126]. The structure of **7.3** is presented in Figure 7.3 and relevant bond lengths can be found in Table 7.1.

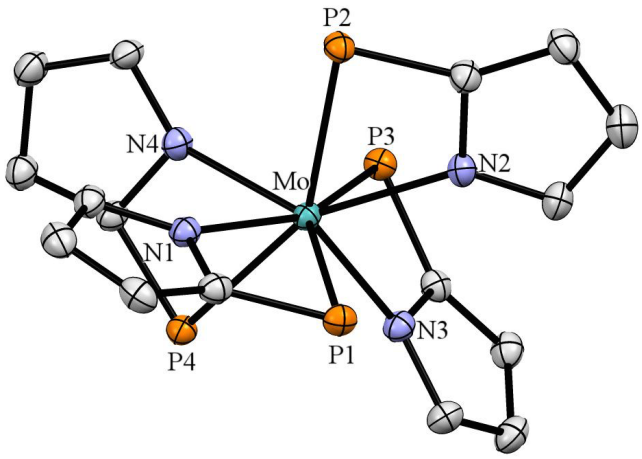

Figure 7.3. 50% thermal ellipsoid drawing of **7.3**. Phenyl groups have been removed and Hydrogen atoms and solvent omitted for clarity.

An analogous reaction was performed with WCl_4; however, this resulted in formation of multiple diamagnetic products by ^{31}P NMR. From this mixture $W_2(\mu_2\text{-NP})_4$ (**7.4**) was crystallized. Similar to **7.3**, a tungsten center in **7.4** has been reduced, most likely by free phosphine in solution. Accordingly, treatment of two equivalents of WCl_4 with four equivalents of LiNP and 4 equivalents of KC_8 leads to cleaner product formation. The structure of **7.4** is presented in Figure 7.4 and relevant bond lengths can be found in Table 7.1. Complex **7.4** contains four κ^2 ligands that bridge the W centers. In contrast to **7.2**, all NP ligands are oriented in the same direction, giving formally $P_4W(0)$ and $N_4W(IV)$ metal centers. This difference likely arises from the fact that Cr prefers lower oxidation states. Both centers are square pyramidal with the other tungsten center occupying the axial site. The W-W bond is short, 2.2432(2) Å (FSR =0.86), consistent with a metal-metal triple bond. Complex **7.4** contains a single resonance *via* ^{31}P NMR (J_{WP} = 323 Hz), consistent with other W-P complexes [248]. Complex **7.4** is isostructural and isoelectronic with the previously reported $Ti(NP)_4Fe$ (**4.1**) complex, which also contains a metal-metal triple bond [219].

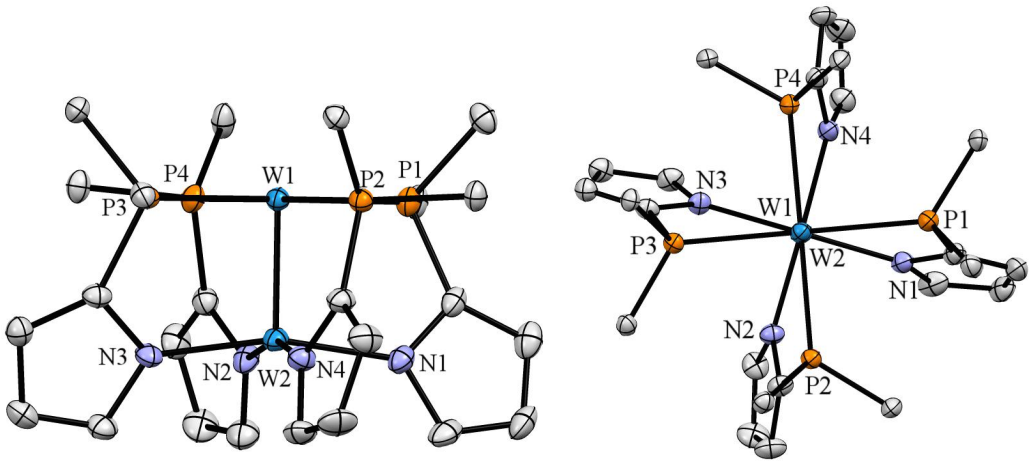

Figure 7.4. 50% thermal ellipsoid drawings of **7.4** side-on (left) and top-down (right). Select phenyl groups have been reduced to the ipso carbon and hydrogen atoms and solvent omitted for clarity.

Table 7.1. Relevant bond lengths (Å) and angles (°) for **7.1**-**7.4**.

	7.1	**7.2**	**7.3**	**7.4**
M-M (Å)	-	2.0011(7)	-	2.2432(2)
FSR[a]	-	0.85	-	0.86
P-M (Å)	2.493(1)	2.5283(9)	2.5881(6)	2.495(1)
	2.507(1)	2.5206(9)	2.5799(7)	2.497(1)
	2.488(1)	2.5243(9)	2.6227(6)	2.487(1)
		2.5384(9)	2.6044(7)	2.500(1)
M-N (Å)	1.999(3)	2.018(2)	2.158(2)	2.091(3)
	1.987(3)	2.015(3)	2.160(2)	2.086(4)
	1.997(3)	2.020(2)	2.184(2)	2.084(4)
		2.026(2)	2.188(2)	2.081(4)
Torsional Angle (P-M-M-N) (°)	-	13.81	-	17.23
		14.26		21.12
		14.80		19.98
		14.10		17.83

[a]FSR = $M_D/\sum(M_c)$: M_D = Metal-metal distance, M_c= Covalent Radii [151].

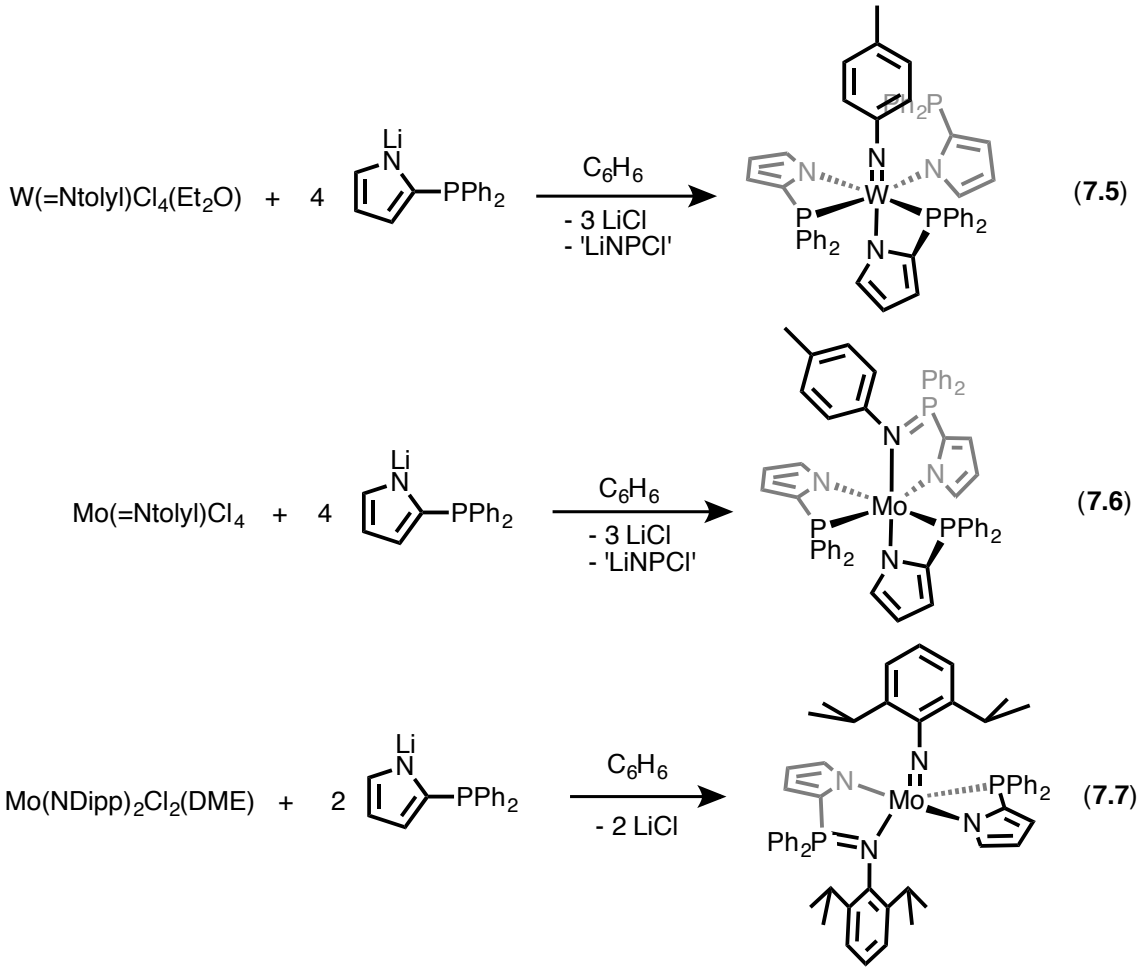

Scheme 7.2: Synthesis of group 6 imido complexes ligated by phosphinopyrrolides.

Group 6 imido complexes were also selected due to their ease of preparation, our group's interest in fundamental imido reactivity, and their electron richness, which may increase phosphine labilization. The trisubstituted complex W(V) complex W(=Ntolyl)(κ^2-NP)(κ^1-NP) (**7.5**) was synthesized in moderate yield via the salt metathesis of WCl_4(=NTolyl)(Et_2O) and 4 equivalents of Li(NP) (Scheme 7.2). Similar reductions of W(VI) to W(V) have been reported in the presence of phosphines at elevated temperatures [249]. Complex **7.5** is octahedral in the solid state and contains two κ^2-NP ligands, while the third NP phosphine arm is uncoordinated (W-P ~3.63 Å). The structure of **7.5** is presented in Figure 7.5 and relevant bond lengths can be found in

Table 7.2. The ^{1}H NMR of this d^{1} species contains a number of broad resonances, consistent with a paramagnetic and fluxional species.

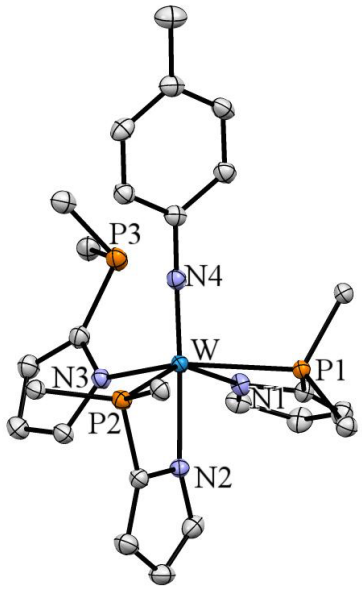

Figure 7.5. Thermal ellipsoid drawing of **7.5.** Solvent and Hydrogen atoms have been removed and the phosphine phenyl rings reduced to the *ipso* carbons for clarity.

An analogous reaction was performed with the group 6 congener, $MoCl_4$(=Ntolyl) which resulted in the formation of a reduced octahedral species, Mo(III)(κ^2-NP)$_2$(κ^2-NPNtolyl) (**7.6**) (Scheme 7.2). The structure of **7.6** is presented in Figure 7.6 and relevant bond lengths can be found in Table 7.2. Suprisingly, the imido group has inserted into one the Mo-P bonds resulting in a phosphinimide (N-P = 1.621(3) Å). This complex is likely proceeded by the formation of Mo(=Ntolyl)(κ^2-NP)(κ^1-NP), which then undergoes facile N-P bond formation concomitant with metal reduction of the metal center to give **7.6**.

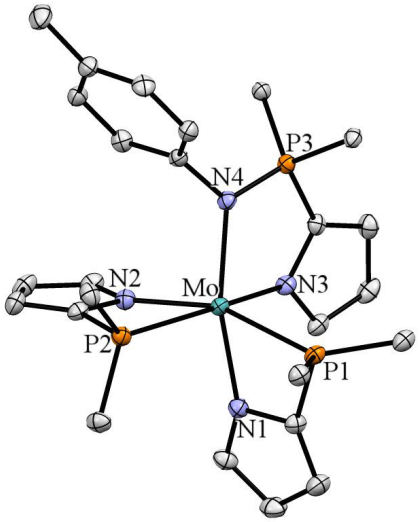

Figure 7.6. 50% thermal ellipsoid drawing of **7.6**. Select phenyl groups have been reduced to the ipso carbon and hydrogen atoms and solvent omitted for clarity.

Reaction of a molybdenum diimido species, $Mo(=NDipp)_2Cl_2(DME)$, with two equivalents of Li(NP) also gave a product containing a P=N double bond, $Mo(=NDipp)(\kappa^2\text{-NP})(\kappa^2\text{-NPNDipp})$ (**7.7**) (Scheme 7.2). Complex **7.7** is square pyramidal in the solid state with the imido occupying the axial site and contains one κ^2 bound NP ligand. The structure of **7.7** is presented in Figure 7.7 and relevant bond lengths can be found in Table 7.2. Formation of this complex likely proceeds from the salt metathesis product, $Mo(NDipp)_2(\kappa^2\text{-NP})(\kappa^1\text{-NP})$. The ^1H NMR of this diamagnetic complex contains three inequivalent isopropyl methyne peaks, most likely due to hindered rotation of the equatorial DIPP ligand. The ^{31}P NMR consists of two singlets with one significantly shifted downfield, consistent with phosphorous oxidation. Further heating of a C_6D_6 solution **7.7** at 90°C does not result in a second insertion event.

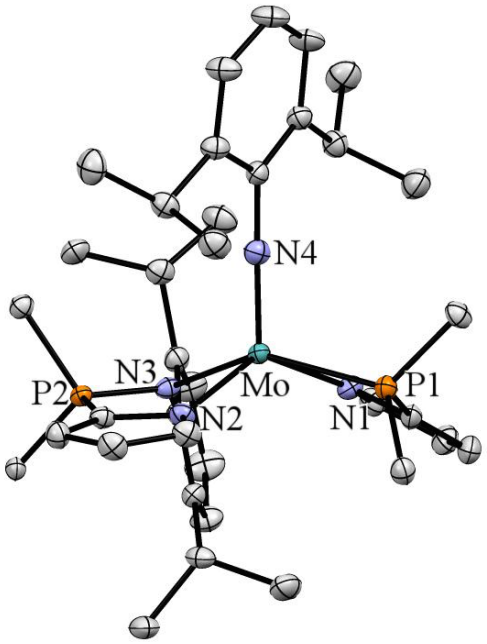

Figure 7.7. 50% thermal ellipsoid drawing of **7.7**. Select phenyl groups have been reduced to the ipso carbon and hydrogen atoms and solvent omitted for clarity.

Table 7.2. Relevant bond lengths (Å) for **7.5-7.7**.

	7.5	**7.6**	**7.7**
M=N (imido) (Å)	1.760(3)	-	1.734(2)
P-M (Å)	2.5395(9)	2.5935(8)	2.4749(8)
	2.5622(7)	2.5890(8)	
M-N (pyrrole) (Å)	2.092(3)	2.142(3)	2.128(3)
	2.088(2)	2.134(3)	2.104(2)
	2.176(3)	2.129(2)	
N-P (Å)	-	1.621(3)	1.621(3)
M-N (imine)	-	2.165(2)	2.153(2)

With a suite of potentional metalloligands in hand, we next sought to treat them with various late metal precursors to synthesize the desired heterobimetallic complexes (Scheme 7.3). Of complexes **7.1**, **7.3**, and **7.5**-**7.7**, only complex **7.5** proved to be a viable metalloligand. Treatment of **7.1** with excess $Ni(COD)_2$ at elevated temperatures did not result in incorporation of a Ni center. Instead, **7.1** was reisolated in lower yield. Presumably the Cr-P bonds in an octahedral ligand field are not sufficiently labile to incorporate a second metal center. In the case of **7.3**, treatment with $Ni(COD)_2$ resulted in decomposition of **7.3** as shown by loss of the characteristic paramagnetic resonances. Synthesis of a bimetallic species using **7.3** may be possible with less reactive reagents such as metal carbonyls or metal halides. However, only metallations with $Ni(COD)_2$ were performed. Similar to complex **7.1**, **7.6** is octahedral in the solid-state and is unlikely to have labile phosphines. **7.7** contains only one available phosphine arm, making it difficult to encapsulate a second metal center. Therefore, **7.6** and **7.7** were not further persued as metalloligands.

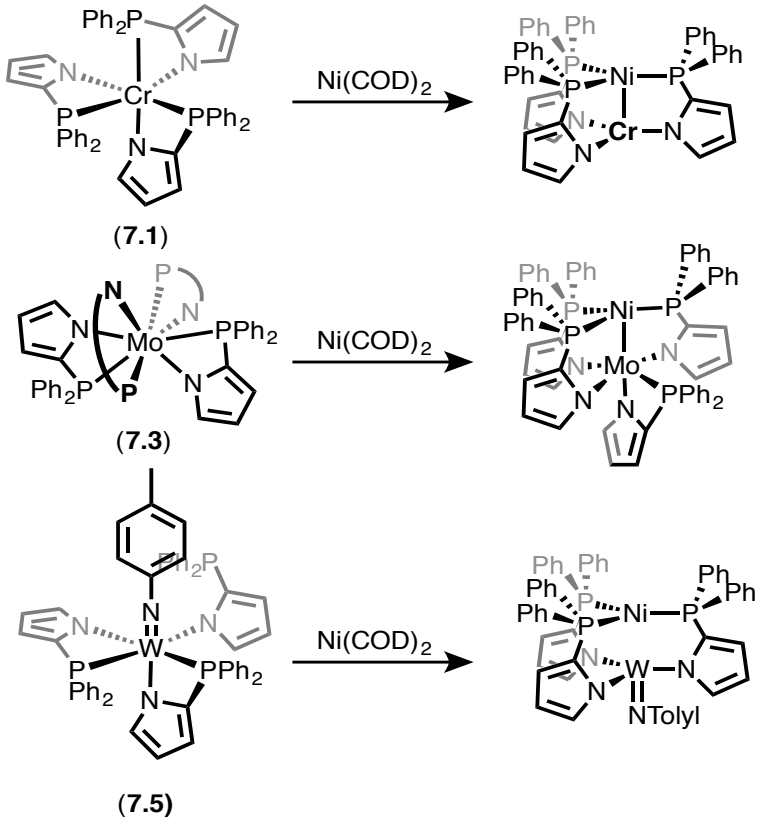

Scheme 7.3: Potential routes to heterobimetallics based on group 6 metalloligands.

Treatment of **7.5** with $Ni(COD)_2$ resulted in a new paramagnetic species that decomposes over the course of a day. To circumvent this, more stable late metal precursors were utilized. Treatment of **7.5** with a half equivalent of $Co_2(CO)_8$ resulted in effervescence of CO and an immediate color change to dark red. Single crystal diffraction revealed a new bimetallic species, (κ^2-NP)W(=NTolyl)(μ-NP)$_2$(μ-CO)Co(CO)$_2$. (**7.8**) (Scheme 7.4). Complex **7.8** contains two NP ligands that bridge the metal centers while the other NP ligand remains bound κ^2 to W. Additionally, one carbonyl bridges the metal centers while two remain bound to Co, rendering the geometry about Co pseudo-square pyramidal. The tungsten-cobalt distance is 2.7822(5) Å (FSR = 1.13), too long for significant bonding interactions. However, given that **7.8** is diamagnetic, there must be some degree of electronic communication between the metal centers, most likely antiferromagnetic coupling. The ^{31}P NMR of this d^{10} species consists of three inequivalent phosphine resonances, where one is significantly upfield consistent with a single W bound phosphine. Complex **7.8** decomposes over the course of days to give a new product, (κ^2-NPNTolyl)W(μ_2-NP)$_2$(μ-CO)$_2$Co(CO) (**7.9**). Similar to the Mo complexes **7.6** and **7.7**, **7.9** has undergone P-N bond formation concurrent with formal reduction of the metal center, making this a formally d^{12} W((III)Co(0) complex. This species is also diamagnetic, containing ^{31}P resonances in a 2:1 ratio. The structures of **7.8** and **7.9** are presented in Figure 7.8 and relevant bond lengths can be found in Table 7.3.

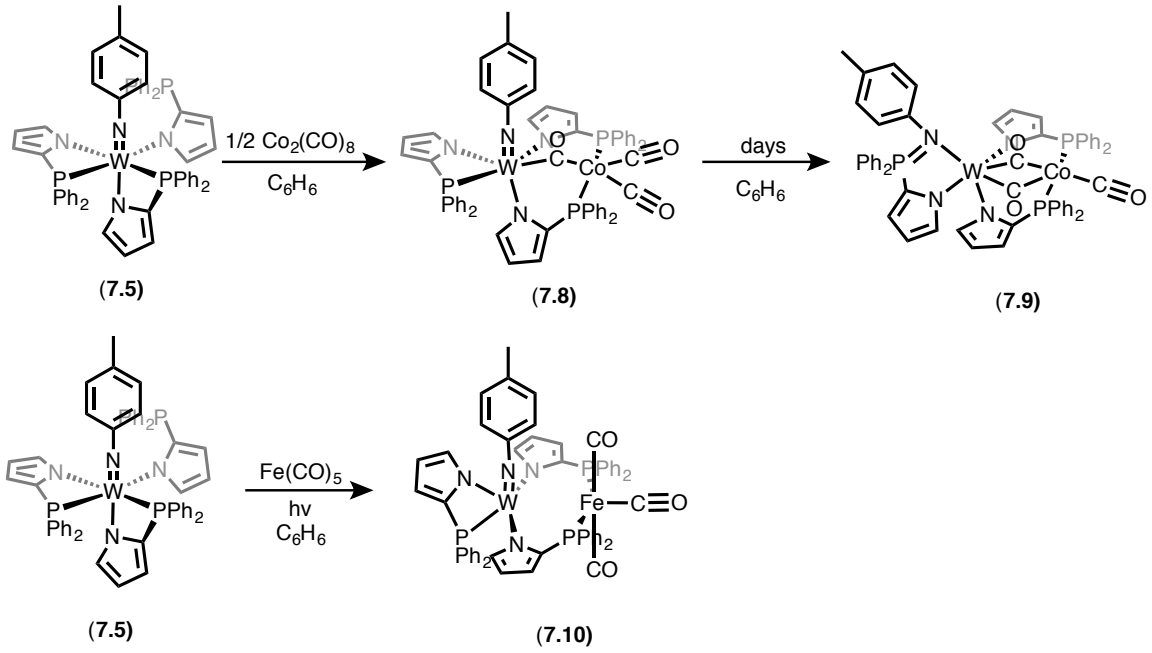

Scheme 7.4: Synthesis of WM (M = Fe and Co) complexes.

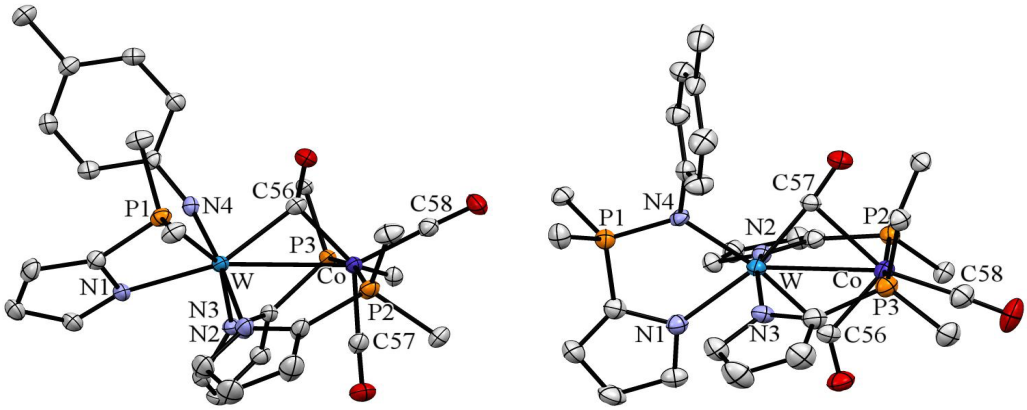

Figure 7.8: Thermal ellipsoid drawings of complex **7.8** (left) and **7.9** (right). Select phenyl groups, hydrogens atoms, and solvent have been reduced or eliminated for clarity.

Complex **7.5** was photolyzed in the presence of $Fe(CO)_5$ to yield complex **7.10**, (κ^2-NP)W(=Ntolyl)(μ_2-NP)$_2$Fe(CO)$_3$ (Scheme 7.4). Similar to complex **7.8**, **7.10** contains two bridging NP ligands (Fe-P: 2.2413(6) Å and 2.2392(6) Å), while the third NP ligand

remains κ ^{2} bound to W. The W-P1 bond is long, 2.8195(6) Å, and is pseudo *trans* from the imido. The geometry about Fe is square pyramidal, where the phosphines are *trans* to each other. The W-Fe bond distance is also long: 2.8365(3) Å. The Fe-CO bond lengths are all similar: 1.789(2) Å, 1.800(2) Å, and 1.784(2) Å. The ^{1}H NMR of this d^9 paramagnetic complex contains a number of broad resonances ranging from 6-10 ppm. The structure of **7.10** is presented in Figure 7.9 and relevant bond lengths can be found in Table 7.3.

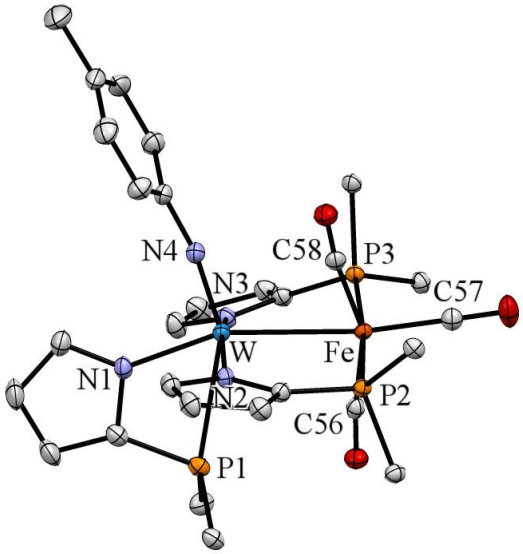

Figure 7.9. 50% thermal ellipsoid drawing of **7.10**. Select phenyl groups have been reduced to the ipso carbon and hydrogen atoms and solvent omitted for clarity.

Table 7.3. Relevant bond lengths (Å) for **7.8**-**7.10**.

	7.8	**7.9**	**7.10**
W-M (Å)	2.7822(5)	2.6844(6)	2.8365(3)
FSR[a]	1.13	1.09	1.15
P-W (Å)	2.555(1)	-	2.8195(6)
W-N (Å)	2.219(4)	2.136(4)	2.102(2)
	2.124(4)	2.135(4)	2.090(2)
	2.128(4)	2.194(3)	2.118(2)
		2.074(3)[b]	
W=N(Å)	1.760(4)	-	1.735(1)
M-P	2.217(1)	2.219(1)	2.2413(6)
	2.235(1)	2.225(1)	2.2392(6)
W-C	2.128(4)	2.213(4)	-
		1.928(4)	
M-C	1.779(4)	1.750(5)	1.800(2)
	1.816(4)	1.935(5)[c]	1.789(2)
	1.964(3)[c]	2.248(4)[c]	1.784(2)

[a]FSR = $M_D/\sum(M_c)$: M_D = Metal-metal distance, M_c= Covalent Radii [151]. [b]W-imine bond. [C]Bridging CO.

Use of molybdenum and tungsten metalloligands in the synthesis of early-late heterobimetallic complexes has a rich history [79]. The resulting complexes have been targeted for catalytic applications as well as the development of thin films prepared *via* vapor deposition. Accordingly, there are numerous examples of WFe and WCo early-late heterobimetallic complexes in the literature. However, most of these complexes contain tungsten in a low oxidation state in the form of tungsten carbonyls. For example, a suite of $L(CO)_3W(\mu_2\text{-}PPh_2)(\mu_2\text{-}CO)FeCp(CO)$ (L = CO or phosphine) complexes were synthesized by Shyu and Wen and contain metal-metal contacts slightly longer than 2.8 Å [249-252]. Similar to these iron complexes, Co derivates have also been synthesized by

Wang. $(CO)_3CpWCo(CO)_4$ complexes with varying substituents on the Cp rings were synthesized that feature unsupported metal-metal bonds [253-255]. Miller has used cyclopentadienyl rings bearing phosphine substituents to link tungsten to iron, resulting in a family of $(CO)_2XCpW(Ph_2PC_5H_4)FeMe(CO)_2$ (X = Cl, Me) complexes [256].

Similar to **7.8** and **7.10**, there are also WFe complexes that contain imido moieties. The unbridged heterobimetallic complexes $Cp(^tBu{=}N)WFeCp(CO)_2$ and $(^tBu{=}N)W(FeCp(CO)_2)_2$ were synthesized *via* salt metathesis with $NaFeCp(CO)_2$, a common reagent in the synthesis of many Fe based heterobimetallics [257-258]. Since single crystal data was not reported for many of these complexes, structural assignments were made *via* NMR and IR. This makes it difficult to draw direct comparisons between these complexes and **7.8** and **7.10**. However, the bond distances in **7.8** and **7.10** are of similar lengths to other reported WFe and WCo complexes in the literature [79]. The late metal center in all of the mentioned complexes contains CO ligands, which act as an electron sink, reducing their ability to form dative bonds with W. Therefore, the metal-metal bonds are often weak or nonexistent, similar to **7.8** and **7.10**.

7.4 CONCLUSIONS

The homoleptic group 6 metalloligands $M(\kappa^2\text{-NP})_3$ and $M(\kappa^2\text{-NP})_4$ (M = Cr, Mo, W) were targeted for application as metalloligands. In the case of Cr, the trisubstituted $Cr(\kappa^2\text{-NP})_3$ and tetra substrituted complex $Cr_2(\mu_2\text{-NP})_2(\mu_2\text{-PN})_2$ were synthesized *via* salt metathesis. The tetrasubstituted complexes, $Mo(\kappa^2\text{-NP})_4$ and $W_2(\mu\text{-NP})_4$ were also synthesized *via* salt metathesis. Secondary metallations with $Cr(\kappa^2\text{-NP})_3$ and $Mo(\kappa^2\text{-NP})_4$ were attempted with $Ni(COD)_2$ and were unsuccessful. These reactions resulted in reisolation of starting material or decomposition, respectively. The homobimetallic complexes $Cr_2(\mu_2\text{-NP})_2(\mu_2\text{-PN})_2$ and $W_2(\mu_2\text{-NP})_4$ contain short metal-metal distances, consistent with metal-metal triple bonds. Heteroleptic complexes containing imido ligands were then targeted. In the case of Mo, the complexes undergo P-N bond formation rendering them ineffective as metalloligands. However, the tungsten complex, $W(=Ntolyl)(\kappa^2\text{-NP})(\kappa^1\text{-NP})$, can be synthesized in good yield and treatment of this species with late metal carbonyls results in clean formation of new heterobimetallic

species of cobalt and iron. Future work will focus on photolyzing these species to generate complexes with lower ligand numbers that contain strong metal-metal bonds.

7.5 Experimental Considerations

General Considerations and Instrumentation. All air- and moisture-sensitive compounds were manipulated in a glovebox under a nitrogen atmosphere. Solvents for air- and moisture-sensitive reactions were vacuum transferred from sodium benzophenone ketyl (THF, Et_2O, pentane, d_6-benzene and d_8-toluene) or predried by passing through activated alumina columns of a SG Water solvent purification system. ^1H, ^{13}C and ^{31}P spectra were recorded on Varian INOVA 500 MHz or Bruker Avance III 400 MHz spectrometers. $Mo(NDipp)_2Cl_2(DME)$, $MoCl_4(NTolyl)$, $WCl_4(Ntolyl)(Et_2O)$, and $MoCl_4(THF)_2$ were prepared according to literature procedure [259-262]. $CrCl_2$, $CrCl_3$, $MoCl_5$, WCl_4, $Fe(CO)_5$, $Co_2(CO)_8$ were purchased from Strem Chemicals and used without further preperation. Chemical shifts are reported with respect to residual protio-solvent impurity for ^1H (*s*, 7.16 ppm for C_6D_5H), solvent carbons for ^{13}C (*t*, 128.39 ppm for C_6D_6), and PPh_3 for ^{31}P (*s*, -6 ppm for C_6D_6).

X-ray Crystal Data: General Procedure. Crystals were removed quickly from a scintillation vial to a microscope slide coated with oil. Samples were selected and mounted on the tip of a 0.1 mm diameter glass capillary. Data collection was carried out on a Bruker APEX II CCD diffractometer with a 0.71073 Å Mo Kα source or on a Bruker-AXS D8 Venture diffractometer with a 1.54178 Å Cu Kα source. The structures were solved by direct methods. All non-hydrogen atoms were refined anisotropically. Details regarding refined data and cell parameters are available in Tables 7.4-7.6.

Synthesis of $Cr((2\text{-}Ph_2P)C_4H_3N)_3$, $Cr(\kappa^2\text{-}NP)_3$ (7.1). Solid $CrCl_3$ (16.65 mg, 0.105 mmol, 1 equiv) and LiNP (81.2 mg, 0.315 mmol, 3 equiv) were dissolved in 5 mL of THF and stirred overnight. The volatiles of the resulting green solution were removed *in vacuo*. The solid was then extracted with 10 mL of benzene and filtered through celite and volatiles were removed *in vacuo* to yield pure **7.1** in 40% yield. X-Ray quality crystals were grown from a concentrated toluene solution of **7.1** cooled to -35°C. ^1H

NMR (300 MHz, C_6D_6) δ, ppm: 1.7 (br), 4.4(br), 11.2(br), 14.2(br). Evans' method U_{eff} = 3.37 BM.

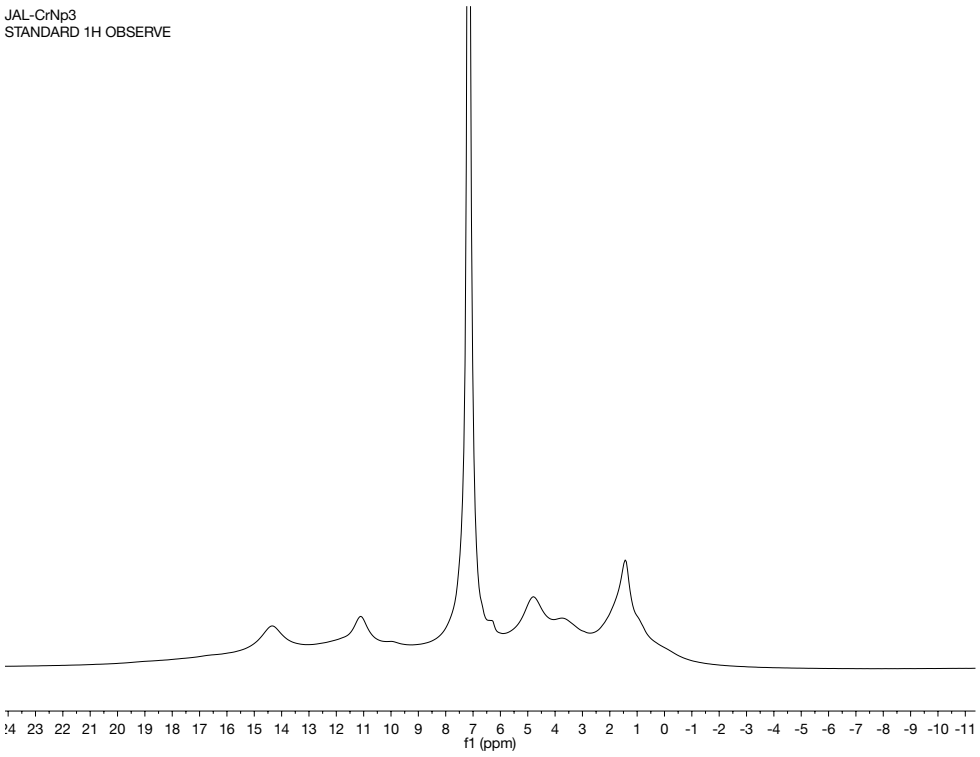

Figure 7.10. ^{1}H NMR of **7.1** in C_6D_6. Taken from JAL01013.

Synthesis of $Cr_2((2\text{-}Ph_2P)C_4H_3N)_4$, $Cr_2(\mu_2\text{-}NP)_4$ (7.2). Solid $CrCl_2$ (55.5 mg, 0.45 mmol, 1 equiv) and LiNP (232 mg, 0.90 mmol, 2 equiv) were dissolved in 5 mL of THF and let stir overnight. The volatiles of the resulting green solution were removed *in vacuo*. The solid was then extracted with benzene and filtered through celite. Single crystals of **7.2** were grown by slow evaporation of pentane into a benzene concentrated solution of **7.2**. ^{1}H NMR (300 MHz, C_6D_6) δ, ppm: 6.021 (s, 4H, aryl), 6.503 (m, 4H, aryl), 6.83-6.87 (m, 20H, aryl), 6.88-6.92 (m, 8H, aryl), 7.00-7.05 (m, 16H, aryl). ^{31}P NMR (121 MHz, C_6D_6) d, ppm: 0 to 3 (br, 4P).

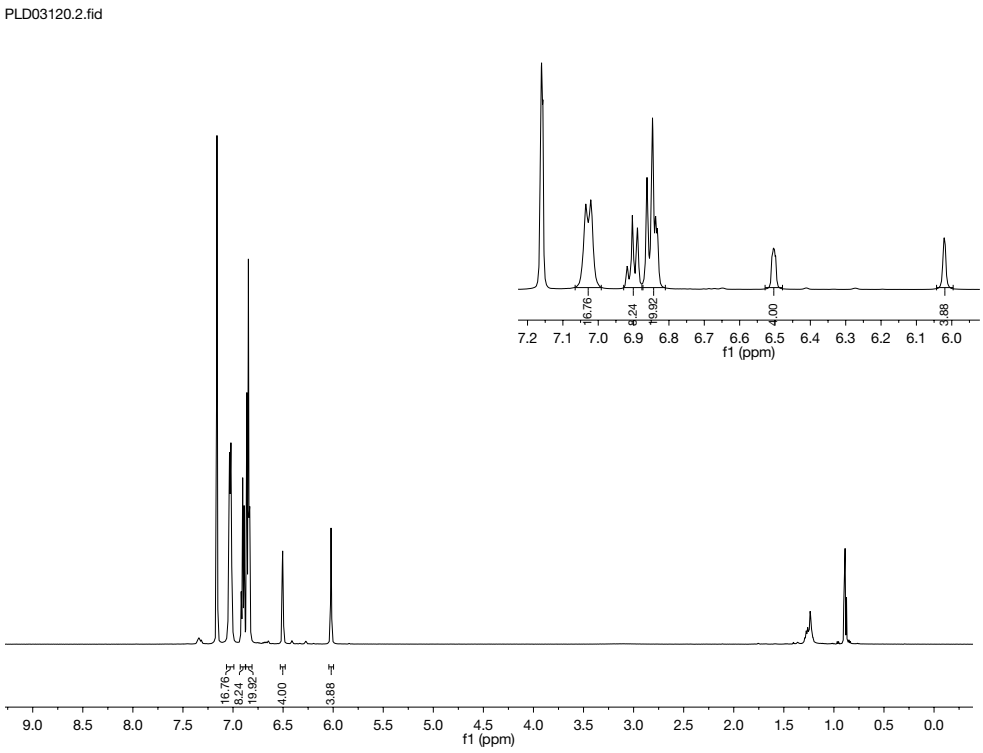

Figure 7.11. ^{1}H NMR of **7.2** in C_6D_6. Taken from PLD03120.

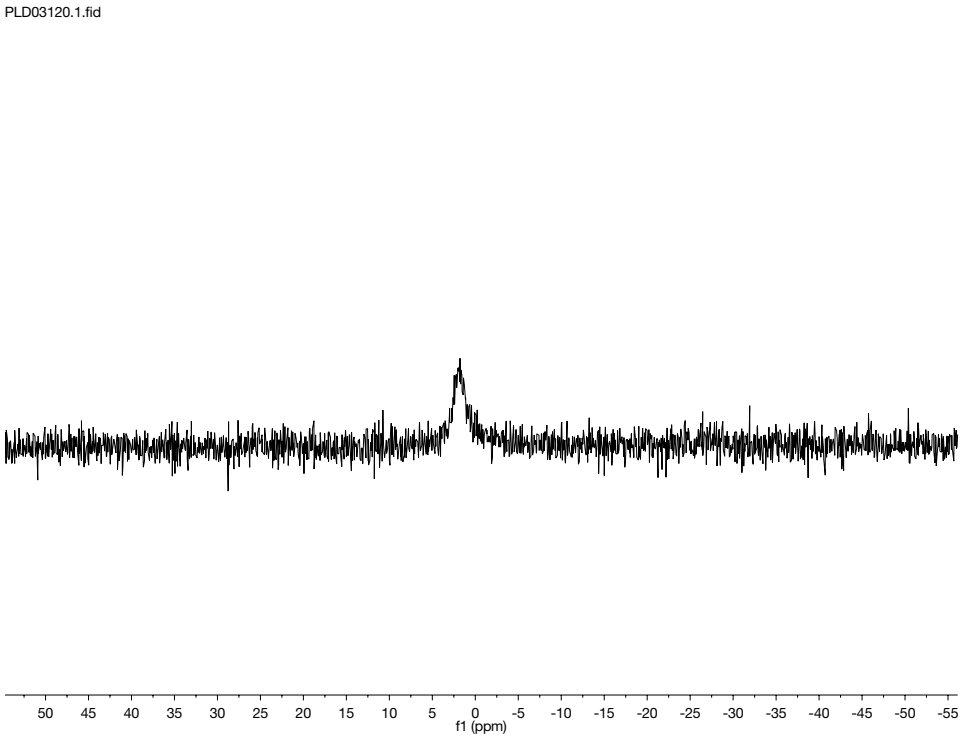

Figure 7.12. ^{31}P NMR of **7.2** in C_6D_6. Taken from PLD03120.

Synthesis of Mo((2-Ph$_2$P)C$_4$H$_3$N)$_4$, Mo(κ^2-NP)$_4$ (7.3). Solid $MoCl_5$ (25.5 mg, 0.0933 mmol, 1 equiv) and LiNP (127 mg, 0.495 mmol, 5.3 equiv) were dissolved in 5 mL THF and stirred overnight. The volatiles were removed *in vacuo* and the product extracted with benzene and filtered through celite. Single crystals were grown by slow evaporation of pentane into a concentrated benzene solution of crude **7.3.** ^{1}H NMR (300 MHz, C_6D_6) δ, ppm: -75 to -73 (br), -38.4 to -36 (br), -31 to -28.5 (br), 4.56- 5.34 (br), 9.90 to 10.84 (br), 11.1 to 12.6 (br).

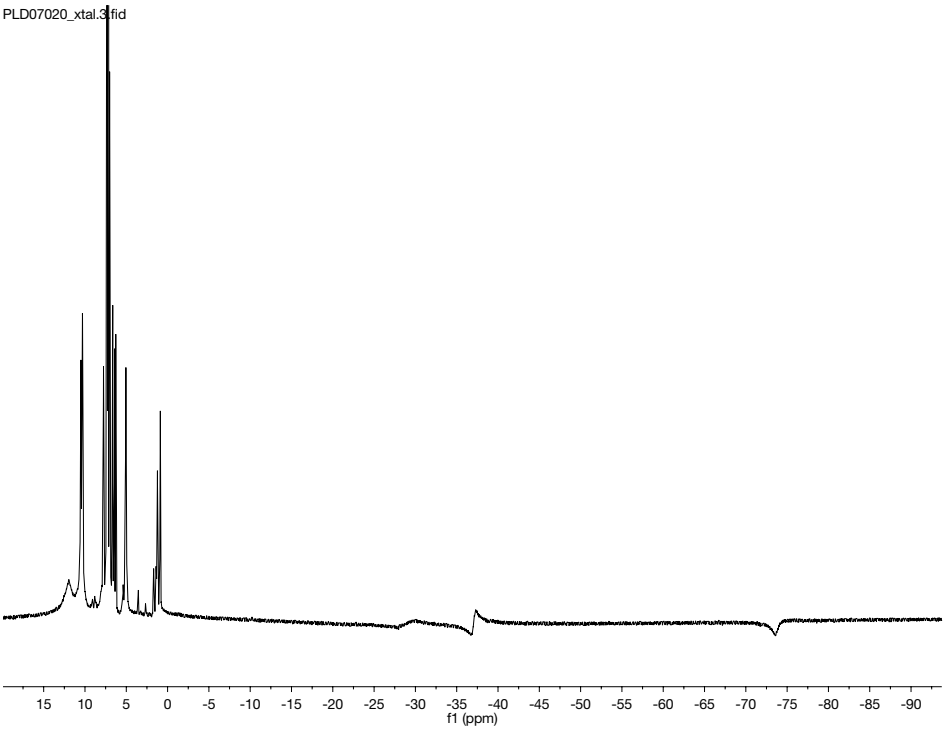

Figure 7.13: Crude ^{1}H NMR of **7.3** in C_6D_6. Taken from PLD07020.

Synthesis of W$_2$((2-Ph$_2$P)C$_4$H$_3$N)$_4$, W$_2$(μ$_2$-NP)$_4$ (7.4). Solid WCl_4 (184 mg, 0.565 mmol, 2 equiv) and LiNP (292 mg, 1.13 mmol, 4 equiv) were dissolved in 5 mL of THF and cooled to -35 °C. KC_8 (150 mg, 1.13 mmol, 4 equiv) was added and the reaction is allowed to warm to room temperature over two hours. Volatiles were removed under reduced pressure and the product is extracted with benzene through celite and dried *in vacuo*. Single crystals were grown by slow evaporation of pentane into a concentrated

benzene solution of crude **7.4.** ^{1}H NMR data cannot be provided at this time. ^{31}P NMR (121 MHz, C_6D_6) δ, ppm: 25.90 (t, J_{WP} = 323 Hz, 4P).

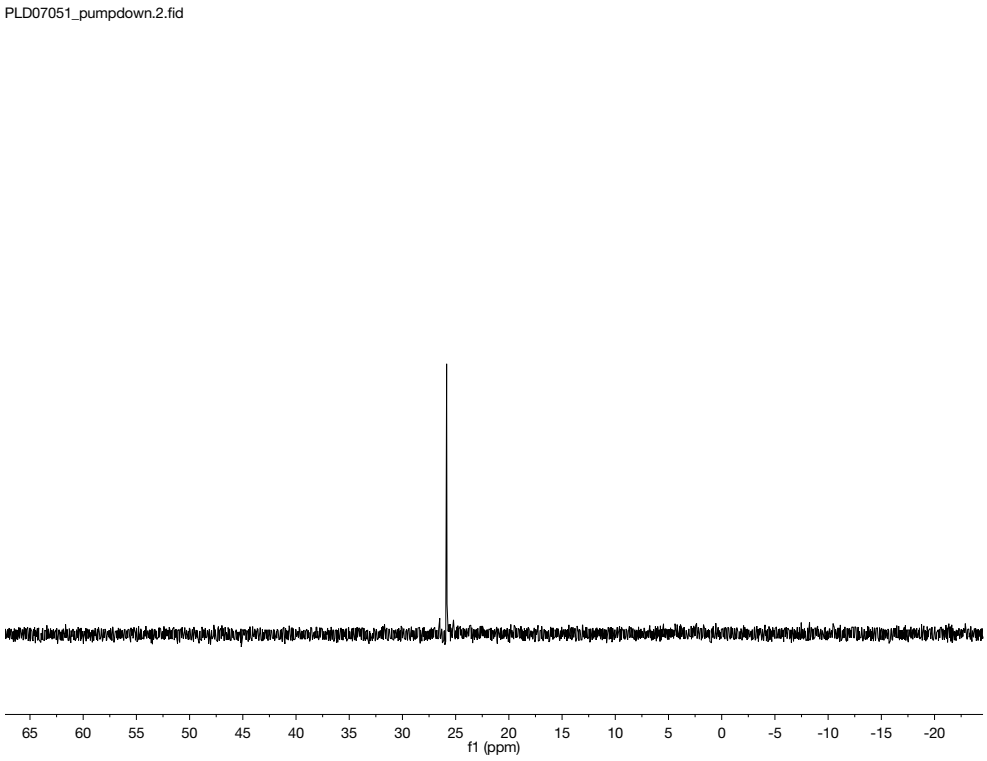

Figure 7.14: ^{31}P NMR of **7.3** in C_6D_6. Taken from PLD07051.

Synthesis of (κ^1-NP)W(κ^2-NP)$_2$(NTolyl) (7.5)

Solid W(NTolyl)$Cl_4(Et_2O)$ (166 mg, 0.33 mmol, 1 equiv) was dissolved in 5 mL benzene and solid LiNP (423 mg, 1.32 mmol, 4 equiv) was added. The solution was stirred overnight. The dark red/brown solution was then filtered over celite. Volatiles were removed to leave a red/brown powder, which was taken up in benzene and layered with pentane. The resulting solution was allowed to rest for 3 days. The red/brown precipitate was then filtered over a fine frit, washed with pentanes, and dried to yield 260 mg (75% yield) of **7.5** as a dark red/brown powder. Single crystals were grown by slow evaporation of pentane into a concentrated benzene solution of crude **7.5**. ^{1}H NMR

(300MHz, C_6D_6) δ, ppm: 5.46 to 5.71 (br), 5.86 to 6.08 (br), 6.8 to 7.4 (br), 7.9 to 8.7 (br).

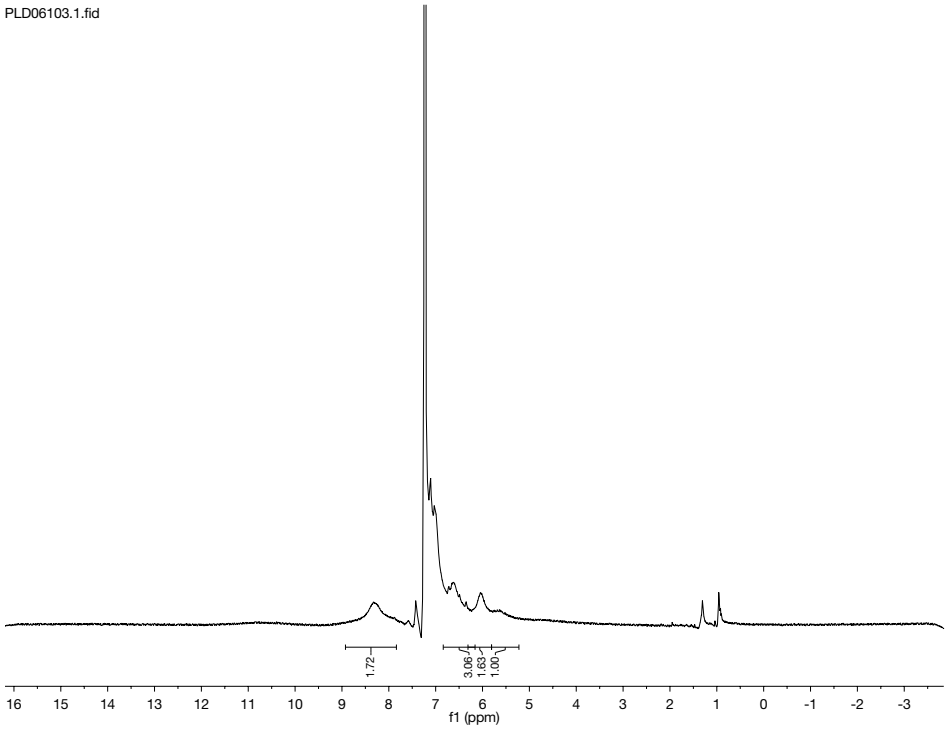

Figure 7.15. ^{1}H NMR of **7.5** in C_6D_6**.** Taken from PLD06103.

Synthesis of Mo(κ^{2}NPNTolyl)(κ^2-NP)$_2$, (7.6)

Solid $MoCl_4$(NTolyl)(THF) (33 mg, 0.096 mmol, 1 equiv) and LiNP (111 mg, 0.43 mmol, 4.5 equiv) were dissolved in 5 mL of benzene and stirred overnight. The solution was filtered over celite and volatiles were removed *in vacuo*. Single crystals were grown by slow evaporation of pentane into a concentrated benzene solution of crude **7.6.** ^{1}H NMR data cannot be provided.

Synthesis of Mo(NDipp)(κ^2-NPNDipp)(κ^2-NP), (7.7)

Solid $MoCl_2$(NDipp)$_2$(DME) (111.8 mg, 0.199 mmol, 1 equiv.) and LiNP (102.5 mg, 0.398 mmol, 2 equiv.) were dissolved in 5 mL of benzene and stirred overnight. The crude solution was filtered through celite and volatiles were removed *in vacuo*. Single crystals were grown by slow evaporation of pentane into a concentrated benzene solution

of crude **7.7.** ^{1}H NMR (300MHz, C_6D_6) δ, ppm: -0.050 (d, 3H, methyl), 0.225 (d, 3H, methyl), 0.479 (d, 3H, methyl), 0.566(d, 3H, methyl), 0.716 (d, 3H, methyl), 1.245 (d, 3H, methyl), 1.334 (d, 3H, methyl), 1.429 (d, 3H, methyl), 2.82-2.84 (m, 1H, methine), 3.024 (septet, 1H, methine), 3.757 (septet, 1H, methine), 6.058 (dq, 1H, aryl), 6.468 (ddd, 1H, aryl), 6.684 (m, 3H, aryl), 6.81-7.14 (m, 19H, aryl), 7.243 (m, 1H, aryl), 7.60-7.70 (m, 5H, aryl), 7.85-7.93 (m, 4H, aryl). ^{31}P NMR (121 MHz, C_6D_6) δ, ppm: 8.60 (s, 1P), 31.77 (s, 1P).

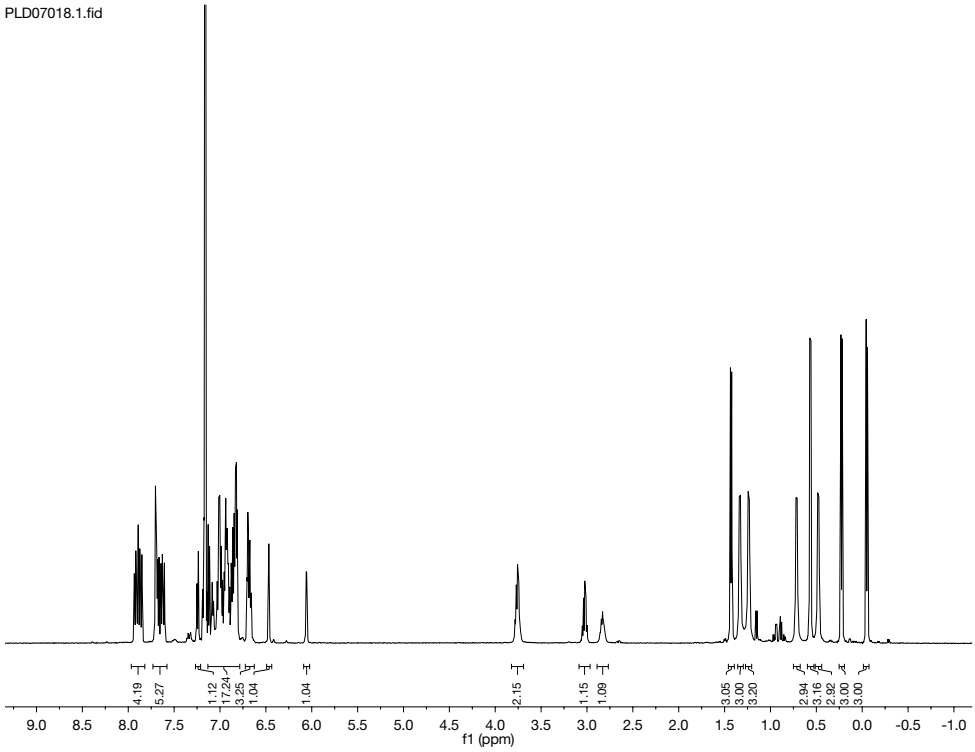

Figure 7.16: ^{1}H NMR of **7.7** in C_6D_6. Taken from PLD07018.

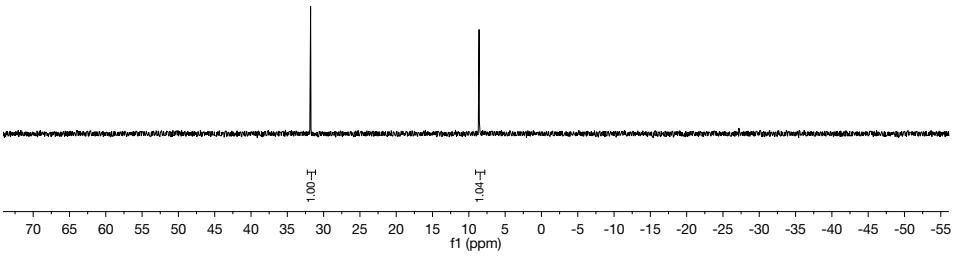

Figure 7.17: ^{31}P NMR of **7.7** in C_6D_6. Taken from PLD07018.

Synthesis of (κ^2-NP)(NTolyl)W(μ_2-NP)(μ_2-CO)Co(CO)$_2$, 7.8

Solid W(NP)$_3$(NTolyl) (25 mg, 0.024 mmol, 1 equiv.) and $Co_2(CO)_8$ (4.11 mg, 0.012 mmol, 1/2 equiv.) were dissolved in 0.5 mL of C_6D_6. CO is effervesced concurrent with a color change to deep red. Single crystals were grown by slow evaporation of pentane into a concentrated benzene solution of crude **7.8.** ^{1}H NMR (300MHz, C_6D_6) δ, ppm: 1.78 (s, 3H, tolyl), 6.10-6.31 (br, 6H, aryl), 6.41-6.44 (br, 1H), 6.48-6.52 (br, 2H), 6.56-6.75 (br, 10H), 6.78-6.82 (br, 1H), 6.83-7.05 (br, 14H), 7.23-7.29 (br, 3H), 7.55-7.67 (br, 6H), 7.89-7.94 (br, 2H), 8.59-8.62 (br, 1H), 8.77-8.81 (br, 1H). ^{31}P NMR (121 MHz, C_6D_6) δ, ppm: -31.69 (br, 1P), 24.14 (br, 1P), 38.1(br, 1P).

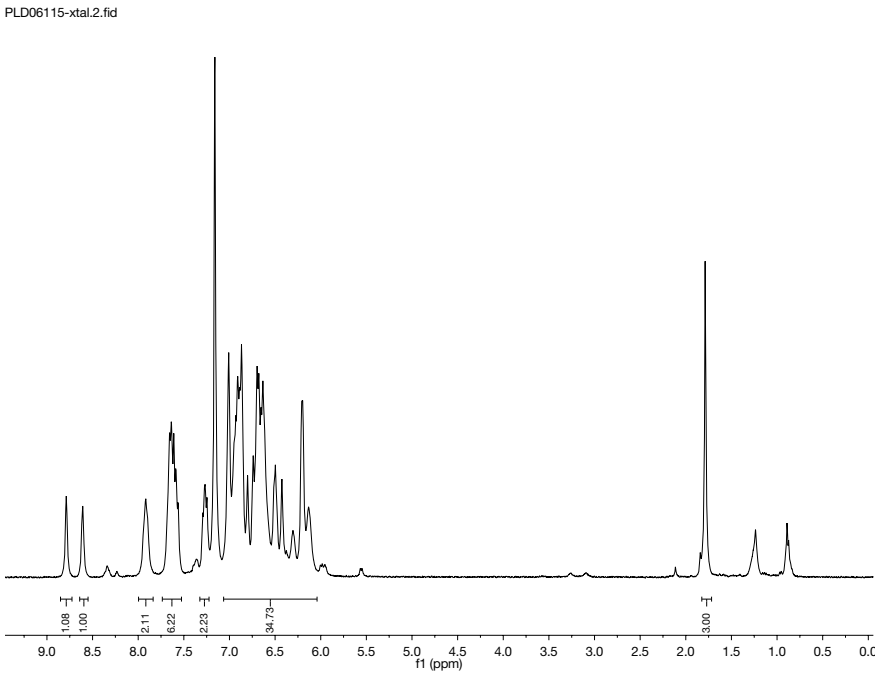

Figure 7.18: ^{1}H NMR of **7.8** in C_6D_6. Taken from PLD06115.

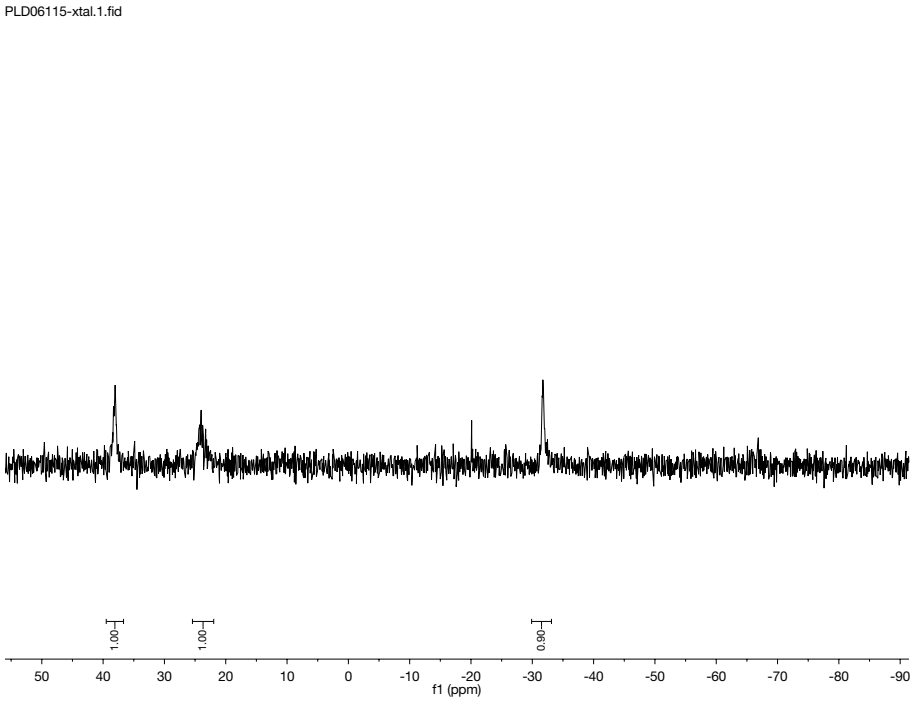

Figure 7.19: ^{31}P NMR of **7.8** in C_6D_6. Taken from PLD06115.

Synthesis of (NTolyl)(κ^2-NP)W(μ_2-NP)$_2$Fe(CO)$_3$, 7.10

Solid W(NP)$_3$(NTolyl) (55 mg, 0.053 mmol, 1 equiv.) and Fe(CO)$_5$ (10.5 mg, 0.053 mmol, 1 equiv.) were dissolved in 0.5 mL of C_6D_6 in a J. Young tube. The sample was exposed to a UV source overnight. Single crystals were grown by slow evaporation of pentane into a concentrated benzene solution of crude **7.10.** ^{1}H NMR (300MHz, C_6D_6) δ, ppm: 6.41-6.56 (br), 6.57-6.80 (br), 7.27-7.50 (br), 7.51-8.17 (br).

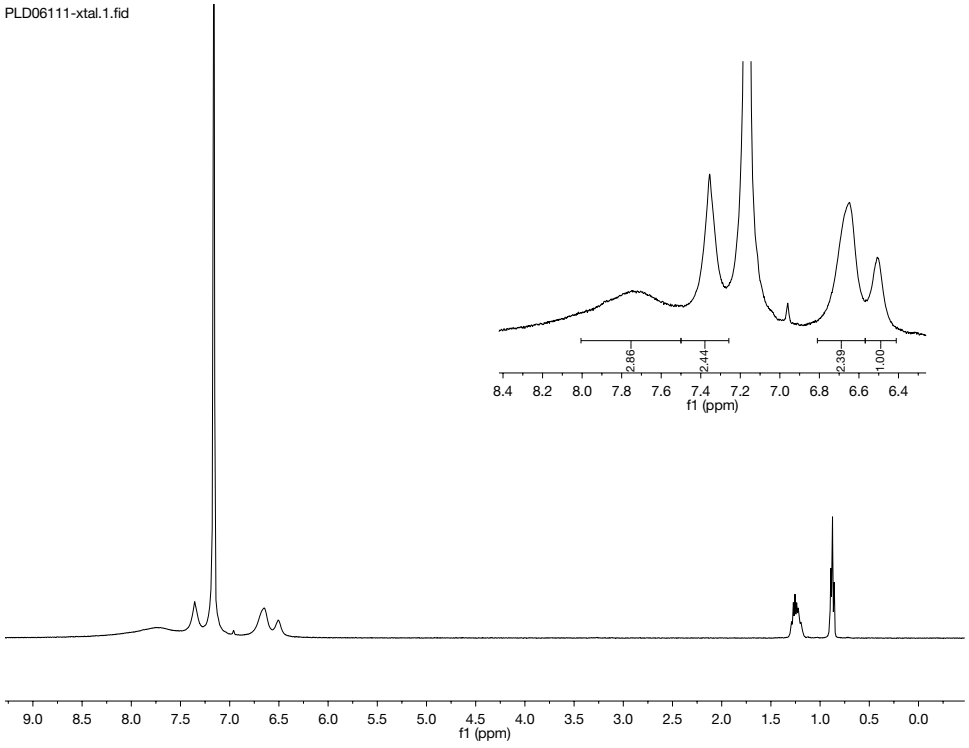

Figure 7.20: ^{1}H NMR of **7.10** in C_6D_6. Taken from PLD06111.

Table 7.4. Crystal and refinement data for complexes **7.1-7.4**.

	7.1	**7.2**	**7.3**	**7.4**
CCDC Number	1841981	1841982	1841983	1841984
Empirical Formula	$CrN_3P_3C_{48}H_{39}$ • C_7H_8	$C_{64}H_{52}N_4P_4Cr_2$ • 2.5(C_6H_6)	$C_{64}H_{52}N_4P_4Mo$ • C_6H_6	$C_{64}H_{52}N_4P_4W_2$ • 3(C_6H_6)
Formula weight	894.87	1300.25	1175.03	1602.98
T (K)	123(2)	123(2)	123(2)	100(2)
a, Å	16.6888(7)	17.058(2)	13.44300	12.50800
b, Å	21.7123(9)	23.557(3)	18.47900	25.95100
c, Å	77.115(3)	33.302(4)	22.52000	20.73500
α, deg	90	90	90	90
β, deg	90	90	95.5200	90.9000
γ, deg	90	90	90	90
Volume, Å^3	27943(2)	13382(3)	5568.323	6729.649
Z	24	8	4	4
Crystal System	Orthorhombic	Orthorhombic	Monoclinic	Monoclinic
Space Group	Pbca	Pbca	P2(1)/n	P2(1)/n
d_{calc}, g/cm^3	1.276	1.291	1.402	1.582
θ Range, deg	2.293 to 72.157	2.169 to 22.644	2.378 to 29.217	2.2585 to 29.529
μ, mm^{-1}	3.301	0.468	0.399	3.561
Abs. Correction	Multi-scan	Multi-scan	Multi-scan	Multi-scan
GOF	1.034	1.087	1.076	1.126
R_1 ,[a]	R1 = 0.0644	R1 = 0.0414	R1 = 0.0446	R1 = 0.0395
wR_2 [b] [I>2σ (I)]	wR2 = 0.1640	wR2 = 0.1211	wR2 = 0.1181	wR2 = 0.0939

[a] $R_1 = \sum||F_o| - |F_c||/\sum|F_o|$. [b] $wR_2 = [\sum[w(F_o^2-F_c^2)^2]/\sum[w(F_o^2)^2]]^{1/2}$.

Table 7.5. Crystal and refinement data for complexes **7.5-7.8**.

	7.5	**7.6**	**7.7**	**7.8**
CCDC Number	1841978	1841975	1841980	1841979
Empirical Formula	$C_{55}H_{46}N_4P_3W$ • C_6H_6	$C_{55}H_{46}N_4P_3Mo$ • 0.5 (C_6H_6)	$C_{56}H_{60}N_4P_2W$ • C_6H_6	$C_{58}H_{47}N_4O_3P_3WCo$ • 2 (C_6H_6)
Formula weight	1117.82	990.86	1025.07	1339.90
T (K)	123(2)	123(2)	123(2)	123(2)
a, Å	12.0423(8)	9.0478(5)	12.01500	10.2902(4)
b, Å	17.7401(11)	22.2409(14)	19.01500	12.6491(4)
c, Å	24.0961(17)	23.4281(14)	23.08900	20.7982(8)
α, deg	90	90	90	95.429(1)
β, deg	100.681(2)	91.431(2)	90	101.865(1)
γ, deg	90	90	90	100.738(1)
Volume, Å^3	5058.5(6)	4713.0(5)	5275.034	100.738(1)
Z	4	4	4	2
Crystal System	Monoclinic	Monoclinic	Orthorhombic	Triclinic
Space Group	P2(1)/c	P2(1)/n	P2(1)2(1)2(1)	P-1
d_{calc}, g/cm^3	1.468	1.396	1.291	1.4566
θ Range, deg	2.47 to 30.54	2.43 to 30.495	2.440 to 30.393	2.661 to 29.171
μ, mm^{-1}	2.423	0.420	0.353	2.695
Abs. Correction	Multi-scan	Multi-scan	Multi-scan	Multi-scan
GOF	1.112	1.039	1.093	1.067
R_1 ,[a]	R1 = 0.0331	R1 = 0.0562	R1 = 0.0462	R1 = 0.0448
wR_2 [b] [I>2σ (I)]	wR2 = 0.0971	wR2 = 0.1328	wR2 = 0.1151	wR2 = 0.1101

[a] $R_1 = \sum||F_o| - |F_c||/\sum|F_o|$. [b] $wR_2 = [\sum[w(F_o^2-F_c^2)^2]/\sum[w(F_o^2)^2]^{1/2}$.

Table 7.6. Crystal and refinement data for complexes **7.9-7.10**.

	7.9	**7.10**
CCDC Number	1841977	1841976
Empirical Formula	$C_{58}H_{47}N_4O_3P_3W$ • 2 (C_6H_6)	$C_{58}H_{46}N_4O_3P_3WFe$
Formula weight	1339.90	1179.59
T (K)	123(2)	123(2)
a, Å	12.7671(12)	16.9297(13)
b, Å	17.2113(13)	18.5771(16)
c, Å	27.226(3)	17.5446(16)
α, deg	90	90
βσ, deg	90	90.701(3)
γ, deg	90	90
Volume, Å^3	5982.6(10)	5517.4(8)
Z	4	4
Crystal System	Orthorhombic	Monoclinic
Space Group	P2(1)2(1)2(1)	P2(1)/n
d_{calc}, g/cm^3	1.488	1.420
θ Range, deg	2.370 to 30.498	2.408 to 32.633
μ, mm^{-1}	2.331	2.479
Abs. Correction	Multi-scan	Multi-scan
GOF	1.067	1.092
R_1 ,[a]	R1 = 0.0364	R1 = 0.0299
wR_2 [b] [I>2σ (I)]	wR2 = 0.0969	wR2 = 0.0681

[a] $R_1 = \sum||F_o| - |F_c||/\sum|F_o|$. [b] $wR_2 = [\sum[w(F_o^2-F_c^2)^2]/\sum[w(F_o^2)^2]^{1/2}$.

Bibliography

1.) Bullock, R. M. Catalysis without Precious Metals, Wiley, 201.

2.) Bolm, C. *Nat. Chem.* **2009**, 1, 420.

3.) Carin, C. C.; Seechurn, J.; Kitching, M. O.; Colacot, T. J.; Snieckus, V. *Angew. Chem. Int. Ed.* **2012**, 51, 5062.

4.) De Meijere, A.; Diederich, F. *Metal-Catalyzed Cross-Coupling Reactions*, Wiley-VCH, Weinheim 2004.

5.) Negishi, E.; De Meijere, A. *Handbook of Organopalladium Chemistry for Organic Synthesis*, Wiley, New York, 2002.

6.) Tsou, T. T.; Kochi, J. K. *J. Am. Chem. Soc.* **1979**, 101, 6319.

7.) Tsou, T. T.; Kochi, J. K. *J. Am. Chem. Soc*. **1979**, 101, 7547.

8.) Tamao, K.; Sumitani, K.; Kumada, M. *J. Am. Chem. Soc.* **1972**, *94*, 4374.

9.) Rosen, B.M.; Quasdorf, K.W.; Wilson, D.A.; Zhang, N.; Resmerita, A.-M.; Garg, N.K.; Percec, V. *Chem. Rev.* **2011**, *111*, 1346.

10.) Shi, S.; Meng, G.; Szostak, M. *Angew. Chem. Int. Ed.* **2016**, *55*, 6959.

11.) Tasker, S. Z.; Standley, E. A.; Jamison, T. F. *Nature* **2014**. 509, 299.

12.) Jana, R.; Pathak, T. P.; Sigman, M. S. *Chem. Rev*. **2011**, 111, 1417.

13.) Hu, X. *Chem. Sci*. **2011**, 2, 1867.

14.) Jones, G. D.; McFarland, C.; Anderson, T. J.; Vicic, D. D. *Chem. Commun.* **2005**, 4211.

15.) Jones, G. D.; Martin, J. L.; McFarland, C.; Allen, O. R.; Hall, R. E.; Haley, R. J.; Brandon, T.; Konovalova, P. J.; Desrochers, P.; Vicic, D. A. *J. Am. Chem. Soc.* **2006**, 128, 13175.

16.) Csok, Z.; Vechorkin, O.; Harkins, S. B.; Scopelliti, R.; Hu, X. L. *J. Am. Chem. Soc*. **2008**, 130, 8156.

17.) Vechorkin, O.; Csok, Z.; Scopelliti, R.; Hu, X. L. *Chem.–Eur. J*. **2009**, 15, 3889.

18.) Vechorkin, O. Ph.D. Thesis EPFL, Lausanne, 2011.

19.) Breitenfeld, O.; Vechorkin, C.; Corminboeuf, C.; Scopelliti, R.; Hu, X. L. *Organometallics*, **2010**, 29, 3686.

20.) Chirik, P. J.; Wieghardt, K. *Science* **2010**, 327, 794.

21.) Chirik, P. J. *Inorg. Chem*. **2011**, 50, 9737.

22.) Blackmore, K. J.; Ziller, J. W.; Heyduk, A. F. *Inorg. Chem*. **2005**, 44, 5559.

23.) Haneline, M. R.; Heyduk, A. F. *J. Am. Chem. Soc*. **2006**, 128, 8410.

24.) Small, B. L.; Brookhart, M.; Bennett, A. M. A. *J. Am. Chem. Soc*. **1998**, 120, 4049.

25.) Bart, S. C.; Chlopek, K.; Bill, E.; Bouwkamp, M. W.; Lobkovsky, E.; Neese, F.; Wieghart, K.; Chirik, P. J. *J. Am. Chem. Soc.*, **2006**, *128*, 13901.

26.) Bouwkamp, M. W.; Bowman, A. C.; Lobkovsky, E.; Chirik, P. J.; *J. Am. Chem. Soc*. **2006**, 128, 13340.

27.) Sylvester, K. T.; Chirik, P. J. *J. Am. Chem. Soc*. **2009**, 131, 8772.

28.) Smith, A. L.; Hardcastle, K. I.; Soper, J. D. *J. Am. Chem. Soc*. **2010**, 132, 14358.

29.) Chaudhuri, P.; Hess, M.; Müller, K.; Hildenbrad, K., Bill, E.; Weyhermüller, T.; Wieghardt, K. *J. Am. Chem. Soc*. **1999**, 121, 9599.

30.) Frazier, B. A.; Wolczanski, P. T.; Keresztes, I.; Debeer, S.; Lobkovsky, E. B.; Pierpont, A. W.; Cundari, T. R. *Inorg. Chem*. **2012**, 51, 8177

31.) Volpe, E. C.; Wolczanski, P. T.; Darmon, J. M.; Lobkovsky, E. B. *Polyhedron* **2013**, 52, 406.

32.) Williams, V. A.; Hulley, E. B.; Wolczanski, P. T.; Lancaster, K. M.; Lobkovsky, E. B. *Chem. Sci*. **2013**, 4, 3636.

33.) Williams, V. A.; Wolczanski, P. T.; Sutter, J.; Meyer, K.; Lobkovsky, E. B.; Cundari, T. R. *Inorg. Chem*. **2014**, 53, 4459.

34.) Feller, M.; Ben-Ari, E.; Diskin-Posner, Y.; Carmieli, R.; Weiner, L.; Milstein, D. *J. Am. Chem. Soc*. **2015**, 137, 4634.

35.) Zell, T.; Milstein, D. *Acc. Chem. Res*. **2015**, 48, 1979.

36.) Gunanathan, C.; Milstein, D. *Chem. Rev.* **2015**, 114, 12024.

37.) Noyori, R.; Ohta, M.; Hsiao, Y.; Kitamura, M.; Ohta, T.; Takaya, H. *J. Am. Chem. Soc.* **1986**, 108, 7117.

38.) Ohkuma, T.; Koizumi, M.; Doucet, H.; Pham, T.; Kozawa, M.; Murata, K.; Katayama, E.; Yokozawa, T.; Ikariya, T.; Noyori, R. *J. Am. Chem. Soc.* **1998**, 120, 13529.

39.) Ohkuma, T.; Ooka, H.; Ikariya, T.; Noyori, R. *J. Am. Chem. Soc.* **1995**, 117, 10417.

40.) Ohkuma, T.; Ikehira, H.; Ikariya, T.; Noyori, R. *Synlett* **1997**, 467.

41.) Shvo, Y.; Czarkie, D.; Yochevedm, R.; Chodosh, D. F. *J. Am. Chem. Soc*. **1986**, 108, 23, 7400.

42.) Conley, B. L.; Pennington-Boggio, M. K.; Boz, E.; Williams, T. J. *Chem. Rev*. **2010**, 110, 2294.

43.) Casey, C. P.; Singer, S. W.; Powell, D. R.; Hayashi, R. K., Kavana, M. *J. Am. Chem. Soc.* **2001**, 123, 1090

44.) Pang, K.; Tanski, J. M.; Parkin, G. *Chem. Commun.* **2008**, 1008.

45.) Harman, W. H.; Peters, J. C. *J. Am. Chem. Soc.* **2012**, 134, 5080.

46.) Harman, W. H.; Lin, T. P.; Peters, J. C. *Angew. Chem., Int. Ed*. **2014**, 53, 1081.

47.) Mazzacano, T. J.; Mankad, N. P. *J. Am. Chem. Soc*. **2013**, 135, 17258.

48.) Karunananda, M. K.; Mankad, N. P. *J. Am. Chem. Soc*. **2015**, 137, 14598.

49.) Pye, D. R.; Cheng, L.-J.; Mankad, N. P. *Chem. Sci.* **2017**, 8, 4750.

50.) Thomas, C. M.; Napoline, J. W.; Rowe, G. T.; Foxman, B. M. *Chem. Commun*. **2010**, 46, 5790.

51.) Zhou, W.; Napoline, J. W.; Thomas, C. M. *Eur. J. Inorg. Chem.* **2011**, 2011, 2029.

52.) Wu, B.; Hernandez Sanchez, R.; Bezpalko, M. W.; Foxman, B. M.; Thomas, C. M. *Inorg. Chem.* **2014**, 53, 10021.

53.) Marquard, S. L.; Bezpalko, M. W.; Foxman, B. M.; Thomas, C. M. *J. Am. Chem. Soc.* **2013**, 135, 6018.

54.) Krogman, J. P.; Foxman, B. M.; Thomas, C. M. *J. Am. Chem. Soc*. **2011**, 133, 14582.

55.) Wu, B.; Bezpalko, M. W.; Foxman, B. M.; Thomas, C. M. *Chem. Sci.* **2015**, 6, 2044.

56.) Cammarota, R. C.; Lu, C. C. *J. Am. Chem. Soc.* **2015**, 137, 12486.

57.) Cammarota, R. C.; Vollmer, M. V.; Xie, J.; Ye, J.; Linehan, J. C.; Burgess, S. A.; Appel, A. M.; Gagliardi, L.; Lu, C. C. *J. Am. Chem. Soc*. **2017**, 139.

58.) Siedschlag, R. B.; Bernales, V.; Vogiatzis, K. D.; Planas, N.; Clouston, L. J.; Bill, E.; Gagliardi, L.; Lu, C. C. *J. Am. Chem. Soc.* **2015**, 137, 4638.

59.) L. J. Clouston, V. Bernales, R. K. Carlson, L. Gagliardi, C. C. Lu, *Inorg. Chem.*

2015, 54, 9263.

60.) Tsutsumi, H.; Sunada, Y.; Shiota, Y.; Yoshizawa, K.; Nagashima, H. *Organometallics* **2009**, 28, 1988.

61.) Walker, W. K.; Kay, B. M.; Michaelis, S. A.; Anderson, D. L.; Smith, S. J.; Ess, D. H.; Michaelis, D. J. *J. Am. Chem. Soc.* **2015**, 137, 7371.

62.) Berry, J. F. *J. Chem. Sci.* **2015**, 127, 209.

63.) Kornecki, K. P.; Briones, J. F.; Boyarskikh, V.; Fullilove, F.; Autschbach, J.; Schrote, K. E.; Lancaster, K. M.; Davies, H. M. L.; Berry, J. F. *Science* **2013**, 342, 351.

64.) Berry, J. F. *Dalton Trans.* **2012**, 41, 700.

65.) Cotton, F. A.; Murillo, C. A.; Walton, R. A. Multiple Bonds Between Metal Atoms, Springer Science and Business Media, Inc., New York, 2005.

66.) Collman, J. P.; Boulatov, R. *Angew. Chem. Int. Ed.* **2002**, 41, 3948.

67.) Chisholm, M. H. *Chem. Rev.* **2000**, 1, 12.

68.) Roizen, J. L.; Harvey, M. E.; Du Bois, J. *Acc. Chem. Res.* **2012**, 45, 911.

69.) Kornecki, K. P.; Berry, J. F.; Powers, D. C.; Ritter, T.; *Prog. Inorg. Chem.* **2014**, 58, 223.

70.) Powers, D. C.; Ritter, T. *Acc. Chem. Res.* **2012**, 45, 840.

71.) Durrell, A. C.; Jackson, M. N.; Nazari, N.; Gray, H. B.; *Eur. J. Inorg. Chem.* **2013**, 7, 1134.

72.) Hruszkewycz, D. P.; Wu, J.; Hazari, N.; Incarvito, C. D. *J. Am. Chem. Soc.* **2011**, 133, 3280.

73.) Van den Beuken, D. P.; Feringa, B. L.; *Tetrahedron* **1988**, 54, 12985.

74.) Powers, T. M.; Betley, T. A. *J. Am. Chem. Soc*. **2013**, 135, 12289.

75.) Kanady, J. S.; Mendoza-Cortes, J. L.; Tsui, E. Y.; Nielsen, R. J.; Goddard III, W. A.; Agapie, T. *J. Am. Chem. Soc.* **2013**, 135, 1073.

76.) Lionetti, D.; Day, M. W.; Agapie, T. *Chem. Sci.* **2013**, 4, 785.

77.) Anderson, J. S.; Rittle, J.; Peters, J. C. *Nature* **2013**, 501, 84.

78.) Stephan, D. W. *Coord. Chem. Rev.* **1989**, 95, 41.

79.) Wheatley, N.; Kalck, P. *Chem. Rev.* **1999**, 99, 3379.

80.) Cooper, B. G.; Napoline, J. W.; Thomas, C. M. *Catal. Rev. Sci. Eng.* **2012**, 54, 1.

81.) Kühl, O.; Blaurock, S.; Sieler, J.; Hey-Hawkins, E. *Polyhedron* **2001**, 20, 2171.

82.) Ferguson, G. S.; Wolczanski, P. T.; Párkányi, L.; Zonnevylle, M. C. *Organometallics,* **1988***,* 7, 1967.

83.) Slaughter, L. M.; Wolczanski, P. T. *Chem. Commun.* **1997**, 2109.

84.) Diaconescu, P. L. *Comments Inorg. Chem.* **2010**, 31, 196.

85.) Diaconescu, P. L. *Acc. Chem. Res.* **2010**, 43, 1352.

86.) Schubart, M.; Mitchel, G.; Gade, L. H.; Kottke, T.; Scowen, I. J.; McPartlin, M. *Chem. Commun.* **1999**, 233.

87.) Nagashima, H.; Sue, T.; Oda, T.; Kanemitsu, A.; Matsumoto, T.; Motoyama, Y.; Sunada, Y. *Organometallics* **2006**, 25, 1987.

88.) Sunada, Y.; Sue, T.; Matsumoto, T.; Nagashima, H. *J. Organomet. Chem.* **2006**, 691, 3176.

89.) Sue, T.; Sunada, Y.; Nagashima, H. *Eur. J. Inorg. Chem.* **2007**, 2897.

90.) Tsutsumi, H.; Sunada, Y.; Shiota, K.; Yoshizawa, K.; Nagashima, H. *Organometallics* **2009**, 28, 1988.

91.) Amgoune, A.; Bourissou, D. *Chem. Commun.* **2011**, 47, 859.

92.) Hill, A. F.; Owen, G. R.; White, J. P.; Williams, D. J. *Angew. Chem. Int. Ed.* **1999**, 38, 2759.

93.) Figueroa, J. S.; Melnick, J. G.; Parkin, G. *Inorg. Chem.* **2006**, 45, 7056.

94.) Pang, K.; Quan, S. M.; Parkin, G. *Chem. Commun.* **2006,** 5015.

95.) Pang, K.; Tanski, J. M.; Parkin, G. *Chem. Commun.* **2008,** 1008.

96.) Rudd, P. A.; Liu, S.; Gagliardi, L.; Young Jr, V. G.; Lu, C. C. *J. Am. Chem. Soc.* **2011**, 133, 2072.

97.) Rudd, P. A.; Planas, N.; Bill, E.; Gagliardi, L.; Lu, C. C. *Eur. J. Inorg. Chem.* **2013**, 3898.

98.) Greenwood, B. P.; Forman, S. I.; Rowe, G. T.; Chen, C. -H.; Foxman, B. M.; Thomas, C. M. *Inorg. Chem.* **2009**, 48, 6251.

99.) Greenwood, B. P.; Rowe, G. T.; Chen, C. -H.; Foxman, B. M.; Thomas, C. M. *J. Am. Chem. Soc.* **2010**, 132, 44.

100.) Cooper, B. G.; Fafard, C. M.; Foxman, B. M.; Thomas, C. M. *Organometallics* **2010**, 29, 5179.

101.) Thomas, C. M. *Comments Inorg. Chem.* **2011**, 32, 14.

102.) Thomas, C. M.; Napoline, J. W.; Rowe, G. T.; Foxman, B. M. *Chem. Commun*. **2010**, 46, 5790.

103.) Zhou, W.; Napoline, J. W.; Thomas, C. M. *Eur. J. Inorg. Chem.* **2011**, 2029.

104.) Krogman, J. P.; Foxman, B. M.; Thomas, C. M. *J. Am. Chem. Soc.* **2011**, 133, 14582.

105.) Zhou, W.; Marquard, S. L.; Bezpalko, M. W.; Foxman, B. M.; Thomas, C. M. *Organometallics* **2013**, 32, 1766.

106.) Napoline, J. W.; Krogman, J. P.; Shi, R.; Kuppuswamy, S.; Bezpalko, M. W.; Foxman, B. M.; Thomas, C. M. *Eur. J. Inorg. Chem.* **2013**, 3874.

107.) Napoline, J. W.; Bezpalko, M. W.; Foxman, B. M.; Thomas, C. M. *Chem. Commun.* **2013** 49, 4388.

108.) Krogman, J. P.; Thomas, C. M. *Chem. Commun*. **2014**, 50, 5115.

109.) Zall, C. M.; Zherebetskyy, D.; Dzubak, A. L.; Bill, E.; Gagliardi, L.; Lu, C. C. *Inorg. Chem.* **2012**, 51, 728.

110.) Rudd, P. A.; Liu, S.; Planas, N.; Bill, E.; Gagliardi, L.; Lu, C. C. *Angew. Chem. Int. Ed.* **2013***,* 52, 4449.

111.) Zall, C. M.; Clouston, L. J.; Young, V. G., Jr.; Ding, K.; Kim, H. J.; Zherebetsky, D.; Cheng, Y.-S.; Bill, E.; Gagliardi, L.; Lu, C. C. *Inorg. Chem.* **2013**, 52, 9216.

112.) Clouston, L. J.; Siedschlag, R. B.; Rudd, P. A.; Planas, N.; Hu, S.; Miller, A. D.; Gagliardi, L.; Lu, C. C. *J. Am. Chem. Soc.* **2013**, 135, 13142.

113.) Tereniak, S. J.; Carlson, R. K; Clouston, L. J.; Young, V. G., Jr.; Bill, E.; Maurice, R.; Cheng, Y.-S.; Kim, H. J.; Gagliardi, L.; Lu. C. C. *J. Am. Chem. Soc.* **2014**, 136, 1842.

114.) Kuppuswamy, S.; Cooper, B. G.; Bezpalko, M. W.; Foxman, B. M.; Powers, T. M.; Thomas, C. M. *Inorg. Chem.* **2012**, 51, 1866.

115.) Kuppuswamy, S.; Bezpalko, M. W.; Powers, T. M.; Turnbull, M. M.; Foxman, B. M.; Thomas, C. M. *Inorg. Chem.* **2012**, 51, 8225.

116.) Kuppuswamy, S.; Powers, T. M.; Johnson, B. M. J.; Bezpalko, M. W.; Brozek, C. K.; Foxman, B. M.; Berben, L. A.; Thomas, C. M. *Inorg. Chem.* **2013**, *52*, 4802.

117.) Mathialagan, R.; Kuppuswamy, S.; De Denko, A. T.; Bezpalko, M. W.; Foxman, B. M.; Thomas, C. M. *Inorg. Chem.* **2013**, *52*, 701.

118.) Kuppuswamy, S.; Powers, T. M.; Krogman, J. P.; Bezpalko, M. W.; Foxman, B. M.; Thomas, C. M. *Chem. Sci.* **2013**, *4*, 3557.

119.) Bradley, D. C.; Thomas, L. M.; *J. Chem. Soc.* **1960**, 3857.

120.) Benzing, E.; Kornicker, W. *Chem. Ber.* **1961**, 94, 2263.

121.) Semmelhack, M. F.; Chlenov, A.; Ho, D. M. *J. Am. Chem. Soc.* **2005**, 127, 7759.

122.) Allen, D. W.; Charlton, J. R.; Hutley, B. G. *Phosphorus* **1976**, 6, 191.

123.) Bruno, I. J.; Cole, J. C.; Edgington, P. R.; Kessler, M.; Macrae, C. F.; McCabe, P.; Pearson, J.; Taylor, R. *Acta Cryst*. B58 (2002) 389-397. Searches conducted March 2014.

124.) Kozak, C. M.; Mountford, P. *Zirconium & Hafnium: Inorganic & Coordination Chemistry* in *Encyclopedia of Inorganic Chemistry*, Wiley (2006).

125.) Hoard, J. L.; Silverton, J. V. *Inorg. Chem.* **1963**, 2, 235.

126.) Lippard, S. J.; Russ, B. J. *Inorg. Chem.* **1968**, 7, 1686.

127.) Kühl, O.; Koch, T.; Somoza Jr., F. B.; Junk, P. C.; Hey-Hawkins, E.; Plat, D.; Eisen, M. S. *J. Organomet. Chem.* **2000**, 604, 116.

128.) Bonds Jr., W. D.; Archer, R. D. *Inorg. Chem.* **1971**, 10, 2057.

129.) Takashima, Y.; Nakayama, Y.; Hashiguchi, M.; Hosada, T.; Yasuda, H.; Hirao, T.; Harada, A. *Polymer* **2006**, 47, 5762.

130.) Gielen, M.; Willem, R.; Wrackmeye, B. *Fluxional Organometallic Coordination Compounds*, Wiley (2008).

131.) Dunn, P. L.; Reath, A. H.; Clouston, L. J.; Young Jr., V. G.; Tonks, I. A. *Polyhedron*, **2014**, 84, 111.

132.) Setty, V. N.; Zhou, W.; Foxman, B. M.; Thomas, C. M. *Inorg. Chem.* **2011**, *50*, 4647.

133.) Eisenhart, R. J.; Clouston, L. J.; Lu, C. C. *Acc. Chem. Res.* **2015**, 48, 2885.

134.) Wender, P. A.; Smith, T. E. *EROS Encyclopedia of Reagents for Organic Synthesis*. 2001.

135.) Manxzer, L. E.; Deaton, J.; Sharp, P.; Schrock, R. R. Inorganic Syntheses **1982**, 21.

136.) Gaussian 09, Revision, Frisch, M. J.; Trucks, G.W.; Schlegel, H. B.; Scuseria, G. E.; Robb, M. A.; Cheeseman, J. R.; Scalmani, G.; Barone, V.; Mennucci, B.;

Petersson, G. A.; Nakatsuji, H.; Caricato, M.; Li, X.; Hratchian, H. P.; Izmaylov, A. F.; Bloino, J.; Zheng, G.; Sonnenberg, J. L.; Hada, M.; Ehara, M.; Toyota, K.; Fukuda, R.; Hasegawa, J.; Ishida, M.; Nakajima, T.; Honda, Y.; Kitao, O.; Nakai, H.; Vreven, T.; Montgomery Jr., J. A.; Peralta, J. E.; Ogliaro, F.; Bearpark, M.; Heyd, J. J.; Brothers, E.; Kudin, K. N.; Staroverov, V. N.; Kobayashi, R.; Normand, J,; Raghavachari, K.; Rendell, A.; Burant, J. C.; Iyengar, S. S.; Tomasi, J.; Cossi, M.; Rega, N.; Millam, J. M.; Klene, M.; Knox, J. E.; Cross, J. B.; Bakken, V.; Adamo, C.; Jaramillo, J.; Gomperts, R.; Stratmann, R. E.; Yazyev, O.; Austin, A. J.; Cammi, R.; Pomelli, C.; Ochterski, J. W.; Martin, R. L.; Morokuma, K.; Zakrzewski, V. G.; Voth, G. A.; Salvador, P.; Dannenberg, J. J.; Dapprich, S.; Daniels, A. D.; Farkas, O.; Foresman, J. B.; Ortiz, J. V.; Cioslowski, J.; Fox, D. J., Gaussian, Inc., Wallingford CT, 2009.

137.) Zhao, Y.; Truhlar, D. G. *J. Chem. Phys.* **2006**, 125, 194101.

138.) A.) McLean, A. D.; Chandler, G. S. *J. Chem. Phys.* **1980,** 72 ,5639. B.) Raghavachari, K.; Binkley, J. S.; Seeger, R.; Pople, J, A. *J. Chem. Phys*. **1980**, 72, 650. C.) Wachters, A. J. H. *J. Chem. Phys*. **1970**, 52, 1033. D.) Hay, P. J. *J. Chem. Phys*. **1977**, 66, 4377. E.) Clark, T.; Chandrasekhar, J.; Spitznagel, G. W.; Schleyer, G. W. *J. Comp. Chem*. **1983**, 4 , 294. F.) Frisch, M. J.; Pople, J. A., Binkley, J. S.; *J. Chem. Phys*. **1984**, 80, 3265.

139.) Hariharan, P. C.; Pople, J. A. *Theor. Chem. Acc*. **1973**, 28 , 213.

140.) Hehre, W. J.; Ditchfield, R. Pople, J. A. *J. Chem. Phys*. **1972,** 56, 2257.

141.) Andrae, D.; Haeussermann, U.; Dolg, M.; Stoll, H.; Preuss, H. *Theor. Chim. Acta*, **1990**, 77, 123.

142.) Mayer, I. *Chem. Phys. Lett.* **1983**, 97, 270; Mayer, I. *Int. J. Quantum Chem*. **1984**, 26, 151.

143.) Roos, B. O.; Taylor, P. R.; Siegbahn, P. E. M. *Chem. Phys.* **1980**, *48*, 157.

144.) Andersson, K.; Malmqvist, P. A.; Roos, B. O.; Sadlej, A. J.; Wolinski, K. *J. Phys. Chem.* **1990**, *94*, 5483.

145.) Aquilante, F.; De Vico, L.; Ferre, N.; Ghigo, G.; Malmqvist, P. A.; Neograd y, P.; Pederson, T. B.; Pitonak, M.; Reiher, M.; Roos, B. O.; Serrano-Andres, L.; Urban, M.; Veryazov, V.; Lindh, R. *J. Comp. Chem.* **2010,** *31*, 224.

146.) A.) Roos, B. O.; Lindh, R.; Malmqvist, P. A.; Veryazov, V.; Widmark, P. O. *J. Phys. Chem. A*. **2004**, 108, 2851. B.) Roos, B. O.; Lindh, R.; Malmqvist, P. A.; Veryazov, V.; Widmark, P. O. *J. Phys. Chem. A*. **2005**, 109, 6575.

147.) Hess, B. A. *Physical Review A.* **1986,** *33*, 3742.

148.) Bruno, I. J.; Cole, J. C.; Edgington, P. R.; Kessler, M.; Macrae, C. F.; McCabe, P.; Pearson, J.; Taylor, R. *Acta Crystallogr*., Sect. B 58 (2002) 389 (Searches conducted January 2016).

149.) Mugnier, Y.; Moise, C.; Laviron, E. *J. Organomet. Chem.* **1981**, *204*.

150.) Fakhr, A.; Mugnier, Y.; Gautheron, B.; Laviron, E. *J. Organomet. Chem.* **1986**, 3, C7-C9.

151.) Pauling, L. *J. Am. Chem. Soc*. **1947**, 69, 542.

152.) Chapman, A. M.; Wass, D. F. *Dalton Trans.* **2012**, 41, 9067.

153.) Chapman, A. M.; Haddow, M. F.; Wass, D. F. *Eur. J. Inorg. Chem*. **2012**, 1546.

154.) Lindahl, P.A.; *J. Inorg. Biochem*, **2012**, *106*, 172.

155.) Blackburn, N. J.; Barr, M. E.; Woodruff, W. H; van der Ooost, J.; de Vries, S. *Biochemistry*, **1994**, *33*, 10401.

156.) Farmer, J. A.; Campbell, C.T. *Science* **2010**, *329*, 933.

157.) Fu, Q.; Yang, F.; Bao. X. *Acc. Chem. Res*. **2013**, *46*, 1692.

158.) Schauermann, S.; Nilius, N.; Shaikhutdinov, S.; Freund, H. J. *Acc. Chem. Res*. **2012**, *46*, 1673.

159.) Campbell, C.T. *Acc. Chem. Res*. **2013**, *46*, 1712.

160.) Wu, B.; Wilding, M. J. T.; Kuppuswamy, S.; Bezpalko, M. W.; Foxman, B. M.; Thomas, C. M. *Inorg. Chem.* **2016**, *55*, 12137.

161.) Eisenhart, R. J.; Carlson, R. K.; Clouston, L. J.; Young, V. G., Jr.; Cheng, Y.-S.; Bill, E.; Gagliardi, L.; Lu, C. C. *Inorg. Chem.* **2015**, *54*, 11330.

162.) Clouston, L. J.; Bernales, V.; Cammarota, R. C.; Carlson, R. K.; Bill, E.; Gagliardi, L.; Lu, C. C. *Inorg. Chem.* **2015**, *54*, 11669.

163.) Dunn, P. L.; Carlson, R. K.; Gagliardi, L.; Tonks, I. A. *Dalton Trans*. **2016**, *45*, 9892.

164.) Talley, M. R.; Stokes, R. W.; Walker, W. K.; Michaelis, D. J. *Dalton Trans*. **2016**, *45*, 9770.

165.) Cotton, F. A.; Curtis, N. F.; Harris, C. B.; Johnson, F. G.; Lippard, S. J.; Mague, J. T.; Robinson, W. R.; Wood, J. S. *Science* **1964**, *145*, 1305.

166.) Cotton, F. A. *Inorg. Chem.* **1965**, *4*, 334.

167.) Ottmers, D. M.; Rase, H. F. *Carbon* **1966**, *4*, 1, 125.

168.) Zhao, Y.; Truhlar, D.G. *Theor. Chem. Acc.* **2008,** *120*, 215.

169.) Deeming, A. J.; Shinhmar, M. K. A. *J. Organomet. Chem.* **1999**, *592*, 2, 235

170.) Orpen, A. G.; Connelly, N. G. *Organometallics* **1990**, *9*, 1206.

171.) Collman, J. P.; Wagenknecht, P. S.; Hutchison, J. E. *Angew. Chem. Int. Ed.* **1994**, 33, 1537.

172.) Shoshani, M. M.; Johnson, S. A. *Nat. Chem.* **2017**, 9, 1282.

173.) Hu, S.; Shima, T.; Hou, Z. *Nature* **2014**, 512, 413.

174.) Nakajima, Y.; Suzuki, H. *Organometallics* **2005**, 24, 1860.

175.) Shima, T.; Hu, S.; Luo, G.; Kang, X.; Luo, Y.; Hou, Z. *Science* **2013**, 340, 1549.

176.) Powers T. M.; Fout, A. R.; Zheng, S.-L.; Betley, T. A. *J. Am. Chem. Soc.* **2011**, 133, 3336.

177.) Tsui, E. Y.; Tran, R.; Yano, J.; Agapie, T. *Nat. Chem*. **2013**, 5, 293.

178.) Kanaday, J. S.; Tsui, E. Y.; Day, M. W.; Agapie, T. *Science* **2011**, 333, 733.

179.) Lionetti, D.; Ruiter G. D.; Agapie, T. *J. Am. Chem. Soc.* **2016**, 138, 15, 5008.

180.) Murray, L. J.; Weare, W. W.; Shearer, J.; Mitchell, A. D.; Abboud, K. A. *J. Am. Chem. Soc.* **2014**, 136, 13502.

181.) Chao, S. T.; Lara, N. C.; Lin, S.; Day, M. W.; Agapie, T. *Angew. Chem. Int. Ed*. **2011**, 50, 7529.

182.) Lin, S.; Day, M. W.; Agapie, T. *J. Am. Chem. Soc*. **2011**, 133, 3828.

183.) Velian, A.; Lin. S.; Miller, A. J. M.; Day, M. W.; Agapie, T. *J. Am. Chem. Soc*. **2010,** 132, 6296.

184.) Pal, S.; Uyeda, C. *J. Am. Chem. Soc*. **2015**, 137, 8042.

185.) Pal, S.; Zhou, Y. –Y.; Uyeda, C.; *J. Am. Chem. Soc*. **2017**, 139, 11686.

186.) Hartline, D. R.; Zeller, M. Uyeda, C. *J. Am. Chem. Soc*. **2017**, 139, 13672.

187.) Behlen, M. J.; Zhou, Y. –Y.; Steiman, T. J.; Pal, S.; Hartline, D. R.; Zeller, M.; Uyeda, C. *Dalton Trans.* **2017**, 46, 5493.

188.) Hartline, D. R.; Zeller, M.; Uyeda, C. *Angew. Chem. Int. Ed.* **2016**, 128, 6188.

189.) Zhou, Y. –Y.; Uyeda, C. *Angew. Chem. Int. Ed.* **2016**, 128, 3223.

190.) Steiman, T. J.; Uyeda, C. *J. Am. Chem. Soc.* **2015**, 137, 6104.

191.) Zhou, Y. –Y.; Hartline, D. R.; Steiman, T. J.; Fanwick, P. E.; Uyeda, C. *Inorg. Chem*. **2014**, 53, 11770.

192.) Powers, I. G.; Andjaba, J. M.; Luo, X.; Mei, J.; Uyeda, C. *J. Am. Chem. Soc.* DOI: 10.1021/jacs.8b00503

193.) DeLaet, D.; Fanwick, P. E.; Kubiak, C. P.; *Organometallics* **1986**, 5, 1807.

194.) Barrios-Francisco, R.; Benitez-Paez, T.; Flores-Alamo, M.; Arevalo, A.; Garcia, J. J.; *Chem. Asian J.* **2011**, 6, 842.

195.) Gambarotta, S.; Floriana, C.; Chiesi-Villa, A.; Gustini, C. *J. Chem. Soc., Chem Commun*. **1982**, 0, 1015.

196.) Ikeda, H.; Nishi, K.; Tsurugi, H.; Mashima, K. *Chem. Comm.* DOI: 10.1039/c7cc08570b

197.) F. A. Cotton, S. A. Duraj and W. J. Roth, *J. Am. Chem. Soc*. **1984**, 106, 4749.

198.) J. A. M. Canich, F. A. Cotton, S. A. Duraj and W. J. Roth, *Polyhedron* **1986**, 5, 895.

199.) Hill, J.E.; Fanwick, P. E.; Rothwell, I. P. *Inorg. Chem.* **1991**, 30, 1143.

200.) Kilgore, U. J.; Yang, X.; Tomaszewski, J.; Huffman, J. C.; Mindiola, D. J. *Inorg. Chem*. **2006**, 45, 10712.

201.) Monillas, W. H.; Yap, G. P. A.; MacAdams, L. A.; Theopold, K. H. *J. Am. Chem. Soc.* **2007**, 129, 8090.

202.) Lockwood, M. A.; Fanwick, P. E.; Eisenstein, O.; Rothwell, I. P. *J. Am. Chem. Soc.* **1996**, 118, 2762.

203.) Tsai, Y.-C.; Wang, P.-Y.; Chen, S.-A.; Chen, J.-M. *J. Am. Chem. Soc*. **2007**, 129, 8066.

204.) Aubart, M. A.; Bergman, R. G. *Organometallics* **1999**, 18, 811.

205.) Kaleta, K.; Arndt, P.; Beweries, T.; Spannenberg, A.; Theilmann, O. *Organometallics* **2010**, 29, 2604.

206.) Milsmann, C.; Turner, Z. R.; Semproni, S. P.; Chirik, P. J. *Angew. Chem., Int. Ed*. **2012**, 51, 5386.

207.) Shaver, M. P.; Fryzuk, M. D. *J. Am. Chem. Soc*. **2005**, 127, 500.

208.) Wu, B.; Gramigna, K.; Bezpalko, M. W.; Foxman, B. M.; Thomas, C. M *Inorg. Chem*. **2015**, 54, 10909.

209.) Verma, A. K.; Lee, S. C. *J. Am. Chem. Soc.* **1999**, *121*, 10838.

210.) Kiernicki, J. J.; Zeller, M.; Szymczak, N. K. *J. Am. Chem. Soc*. **2017**, 139, 18194.

211.) Bellows, S. M.; Arnet, N. A., Prabhuodeyara, M. G.; Brennessel, W.W.; Eckhard, B.; Cundari, T. R.; Holland, P. L. *J. Am. Chem. Soc.* **2016**, 138, 12112.

212.) Waterman, R.; Hillhouse, G. L.; *J. Am. Chem. Soc.* **2008**, 130, 12628.

213.) Mindiola, D. K.; Hillhouse, G. L. J. *Am. Chem. Soc.* **2001**, 123, 2001.

214.) Jenkins, D. M.; Betley, T. A.; Peters, J. C.; *J. Am. Chem. Soc.* **2002**, 124, 11238.

215.) Cotton, F. A.; Curtis, N. F.; Harris, C. B.; Johnson, B. F. G.; Lippard, S. J.; Mague, J. T.; Robinson, W. R.; Wood, J. S. *Science* **1964**, 145, 1305.

216.) Cotton, F. A. *Inorg. Chem.* **1965**, 4, 334.

217.) Cotton, F. A.; Harris, C. B. *Inorg. Chem.* **1965**, 4, 330.

218.) Cotton, F. A. *J. Chem. Educ*. **1983**, 60, 713.

219.) Dunn, P. L.; Carlson, R. K.; Tonks, I. A. *Inorg. Chim. Acta* **2017**, 460, 43.

220.) Gade, L. H. *Angew. Chem., Int. Ed.* **2000**, 39, 2658.

221.) Culcu, G.; Iovan, D. A.; Krogman, J. P.; Wilding, M. J. T.; Bezpalko, M. W.; Foxman, B. M.; Thomas, C. M. *J. Am. Chem. Soc*. **2017**, 139, 9627.

222.) Bruno, I. J.; Cole, J. C.; Edgington, P. R.; Kessler, M.; Macrae, C. F.; McCabe, P.; Pearson, J.; Taylor, R. *Acta Crystallogr*. Sect. B 58 (2002) 389 (Searches conducted January 2018).

223.) Butts, M. D.; Bergman, R. G. *Organometallics* **1994,** *13*, 1899.

224.) Laskar, P.; Yamamoto, K.; Srinivas, A.; Mifleur, A.; Nagae, H.; Tsurugi, H.; Mashima, K. *Dalton Trans*. **2017**, 46, 13043.

225.) Pätow, R.; Isaac, I.; Fenske, D. *Z. anorg. allg. Chem*. **2003,** 629, 1437.

226.) Kuppuswamy, S.; Cass, T. R., Bezpalko, M. W., Foxman, B. M., Thomas, C. M. *Inorg. Chim. Acta.* **2015**, 424, 167.

227.) Moore, J. T.; Smith, N. E.; Lu, C. C. *Dalton Trans*. **2017**, 46, 5689.

228.) Leelasubcharoen, S.; Zhizhko, P. A.; Kuzmina, L. G.; Churakov, A. V.; Howard, J. A. K.; Nikonov, G. I. *Organometallics* **2009**, 28, 4500.

229.) Nikonov, G. I.; Lemenovskii, D. A.; Kuzmina, L. G.; *J. Organomet. Chem*. **1995,** 496, 187.

230.) Findlay, A. E.; Leelasubcharoen, S.; Kuzmina, L. G.; Howard, J. A. K.; Nikonov, G. I. *Dalton Trans*, **2010**, 39, 9264.

231.) Yamamoto, K.; Higashida, K.; Nagae, H.; Tsurugi, H.; Mashima, K. *Helv. Chim. Acta*, **2016**, 99, 848.

232.) Oishi, M.; Kino, M.; Saso, M.; Oshima, M.; Suzuki, H. *Organometallics* **2012**, 31, 4658.

233.) Butts, M. D.; Bergman, R. G. *Organometallics* **1994**, 13, 2668.

234.) Hostetler, M. J.; Butts, M. D.; Bergman, R. G. *Inorg. Chim. Acta*. **1992***,* 198, 337.

235.) Hostetler, M. J.; Bergman, R. G. *J. Am. Chem. Soc*. **1990**, 112, 8621.

236.) Goldberg, K. I.; Bergman, R. G. *J. Am. Chem. Soc.* **1988**, 110, 4853.

237.) Marchetti, F.; Pampaloni, G.; Zacchini, S. *Inorg. Chem*. **2008**, 47, 365.

238.) Schunn, R. A.; Ittel, S. D.; Cushing, M. A. *Inorganic Syntheses*. **1990**, 28, 94.

239.) Chen, H.-Z.; Liu, S.-C.; Yen, C.-H.; Yu, J.-S. K.; Shieh, Y.-J.; Kuo, T.-S.; Tsai, Y.-C. *Angew. Chem. Int. Ed*. **2012**, 51, 10342.

240.) Noor, A.; Wagner, Frank R.; Kempe, R. *Angew. Chem. Int. Ed*. **2008**, 47, 7246.

241.) Noor, A.; Glatz, G.; Müller, R.; Kaupp, M.; Demeshko, S.; Kempe, R. *Z. anorg. allg. Chem.* **2009**, 635, 1149.

242.) Noor, A.; Glatz, G.; Muller, R.; Kaupp, M.; Demeshko, S.; Kempe, R. *Nat. Chem*. ***2009****,* 1, 332.

243.) Noor, A.; Bauer, T.; Todorova, T. K.; Weber, B.; Gagliardi, L.; Kempe, R. *Chem. Eur. J*. **2013,** 19, 9825.

244.) Hsu, C.-W.; Yu, J.; Shiang K.; Yen, C.-H.; Lee, G.-H.; Wang, Y.; Tsai, Y.-C. *Angew. Chem. Int. Ed*. **2008**, 47, 9933.

245.) Cotton, F. A.; Niswander, R. H.; Sekutowski, J. C.; *Inorg. Chem.* **1979,** 18, 1152.

246.) Chiarella, G. M.; Cotton, F. A.; Durivage, J. C.; Lichtenberger, D. L.; Murillo, C. A. *J. Am. Chem. Soc*. **2013,** *135*, 17889.

247.) Kuppuswamy, S.; Bezpalko, M. W.; Powers, T. M.; Wilding, M. J. T.; Brozek, C. K.; Foxman, B. M.; Thomas, C. M. *Chem. Sci.* **2014**, *5*, 1617.

248.) Matter, G. G.; Pidcock, A. *J. Chem. Soc. A*, **1970**, 0, 1226.

249.) Shyu, S.-G.; Lin, P.-J.; Lin, K.-J.; Chang, M.-C.; Wen, Y.-S. *Organometallics* **1995**, *14*, 2253.

250.) Shyu, S.-G.; Lin, P.-J.; Wen, Y.-S. *J. Organomet. Chem.* **1993**, *443*, 115.

251.) Shyu, S.-G.; Lin, P.-J.; Dong, T.-Y.; Wen, Y.-S. *J. Organomet. Chem.* **1993**, *460*, 229.

252.) Shyu, S.-G.; Hsiao, S.-M.; Lin, K.-J.; Gau, H.-M. *Organometallics* **1995**, *14*, 4300.

253.) Shyu, S.-G.; Wu, J.-S.; Chuang, S.-H.; Chi, K.-M.; Sung, Y.-S. *Chem. Commun*. **1996**, 2239.

254.) Song, L.-C.; Wang, J.-Q.; Zhao, W.-J.; Hu, Q.-M.; Fang, Y.-Q.; Zhang, S.-J.; Wang, R.-J.; Wang, H.-G. *J. Organomet. Chem*. **1993**, *453*, 105.

255.) Song, L.-C.; Shen, J.-Y.; Wang, J.-Q.; Hu, Q.-M.; Wang, R.-J.; Wang, H.-G. *Polyhderon* **1994**, *13*, 3235.

256.) Stille, J. K.; Smith, C.; Anderson, O. P.; Miller, M. M. *Organometallics* **1989**, *8*, 1040.

257.) Sundermeyer, J.; Runge, D. *Angew. Chem*., *Int. Ed. Engl*. **1994**, *33*, 1255.

258.) Sundermeyer, J.; Runge, D.; Field, J. S. *Angew. Chem*., *Int. Ed. Engl*. **1994**, *33*, 678.

259.) Bradley, D. C.; Hursthouse, M. B.; Malik, K. M. A.; Nielson, A. J.; Short, R. L. *J. C. S. Dalton.* **1983**, 2651.

260.) Schrock, R. R.; Murdzek, J. S.; Bazan, G. C.; Robbins, J.; DiMare, M.; Oregan, M. *J. Am. Chem. Soc.* **1990,** *112*, 3875.

261.) Chou, C. Y.; Huffman, J. C.; Maatta, E. A. *J. Chem. Soc. Chem. Commun.* **1984**, 1184.

262.) Maria, S.; Poli, R.; Gallagher, K. J.; Hock, A. S.; Johnson M. J. A. *Inorganic Syntheses* **2014**, 36.

Appendix A

Table A.1: Bond XRD and DFT bond metrics for **3.2-3.4**.

	3.2	**3.2** DFT	**3.3**	**3.3** DFT	**3.4**	**3.4** DFT
M-M	2.267	2.266	2.373	2.396	2.413	2.437
P-Ni	2.218, 2.191, 2.235	2.193, 2.239, 2.212	2.216, 2.225, 2.198	2.235, 2.198, 2.213	2.207, 2.217, 2.195	2.192, 2.206, 2.230
<P-Ni-P	112.47, 135.91, 110.19	111.27, 112.13, 135.81	118.74, 131.62, 110.12	112.42, 134.34, 113.84	110.61, 131.52, 117.71	134.18, 112.44, 113.38
M-N	2.08, 2.043, 2.109, 2.105	2.134, 2.094, 2.063, 2.083	2.222, 2.191, 2.174, 2.228	2.195, 2.257, 2.215, 2.217	2.151, 2.176, 2.205, 2.202	2.247, 2.206, 2.205, 2.183
M-P	2.2722	2.740	2.88	2.870	2.854	2.856
<N-Ti-N	94.10, 104.42	106.95, 93.63	96.99, 103.49	95.94, 108.45	96.34, 103.02	95.72, 107.59
<N-Ti-P	83.71, 76.23	76.93, 81.05	79.32, 79.75	75.71, 79.37	80.14, 80.21	76.30, 80.00
Torsion Angles (P-Ni-M-N)	5.83, 20.71, 26.53	9.05, 27.44, 32.05	3.46, 30.80, 24.16	7.86, 22.99, 29.75,	2.45, 28.68, 21.4	8.23, 25.59, 30.47

Table A.2. 3.5 CASSCF spin density.

	Ti	Ni
spin density	1.0061	-0.0144

Table A.3. 3.5 CASSCF Mulliken charges.

Complex #	M	Ni
3.2	1.4948	0.05390
3.5	1.5537	-0.0992
3.3	2.5469	-0.2921
3.4	2.2678	-0.1891

Table A.4. CASSCF electron count and effective oxidation state for **3.5.**

#	type	%Ti	%Ni	total elec	Ti elec	Ni elec
	d	0	100	1.96	0	1.96
	d	0	100	1.96	0	1.96
	d’	0	100	0.03	0	0.03
	d’	0	100	0.03	0	0.03
	sigma	9.4	90.6	1.90	0.18	1.72
	d’	0	86.8	0.04	0	0.03
	sigma*	38.0	40.7	0.10	0.04	0.04
	d	0	100	1.97	0	1.97
	d’	0	90.8	0.04	0	0.03
	d	0	100	1.97	0	1.97
	d	100	0	1.00	1.00	0.00
	d’	0	100	0.01	0	0
Total elec					1.22	9.75
ox state					+2.78	+0.25

Table A.5. CASSCF electron count and effective oxidation state for **3.2.**

#	type	%Ti	%Ni	total elec	Ti elec	Ni elec
	d	0	100	1.98	0	1.98
	d	0	100	1.98	0	1.98
	sigma	5.7	94.2	1.87	0.11	1.76
	pi	28.8	71.2	1.63	0.47	1.16
	sigma *	76.5	13.8	0.12	0.09	0.02
	pi*	66.3	30.3	0.36	0.24	0.11
	d’	2.6	97.4	0.03	0.00	0.02
	d’	5.8	93.0	0.01	0.00	0.01
	d	0	100	1.97	0.00	1.97
	d’	0	100	0.02	0.0	0.02
	d’	0	100	0.02	0.0	0.02
	d’	29.0	70.9	0.01	0.0	0.01
Total elec					0.91	9.06
ox state					+3.09	+0.94

Table A.6. CASSCF electron count and effective oxidation state for **3.3.**

#	type	%Zr	%Ni	total elec	Zr elec	Ni elec
	d	0	100	1.96	0	1.96
	d	0	100	1.97	0	1.97
	d	0	100	1.97	0	1.97
	d	0	100	1.93	0	1.93
	d’	0	100	0.03	0	0.03
	sigma	5.8	94.2	1.92	0.11	1.81
	sigma*	48.1	40.4	0.07	0.03	0.03
	d’	12.5	84.4	0.04	0.01	0.04
	d’	39.2	48.0	0.06	0.03	0.03
	d’	0	100	0.03	0	0.03
	d’			0.004		
	d’			0.004		
Total elec					0.18	9.80
ox state					+3.82	+0.20

Table A.7. CASSCF electron count and effective oxidation state for **3.4.**

#	type	%Hf	%Ni	total elec	Hf elec	Ni elec
	d	0	100	1.97	0	1.97
	d	0	100	1.97	0	1.97
	d	2.2	97.7	1.94	0.04	1.89
	d	0	100	1.96	0	1.96
	sigma	6.6	93.3	1.92	0.13	1.80
	d’	29.9	57.5	0.06	0.02	0.03
	d’	0	100	0.03	0	0.03
	d’	7.2	89.6	0.04	0.00	0.04
	sigma*	40.6	43.5	0.07	0.03	0.03
	d’	0	100	0.03	0	0.03
	d’			0.003		
	d’			0.004		
Total elec					0.36	9.72
ox state					+3.64	+0.28

Table A.8. **3.2** neutral relative spin state energies (kcal/mol).

	CASSCF	CASPT2
singlet	0.0	0.0
triplet	7.0	26.1

Table A.9. **3.5** relative spin state energies (kcal/mol).

	CASSCF	CASPT2
doublet	0.0	0.0
quartet	31.6	42.2

Table A.10. 3.3 relative spin state energies (kcal/mol).

	CASSCF
singlet	0.0
triplet	56.1

Table A.11. 3.4 relative spin state energies (kcal/mol).

	CASSCF
singlet	0.0
triplet	141.7

*CASPT2 calculations were not performed since the spins states were well separated at the CASSCF level.

Table A.12. DFT orbital relative energies on M06L optimized structures (eV) of **3.5.**

	M06L	M06 (single point on M06L geom)
Ni xz	0.00	0.00
Ni yz	0.09	0.04
sigma/dz^2	0.12	0.18
Ni xy	0.50	0.93
Ni X^2-y^2	0.76	1.26
Ti xz SOMO	2.24	3.26
Ti yz LUMO	2.65	4.70

Table A.13. DFT orbital relative energies on M06L optimized geometries (eV) of **3.2.**

	M06L	M06 (Single point on M06L geom)
Ni yz	0.11	0.00
pi/xz	0.13	0.07
sigma/dz^2	0.00	0.24
Ni xy	1.19	1.84
Ni X^2-y^2 (HOMO)	1.46	1.94
Ti xz (LUMO)	3.07	5.15
Ti yz	3.17	5.28

Table A.14. DFT orbital relative energies on M06L optimized structure (eV) of **3.3.**

	M06L	M06 (single point on M06L geom)
Ni xz	0.00	0.00
Ni yz	0.08	0.04
sigma/dz^2	0.13	0.29
Ni xy	1.11	1.60
Ni X^2-y^2 (HOMO)	1.35	1.73
Zr xz (LUMO)	3.68	5.66
Zr yz	3.89	5.84

Table A.15. DFT orbital relative energies on M06L optimized strucutre (eV) of **3.4.**

	M06L	M06 (single point on M06L geom)
Ni yz	0.00	0.00
Ni xz	0.06	0.10
sigma/dz^2	0.11	0.12
Ni xy	0.98	0.80
Ni X^2-y^2 (HOMO)	1.24	1.15
Hf dz (LUMO)	3.62	3.18

Table A.16. Relative Molecular Orbital Energies (ev) for **4.1.**

	M06L	M06 (single point on M06L geometry)
pi (dxz)	0.0	0.0
pi (dyz)	0.0	0.0
sigma (dz^2)	0.1	0.3
Fe dxy	0.2	0.5
Fe dx^2-y^2	3.0	5.5

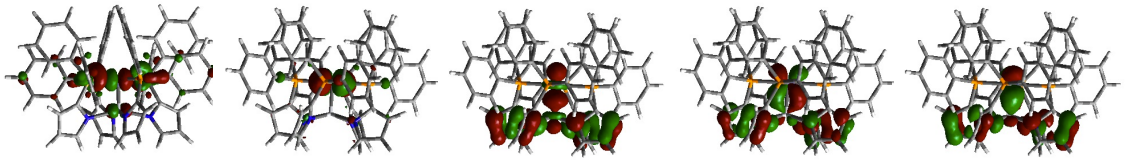

Figure A.1. DFT computed molecular orbital for complex **4.1**. From left to right, dx2-y2, dxy, dz2, pi(dxz), and pi(dyz).

Table A.17. Relative Molecular Orbital Energies (ev) for **4.2.**

	M06L	M06 (single point on M06L geometry)
pi (dxz)	0.0	0.0
pi (dyz)	0.04	0.06
sigma (dz^2)	0.2	0.4
Fe dxy (HOMO)	1.2	1.5
Fe dx^2-y^2 (LUMO)	1.3	1.7

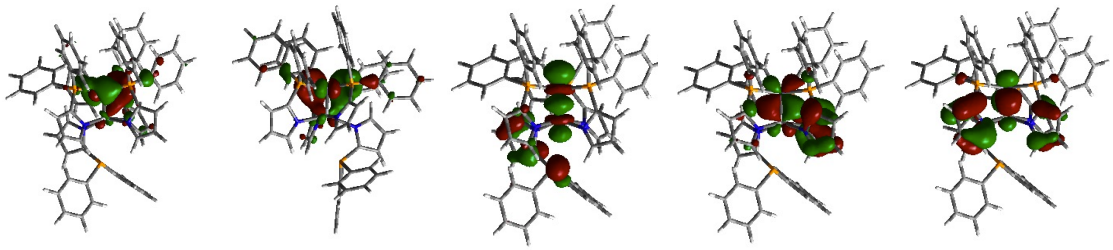

Figure A.2. DFT computed molecular orbitals for complex **4.2**. From left to right, dxy, dx2-y2, dz2, pi(dxz), and pi(dyz).

Table A.18. Relevant bond lengths (Å) and angles (°) for **4.1** and **4.2** from M06L geometries.

	4.1	**4.2**
Ti-Fe (Å)	2.022	1.920
Mayer Bond order	1.48	1.83
P-Fe (Å)	2.375	2.199
		2.210
		2.210
P-Fe-P (°)	89.991(1)	106.9
	89.998(1)	119.9
		130.0
Ti-N (Å)	2.099	2.151
		2.179
		2.184
		2.204
Torsional Angle (P-Fe-Ti-N) (°)	27.9	-17.4
		11.6
		30.2
Mulliken Charge Fe		
Ti	-0.4674	-0.0363
	1.4175	0.3799